

Technische Universität München

Ingenieur fakultät Bau Geo Umwelt

Lehrstuhl für Astronomische und Physikalische Geodäsie

**Investigation of the residual terrain modelling (RTM)
technique for
high-frequency gravity calculations**

Meng Yang

Vollständiger Abdruck der von der Ingenieur fakultät Bau Geo Umwelt der Technischen Universität München zur Erlangung des akademischen Grades eines

Doktor-Ingenieurs (Dr.-Ing.)

genehmigten Dissertation.

Vorsitzender:

Prof. Dr.-Ing. Liqiu Meng

Prüfer der Dissertation:

1. Hans-Fischer-Fellow Dr.-Ing. Christian Hirt

2. Prof. Dr.techn. Roland Pail

3. Prof. Dr.-Ing. Dimitrios Tsoulis, Aristotle University of Thessaloniki

Die Dissertation wurde am 16.10.2019 bei der Technischen Universität München eingereicht und durch die Ingenieur fakultät Bau Geo Umwelt am 16.12.2019 angenommen.

Acknowledgments

First and foremost, I express my deepest gratitude to my supervisors Univ.-Prof. Dr.techn. Mag.rer.nat. Roland Pail and Dr.-Ing. Christian Hirt for their keen interest, innovative suggestions, guidance and scientific support throughout the course of this research. I have been incredibly fortunate to have them as my supervisors. Dr. Christian Hirt was pivotal in developing the study design, was supportive during my fieldwork, patiently gave me research directions and scientific guidance, and provided insightful comments during the preparation and review of all manuscripts for publication and an indepth review of my PhD thesis. Prof. Roland Pail always gave me valuable scientific assistance as needed, and has undergone a comprehensive review of this thesis, and provided constructive suggestions for future work plan.

I cordially acknowledge all my colleagues at the IAPG for their help and encouragement during my time at TUM. I would like to thank Prof. Reinhard Rummel who was so generous with his time in reviewing this thesis. Special thanks goes to Dr. Moritz Rexer for kindly sharing his experiences and for providing the software for numerical evaluation of forward moelling in the spectral domain. I offer my sincere thanks to Dr.-Ing. Thomas Gruber and Dipl.-Ing. Anna Purkhauser for their assistance. I am also indebted to my manuscript co-authors Michael Kuhn, Robert Tenzer, Blazej Bucha, Moritz Rexer and Dai Yamazaki for discussions and their assistance with field work. Funding for this PhD research was provided by the China Scholarship Council which is hereby acknowledged.

Many thanks to my Chinese friends, Shan Zhao, Guangxin Sun, Jun Yang, Xiaohan Leng, Pu Li, Bingbing Duan, Ningbo Wang, Qingchen Zhang, Wei Liang, and Xingchi He for making my time in Munich enjoyable and memorable.

Lastly, I could not have made it without the love and support from my beautiful family, particularly my parents and my sister. From them, I have received endless encouragement, concern, and strength all these years. I would also like to express my heartfelt gratitude and love to my husband, LI Fei, who has stood by me and encouraged me throughout this endeavour.

Zusammenfassung

Die schnelle und genaue Vorwärtsmodellierung des topographischen Gravitationspotentials, seiner Gradienten und zweiten Ableitungen, generiert durch eine beliebig geformte 3D-Geometrie und zugehöriger Massendichteverteilung, stellt eine Voraussetzung für viele geodätische und geophysikalische Anwendungen dar. Zu diesem Zweck wurde im Rahmen dieser Arbeit eine neue Matlab-basierte Software TGF entwickelt, welche die Berechnung von zehn Schwerefeldfunktionalen bei unterschiedlicher spektraler Bandbreite ermöglicht. Dies inkludiert die hochfrequente sowie die topographische Modellierung über alle Skalen hinweg und wird realisiert durch eine Kombination von vier Arten von elementaren Massenelementen, d.s. Polyeder, Prisma, Tesseroid und Punktmasse. Als Eingangsdaten werden digitale Geländemodelle (engl. digital elevation models, DEM) und Informationen zur Massendichte verwendet. Die internen und externen Validierungen zeigen eine Genauigkeit von TGF im sub-mGal-Bereich bei Berechnung der vollständigen wie auch der residualen geländemodellierten (RTM – residual terrain modelling) Schwerestörungen.

Mit dem Fokus auf hochfrequenter Schwerefeldmodellierung wurden drei RTM-Berechnungsvarianten (RTM-A, RTM-B und RTM-C), die auf unterschiedlichen Vereinfachungen und Annahmen basieren, wie z.B. Fehler aufgrund der harmonischen Korrektur, Vereinfachungen in der Massenverteilung, und Inkonsistenzen hinsichtlich der Lage des Berechnungspunkts, untersucht und miteinander verglichen. Die RTM-A Lösungen unter Verwendung eines detaillierten und eines langwelligen Geländemodells erzielten in einem Testgebiet mit sehr rauer Topografie die beste Übereinstimmung mit einem RMS der Differenzen im sub-mGal-Bereich im Vergleich zu einer hochgenauen RTM-Referenzlösung. Die Tatsache, dass die Differenzen vorwiegend positiv waren, deutet auf eine unzureichende harmonische Korrektur mittels der häufig verwendeten Kondensationstechnik hin. Im Rahmen der RTM-A Methode können die Differenzen im sub-mGal-Bereich zwischen ellipsoidischer und sphärischer Approximation vernachlässigt werden.

Um die häufig verwendete konstante Dichteannahme zu vermeiden, wurde eine Kombination der RTM-A Methode mit 1) einem hochauflösenden Massendichte-Modell, oder 2) berechneten optimalen regionalen Dichten im Testgebiet Neuseeland untersucht. Es ergaben sich Dichtewerte von $\sim 2,500 \text{ kg/m}^3$ für die Nordinsel, $\sim 2,600 \text{ kg/m}^3$ für die Südinsel, und $\sim 2,590 \text{ kg/m}^3$ als Mittelwert für die gesamte Region Neuseelands. Die RTM-Schwere wurde mit unterschiedlichen Kombinationen von Höhenmodellen und Dichteannahmen berechnet und dann mit terrestrischen Schwerebeobachtungen und GPS/Nivellement-Beobachtungen verglichen. Da sich die Dichtekarte vorwiegend auf Bereiche nahe der Oberfläche bezieht, ergaben sich die besten Ergebnisse in Gebieten mit kleinen residualen Höhen, während tieferliegende Dichteanomalien die Resultate mit

größeren residualen Höhen stark beeinflussten. Dieser Effekt macht bis zu 30 mGal im Bereich der Alpenin Verwerfung der Südinsel aus.

Außerdem wurde der Effekt der Vegetation auf die Schwerefeldmodellierung untersucht. Die spektrale Vorwärtsmodellierung wurde in globalem Maßstab angewandt, um ein globales Vegetations-Bias Modell mit 1 km Auflösung zu analysieren und seine Auswirkungen auf globale Schwerefeldmodellierung zu quantifizieren. Regional verwendeten wir das SRTM V4.1 Modell (das den Vegetationsbias enthält) und das MERIT DEM (das die Gelände-Oberkante widerspiegelt). Der Effekt des Vegetationsbias wurde in den Regionen Tasmanien, Australische Alpen, kanadische Rocky Mountains und dem Amazonas-Regenwald untersucht. Im Allgemeinen verursacht die in Geländemodellen enthaltene Vegetationshöhe einen positiven Bias in den vollen topografischen Schwerestörungen mit Werten bis zu ~ 2.7 mGal, und einen hochfrequenten Effekt bei RTM-Berechnungen mit maximalen Amplituden von 1 – 2 mGal an Waldrändern. Zahlreiche Validierungsexperimente, in welchen modellierte und real beobachtete Schwerewerte verglichen wurden, demonstrierten die bessere Performance des MERIT-DEM.

Abstract

Due to the inhomogeneous distribution and variable quality of available gravity datasets, derived models of Earth's external gravity field generally provide limited level of details, e.g., the state-of-the-art global gravity model EGM2008 does not provide signals finer than ~ 9 km. Assuming the spectral consistency between topography and its implied gravity field, the finer gravity signals can be obtained by residual terrain modelling (RTM) technique, which relies exclusively on the knowledge of topography as provided by digital elevation model and mass-density distribution commonly with constant density assumption. With a focus on the high-frequency gravity forward modelling (GFM), this thesis contributes to state-of-the-art GFM in the space domain by investigating various approximation effects in the RTM GFM and by providing a new software for effective and accurate GFM.

In this thesis, three different RTM variants (RTM-A, RTM-B, and RTM-C) which are based on various simplifications and assumptions, e.g., errors due to harmonic correction, mass simplification, and computation point inconsistency, were studied in a comparative manner. The RTM-A solutions, by using a detailed and a reference topography grid, achieved the best agreement (at sub-mGal level in terms of RMS) with RTM-baseline solutions over the roughest mountains, but were affected by errors associated with the harmonic correction over areas of non-harmonicity. With RTM-A technique, the differences at sub-mGal level caused by applications of ellipsoidal or spherical approximations could be neglected for the mGal-level gravity field determination.

In order to avoid the conventionally used constant rock-density assumption, another effort was made through combining the RTM-A technique with 1) a high-resolution mass-density model, or 2) calculated regional optimum densities, $\sim 2,500 \text{ kg/m}^3$ for North Island, $\sim 2,600 \text{ kg/m}^3$ for South Island of, and $\sim 2,590 \text{ kg/m}^3$ the whole New Zealand. The RTM gravity quantities were computed with different combinations of elevation models and mass-density assumptions, and then validated using ground gravity and GPS/leveling measurements. Due to the shallow representation of the mass-density map, the density model performed best over areas with small residual heights, while subsurface density variations appeared to affect the performance over areas with large residual heights.

The role of the tree canopy effect on GFM was studied globally based on spectral forward modelling technique and regionally with spatial domain integration method. In terms of datasets, a 1 km global tree-bias map, SRTM V4.1 model (containing vegetation biases) and MERIT-DEM (the bare-ground elevations) were used for GFM, and terrestrial gravity observations for validation. In general, the tree canopy generates a positive

bias in the full-scale topographic gravity disturbances with values ranging from 0 to ~ 2.7 mGal, and a high-frequency effect on RTM calculations which reaches extreme amplitudes of $\sim 1-2$ mGal occurring at forest boundaries.

To handle the increased computational demand, we developed a new Matlab-based program, TGF, that enables calculation of ten various gravity field functionals at different spectral bandwidths, through a combination of four different types of elementary mass-elements, i.e., polyhedron, prism, tesseroid and point mass. The internal and external numerical validations suggest sub-mGal accuracy of TGF in calculation of the full-scale and the RTM gravity disturbances.

Contents

Acknowledgments	III
Zusammenfassung	V
Abstract	VII
Contents	X
Abbreviations	XI
1 Introduction	1
1.1 Background and motivation	1
1.2 Research objectives	5
1.3 Outline	6
2 Foundation	9
2.1 General aspects	9
2.1.1 Coordinate systems	9
2.1.2 General aspects of potential theory	12
2.2 Gravity Forward Modelling	15
2.2.1 Numerical evaluation of Newtonian integral	16
2.2.2 Spectral domain methods	17
2.2.3 Spatial domain methods	19
2.3 RTM and all variants	29
2.4 Combination of GGM and RTM	39
3 Databases	41
3.1 Forward modelling datasets and preprocessing	42
3.1.1 DEM Models	42
3.1.2 Global Tree Canopy models	48
3.1.3 Density Models	49
3.2 Ground measurements and models for validation	51
3.2.1 Terrestrial Gravity Measurements	51

3.2.2	GPS/leveling datasets	52
3.2.3	GGM gravity field	53
4	Software development	55
4.1	Description of the software	56
4.1.1	TGF: combination of geometric models	56
4.1.2	TGF: structure and function	60
4.2	Numerical test and validation of the software	64
4.2.1	Computation time of four forwarding methods	64
4.2.2	External validation in topographic field calculation	65
4.2.3	External validation of RTM gravity field calculation	67
4.2.4	Efficiency and internal validation	70
4.2.5	Polyhedron and prism comparison	73
4.2.6	RTM gravity field over Zugspitze area	75
5	Numerical examination of RTM techniques	79
5.1	Modelling errors	80
5.1.1	RTM modelling error	80
5.1.2	Reference geometry error	84
5.2	Observation errors	86
5.2.1	Mass-density errors	86
5.2.2	DEM errors	101
5.2.3	Summary	120
6	Summary and outlook	121
6.1	Summary	121
6.2	Recommendations for future work	125
	Bibliography	137
	A Appendix A	139
	Publications	139
	B Appendix B	141
	Statement of contribution of others	141
B.1	Publication I: Experiences with the use of mass density maps in residual gravity forward modelling	141

Abbreviations

3D	three dimensions
ALOS	Advanced Land Observing Satellite
ASTER	Advanced Spaceborne Thermal Emission and Reflection
AW3D	ALOS World 3D
BVP	Boundary Value Problem
CHAMP	Challenging Minisatellite Payload
DBM	Digital Bathymetric Model
DEM	Digital Elevation Model
DSM	Digital Surface Model
DTM	Digital Terrain Model
EGM2008	Earth Gravitational Model 2008
FFT	Fast-Fourier Transform
GECO	GOCE and EGM2008 combination
GGM	global gravity model
GGMplus	Global Gravity Model plus
GLQ	Gauss-Legendre Quadrature
GPS	Global Positioning System
GOCE	Gravity field and steady-state Ocean Circulation Explorer
GRACE	Gravity Recovery and Climate Experiment
LiDAR	Light Detection And Ranging
MERIT	Multi-Error-Removed Improved-Terrain
NI	Numerical Integration
PEM	Parameter Earth Model
PREM	Preliminary Reference Earth Model
RCR	Remove-Compute-Restore
RET	Rock-Equivalent-Topography

RMS	Root-Mean-Square
RTM	Residual Terrain Modelling
SGM	Spectral Gravity Modelling
SH	Spherical harmonic
SHA	Spherical Harmonic Analysis
SHC	Spherical Harmonic Coefficient
SHS	Spherical Harmonic Synthesis
SRTM	Shuttle Radar Topography Mission
TanDEM-X	TerraSAR-X-Add-on for Digital Elevation Measurements
TGF	Terrain Gravity Field

List of Figures

2.1	The spherical and ellipsoidal coordinate systems, (a) the spherical coordinate system, (b) the ellipsoidal coordinate system.	10
2.2	Global Cartesian coordinate system and local north-oriented coordinate system (LNCS).	11
2.3	Local coordinate system and geometry of polyhedron element	21
2.4	Prism-based local Cartesian coordinate system and geometry of prism element	22
2.5	Transformation between the station-based and prism-based Cartesian coordinate system, adapted from Heck and Seitz (2007, P.126).	24
2.6	Geometry of tesseroid, adapted from Grombein et al (2013, P647)	26
2.7	General flow chart of RTM technique in the spatial domain.	30
2.8	RTM in spectral domain and with combined technique.	31
2.9	RTM principle of residual terrain masses over point P_1 located exterior to the residual masses and point P_2 above or on the Earth's surface but below the reference surface.	31
2.10	RTM forward modeling methods	35
3.1	SRTMV4.1 geolocation shifts over Amazon area: (a) Height differences between MERIT elevation H_{MERIT} and SRTM V4.1 elevation $H_{SRTMV41}$; (b) Height differences between MERIT elevation and shifted SRTM V4.1 elevation $H_{SRTMV41}^{shift}$	46
3.2	SRTMV4.1 geolocation shifts over Tasmania area south of -43° latitude: (a) Height differences between MERIT elevation H_{MERIT} and SRTM V4.1 elevation $H_{SRTMV41}$; (b) Height differences between MERIT elevation and shifted SRTM V4.1 elevation $H_{SRTMV41}^{shift}$	46
3.3	Global tree bias map in 1 km resolution (Yamazaki et al (2017)).	49
3.4	New Zealand density model (modified after Tenzer et al., 2011a)	50
4.1	Discretization and regularization of the mass-distributions	57
4.2	Leakage problem between polyhedral-zone and prism-zone	58
4.3	Special cases for polyhedral	59
4.4	TGF software GUI interface	61
4.5	The grid2bin interface	62
4.6	Relative computation time of various forward modeling methods	64

4.7	External validation over Himalaya mountainous area. δg_{CNI} represents topographic gravity disturbances calculated by Curtin software, δg_{TGF} represents topographic gravity disturbances calculated by TGF software.	65
4.8	External validation based on baseline (<i>Hirt et al (2019a)</i>) over Himalaya mountainous area. H_{RTM} represents RTM height, it is the height difference between surface topography and reference topography, with $H_{RTM} = H - H_{REF}$	68
4.9	External validation based on baseline (<i>Hirt et al (2019a)</i>) over Switzerland. H_{RTM} represents RTM height, it is the height difference between surface topography and reference topography, with $H_{RTM} = H - H_{REF}$	69
4.10	Forward modeling internal accuracy and efficiency with radius of polyhedron (r_1) and prism (r_2). (r_1) is the radius of using polyhedron, varying from 0.00° to 0.33° with step of 0.01° , (r_2) is the radius of using prism, varying from 0.00° to 0.33° with step 0.01° . Left: Inertial accuracy; Right: evaluation points per second	71
4.11	Forward modeling internal accuracy and efficiency with radius of spheroid (r_3) and point-mass (r_4). (r_3) is the radius of using spheroid, varying from 0.05° to 1° with step of 0.05° , (r_4) is the radius of using point-mass, varying from 0.2° to 2° with step 0.01° . Left: Internal accuracy; Right: evaluation points per second	71
4.12	Comparison of prism and polyhedron. Left: RTM-baseline minus RTM-A results using polyhedron in the adjacent zones; right: differences of RTM-A results using polyhedron and prism . . .	73
4.13	Comparison of prism and polyhedron over New Zealand. Left: $\delta g_{obs} - \delta g_{egm} - \delta g^{RTM-poly}$; right: $\Delta \delta g = \delta g_{obs} - \delta g_{egm} - \delta g^{RTM-prism} - \delta g_{obs} - \delta g_{egm} - \delta g^{RTM-poly} $	74
4.14	Comparison of prism and polyhedron over Canada. Left: $\delta g_{obs} - \delta g_{egm} - \delta g^{RTM-poly}$; right: $\Delta \delta g = \delta g_{obs} - \delta g_{egm} - \delta g^{RTM-prism} - \delta g_{obs} - \delta g_{egm} - \delta g^{RTM-poly} $	76
4.15	Residual height over Zugspitze (German Alps) area	76
4.16	Residual gravity field calculated by TGF software. With τ_{RTM} indicating residual geoid height signals, σ_{RTM} residual gravity disturbances, ξ_{RTM} and η_{RTM} representing north-south and east-west components of vertical deflection separately.	77
4.17	RTM tensor components of gravity field over Zugspitze (German Alps) area.	78
5.1	RTM error sources.	79
5.2	RTM techniques validation over Himalayas areas. With $\delta g_{baseline}$ indicating the RTM baseline solution, δg_{RTM-A} RTM gravity disturbances via RTM-A technique, δg_{RTM-B} RTM gravity disturbances via RTM-B technique, and δg_{RTM-C} RTM gravity disturbances via RTM-C technique.	81
5.3	RTM techniques validation over Swiss Alps. With $\delta g_{baseline}$ indicating the RTM baseline solution, δg_{RTM-A} RTM gravity disturbances via RTM-A technique, δg_{RTM-B} RTM gravity disturbances via RTM-B technique, and δg_{RTM-C} RTM gravity disturbances via RTM-C technique.	82

- 5.4 RTM truncation error over Himalaya areas. δg_{RTM}^{50km} , δg_{RTM}^{100km} , δg_{RTM}^{150km} , δg_{RTM}^{200km} and δg_{RTM}^{300km} indicate the RTM gravity disturbances with integration radius extended to the distances of 50 km, 100 km, 150 km, 200 km and 300 km respectively. 85
- 5.5 The comparison between RTM gravity disturbances calculated based on the ellipsoidal approximation δg_{ell}^{200km} and spherical approximation δg_{sph}^{200km} over Himalaya areas (panel (a)) and Switzerland areas (panel (b)). The differences range from ~ -0.15 mGal to ~ 0.12 mGal, with a mean value of differences of 0 mGal and a RMS of ~ 0.03 mGal at Himalayas, and vary between ~ -0.26 mGal to ~ 0.17 mGal, with a mean of ~ -0.01 mGal and a RMS of ~ 0.04 mGal over Switzerland areas. 87
- 5.6 Gravity disturbances over New Zealand. Panel a: observed gravity disturbances (from the NZ gravity data base), panel b: residuals when subtracting EGM2008 gravity and RTM gravity based on a constant mass-density value, panel c: The same, but the RTM is based on the mass-density map, panel d: comparison between the residuals in panel b and c. In panel d, red indicates better performance of the mass-density map. All units in mGal. 92
- 5.7 residual height and residual gravity disturbance comparison over the North Island. Panel a: residual height over North Island, units in meter; panel b: comparison between the residual gravity disturbances based on density map and constant density, units in mGal. 93
- 5.8 residual height and residual gravity disturbance comparison over the South Island. Panel a: residual height over South Island, units in meter; panel b: comparison between the residual gravity disturbances based on density map and constant density, units in mGal. 93
- 5.9 Heights, mass-densities, and gravity disturbances in South Alps Fault. Panel a: residual height in South Alps Fault, units in meter; panel b: density distribution in South Alps Fault from New Zealand density map, units in g/cm^3 ; panel c: residual gravity disturbance, RTM is based on the mass-density map, units in mGal; panel d: comparison between the residuals based on density map and constant density assumption, units in mGal. 94
- 5.10 Heights, mass-densities and gravity disturbances along Mary Range. Panel a: residual height along Mary Range, units in meter; panel b: density distribution along Mary Range from New Zealand density map, units in g/cm^3 ; panel c: residual gravity disturbance, RTM is based on the mass-density map, units in mGal; panel d: comparison between the residuals based on density map and constant density assumption, units in mGal. 95
- 5.11 Comparison between the residual height anomalies based on constant density $\Delta\zeta_{const}^{SRTM30m}$ and density map $\Delta\zeta_{densitymap}^{SRTM30m}$, Units in cm. Higher values indicate better performance of the mass-density map. 98

5.12 Results of the density optimization test. Panel a: RMS of residual gravity disturbances, the RTM is based on the density approximation from $2300kg/m^3$ to $3300kg/m^3$ over North Island; panel b: the same with panel a, but the test area is addressed over South Island; panel c: the same, but the test area is located in the whole New Zealand. The all units are in mGal. Blue line means the masses for RTM include both ocean and land masses within the integral radius, the RMS represented by green line just considered the effect of land masses. 99

5.13 Tree canopy effect in forward modelling procedure. The green dashed line represents the DSM surface, the black line is the DTM surface, their differences indicate the tree bias; The blue dashed line represents the smooth surface computed directly from DSM, while the fine black line is the DTM smooth reference surface; and the black dashed line stands for the sea level. . . 102

5.14 Flowchart for SFM in global tree bias effect study. 104

5.15 Degree variances of the tree bias implied topographic potential. Left: degree variances of the 1 km tree bias implied topographic potential. Right: degree variances of the smoothed tree bias implied topographic potential. 105

5.16 a) topographic and b) RTM gravity disturbances encountered in global tree canopy model 106

5.17 Tree bias and its effects in high-frequency gravity field modelling. (a) and (b) are tree bias height over Indonesian and Africa rainforest areas; (c) and (d) are tree bias effect in high-frequency gravity field modelling over Indonesian and Africa rainforest areas. 107

5.18 The (a) RTM geoid height and (b) RTM vertical gradient encountered in global tree-canopy model.108

5.19 Tree canopy effect in regionally high-frequency gravitational field modeling over the Tasmania area. (a) MERIT elevations; (b) Height differences between MERIT DEM and shifted SRTM V4.1 DEM; (c) Topographic gravity disturbances implied by the MERIT DEM; (d) Tree canopy effect in topographic gravity disturbances; (e) RTM gravity disturbances based on RTM data using the MERIT DEM and its degree-2160 reference surface as boundaries; (f) Tree canopy effect in RTM gravity disturbances modeling. 111

5.20 Tree canopy effect in regionally high-frequency gravitational field modeling over the Amazon area. (a) MERIT elevations; (b) Height differences between MERIT DEM and shifted SRTM V4.1 DEM; (c) Topographic gravity disturbances implied by the MERIT DEM; (d) Tree canopy effect in topographic gravity disturbances; (e) RTM gravity disturbances based on RTM data using the MERIT DEM and its degree-2160 reference surface as boundaries; (f) Tree canopy effect in RTM gravity disturbances modeling. 112

5.21 Tree canopy effect in regionally high-frequency gravitational field modeling over the Australian Alps mountainous area. (a) MERIT elevations; (b) Height differences between MERIT DEM and shifted SRTM V4.1 DEM; (c) Topographic gravity disturbances implied by the MERIT DEM; (d) Tree canopy effect in topographic gravity disturbances; (e) RTM gravity disturbances based on RTM data using the MERIT DEM and its degree-2160 reference surface as boundaries; (f) Tree canopy effect in RTM gravity disturbances modeling. 113

- 5.22 Tree canopy effect in regionally high-frequency gravitational field modeling over the Canadian Rocky mountainous area. (a) MERIT elevations; (b) Height differences between MERIT DEM and shifted SRTM V4.1 DEM; (c) Topographic gravity disturbances implied by the MERIT DEM; (d) Tree canopy effect in topographic gravity disturbances; (e) RTM gravity disturbances based on RTM data using the MERIT DEM and its degree-2160 reference surface as boundaries; (f) Tree canopy effect in RTM gravity disturbances modeling. 114
- 5.23 Validation over Tasmania area with ground gravity observations. (a) Ground gravity disturbances; (b) Removing EGM2008 gravity disturbances from observation; (c) residual gravity disturbances after removal of EGM2008 and RTM gravity disturbances from observation; (d) magnitude differences between SRTM-based residual signals and MERIT-based residual signals, where red indicates MERIT performs better than SRTM V4.1. 116
- 5.24 Validation over Australian Alps area with ground gravity observations. (a) Ground gravity disturbances; (b) Removing EGM2008 gravity disturbances from observation; (c) residual gravity disturbances after EGM2008 and RTM gravity disturbances from observation; (d) magnitude differences between SRTM-based residual signals and MERIT-based residual signals, where red indicates MERIT performs better than SRTM V4.1. 118
- 5.25 Validation over Canadian Rocky Mountainous area with ground gravity observations. (a) Ground gravity disturbances; (b) Removing EGM2008 gravity disturbances from observation; (c) residual gravity disturbances after EGM2008 and RTM gravity disturbances from observation; (d) magnitude differences between SRTM-based residual signals and MERIT-based residual signals, where red indicates MERIT performs better than SRTM V4.1. 119

List of Tables

2.1	Publicly available algorithms for forward modeling in the spatial domain	29
2.2	RTM variants with different definitions	34
3.1	Summary of basic characteristics of global DEMs	44
3.2	Publicly available SRTM DEMs	45
4.1	Parameter specification for TGF forward modeling	63
4.2	The resolutions and extensions in topographic and RTM gravity field calculation	66
4.3	External validation for topographic gravity calculation over Himalaya regions (Unit: mGal)	66
4.4	External validation through baseline over Himalayas and Switzerland areas	67
4.5	Descriptive statistics of gravity differences between baseline, and RTM gravity disturbances based on polyhedron and prism approximation respectively	73
4.6	Descriptive statistics of gravity differences between ground observations, EGM2008 and RTM gravity disturbances based on polyhedron and prism approximation respectively	75
5.1	Comparison of various RTM techniques over Himalayas and Switzerland (cf. <i>Hirt et al (2019a)</i>)	83
5.2	Parameter specification for reference approximations	85
5.3	The statistical information of gravity disturbances δg_{obs} and differences with respect to various models over New Zealand. $\kappa[\%]$ indicates improvement rate	89
5.4	Descriptive statistics of calculated RTM quasi-geoid heights at 3609 GPS/levelling points	96
5.5	LVD offsets obtained based on different methods [Units: m]	97
5.6	Descriptive statistics of residual height anomaly. where: $\Delta\zeta_{const}^{SRTM30m} = \zeta_{GPS/levelling} - \zeta_{EGM2008} - \zeta_{const}^{SRTM30m}$, $\Delta\zeta_{densitymap}^{SRTM30m} = \zeta_{GPS/levelling} - \zeta_{EGM2008} - \zeta_{densitymap}^{SRTM30m}$	97
5.7	Optimum density and RMS	100
5.8	Optimum density and RMS	101
5.9	Statistical information of tree height effect on gravity disturbances over Tasmania	116
5.10	Statistical information of tree height effect on gravity disturbances in the Australian Alps based on 23,260 ground gravity observations	117
5.11	Statistical information of tree height effect on gravity disturbances in Canadian Rocky Mountain area based on 962 ground gravity observations	117
5.12	The error sources and its effect in RTM gravity forward modelling (Units: mGal)	120

B.1 Statement of Co authorship 141

Chapter 1

Introduction

1.1 Background and motivation

Gravity field and significance: The Earth's gravity potential W is the composite contribution of: 1) the gravitational potential, V , of the Earth generated by its total mass density distribution, and 2) the centrifugal potential, Z , resulting from the Earth's rotation (*Hofmann-Wellenhof and Moritz (2006)*). The Earth's gravity potential W is a fundamental quantity in geodesy and geophysical studies. Due to density variations in the Earth's interior, on the Earth's surface, and above in the atmosphere, the gravity varies in different regions, for example, mountain ranges, glaciers, water storage on land, or deep ocean trenches. These heterogeneously distributed masses cause different values in gravity and therefore influence the characteristics of the Earth's gravity field. Therefore, knowledge about the Earth's external gravity field is fundamental for understanding the Earth's interior mass distributions and changes in time, as well as their influence on near subjects. In addition, it is fundamental for the determination of the Earth's figure which can be mathematically represented by the geoid, i.e., the surface of constant potential value $W = W_0$ (*Hofmann-Wellenhof and Moritz (2006)*, *Jekeli (2015)*) that coincide with the surface of the global ocean. The geoid provides a vertical datum for many geodetic and geophysical applications, such as regional height system unifications, or for a number of time-dependent geodynamic processes and interactions that are subject to mass-distribution changes, e.g., ocean circulation, ice mass variation, sea level changes, earthquake and volcanism, influence the gravity field (*Jekeli (2015)*, *Tamisiea et al (2001)*, *Tapley et al (2003)*, *Ramillien et al (2006)*). Second, the Earth's interior mass inhomogeneities are a prerequisite to understanding the dynamics and evolution of the Earth, in particular detecting physical properties of minerals and melts (*Jacoby and Smilde (2009)*).

Measurement and determination of the gravity field: The accuracy of a calculated gravity field model depends on the amount and quality of available datasets and the structure of the gravity field. Over the past decades, a variety of gravity measurement techniques have been developed enabling the understanding of the gravity field in the spectral domain as well as in the spatial domain. The satellite-based gravity projects CHAMP, GRACE, GOCE and GRACE follow-on measure the gravity field homogeneously and near-globally, down to half wavelengths of ~ 100 km (*Reigber et al (2003)*, *Pail et al (2010)*). However, these observations

are affected by the attenuation effect of gravity signal with altitude. The recovered gravity field is therefore restricted in spectral resolution, however, also the spatial resolution is limited depending on the satellite orbit design. Nowadays, with combination of gravity observations from GRACE and GOCE, kinematic orbits from satellite missions (like CHAMP, GRACE, GOCE, TanDEM-X), SLR observations to LAGEOS 1/2, and terrestrial information over polar gap areas, the satellite-only gravity field model is possible to be derived down to a scale of ~ 70 km (Zingerle (2019), Kvas *et al* (2019)). The regional measurements of ground-, airborne- and shipborne-based data provide finer gravity structures and are routinely used in local or regional studies (Denker (2013), Bucha *et al* (2016), Willberg *et al* (2019)). However, ground data sets are generally inhomogeneously distributed and are of varying quality. Moreover, dense and accurate terrestrial gravity observations are rarely available especially over developing regions, such as parts of Asia, Africa and South America. Therefore, a combination of multiple data sources would be preferred in the calculation of accurate and high-resolution global, local or regional gravity field. Over the past decade, notable achievements have been made in global gravity field modeling. The global gravity models (GGMs) are commonly parametrized in terms of harmonic coefficients (HCs) and model the Earth's external gravity field at a limited level of detail. Some of the most significant achievements were manifested by resolving the gravity field down to spatial details of ~ 9 km, such as the development of the EGM2008 (Pavlis *et al* (2012), Pavlis *et al* (2013)), EIGEN-6C4 (Förste *et al* (2014)), and the GECO models (Gilardoni *et al* (2016)).

Significance of high-frequency signals in gravity field modeling: High-frequency gravity signals finer than the resolution commensurate with gravity observations are not accounted for in the recovered global gravity field models. This effect is known as omission error (Sansò and Sideris (2013), Hirt *et al* (2010b), Rexer and Hirt (2015), Willberg *et al* (2017), Yang *et al* (2018)). Subjecting to the omission error of recovered GGMs, local applications demanding precise knowledge of the Earth's gravity field (Jacoby and Smilde (2009), Hirt *et al* (2013)) at high-frequency bands are restricted. A possible method to extend the contents of the derived gravity field is to augment the GGMs with forward modeled gravity field (Forsberg and Tscherning (1981), Forsberg (2010), Hirt *et al* (2010a), Hirt (2010), Hirt *et al* (2013), Bucha *et al* (2016)). Because the Earth's external gravitational field decays with distance increasing from the evaluation point to the Earth's center, the mass-anomalies relating to the topography including the effects of the visual continental topography, oceans, inland water bodies, and ice-sheets, dominate the local variation of the gravity field, especially at the short-scale wavelengths. In a near-global gravity field model GGMplus (Hirt *et al* (2013)), the topographic gravity field has been included at spatial scales of ~ 10 km to ~ 250 m over all continental areas where SRTM data is available. Depending on the terrain roughness, the topography-generated gravity field would vary between ~ -28 and ~ 30 cm for geoid heights, and from ~ -362 to ~ 140 mGal for gravity disturbances at scales of ~ 10 km to ~ 250 m (Hirt *et al* (2014)). Local extreme values of gravity signals not modeled in contemporary GGMs might reach value as large as ~ 38 mGal at Himalayas (Rexer and Hirt (2015)). Therefore, as a part of the efforts toward the calculation of the 'one-centimeter or millimeter-level geoid' (Foroughi *et al* (2019), Wang (2012)), high-frequency gravity signals caused by topographic masses must be carefully taken into consideration.

High-frequency gravity field determination using topographic data: The calculation of the topographic gravity field, with detailed knowledge of geometry and density-distribution of the Earth's topography, is basically a problem of numerical integration expressed by Newton's integral which is denoted as forward modelling technique (*Hirt and Kuhn (2014), Hirt et al (2016a), Hirt et al (2019a), Kuhn and Seitz (2005), Tenzer et al (2012)*). There are basically two categories of methods for the numerical evaluation of Newtonian integration:

- The spatial domain technique (*Forsberg (1984), Nagy et al (2000), Nagy et al (2002), Heck and Seitz (2007), Wild-Pfeiffer (2008), Tsoulis et al (2009), Tenzer et al (2010), Tsoulis (2012), Grombein et al (2013), Deng et al (2016), Uieda et al (2016), Yang et al (2018), Hirt et al (2019a)*) is based on a discretized Newtonian integration which calculates the gravitational potential and its derivatives generated by regularly shaped geometries.
- The spectral domain technique (*Rummel et al (1988), Pavlis and Rapp (1990), Balmino (1994), Kuhn and Seitz (2005), Wieczorek (2007), Balmino et al (2012), Claessens and Hirt (2013), Hirt and Kuhn (2014), Rexer and Hirt (2015), Tenzer et al (2015a), Grombein et al (2016), Hirt et al (2016a), Rexer et al (2016), Hirt et al (2019a)*) is carried out by spherical harmonic analysis (SHA) and synthesis (SHS) of height and density functions.

More specifically, with the spatial domain technique, the topography is generally represented by a set of digital elevation models (DEMs) (*Bucha et al (2016), Forsberg and Tscherning (1981), Hirt et al (2010a), Hirt (2010), Hirt et al (2013), Tsoulis (2001), Yang et al (2018)*) which discretize the continuous masses by a series of mass-elements. The general mass elements are then approximated by some primitive geometries such as prism (*Nagy et al (2000), Nagy et al (2002)*), tetrahedra (*Casenave et al (2016)*), tesseroid (*Deng et al (2016), Grombein et al (2013), Heck and Seitz (2007)*) or polyhedron (*Tsoulis and Petrović (2001), Tsoulis (2012)*), the gravitational fields of which can be computed with analytical or numerical series expressions. The topographic gravitational field is the composite contribution of all mass elements. In the spatial domain technique, gravitational field over each computation point is computed independently. Therefore, the total computation time is directly related to the number of computation points and the number of discretized elements. Alternatively, with the spectral domain technique, harmonic coefficients (HCs) of gravitational potential are obtained through SHA of height-density function over the entire globe (*Balmino (1994), Hirt and Kuhn (2014), Wieczorek (2007)*), or located inside or outside a spherical cap (*Bucha et al (2019)*). Benefiting from Fast-Fourier Transform (FFT) technique, the spectral gravity modelling (SGM) technique shows great efficiency in global gravity field studies at scales of long- and medium-wavelengths, such as in the computation of topographic gravitational field based on rock-equivalent topography (*Claessens and Hirt (2013)*) and multi-density layer-based topography (*Grombein et al (2014), Rexer et al (2016)*). However, to properly handle the convergence behavior, the SGM technique generally requires to model the very high-frequency spectral gravity signals which usually cause high numerical cost (*Hirt and Kuhn (2014)*), especially when ultra-high resolution DEMs are used.

Many procedures for an efficient evaluation of topographic gravitational field signals have been proposed. The most famous methods rely on splitting the topographic effect into two parts according to spectral bandwidths as:

- the long-wavelength gravity signal generated by a Bouguer plate or a Bouguer spherical shell,
- and the high-frequency part that is modeled as the effect of irregular elevation nearby the computation point, denoted as terrain correction;

or by:

- the long-wavelength gravity signal which can be efficiently calculated through the SGM technique,
- and the high-frequency part modeled by residual terrain model (RTM) technique in the spatial domain.

Different from the calculation of full-scale topographic gravitation field which requires numerical integration over the entire globe, the limited integration radius is considered an advantage in the evaluation of RTM and terrain implied gravity field. This is because it greatly reduces the number of mass-elements and computation time.

Introduction of RTM as special case: The RTM technique was first introduced by *Forsberg and Tscherning* (1981) as a remove-compute-restore technique for improving gravity field modeling in mountainous terrain. As the basic idea of the RTM technique, the residual terrain model was obtained by removing some reformulate reference surfaces from a model of the topographic masses — often a detailed DEM. Assuming the spectral consistency between topography and its implied gravity signals, the RTM technique therefore delivers the high-frequency parts of topographic gravitational functionals. The RTM technique has been broadly applied in geodesy and geophysics, for example, smoothing of gravity observations prior to their interpolation e.g. in the framework of remove-compute-restore procedure (*Forsberg and Tscherning* (1981), *Forsberg* (1984), *Tziavos and Sideris* (2013)), prediction of high-frequency gravity field constituents (*Hirt et al* (2014), *Hirt et al* (2019b)), augmentation of GGMs recovered gravity functionals at high-frequency bands (*Hirt* (2010), *Hirt et al* (2010a), *Hirt et al* (2013), *Šprlák et al* (2012), *Vergos et al* (2014), *Willberg et al* (2017), *Vergos et al* (2018)), or as fill-in data in combined global gravity field modelling over remote countries where devoid of gravity measurements (*Pavlis et al* (2007), *Pavlis et al* (2012)). Besides, RTM recovered gravity was also applied in gravity reduction to detect the near-surface mass-density anomalies (*AllahTavakoli et al* (2015)).

Motivation: Forward modelling, as a very powerful technique, has been widely applied in subjects of finer-grained topographic models. For example, high-resolution topographic gravity field models have been successfully computed over local areas (e.g. *Cella* (2015), *Tsouliis* (2001)) at a resolution commensurate with the local DEMs, or in global grids at a resolution of ~ 2 to ~ 10 km in the context of UNESCO's World Gravity Map project (*Balmino et al* (2012), *Bonvalot et al* (2012)), also at the near-global continental area at scale of ~ 250 m (*Hirt et al* (2013), *Hirt et al* (2014)). With the availability of finer and accurate regional or global DEMs, such as SRTM DEMs at 90 m and 30 m resolutions, there has been an increasing interest in topographic

gravity to the finest detail, such as the SRTM2gravity model constitutes full-scale and high-frequency gravity field signals generated by the 3" SRTM-based (MERIT) DEM (*Hirt et al (2019b)*). Accompanying challenges in computational efficiency are encountered in the numerical evaluation of the Newton's integral. Additionally, assumptions and simplifications are sometimes made in practical calculations, which propagate into the forward modeled gravity functionals. For the fast and accurate calculations of high-frequency gravity field, its gradients and second derivatives, errors due to assumptions and simplifications need to be reduced to a minimal level.

1.2 Research objectives

Considering the accuracy of the mathematical modelling and the quality of input datasets, any forward modelled gravitational field therefore can only be an estimation of the true topography-related gravity field. In this thesis, efforts toward an accurate and efficient calculation of high-frequency gravity field via the RTM technique will be made and the following aspects will be discussed:

- **RTM mathematical modelling errors:** three types of often used RTM techniques will be discussed in this thesis. These three RTM techniques are all affected by one or two sources of RTM-specific approximation and simplification errors related to the 1) inaccurate harmonic correction, 2) mass simplification, or 3) vertical computation point inconsistency. In this study, we will assess these three RTM techniques through the comparison with an independent RTM solution – called RTM baseline solution in the following – which avoids the above mentioned errors. Comparison results will demonstrate their performance in high-frequency gravity forward modelling, especially in terms of GGM augmentation at short scales.
- **The Earth's approximation and reference system:** Accurate topographic gravity forward modelling in the spatial domain requires integration over the domain of all mass-sources, which often extends to the entire globe for the full-scale gravity field calculations and up to tens of kilometers for RTM gravity field computations. Considering the Earth's curvature, in such cases, the often used local planar approximation is usually not sufficient for the accurate calculations. In this thesis, we will adopt more rigorous spherical or ellipsoidal approximation methods.
- **Four types of geometric mass-elements combination:** The more detailed mass-distribution and complicated geometry always produces the better gravitational field, but at the expense of calculation efficiency. Based on the inverse distance law of Newtonian integration, to achieve a win-win situation in terms of efficiency and accuracy, four types of primitive geometric elements, i.e., polyhedron, prism, tesseroid and point mass, will be combined by dividing the integration masses into various zones, and manual definition of radius and input data sets of each zone. The attenuation character of gravity disturbances in horizontal and vertical directions will be studied separately, which provides new insights into the choice of the truncation radius and the definition of mass-zones definition.

- **Optimize the RTM retrieved gravity signals using digital mass-density model:** In practical calculations, limited by the density knowledge of the Earth's interior masses, the value of uniform rock density is generally adopted in the topography-related forward modelling. As a consequence, the high-frequency signals generated by a lateral density variation is not included in the results. In this study, efforts were made to handle this problem through a combination of the RTM technique and a regional mass-density model over New Zealand.
- **Tree bias effect in gravity forward modelling:** For global and continental-wide gravitational field determination, the applied DEMs commonly rely on the observations from radar interferometry (e.g., SRTM DEMs or TanDEM-X DEM) and optical images (e.g., ALOS AW3D DEM or ASTER DEM). Over vegetated areas, however, neither of these two techniques is capable of detecting elevations of the bare ground. Depending on the radar penetration characteristics, radar-based DEMs provide the height of an interferometric surface located between the ground and the top of the canopy. The bias between radar-based DEMs and the bareground Earth's surface denotes trees bias which varies from several meters to tens meters. In this study, numerical investigation will be made to study the role of the tree canopy effect in gravity forward modelling.
- **Terrain Gravity Field (TGF) software development:** To facilitate these investigations, we developed a terrain gravity field (TGF) software together with a MATLAB-based graphical user interface. The software is aimed at the purpose of the accurate and efficient calculation of the topographic gravity field through a combination of four geometric mass-elements, polyhedron, prism, tesseroid and point mass. Based on various external and internal validation experiments, the trade-off character of the TGF software between efficiency and accuracy will be studied.

1.3 Outline

This thesis is structured in six main chapters (including the Introduction).

Chapter 2 “Foundation”: this initial section provides a theoretical treatment of forward modelling and its numerical evaluation in the spatial domain and in the spectral domain. Section 2.1 introduces the relevant coordinate system and the general theory of potential and its gradients determination with Newtonian integration in the inertial system. Section 2.2 describes the methodologies of numerical evaluation of Newtonian integration in the spectral and spatial domain separately. The spatial domain technique outlines the gravity field quantities of general geometries including polyhedron, prism, tesseroid and point mass. Section 2.3 discusses the various RTM techniques. The emphasis is on the harmonic correction techniques related to the calculation points located below the reference surface. Section 2.4 consists of a short overview of GGM refinement at short scale with the RTM technique.

Chapter 3 “Databases”: this chapter gives an overview of available and specific data sets used in this work and their pre-processing. We start with databases required for mass modelling in the procedure of forward modelling. At first, a selection of existing DEM models, collected from observations of diverse measurement systems, are presented in Section 3.1.1. The specific errors of now publicly available DEMs, e.g., geo-location shifts and tree canopy bias, which can involve tens of meters errors in the vertical direction, are discussed in Sections 3.1.1 and 3.1.2. Section 3.1.3 then provides some general information and gives an overview of the history and the latest developments in the field of the Earth’s geological density distribution. From comparisons of the modeled gravity field with true measurements, the RTM technique can be validated. Therefore, ground measurements, including ground measured gravity values and GPS/levelling data sets, are introduced in Section 3.2.

Chapter 4 “Software development”: The intention of this chapter is to introduce the TGF software, which has been developed for accurate and effective calculation of the topography implied gravity field. It starts with an overview of the combination and implementation of four discretization methods: polyhedron, prism, tesseroid and point mass (Section 4.1.1). Then we turn to the structure and function of the software (section 4.1.2), where we explain the input datasets, parameters’ definition, and procedures of forward modelling with TGF software. There follows evaluations (Section 4.2) between modeled and ‘true’ values demonstrating the performance of TGF in topographic and RTM gravity field determination, where gravity disturbance is the primary quantity of interest. Because the emphasis is on the RTM gravity disturbance calculations defined at the Earth’s surface, the trade-off between accuracy and efficiency in the RTM gravity field calculations is discussed in Section 4.2.3. Besides, the numerical study over the Zugspitze area proves TGF to be a beneficial tool for studying the short-scale gravitational signals (Section 4.3).

Chapter 5 “Numerical examinations of RTM techniques”: The first goal of this chapter is to further test and validate the mathematical model and TGF software performance, using real data as described in Chapter 3. The second objective is to analyze the error sources in the RTM gravity field modelling and attempt to quantify them. The modelling errors, including mass-distribution errors involved in various RTM techniques, and Earth’s approximation errors, are studied in Section 5.1. In the second part (Section 5.2), observation errors in the input datasets, i.e., density model and DEMs, and their effect on the RTM gravity field modelling are discussed. In Section 5.2.1, we use a high-resolution density model over New Zealand in an attempt to overcome the constant mass-density assumption in the RTM gravity field modelling. Its performance is evaluated by comparison with ground gravity and GPS/levelling measurements. In Section 5.2.2, the effect of tree canopy bias, contained in the frequently applied SRTM DEMs, on gravity forward modelling is modeled globally and regionally. Further evaluation experiments of the performance of ground DTM were carried out over Tasmania, Australian Alps, and Canadian Rocky Mountain areas.

Chapter 6 “Conclusions”: this chapter gives a summary of this project, recommendations and ideas for further studies.

Chapter 2

Foundation

Using the gravity forward modelling techniques to deduce the gravitational field generated by some mass distributions, requires an accurate mass modelling of the Earth (*Hofmann-Wellenhop and Moritz (2006), Jekeli (2015)*). Mass models consist of information about the physical geometry of the Earth as well as with measured interior geological density distributions. A perfect mass geometry would be suitable for modeling both simple and very complex mass distributions in terms of infinitesimal small mass-elements at all 3D positions. Together with the precise algorithm for the numerical evaluation of Newtonian integration over all masses around the evaluation point, it would allow to accurately determine the masses generated gravitational field. The following sections deal with the fundamentals of gravitational field determination generated by topographic mass-distributions using forward modelling techniques, which provide the foundation for the later chapters. The chapter is structured as follows: it starts with the general mathematical background the forward modelling, including the coordinate system and the classical Newtonian integration (section 2.1), and the general theory of gravity field determination (Section 2.1). The numerical evaluation of the Newtonian integration is introduced in Section 2.2, including techniques of spectral gravity modelling (SGM) technique (Section 2.2.1) and with spatial domain numerical integration (NI) (Section 2.2.2). In the NI technique, the gravitational fields of four types of geometric elements, i.e., polyhedron, prism, tesseroid and point mass, are briefly introduced. Special emphasis is given on the way how to refine GGMs through the combination with the residual terrain model (RTM) technique in Section 2.4 and various types of RTM techniques in Section 2.3.

2.1 General aspects

2.1.1 Coordinate systems

Global and local reference systems play an essential role in the modeling of the Earth's gravity potential, and its first and second derivatives. The objective of this section is to present the various local and global reference systems that are frequently used to model the Earth's external gravity field.

1) Spherical coordinate system

In spherical approximation, the figure of the Earth is approximated by a sphere of constant radius R . The 3D coordinates to be used are the spherical coordinates defined as (φ, λ, r) (Denker (2013)) (Fig. 2.1 (a)),

- the geocentric latitude φ of point P is defined by the angle between the equatorial plane and the normal (radial direction) through P on the sphere.
- the geocentric longitude λ of P is the angle from the meridian plane through P to the meridian plane of Greenwich.
- the radius r is the radial distance from the geocenter to point P .

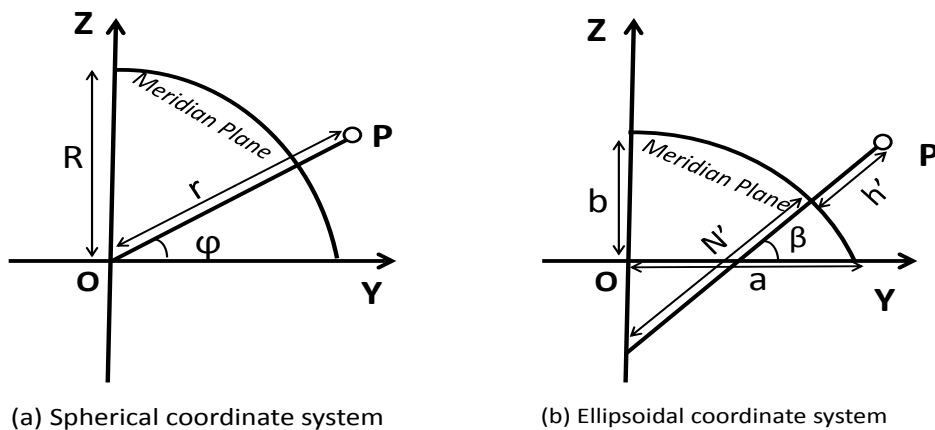


Fig. 2.1 – The spherical and ellipsoidal coordinate systems, (a) the spherical coordinate system, (b) the ellipsoidal coordinate system.

2) Ellipsoidal coordinate system

Considering the nature of flattening of the Earth at poles, the spheroid with a latitude-dependent Earth's radius would be a better approximation of the Earth's figure. This is denoted ellipsoidal approximation. In ellipsoidal approximation, the geodetic coordinates are given as (β, λ, h') (Clynch (2006)) (Fig. 2.1 (b)),

- the geodetic latitude β of point P is the angle between equatorial plane and the ellipsoidal normal line at the P .
- the longitude λ of point P is the angle from the meridian plane through P to the meridian plane of Greenwich.
- the geodetic height h' is the distance from point P to the surface of spheroid measured along the ellipsoidal normal.

Transformation from geodetic coordinates to spherical coordinates follows Denker (2013):

$$\begin{aligned}\lambda &= \lambda; \\ \varphi &= \arctan\left[\left(1 - e^2 \frac{N'}{N' + h'}\right) \tan \beta\right]; \\ r &= \sqrt{[(N' + h') \cos \beta]^2 + [(N'(1 - e^2) + h') \sin \beta]^2};\end{aligned}\quad (2.1)$$

where the radius of curvature in the prime vertical N' is given by

$$N' = \frac{a}{\sqrt{1 - e^2 \sin^2 \beta}} \quad (2.2)$$

With a and b denoting the major and minor semi-axes, the first numerical eccentricity e follows:

$$e = \frac{\sqrt{a^2 - b^2}}{a}. \quad (2.3)$$

3) Global and local Cartesian coordinate system

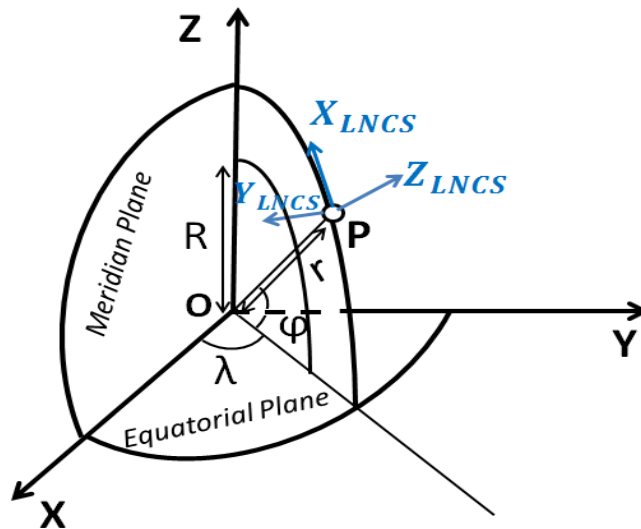


Fig. 2.2 – Global Cartesian coordinate system and local north-oriented coordinate system (LNCS).

It is assumed that the origin of the global Cartesian coordinate system is at the center of the Earth, and that axes X, Y, Z span a right-hand oriented Cartesian coordinate system (*Torge and Müller (2012)*) (Fig. 2.2), with

- Z is pointed to the mean terrestrial North Pole;
- X is directed to the intersection of mean meridian of Greenwich and mean equator;
- Y is at the equatorial plane and forms a right-handed Cartesian system with X and Z .

Transformation from spherical coordinates to global Cartesian coordinates follows *Denker* (2013):

$$\mathbf{X} = \begin{pmatrix} X \\ Y \\ Z \end{pmatrix} = \begin{pmatrix} r \cos \varphi \cos \lambda \\ r \cos \varphi \sin \lambda \\ r \sin \varphi \end{pmatrix} \quad (2.4)$$

For point P , with geodetic latitude β , longitude λ , and geodetic height h' and the radius of curvature in the prime vertical N' , **the transformation from ellipsoidal coordinates to global Cartesian coordinates** follows *Denker* (2013) :

$$\mathbf{X} = \begin{pmatrix} X \\ Y \\ Z \end{pmatrix} = \begin{pmatrix} (N' + h') \cos \beta \cos \lambda \\ (N' + h') \cos \beta \sin \lambda \\ ((1 - e^2)N' + h') \sin \beta \end{pmatrix} \quad (2.5)$$

Transformation from local north-oriented coordinate system to global Cartesian coordinate system: In the local north-oriented coordinate system, the origin is located at the station point P , the coordinate axes are defined by x, y, z . x -axis and y -axis respectively point to local north and east directions, and z -axis coincides with the spherical/ellipsoidal normal. The station-based Cartesian coordinate system x, y, z can be transformed to the X, Y, Z system which follows *Denker* (2013):

$$\begin{pmatrix} X \\ Y \\ Z \end{pmatrix} = \begin{pmatrix} X_0 \\ Y_0 \\ Z_0 \end{pmatrix} + C \begin{pmatrix} x \\ y \\ z \end{pmatrix} \quad (2.6)$$

(X_0, Y_0, Z_0) are the coordinates of station in the global Cartesian coordinate system, and C represents the rotation matrix. Given the spherical coordinates of P (φ, λ, r), C is (*Denker* (2013))

$$C = \begin{pmatrix} -\sin \varphi \cos \lambda & -\sin \lambda & \cos \varphi \cos \lambda \\ -\sin \varphi \sin \lambda & \cos \lambda & \cos \varphi \sin \lambda \\ \cos \varphi & 0 & \sin \varphi \end{pmatrix} \quad (2.7)$$

Given the ellipsoidal coordinates $P(\beta, \lambda, r)$, the transformation matrix is defined according to the Eq. (2.6). The only difference is that the parameter φ is replaced by β (*Denker* (2013)).

2.1.2 General aspects of potential theory

According to Newton's law of gravitation, two point masses m_1 and m_2 separated by a distance l in an inertial system, attract each other with a gravitational force \mathbf{F} which is proportional to the values of the masses, and inversely proportional to the square distance l^2 (*Hofmann-Wellenhof and Moritz* (2006)),

$$\mathbf{F}_{21} = -G \frac{m_1 m_2}{l^2} \frac{\mathbf{l}}{l} \quad (2.8)$$

where G is known as Newton's gravitational constant, which can be determined by experiment, $G = (6.67384 \pm 0.00012) \times 10^{-11} \text{ m}^3 \text{ kg}^{-1} \text{ s}^{-2}$ being the current internationally accepted value (*Mohr et al (2012)*). In Eq. (2.8), $\frac{1}{l}$ is the unit vector pointing from m_2 to m_1 . The quantity \mathbf{F}_{21} is the gravitational force vector directed along the line connecting the points from m_2 to m_1 . The Newton's law is universally true as long as neither massive body nor large velocity is considered (*Hofmann-Wellenhof and Moritz (2006)*, *Jekeli (2015)*).

The gravitational force describes the acceleration of one mass caused by the gravitational attraction of the other. In this case, considering the attracting point mass as a source point, written as m , the gravitational acceleration is given (*Torge and Müller (2012)*),

$$\mathbf{g} = -G \frac{m}{l^2} \frac{\mathbf{l}}{l} \quad (2.9)$$

Following the superposition principle, the gravitational acceleration generated by an extended body, e.g., the Earth, can be superimposed by summing all of the accelerations generated by each individual mass element (*Torge and Müller (2012)*),

$$\mathbf{g} = -G \int_v \frac{\rho}{l^2} \frac{\mathbf{l}}{l} dv \quad (2.10)$$

dv and ρ are infinite volume elements and its density, respectively.

The conservative vector field, composed of the gravitational acceleration vectors \mathbf{g} , is known as potential field. The acceleration vector is the gradient of a scalar function:

$$\mathbf{g} = \text{grad}V \quad (2.11)$$

The gravitational potential V satisfies equation $V = 0$ at infinity (*Denker (2013)*),

$$V = G \int_v \frac{\rho}{l} dv, \text{ with } \lim_{l \rightarrow \infty} V = 0 \quad (2.12)$$

V and its gradients \mathbf{g} are continuous everywhere, e.g., at points located on the boundary surface or inside the mass elements. The second partial derivatives Γ of Newtonian potential V , also known as Marussi tensor, are discontinuous at the boundary surfaces and inside the Earth where abrupt changes of the mass-distribution occur,

$$\Gamma = \begin{pmatrix} V_{xx} & V_{xy} & V_{xz} \\ V_{yx} & V_{yy} & V_{yz} \\ V_{zx} & V_{zy} & V_{zz} \end{pmatrix} \quad (2.13)$$

but satisfy the Poisson's equation there (*Hofmann-Wellenhof and Moritz (2006)*),

$$\nabla^2 V = V_{xx} + V_{yy} + V_{zz} = -4\pi G\rho \quad (2.14)$$

For the evaluation points being outside the attracting masses, density vanishes $\rho = 0$. The Poisson's equation turns to the Laplace equation, i.e., the trace of the Marussi tensor is zero (*Hofmann-Wellenhof and Moritz (2006)*),

$$\nabla^2 V = V_{xx} + V_{yy} + V_{zz} = 0 \quad (2.15)$$

The solutions of the Laplace equation are harmonic functions. They are of great significance in the presentation of the Earth's exterior gravity field.

With knowledge of the density structure and geometry of the entire Earth, the Earth's exterior gravity field could be determined by evaluating the Newton's integral in Eq. (2.12). However, such information is rarely available with sufficient accuracy and resolution, especially regarding the density knowledge. For instance, the modified Preliminary Reference Earth Model (PREM500, *Panning and Romanowicz (2006)*) merely considers radial layer-based density structures, and 3D density models only provide the density structures of upper mantle and crust (e.g., CRUST 1.0 (*Laske et al (2013)*)). In practice, the determination of the Earth's exterior potential field can be divided into two parts, the long- and medium-wavelength part based on gravity observations, and the high-frequency part calculated through forward modelling technique.

- Boundary value problems (BVPs): the long- and medium-wavelength part of gravitational potential is solved by Laplace's equation under a boundary condition based on gravity-related measurements performed on or above the Earth's surface (*Hofmann-Wellenhof and Moritz (2006)*, *Jekeli (2015)*). It should be noted that:

- (1) gravity reduction might be required depending on the boundary conditions (*Hofmann-Wellenhof and Moritz (2006)*, *Jekeli (2015)*). For example, Stokes' formula is broadly applied in geoid determination from gravity anomalies, which requires all topographic masses exterior the geoid to be removed and gravity anomalies should refer to the geoid (*Hofmann-Wellenhof and Moritz (2006)*, *Jekeli (2015)*). Therefore, it is necessary to reduce the terrestrial gravity observations from the Earth's surface to the surface of geoid (*Hofmann-Wellenhof and Moritz (2006)*, *Jekeli (2015)*).
- (2) the recovered gravity fine structure is limited by the spatial distribution of measurements, in other words, gravity signals finer than measurement resolution would not be included in the retrieved gravity field.

Spherical harmonics, as the solution of Laplace's equation in spherical coordinates, are widely used in the global Earth's exterior gravity field V_{GGM} determination (*Hofmann-Wellenhof and Moritz (2006)*, *Pavlis et al (2012)*). The Earth is generally approximated by a sphere of radius R . By introducing spherical coordinates (φ, λ, r) for the evaluation point, the Laplace's equation expressed in the spherical harmonics reads (*Hofmann-Wellenhof and Moritz (2006)*),

$$V_{GGM}(\varphi, \lambda, r) = \frac{GM}{r} \sum_{n=0}^{N_{max}} \left(\frac{R}{r}\right)^n \sum_{m=0}^n (\bar{C}_{nm} \cos m\lambda + \bar{S}_{nm} \sin m\lambda) \bar{P}_{nm}(\sin \varphi) \quad (2.16)$$

where GM , is the product of the universal gravitational constant and the Earth's mass. $\bar{P}_{nm}(\sin \varphi)$ are the fully-normalized Legendre associated functions, n and m are the degree and order of the harmonic expansions, \bar{C}_{nm} and \bar{S}_{nm} are fully normalized spherical harmonic coefficients (SHCs).

- Topography implied high-frequency fluctuation of gravity field: thanks to the availability of high-resolution DEM datasets and knowledge of crustal geological information, the high-frequency gravity field can be calculated from the elevation of the Earth's topography instead of from gravimetric data, assuming the density of the topographic masses is known (*Forsberg and Tscherning (1981), Bucha et al (2016), Hirt et al (2010a), Hirt (2010), Hirt et al (2014), Rexer et al (2018), Yang et al (2018)*).

2.2 Gravity Forward Modelling

Gravity forward modeling denotes all mathematical techniques capable of retrieving the gravity field signals caused by some known mass-density distributions (*Hirt (2016)*). The forward modeled gravity field is given by Newton's integral (Eq. 2.12) and its derivatives, e.g., the gravitational potential V caused by a given three-dimensional body Q with constant density $\rho(Q)$ and arbitrary shape at point P . It is expressed by (*Hofmann-Wellenhop and Moritz (2006)*),

$$V(P) = G \int_v \frac{\rho(Q)}{l(P, Q)} dv \quad (2.17)$$

where dv denotes the infinitesimal volume element, $l(P, Q)$ is the Euclidean distance between evaluation point P and the point of integration Q . In the spherical coordinate system, these points are given as (φ', λ', r') and (φ, λ, r) respectively, and the volume element is given by $dv = r^2 \sin \varphi dr d\varphi d\lambda$. Using h indicates the topographic height measured with respect to the surface of a reference sphere with a constant radius of R , $r = R + h$ is the vertical radius of topography which defines the radial boundaries of integration mass elements. Note that $\frac{1}{l}$ does not exist at $l = 0$, where there is an apparent singularity problem. In this case, using a coordinate system whose origin is at P , the singularity disappears with $dv = l^2 \sin \psi d\alpha d\psi dl$ (*Jekeli (2015)*) for some different colatitude ψ and longitude α .

Because of small quantities, the effect of topographic mass attraction on various gravity field quantities, such as the height anomaly ζ , the deflections of the vertical (DoV) ξ and η , gravity anomaly Δg , gravity disturbance δg and Marussi tensor (E.q. (2.13)) are given as the linear functions or gradients of the potential (*Torge and Müller (2012)*),

height anomaly

$$\zeta = \frac{V}{\gamma} \quad (2.18)$$

deflections of the vertical in North-South and East-West directions

$$\xi = -\frac{1}{r\gamma} \frac{\partial V}{\partial \varphi} \quad (2.19)$$

$$\eta = -\frac{1}{r\gamma \cos \varphi} \frac{\partial V}{\partial \lambda} \quad (2.20)$$

gravity anomaly (in spherical approximation)

$$\Delta g = -\frac{\partial V}{\partial r} - \frac{2}{r}V \quad (2.21)$$

gravity disturbance

$$\delta g = -\frac{\partial V}{\partial r} \quad (2.22)$$

Marussi tensor, E.q. (2.13), indicates the nine components of the second-order partial derivatives of potential with respect to the local Cartesian coordinate system:

$$\begin{aligned} V_{xx} &= \frac{\partial^2 V}{\partial x^2} \\ V_{xy} &= V_{yx} = \frac{\partial^2 V}{\partial x \partial y} \\ V_{xz} &= V_{zx} = \frac{\partial^2 V}{\partial x \partial z} \\ V_{yy} &= \frac{\partial^2 V}{\partial y^2} \\ V_{yz} &= V_{zy} = \frac{\partial^2 V}{\partial y \partial z} \\ V_{zz} &= \frac{\partial^2 V}{\partial z^2} \end{aligned} \quad (2.23)$$

The analytical or numerical solution and expression of these components will be derived in the Sections 2.2.2 and 2.2.3.

2.2.1 Numerical evaluation of Newtonian integral

Newtonian integration of the Earth's masses can be expressed:

- in the spectral domain, named spectral gravity modelling (SGM) approach (Sect. 2.2.2)

Step 1 – Spherical harmonic analysis (SHA): A set of topographic height functions $(\frac{H}{R})^k$ of integer powers $k = 1 \dots k_{max}$ are formed and expanded into spherical harmonic coefficients (SHCs) via surface SHA, with H indicating the elevation of terrain surface;

Step 2 – Transformation: transformation from height SHCs to SHCs of topographic gravitational potential;

Step 3 – Spherical harmonic synthesis (SHS): the gravitational effect over each evaluation point is obtained through SHS of gravitational potential coefficients from **Step 2**.

- in the space domain, named Newtonian Integration (NI) approach (Sect. 2.2.3)

Step 1 – Discretization and regularization: the continuous terrain mass-distributions are generally de-

composed into a series of volume elements that are then approximated by various regular geometries such as polyhedron or prism. In practice, the topographic masses are generally expressed by a DEM referred to a geographical coordinate system.

Step 2 – Gravity field evaluation of individual mass-element: the Newton's integral is solved either analytically or numerically. The analytical gravitational formulas are given for some simple regular geometrical elements, such as prism and point-mass. Either Taylor series expansions or quadrature technique can be used to evaluate the Newtonian integration when no closed solution exists for volume integration.

Step 3 – Summation: The composed effect of all mass elements is obtained by summing up the effects of all mass-elements.

2.2.2 Spectral domain methods

The SGM technique is based on the expression of Newton's integral in the form of spherical harmonics, which has been investigated by many authors, either in the spherical approximation, e.g., (*Rummel et al (1988)*, *Balmino (1994)*, *Balmino et al (2012)*, *Grombein et al (2016)*, *Hirt et al (2012)*, *Kuhn and Seitz (2005)*, *Pavlis and Rapp (1990)*, *Tenzer et al (2015b)*, *Wieczorek (2015)*, *Rexer et al (2016)*), or in the ellipsoidal approximation by, e.g., *Claessens and Hirt (2013)*, *Grombein et al (2016)*, and *Rexer et al (2016)*. In the spherical approximation, the topographic masses are forward modeled referring to a mass sphere with constant radius of R , while in ellipsoidal approximation a reference ellipsoid is used. The SGM framework in the spherical approximation is summarized in the following.

Expressing the reciprocal distance $\frac{1}{r}$ in E.q. (2.17) by a series of Legendre polynomials yields the spherical harmonic expression of Newton's integral for gravitational potential V (e.g., *Rummel et al (1988)*, *Wieczorek (2015)*):

$$V(P) = \frac{GM}{R} \sum_{n=0}^{\infty} \sum_{m=-n}^n \left(\frac{R}{r_P}\right)^{(n+1)} \frac{1}{M(2n+1)} \int_v \left(\frac{r_Q}{R}\right)^n \rho(Q) \bar{Y}_{nm}(\varphi_Q, \lambda_Q) dv \bar{Y}_{nm}(\varphi_P, \lambda_P) \quad (2.24)$$

where M indicates the mass of the Earth, and its mean radius of R . The geographical coordinates $(\varphi_P, \lambda_P, r_P)$ of the evaluation point P are located outside of the Earth's surface. The integration point Q $(\varphi_Q, \lambda_Q, r_Q)$ has constant value of density $\rho(Q)$. Variable \bar{Y}_{nm} is the fully normalized surface Laplace's spherical harmonic function at degree n and order m

$$\bar{Y}_{nm}(\varphi_Q, \lambda_Q) = \bar{P}_{nm}(\cos \varphi_Q) \begin{cases} \cos(m\lambda_Q) & \text{for, } m \leq 0 \\ \sin(m\lambda_Q) & \text{for, } m > 0 \end{cases} \quad (2.25)$$

\bar{P}_{nm} represents the fully normalized associated Legendre functions of the first kind (*Hofmann-Wellenhof and Moritz (2006)*).

With

$$\bar{V}_{nm}(\varphi_P, \lambda_P, r_P) = \frac{1}{M(2n+1)} \int_{\Omega} \left(\frac{r_Q}{R}\right)^n \rho(Q) \bar{Y}_{nm}(\varphi_Q, \lambda_Q) dv_Q \quad (2.26)$$

and inserting Eq. (2.26) to Eq. (2.24), the spherical harmonic expression of gravitational potential is obtained (Rummel et al (1988), Rexer et al (2016), Rexer (2017)):

$$V(P) = \frac{GM}{R} \sum_{n=0}^{\infty} \sum_{m=-n}^n \left(\frac{R}{r_P}\right)^{n+1} \bar{V}_{nm} \bar{Y}_{nm}(\varphi_P, \lambda_P) \quad (2.27)$$

and the gravitational potential is obtained through the infinite sum of fully-normalized SHCs \bar{V}_{nm} .

Using $\bar{\rho}$ representing the mean density of the Earth, M can be replaced by $\frac{4}{3}\pi\bar{\rho}R^3$. In spherical approximation, Eq. (2.26) can be rewritten as (Rexer et al (2016)):

$$\bar{V}_{nm}(\varphi_P, \lambda_P, r_P) = \frac{3}{4\pi\bar{\rho}R(2n+1)} \int_{\lambda=0}^{2\pi} \int_{\varphi=0}^{\pi} \int_{r_Q=R+H_{lower}}^{R+H_{upper}} \left(\frac{r_Q}{R}\right)^{n+2} \rho(Q) \bar{Y}_{nm}(\varphi_Q, \lambda_Q) \cos(\varphi) dr d\varphi d\lambda \quad (2.28)$$

The SHCs \bar{V}_{nm} of the gravitational potential of a homogeneous body are analytically derived from the harmonics describing its shape. Assuming that ρ_Q varies only in the lateral direction, in other words, density is radially invariant. The inner radial integration $\int_{r_Q=R+H_{lower}}^{R+H_{upper}} \rho_Q \left(\frac{r_Q}{R}\right)^{n+2} dr$ yields (Rummel et al (1988), Rexer et al (2016)),

$$\int_{r_Q=R+H_{lower}}^{R+H_{upper}} \rho_Q \left(\frac{r_Q}{R}\right)^{n+2} dr = \rho_Q \frac{R}{n+3} \left(\left(\frac{R+H_{upper}}{R}\right)^{n+3} - \left(\frac{R+H_{lower}}{R}\right)^{n+3} \right) \quad (2.29)$$

where H_{upper} and H_{lower} are the heights of upper and lower boundaries of integration masses.

In order to avoid the explicit computation of $\left(\frac{R+H_{upper}}{R}\right)^{n+3}$ which has to be computed at each grid for each degree, the binomial expansion for term $\left(\frac{R+H}{R}\right)^{n+3}$ (Eq. (2.29)) is introduced, and is truncated at order k_{max} according to the convergency behavior of $\left(\frac{R+H}{R}\right)^{n+3}$ (Rummel et al (1988), Rexer et al (2016)).

$$\left(\frac{R+H}{R}\right)^{n+3} = \sum_{k=1}^{k_{max}} \binom{n+3}{k} \left(\frac{H}{R}\right)^k = \sum_{k=1}^{k_{max}} \frac{1}{k!} \prod_{i=1}^k (n+4-i) \left(\frac{H}{R}\right)^k \quad (2.30)$$

Inserting Eqs. (2.29) and (2.30) into Eq. (2.28), SHCs of the topographic potential generated by masses of volume layers between upper boundary H_{upper} and lower boundary H_{lower} because (Rummel et al (1988), Rexer et al (2016)):

$$\bar{V}_{nm}(\varphi_P, \lambda_P, r_P) = \frac{3}{\bar{\rho}(2n+1)(n+3)} \sum_{k=1}^{k_{max}} \binom{n+3}{k} \bar{H}_{knm} \quad (2.31)$$

The surface SHCs of the topographic height at power k are computed from (Rummel et al (1988), Rexer et al (2016)):

$$\bar{H}_{knm} = \frac{1}{4\pi} \int_{\lambda} \int_{\varphi} \left(\left(\frac{H_{upper}}{R}\right)^k - \left(\frac{H_{lower}}{R}\right)^k \right) \rho(\varphi_Q, \lambda_Q) \bar{Y}_{nm}(\varphi_Q, \lambda_Q) \cos(\varphi_Q) d\varphi d\lambda \quad (2.32)$$

where k is integer power of the term $\frac{H_{upper}}{R}$ and $\frac{H_{lower}}{R}$.

The SGM forward modeled geoid height is (Yang et al (2019)):

$$\zeta(\varphi_P, \lambda_P, r_P) = \frac{GM}{\gamma_P R} \sum_{n=0}^{\infty} \sum_{m=-n}^n \left(\frac{R}{r_P}\right)^n \bar{V}_{nm} \bar{Y}_{nm}(\varphi_P, \lambda_P) \quad (2.33)$$

γ_P is the normal gravity at the evaluation point P .

The radial component of the gravity field calculated by taking the first radial derivative of Eq. (2.24), is given as (Yang et al (2019))

$$\delta g(\varphi_P, \lambda_P, r_P) = \frac{GM}{r_P^2} \sum_{n=0}^{\infty} \sum_{m=-n}^n (n+1) \left(\frac{R}{r_P}\right)^n \bar{V}_{nm} \bar{Y}_{nm}(\varphi_P, \lambda_P) \quad (2.34)$$

and second-radial derivative as (Yang et al (2019)):

$$V_{zz}(\varphi_P, \lambda_P, r_P) = \frac{\partial^2 V(\varphi_P, \lambda_P, r_P)}{\partial r^2} = \frac{GM}{r_P^3} \sum_{n=0}^{\infty} \sum_{m=-n}^n (n+1)(n+2) \left(\frac{R}{r_P}\right)^n \bar{V}_{nm} \bar{Y}_{nm}(\varphi_P, \lambda_P) \quad (2.35)$$

For further details on the SGM techniques in the spherical approximation, see, e.g., *Balmino et al (2012)*, *Bucha et al (2019)*, *Hirt and Kuhn (2014)* and *Rexer et al (2016)*, *Rexer (2017)* and *Rummel et al (1988)*,

The SGM approach shows great efficiency in implementing the terrain gravitational field at long and medium wavelengths, such as the development of layer-based topographical gravitational fields of EARTH2014, i.e., dV_ELL_Earth2014 (*Rexer et al (2016)*) and RWI_TOPO_2015 (*Grombein et al (2016)*) up to order and degree of 2,190, and dV_ELL_Earth2014_5480 to order and degree 5,480 (*Rexer et al (2017)*). The classical library SHTOOLS (*Wieczorek and Meschede (2018)*) allows to expand a given field up to the spherical harmonic degree of 2,800. *Rexer (2016)* improved the SHTOOLS to adapt for ultra-high resolution SHA (e.g., to degree and order of $\sim 46,000$) by including numerically stable routines for computation of the Associated Legendre Functions (ALFS) following *Fukushima (2012)*. For ultra-high degree SHS, free software has been made publicly available with Matlab-based Graflab developed by *Bucha and Janák (2013)* and *Bucha and Janák (2014)*. However, long- and medium-wavelength gravitational expressions are not optimal for local investigations. Additionally, to properly handle the convergence behavior of the binominal series expansions involved during the numerical procedures, SGM requires to model the additional spectral powers which generally leads to high numerical costs, especially with ultra-high resolution mass models.

2.2.3 Spatial domain methods

In contrast to the SGM, where the retrieved gravitational fields are limited by the maximum degree of SHCs, the spatial domain technique theoretically comprises all spectral powers. In the NI method, the continuous terrain masses are commonly divided into a mesh model which can be aligned with the grid of the available geometrical data (e.g., DEMs) and geological parameters (e.g., mass density models), and then approximated

using various types of regular geometries such as polyhedron, prism, tesseroid and point mass. Analytical or numerical integration schemes can be used to evaluate the integral (Eq. (2.17)) over each volume element, and its first and second derivatives. The composite gravity effect over all mass-elements is then obtained through a summation of all individual contributions. In the following, our intent is to briefly explain the meaning of formulas and theorems of the gravitational field generated by four types of regular geometries, i.e., polyhedron, prism, tesseroid and point mass.

1) Case of polyhedron

The analytical formulas of the potential, its first- and second-derivatives generated by a homogeneous arbitrarily shaped polyhedron are presented in a compact form by *Petrović (1996)*, *Tsouliis (2001)* and *Tsouliis (2012)*. The derivations of the gravitational field generated by a polyhedron consist of the common three steps:

- First, transform the volume integral in Eq. (2.17) into a surface integral via rigorously applying the Gauss' divergence theorem. The number of surface integrals equals the number of faces of the polyhedron.
- Second, perform a transformation of the coordinate system and define a new Cartesian system in which the z direction coincides with the direction of the outward normal on the surface;
- Third, convert each of the surface integrals into a set of line integrals through further application of the divergence theorem.

In a local north-oriented coordinate system (Fig. 2.3), the origin of the coordinate system is located at the calculation point, and the unit vector $\mathbf{e}_1, \mathbf{e}_2, \mathbf{e}_3$ are the directions of coordinate system with \mathbf{e}_1 directed to north, \mathbf{e}_2 directed to west, and \mathbf{e}_3 along the vector from the geocenter to the calculation point and toward exterior. According to *Tsouliis and Petrović (2001)*, assuming the attracting source to be a polyhedron with a uniform density value ρ , with n faces and each having m sides, the analytical solutions of the generated gravitational field are the following:

$$V = \frac{G\rho}{2} \sum_{p=1}^n \sigma_p h_p \left[\sum_{q=1}^m \sigma_{pq} h_{pq} LN_{pq} + h_p \sum_{q=1}^m \sigma_{pq} AN_{pq} + SLNG_{\mathcal{A}_p} \right] \quad (2.36)$$

$$V_i = G\rho \sum_{p=1}^n \cos(\mathbf{N}_p, \mathbf{e}_i) \left[\sum_{q=1}^m \sigma_{pq} h_{pq} LN_{pq} + h_p \sum_{q=1}^m \sigma_{pq} AN_{pq} + SLNG_{\mathcal{A}_p} \right] \quad (i = 1, 2, 3) \quad (2.37)$$

$$V_{ij} = G\rho \sum_{p=1}^n \cos(\mathbf{N}_p, \mathbf{e}_i) \left[\sum_{q=1}^m \cos(\mathbf{n}_{pq}, \mathbf{e}_j) LN_{pq} + \sigma_p \cos(\mathbf{N}_p, \mathbf{e}_j) \sum_{q=1}^m \sigma_{pq} AN_{pq} + SLNG_{\mathcal{B}_{pj}} \right] \quad (i, j = 1, 2, 3) \quad (2.38)$$

with

$$LN_{pq} = \ln \frac{s_{2pq} + l_{2pq}}{s_{1pq} + l_{1pq}} \quad (2.39)$$

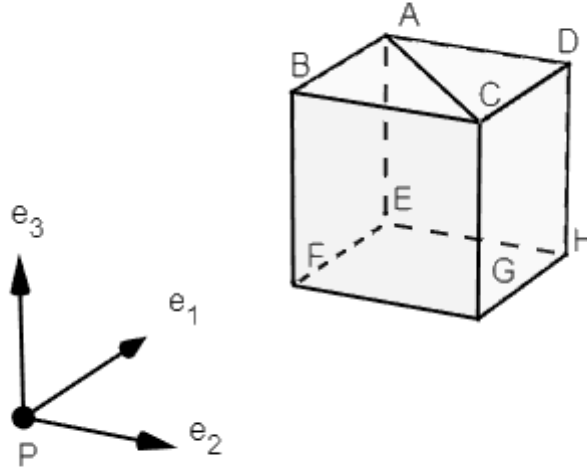


Fig. 2.3 – Local coordinate system and geometry of polyhedron element

$$AN_{pq} = \arctan \frac{h_p s_{2pq}}{h_{pq} l_{2pq}} - \arctan \frac{h_p s_{1pq}}{h_{pq} l_{1pq}} \quad (2.40)$$

using the subscript i indicating the partial derivative components as $V_i = \frac{\partial V}{\partial x_i}$, V_{ij} describes the nine elements of the Marussi tensor according to $V_{ij} = \frac{\partial^2 V}{\partial x_i \partial x_j}$ ($i = 1, 2, 3, j = 1, 2, 3$). p stands for the face elements, running from 1 to n , N_p represents the outer unit normal of the polyhedral plane p , with $\sigma_p = -1$ when N_p points to the half-space containing the calculation point P , and $\sigma_p = 1$ otherwise, h_p is the positive distance between the calculation point P and the polyhedral plane p . q denotes the polyhedral segments (with values from 1 to m), P' is the orthogonal projection of P on the face p of polyhedron, using G_{pq} represents the line segment of face p , P'' is the orthogonal projection of P' on the G_{pq} , h_{pq} is the distance between P' and G_{pq} . The unit vector \mathbf{n}_{pq} stands for the outward unit normal of the segment G_{pq} , $\sigma_{pq} = -1$ when \mathbf{n}_{pq} points to the half-plane containing the point P' and $+1$ if it points to the other half-plane, l_{1pq} and l_{2pq} are the distances in space between calculation point P and the end points of G_{pq} , s_{1pq} and s_{2pq} denote the distances between P'' and the two end points of G_{pq} .

The singularity terms $SIN\mathcal{G}_{A_p}$ and $SIN\mathcal{G}_{B_{pj}}$ handle the singularity problem when the divergence theorem of Gauss is applied to the cases that P' falls on the polyhedral faces (*Tsoullis and Petrović (2001)*).

$$SIN\mathcal{G}_{A_p} = -\theta h_p \quad (2.41)$$

$$SIN\mathcal{G}_{B_{pj}} = -\theta \cos(\mathbf{N}_p, \mathbf{e}_j) \sigma_p \quad (2.42)$$

with θ defining the inner angle of circle around P' which depends on the location of P' in the surface (*Tsoullis and Petrović (2001)*).

2) Case of rectangular prism

One of the most often used methods in modeling the terrain masses is based on the flat-topped rectangular prism. As shown in Fig. 2.4, in a prism-based local Cartesian coordinate system, the origin is located at the center of the prism, the coordinate's axes (e_1, e_2, e_3) are assumed to be parallel to the edges of the prism. Let $\Delta x, \Delta y$ denote the horizontal sides of the prism which coincide with the applied grid resolution, and Δz represents the vertical height of the prism. The prism is then bounded by planes defined by the coordinates $-\frac{\Delta x}{2}, \frac{\Delta x}{2}, -\frac{\Delta y}{2}, \frac{\Delta y}{2}, -\frac{\Delta z}{2}, \frac{\Delta z}{2}$. l is the Euclidean distance from the calculation point $P(x', y', z')$ to the running integration point $Q(x, y, z)$.

Assuming a homogeneous mass-density distribution of ρ in each volume element and carrying out the integration, the closed analytical expressions for gravitational potential follow *Heck and Seitz (2007)*, *Nagy et al (2000)* and *Nagy et al (2002)*:

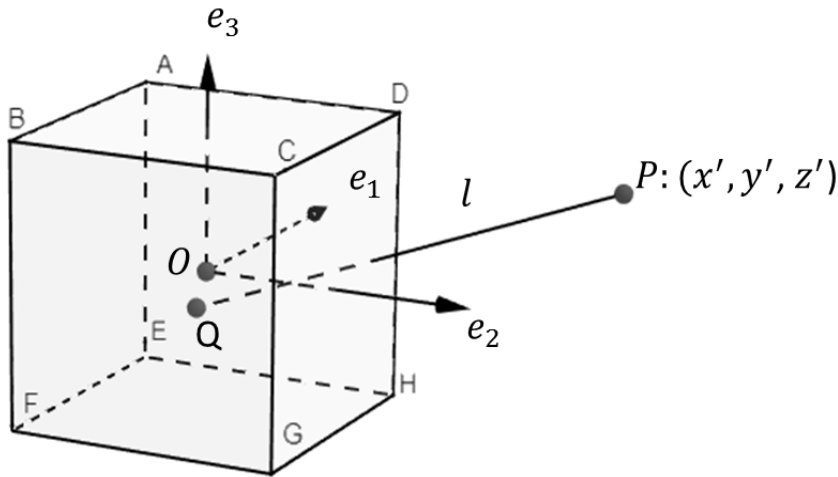


Fig. 2.4 – Prism-based local Cartesian coordinate system and geometry of prism element

$$\begin{aligned}
 V = G\rho \left\| \left\| \left(x' - x \right) \left(y' - y \right) \ln \left| \frac{ \left(z' - z \right) + l }{ \sqrt{ \left(x' - x \right)^2 + \left(y' - y \right)^2 } } \right| + \left(y' - y \right) \left(z' - z \right) \ln \left| \frac{ \left(x' - x \right) + l }{ \sqrt{ \left(z' - z \right)^2 + \left(y' - y \right)^2 } } \right| \right. \right. \\
 \left. \left. + \left(x' - x \right) \left(z' - z \right) \ln \left| \frac{ \left(y' - y \right) + l }{ \sqrt{ \left(x' - x \right)^2 + \left(z' - z \right)^2 } } \right| - \frac{ \left(x' - x \right)^2 }{ 2 } \arctan \frac{ \left(y' - y \right) \left(z' - z \right) }{ \left(x' - x \right) l } \right. \right. \\
 \left. \left. - \frac{ \left(y' - y \right)^2 }{ 2 } \arctan \frac{ \left(x' - x \right) \left(z' - z \right) }{ \left(y' - y \right) l } - \frac{ \left(z' - z \right)^2 }{ 2 } \arctan \frac{ \left(y' - y \right) \left(x' - x \right) }{ \left(z' - z \right) l } \right|_{-\frac{\Delta x}{2}}^{\frac{\Delta x}{2}} \left|_{-\frac{\Delta y}{2}}^{\frac{\Delta y}{2}} \right|_{-\frac{\Delta z}{2}}^{\frac{\Delta z}{2}}
 \end{aligned} \quad (2.43)$$

The gradient of V in x direction is

$$V_x = G\rho \left[(y' - y) \ln \left| \frac{(z' - z) + l}{\sqrt{(x' - x)^2 + (y' - y)^2}} \right| + (z' - z) \ln \left| \frac{(y' - y) + l}{\sqrt{(x' - x)^2 + (z' - z)^2}} \right| - (x' - x) \arctan \frac{(y' - y)(z' - z)}{(x' - x)l} \right]_{-\frac{\Delta x}{2}}^{\frac{\Delta x}{2}} \left|_{-\frac{\Delta y}{2}}^{\frac{\Delta y}{2}} \right|_{-\frac{\Delta z}{2}}^{\frac{\Delta z}{2}} \quad (2.44)$$

The other two first derivatives V_y and V_z can be obtained from Eq. (2.44) by the cyclic permutation which shifts the three elements x , y and z of the combinatorics by one place to the left, with the elements shifted off the end inserted back at the beginning.

The second derivatives are

$$V_{xx} = G\rho \left[-\arctan \frac{(y' - y)(z' - z)}{(x' - x)l} \right]_{-\frac{\Delta x}{2}}^{\frac{\Delta x}{2}} \left|_{-\frac{\Delta y}{2}}^{\frac{\Delta y}{2}} \right|_{-\frac{\Delta z}{2}}^{\frac{\Delta z}{2}} \quad (2.45)$$

$$V_{xy} = G\rho \left[\ln \left| \frac{(z' - z) + l}{\sqrt{(x' - x)^2 + (y' - y)^2}} \right| \right]_{-\frac{\Delta x}{2}}^{\frac{\Delta x}{2}} \left|_{-\frac{\Delta y}{2}}^{\frac{\Delta y}{2}} \right|_{-\frac{\Delta z}{2}}^{\frac{\Delta z}{2}} \quad (2.46)$$

here $l = \sqrt{(x' - x)^2 + (y' - y)^2 + (z' - z)^2}$. The other diagonal elements of gravity tensor V_{yy} , V_{zz} can be obtained from Eq. (2.45), and the partial derivatives V_{xz} , V_{yz} can be obtained from Eq. (2.46) by cyclic permutation.

In order to improve the numerical stability (cf. *Grüniger* (1990)), the logarithmic terms in former equations (Eqs. 43-46) have been transformed with respect to formulas in *Mader* (1951). However, the arctan-functions in the equations (Eqs. 43-46) are not defined when the computation points are located at corners, edges or planes of the prism. Therefore, Eqs. 43-46 show singularities in these cases. To solve the singularity problem, the terms with the arctan-function can be set to zero as shown in *Nagy et al* (2000). The limits for Marussi tensor elements over discontinuity boundaries were also given in *Nagy et al* (2000).

The main disadvantage using prisms is the necessity of repeated evaluation of logarithmic and trigonometric expressions, e.g., 24 log-functions and 24 arctan-functions for potential, 12 log-functions and 6 arctan-functions for the first derivatives, which is computationally demanding especially when one wants to perform computations for a density-spaced grid of computation points. In practice, the prism is therefore usually used for the integration in the vicinity of the computation point.

Another issue should be noted. Using prisms for discretization is usually related to the plane approximation, with which all prisms are assumed to refer to the same horizontal plane defined by the local north-oriented coordinate system with origin at the calculation point. Assume two local Cartesian coordinate systems (x, y, z) with respect to the prism and (x^*, y^*, z^*) relating to the calculation point, x-axis and y-axis respectively point

to local north and east directions, and z-axis coincides with the spherical/ellipsoidal normal, the origins are located at P (φ and λ) and P' (φ' and λ') respectively. Due to the curvature of the Earth, the local Cartesian coordinate system (x^*, y^*, z^*) attached to the computation point and the prism-based Cartesian system (x, y, z) will not be parallel, see Fig. 2.5, which would be obvious for far-zone mass-distributions when l is larger than several km. In such cases, a transformation of the gravity vectors (V_x, V_y, V_z) and the Marussi tensors from the prism-based coordinate system into the station-based local system is necessary (Heck and Seitz (2007), Wild-Pfeiffer (2008)). This relies on the basis transformation between the local Cartesian system and the global Cartesian coordinate system (X, Y, Z) (Fig. 2.5). The transformation from (x, y, z) to (X, Y, Z) follows Hofmann-Wellenhopf and Moritz (2006),

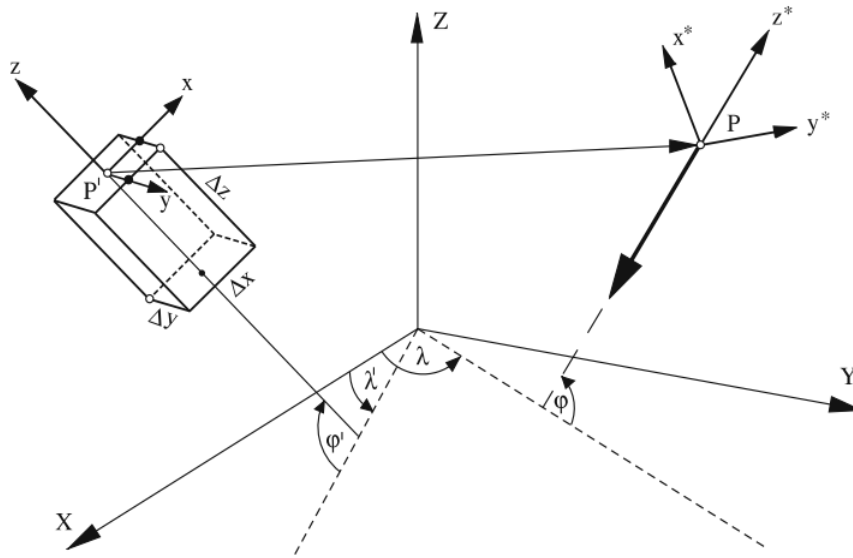


Fig. 2.5 – Transformation between the station-based and prism-based Cartesian coordinate system, adapted from Heck and Seitz (2007, P.126).

$$\begin{pmatrix} X \\ Y \\ Z \end{pmatrix} = R_1 \begin{pmatrix} x \\ y \\ z \end{pmatrix} \quad (2.47)$$

and from (X, Y, Z) to (x', y', z') follows

$$\begin{pmatrix} x' \\ y' \\ z' \end{pmatrix} = R_2 \begin{pmatrix} X \\ Y \\ Z \end{pmatrix} \quad (2.48)$$

Therefore,

$$\begin{pmatrix} x' \\ y' \\ z' \end{pmatrix} = R_2 R_1 \begin{pmatrix} x \\ y \\ z \end{pmatrix} = R \begin{pmatrix} x \\ y \\ z \end{pmatrix} \quad (2.49)$$

the rotation matrices,

$$R_1 = \begin{pmatrix} -\sin \varphi \cos \lambda & -\sin \lambda & \cos \varphi \cos \lambda \\ -\sin \lambda \sin \varphi & \cos \lambda & \cos \varphi \sin \lambda \\ \cos \varphi & 0 & \sin \varphi \end{pmatrix} \text{ and } R_2 = \begin{pmatrix} -\sin \varphi' \cos \lambda' & -\sin \varphi' \sin \lambda' & \cos \varphi' \\ -\sin \lambda' & \cos \lambda' & 0 \\ \cos \varphi' \cos \lambda' & \cos \varphi' \sin \lambda' & \sin \varphi' \end{pmatrix}$$

According to *Hofmann-Wellenhof and Moritz (2006)*, the two rectangular coordinate systems xyz and $x'y'z'$ are related through:

$$\begin{pmatrix} x' \\ y' \\ z' \end{pmatrix} = R \begin{pmatrix} x \\ y \\ z \end{pmatrix}, \begin{pmatrix} x \\ y \\ z \end{pmatrix} = R^T \begin{pmatrix} x' \\ y' \\ z' \end{pmatrix} \quad (2.50)$$

where R is orthogonal matrix and R^T is its transpose. Then the first-order gradients transform of function in two coordinate systems is

$$\begin{pmatrix} V_{x'} \\ V_{y'} \\ V_{z'} \end{pmatrix} = R \begin{pmatrix} V_x \\ V_y \\ V_z \end{pmatrix} \quad (2.51)$$

The second-order transform is

$$\begin{pmatrix} V_{x'x'} & V_{x'y'} & V_{x'z'} \\ V_{y'x'} & V_{y'y'} & V_{y'z'} \\ V_{z'x'} & V_{z'y'} & V_{z'z'} \end{pmatrix} = R \begin{pmatrix} V_{xx} & V_{xy} & V_{xz} \\ V_{yx} & V_{yy} & V_{yz} \\ V_{zx} & V_{zy} & V_{zz} \end{pmatrix} R^T \quad (2.52)$$

3) Case of Tesseroid

The tesseroid can be easily defined when the shape of the Earth is referred to a spherical coordinate system (*Heck and Seitz (2007)*, *Grombein et al (2013)*, *Tsouliis (2001)*) or ellipsoidal coordinate system (*Roussel et al (2015)*). Generally, a tesseroid is bounded by six faces (Fig. 2.6):

- (1) two meridians of longitude λ_1 and λ_2 ,
- (2) two parallels of latitude φ_1 and φ_2 , here φ_1 and φ_2 respectively represent geodetic latitudes in the ellipsoidal coordinate system and spherical latitudes in the spherical coordinates system,
- (3) a pair of concentric spheres or two homothetic ellipsoids with the scaling factors r_1 and r_2 .

In spherical approximation, the fundamental expression for the gravitational potential of the topographic masses with a uniform density value ρ is given according to, e.g. *Grombein et al (2013)*,

$$V(r', \varphi', \lambda') = G\rho \int_{\lambda} \int_{\varphi} \int_r \frac{r^2 \cos \varphi}{l} dr d\varphi d\lambda \quad (2.53)$$

In this equation, the position of the computation point is defined as (r', φ', λ') and the integration running point as (r, φ, λ) . The function l stands for the Euclidean distance between the computation point and the point of integration:

$$l = \sqrt{r^2 + r'^2 - 2rr' \cos \psi} \quad (2.54)$$

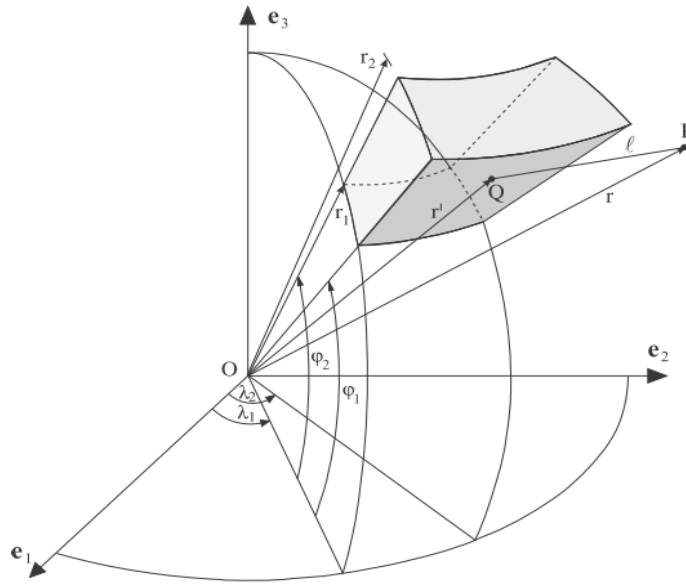


Fig. 2.6 – Geometry of tesseroid, adapted from *Grombein et al (2013, P647)*

The spherical distance between two points is given by the law of cosines

$$\cos \psi = \sin \varphi \sin \varphi' + \cos \varphi \cos \varphi' \cos(\lambda - \lambda') \quad (2.55)$$

There exists no analytical solution either for the potential or for its derivatives because of integrals over elliptic volumes. In such cases, numerical solutions have to be applied. In principle, there are two main computational strategies for the numerical evaluation of these quantities (*Tsoulis et al (2009)*)

- The first possibility is using quadrature technique either directly to the triple integral expressing the potential and its derivatives (e.g., *Asgharzadeh et al (2007)*) or to the surface integral obtained after kernel integration in radial direction (*Martinec (1994)*, *Smith et al (2001)*).
- An alternative method is based on a Taylor series expansion of the kernel function $\frac{r^2 \cos \varphi}{l}$ with respect to geocentric spherical coordinates, then truncating the Taylor series after its second term (*Heck and Seitz (2007)*). In order to calculate the first- and second-derivatives in the moving local Cartesian frame, additional transformations have to be applied which leads to polar singularities (*Tscherning (1976)*). To avoid the transformation problem, the general expression for the tesseroid's gravitational potential and its derivatives in the Cartesian integral kernels can be used that has been formulated in *Grombein et al (2013)*. This method is hereafter referred to as the optimized solution to the tesseroidal modeling method.

In the optimized solution (*Deng et al (2016)*, *Grombein et al (2013)*), the gravitational potential, its first derivatives, and the Marussi tensor generated by a tesseroid of a uniform mass density value ρ can be formulated in a general form as

$$\begin{Bmatrix} V(r', \varphi', \lambda') \\ \frac{\partial}{\partial x_i} V(r', \varphi', \lambda') \\ \frac{\partial^2}{\partial x_i \partial x_j} V(r', \varphi', \lambda') \end{Bmatrix} = G\rho \int_{\lambda} \int_{\varphi} \int_r \frac{1}{l^3} \begin{Bmatrix} \Delta x_i \Delta x_i \\ \Delta x_i \\ \frac{3\Delta x_i \Delta x_j}{l^2} - \delta_{ij} \end{Bmatrix} r^2 \cos \varphi dr d\varphi d\lambda \quad (2.56)$$

where

$$\begin{aligned} \Delta x_1 &= r[\cos \varphi' \sin \varphi - \sin \varphi' \cos \varphi \cos(\lambda - \lambda')], \\ \Delta x_2 &= r \cos \varphi \sin(\lambda - \lambda'), \\ \Delta x_3 &= r[\sin \varphi' \sin \varphi + \cos \varphi' \cos \varphi \cos(\lambda - \lambda')] - r' \end{aligned} \quad (2.57)$$

with $i, j \in 1, 2, 3$, $\Delta x_1, \Delta x_2, \Delta x_3$ indicating the coordinate differences between calculation point and integration point in local Cartesian x, y and z directions respectively, $\Delta x_i \Delta x_i = l^2$, δ_{ij} denoting the Kronecker delta, i.e. $\delta_{ij} = 1$ if $i = j$ and $\delta_{ij} = 0$ otherwise. With Taylor series expansion of the Cartesian integral kernels at the Tesseroid's geometrical center, this approach leads to a numerical solution for equation (Eq. (2.56)) with a fourth-order error in the spatial coordinates (*Grombein et al (2013)*),

$$\begin{Bmatrix} V(r', \varphi', \lambda') \\ \frac{\partial}{\partial x_i} V(r', \varphi', \lambda') \\ \frac{\partial^2}{\partial x_i \partial x_j} V(r', \varphi', \lambda') \end{Bmatrix} = \omega \begin{Bmatrix} K(P, Q) \\ L_i(P, Q) \\ N_{ij}(P, Q) \end{Bmatrix} \Bigg|_{\substack{r=r_0 \\ \varphi=\varphi_0 \\ \lambda=\lambda_0}} + \frac{\omega}{24} \sum_{k=1}^3 \Delta \xi_k^2 \begin{Bmatrix} \partial_k^2 K(P, Q) \\ \partial_k^2 L_i(P, Q) \\ \partial_k^2 N_{ij}(P, Q) \end{Bmatrix} \Bigg|_{\substack{r=r_0 \\ \varphi=\varphi_0 \\ \lambda=\lambda_0}} + \begin{Bmatrix} O(\Delta^4/l_0^5) \\ O(\Delta^4/l_0^6) \\ O(\Delta^4/l_0^7) \end{Bmatrix} \quad (2.58)$$

In this equation, the substitutions $(\xi'_1, \xi'_2, \xi'_3) = (r', \varphi', \lambda')$ and $(\Delta \xi_1, \Delta \xi_2, \Delta \xi_3) = (\Delta r, \Delta \varphi, \Delta \lambda)$ are adopted for a more general notation. The Cartesian integral kernels of Eq. (2.58) are denoted by

$$\begin{Bmatrix} K(P, Q) \\ L_i(P, Q) \\ N_{ij}(P, Q) \end{Bmatrix} = \frac{1}{l^3} \begin{Bmatrix} \Delta x_i \Delta x_i \\ \Delta x_i \\ \frac{3\Delta x_i \Delta x_j}{l^2} - \delta_{ij} \end{Bmatrix} \tau \quad (2.59)$$

where

$$\tau = r^2 \cos \varphi \quad (2.60)$$

The required second-order derivatives in Eq. (2.58) can be represented by (*Grombein et al (2013)*)

$$\begin{Bmatrix} \partial_k^2 K(P, Q) \\ \partial_k^2 L_i(P, Q) \\ \partial_k^2 N_{ij}(P, Q) \end{Bmatrix} = \frac{1}{l^3} \left[\partial_k^2(\tau) \begin{Bmatrix} \alpha \\ \alpha_i \\ \alpha_{ij} \end{Bmatrix} + \partial_k(\tau) \begin{Bmatrix} \beta_k \\ \beta_{ik} \\ \beta_{ijk} \end{Bmatrix} + \tau \begin{Bmatrix} \gamma_k \\ \gamma_{ik} \\ \gamma_{ijk} \end{Bmatrix} \right] \quad (2.61)$$

The remaining algebraic expressions, e.g., of ω , α , β , γ and their derivatives can be found in the work of *Grombein et al (2013)* and *Deng et al (2016)*.

Note that, unacceptably large errors might occur when applying the Taylor series approach for tesseroids in the vicinity of the computation point P . Therefore, special care such as the vertical subdivision of the tesseroid or equivalent prisms or polyhedrons should be taken in the direct vicinity of the computation point.

4) Case of Point mass

Because the gravity potential decreases with increasing distance from the field source, the distant mass-elements can be approximated by geometries of point mass located at the geometrical center Q of mass-elements. The mass of a point mass is assumed to be equal to the mass m of the tesseroid. The gravitational potential V at the calculation point P generated by the point mass m is given by:

$$V(P) = G \frac{m}{l} \quad (2.62)$$

The tesseroid equal mass is defined as (*Wild-Pfeiffer (2008)*):

$$m = \rho \frac{(\lambda_2 - \lambda_1)(r_2^3 - r_1^3)(\sin \varphi_2 - \sin \varphi_1)}{3} \quad (2.63)$$

The gravitational acceleration vector is obtained by calculating the space gradient vector of the scalar potential with respect to the calculation point P (*Wild-Pfeiffer (2008)*):

$$\mathbf{dg}(P) = \nabla(V(P)) = \begin{Bmatrix} V_x \\ V_y \\ V_z \end{Bmatrix} = \begin{Bmatrix} Gm \frac{\Delta x}{l^3} \\ Gm \frac{\Delta y}{l^3} \\ Gm \frac{\Delta z}{l^3} \end{Bmatrix} \quad (2.64)$$

Finally, the gravity gradient tensor, also referred to as Marussi's tensor, cf, also the Eq. (2.23), is obtained by calculating the tensor of space gradients of the gravity vector (*Wild-Pfeiffer (2008)*):

$$\Gamma(P) = \nabla(\mathbf{dg}(P)) = \begin{pmatrix} V_{xx} & V_{xy} & V_{xz} \\ V_{yx} & V_{yy} & V_{yz} \\ V_{zx} & V_{zy} & V_{zz} \end{pmatrix} \quad (2.65)$$

with

$$\begin{aligned} V_{xx} &= Gm \frac{3\Delta x^2 - l^2}{l^5} \\ V_{xy} &= Gm \frac{3\Delta x \Delta y}{l^5} \end{aligned} \quad (2.66)$$

V_{yy} and V_{zz} can be obtained from V_{xx} by the cyclic permutation, while V_{yz} and V_{xz} can be obtained from V_{xy} .

Tab. 2.1 – Publicly available algorithms for forward modeling in the spatial domain

Algorithm	Forward modelling	Numerical technique	Reference
“tc” in GRAVSOFT	flat-topped prism	point-wise direct integration with analytical solution	<i>Forsberg (1984)</i>
“tcfour” in GRAVSOFT	terrain masses in regular grid	FFT grid-wise with Taylor’s expansion	<i>Forsberg (1984)</i>
“tcq” in Fortran	terrain masses in regular grid	Gauss quadrature	<i>Hwang et al (2003)</i>
“Tesseroids” in C++	tesseroid	Gauss-Legendre Quadrature	<i>Uieda et al (2016)</i>
“POLYHEDRON” in Fortran	polyhedron	point-wise direct integration with analytical solution	<i>Tsoulis and Petrović (2001), Tsoulis (2012)</i>
“GTeC” in Matlab	square prism, triangle prism and polyhedron	point-wise integration	<i>Cella (2015)</i>

The calculation time required in NI technique is positively related to the number of computation points and the number of mass-elements for integration. In practice, the calculation is able to be implemented by a point-wise algorithm or by FFT in grid-wise computation. In the first method, the gravitational field over each evaluation point generated by the mass-distributions is calculated separately. This method is ideal for evaluation points being inhomogeneously distributed. The efficiency of the point-wise method depends on the number of evaluation points and amounts of elements of integration. FFT enables a much more efficient computation, but relies on strong hypotheses on the sources that have to lie on a plane and have to be implemented as a regular grid. The planar approximation makes FFT less accurate. A variety of studies and algorithms were implemented and developed over the past decades in the spatial domain technique, some of them are listed in the Tab. 2.1.

2.3 RTM and all variants

In general, the residual terrain modelling (RTM) technique is 1) the numerical evaluation of Newtonian integration 2) over residual masses around the calculation point and 3) extending globally over the Earth approximated by a local plane, a sphere of constant radius, or a spheroid of latitude dependent radii (*Bucha et al (2016), Forsberg and Tscherning (1981), Forsberg (1984), Hirt et al (2010a), Hirt (2010), Omang et al (2012), Rexer et al (2018)*). In the RTM technique, the residual terrain model is obtained as a high-pass-filtered model of terrain masses which are often given as by a detailed DEM. Assuming spectral consistency between filtering in the geometric domain and filtering in the gravity domain, the gravity details at short scales can be calcu-

lated through the evaluation of the Newton's integral in the frame of residual masses as discussed in Sect. 2.2.1.

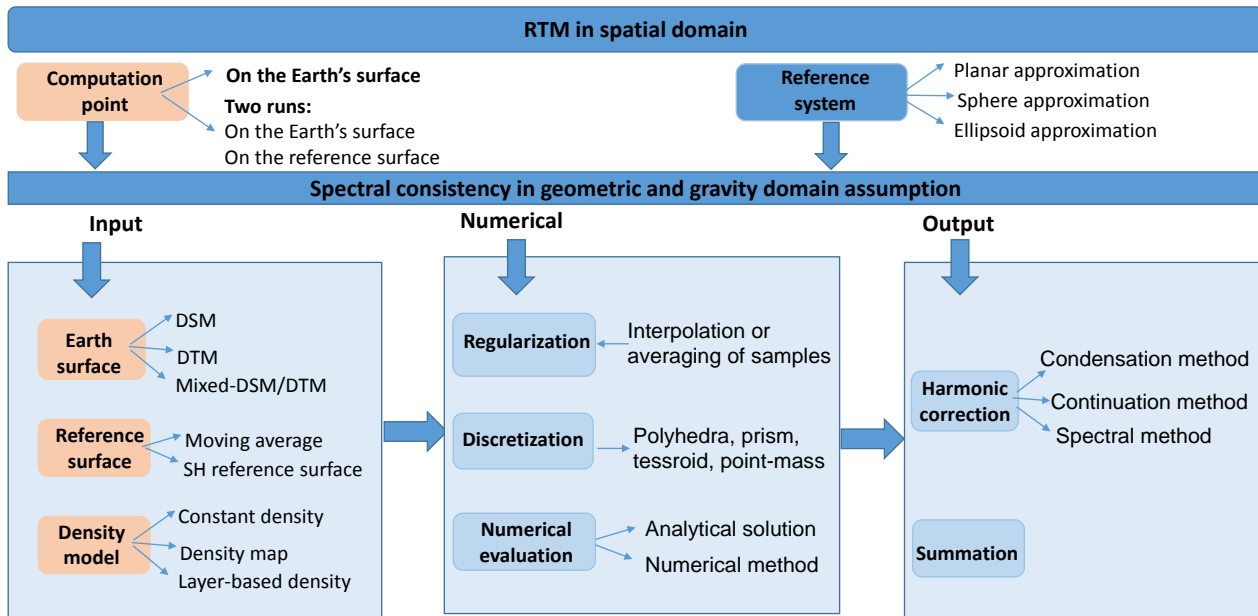


Fig. 2.7 – General flow chart of RTM technique in the spatial domain.

The accuracy of the RTM technique relies on the quality of 1) topographic information, including the detailed Earth's surface and its reference surface, and 2) the validity of the available mass-density information. In practical calculations, the detailed topography is generally modeled by some high-resolution DEMs that can be sourced from various techniques, such as radar-based mixed-DSM/DTMs, photogrammetry-based DSMs, or locally available DTMs (Fig. 2.7). The long-wavelength reference surface can be defined either by a high-degree and order spherical harmonic topography, like DTM2006 (Pavlis *et al* (2007)) or the RET2012 (Hirt *et al* (2012)), or by a down-sampled (e.g., moving average operator) high-resolution topography (Forsberg (1984)). The application of the spherical harmonic topography has been demonstrated in Hirt *et al* (2010a) to perform better in spectral filtering when the RTM is to be used for signal augmentation of GGMs at short scales. Given the complexity and difficulty of obtaining the actual mass-density values, a detailed information of the terrain density distribution is not feasible in practice. In previous works, the majority forward modelling results (e.g., Bonvalot *et al* (2012), Bucha *et al* (2016), Cella (2015), Hirt *et al* (2014), Hirt *et al* (2019b), Tsoulis (2001)) were based on some constant density assumption such as using the uniform rock density of $2,670 \text{ kg/m}^3$ for continental masses.

Over areas covered by water, ice, and other density anomalies, the rock-equivalent topography (RET) concept is often used for simplification of numerical evaluation (Hirt *et al* (2012), Hirt *et al* (2014)), or more precisely using a layer-based density model in separate forward modelling procedures (Grombein *et al* (2016), Rexer *et al* (2016), Rexer (2017)). As the basic idea of the RET concept, the process of compressing all

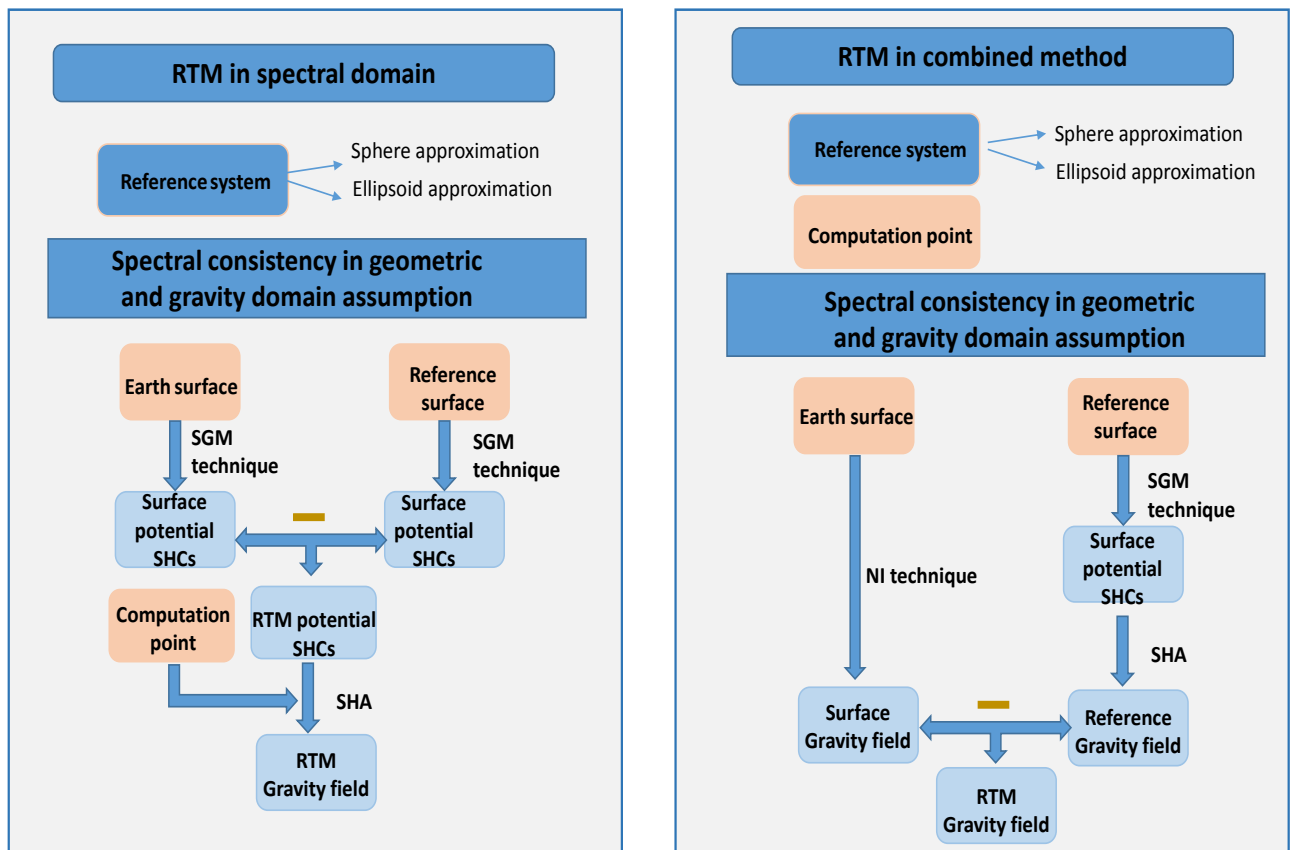


Fig. 2.8 – RTM in spectral domain and with combined technique.

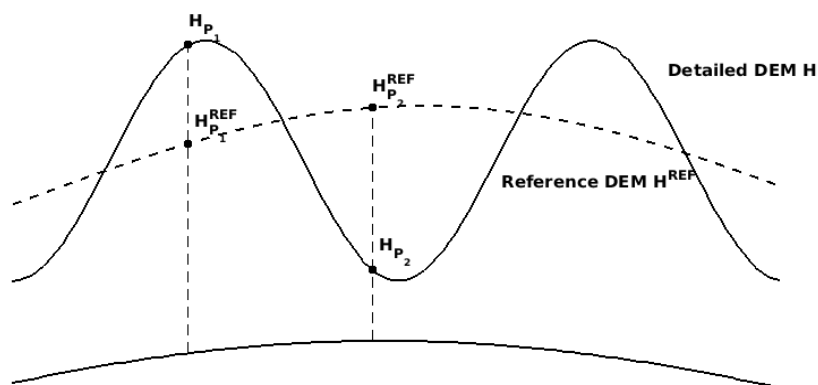


Fig. 2.9 – RTM principle of residual terrain masses over point P_1 located exterior to the residual masses and point P_2 above or on the Earth's surface but below the reference surface.

mass anomalies above the bedrock into rock-equivalent masses, yields the RET model which allows the use of a single consistent mass–density value over all masses (e.g., ocean and continent) of integration:

$$H_{RET} = H_{anomaly} \left(1 - \frac{\rho_{anomaly}}{\rho}\right) \quad (2.67)$$

where $H_{anomaly}$ and $\rho_{anomaly}$ indicate depth and actual density values of mass anomalies. $1,030 \text{ kg/m}^3$ is generally accepted for ocean bodies, and 920 kg/m^3 for ice masses. ρ is rock density of $2,670 \text{ kg/m}^3$. H_{RET} is the obtained RET height. The RET approximation effects on full-scale topographic gravity signals have been shown in *Kuhn and Hirt (2016)* to be 1) smallest for the potential component, with relative error at the level of $\sim 0.06 - 0.08\%$ and 2) $\sim 3 - 7\%$ for first-order derivatives at the Earth's surface, and 3) increasing from $\sim 10\%$ to $\sim 110\%$ for second-order derivatives with elevation heights from 3 km down to near the Earth's surface. The relative error here indicates the ratio between the range in effects to the range in signals. Therefore, in the near-surface evaluation, the use of RET would introduce considerable errors in the derivatives of gravitational potential, which is not recommended.

In theory, the numerical integration that delivers RTM gravity field needs to be done over the global topographic masses in the spatial domain, or through SGM technique. Because of the fluctuating nature of residual topography, and decaying of Newton's functionals with increasing distance, the gravitational effects produced by the masses beyond a limited radius cancel out to a large extent. Therefore, only residual masses within a limited integration radius are considered in practical evaluations. Thus, the computation times and required DEM areas are significantly reduced compared to global integration. However, the limited integration radius produces a truncation error. The trade-off between integration radius and accuracy of the calculated RTM gravity field will be analyzed in-depth in Chapter 4 with a reference surface at a spatial resolution of 5'.

When RTM techniques are applied in gravity field modeling, about 50 % of the RTM elevations have negative heights where the calculation points are above or on the Earth's surface but are buried beneath the reference surface (e.g., point P_2 in Fig. 2.9, see also *Forsberg (1984)*). The direct RTM over these points yields a non-harmonic gravitational potential and does therefore not anymore correspond to values observed or evaluated in harmonic condition, e.g., terrestrial gravity observations and spherical harmonic gravity field which describe the field external to the mass distribution (cf. *Hirt et al (2019a)*). "*The non-harmonic problem over points below the reference is considered to be a major theoretical problem with the RTM technique*" (*Denker (2013)*, *Hirt et al (2019a)*). Conventionally, harmonic correction is made by compressing the mass layer between the computation point and the reference surface into an infinitesimal thick mass layer immediately below the computation point. After compressing, no differences are introduced for the gravitational functionals of exterior points like P_1 in Fig. 2.9, but harmonic corrections are applied to the interior points like point P_2 as

$$\Delta g_{HC} = 4\pi G\rho H_{RTM}, \quad H < H^{REF} \quad (2.68)$$

It is computed for all points with $H < H^{REF}$ and applied as an additive correction to the directly computed 'non-harmonic' gravity values. In the following, this technique is denoted as condensation harmonic correction. The condensation harmonic correction relies on mass condensation and is based on a double Bouguer slab approximation. Therefore, the correction from Eq. (2.68) is only an approximation of a 'true' value of harmonic correction, which has been admitted in the literature, such as *Forsberg (2010)*, *Omang et al (2012)*, *Denker (2013)* and *Hirt et al (2019a)*. Additionally, the condensation harmonic correction was developed only for radial derivatives of potential, e.g., gravity anomalies, and no corrections were derived for other gravitational functionals.

Besides the non-harmonic problem, the RTM technique also suffers from the approximative character of spectral consistency in the geometry and gravity domain. In practice, the spectral inconsistency between filtering in the geometric domain and filtering in the physical domain comes into play. First, the band-limited topographic mass distributions generate gravity signals with spectral energy at full spatial scales. Therefore, in the RTM technique, the forward modeled gravity field contains the spectra above the resolution commensurate with the input reference topographic mass model. This very-high frequency gravity signal implied by the reference surface is also removed during the filtering procedure (*Rexer et al (2018)*). On the other hand, the low-frequency gravity signal encountered in the residual heights should not be included in the RTM gravity signal. High-frequency errors of topographic gravitational signals contained in the band-limited topography was firstly investigated and evaluated through including contributions of the integer powers of $\frac{H}{R}$ to ultra-high degree (*Hirt and Kuhn (2014)*), which already has been applied in RTM technique to recover the very high-frequency gravity signals implied by the reference surface that were removed during filtering procedure, e.g., *Bucha et al (2016)*, *Rexer et al (2018)* and *Hirt et al (2019a)*. The methods for the evaluation of the low-frequency error were introduced in *Rexer et al (2018)* which relies on the spherical harmonic analysis of the global RTM gravity field.

The following, six types of often used RTM techniques can be distinguished. These are listed in Tab. 2.2 either using the SGM technique (in Section 2.2.1) of Fig. 2.8, or using NI technique (in Section 2.2.2) of Fig. 2.7, or through their combination method of Fig. 2.8. We will now explain the differences among the six techniques. Some of these variants have been described in *Hirt et al (2019a)*.

In the RTM-A variant (Fig. 2.10 panel a)), direct RTM integration together with the condensation harmonic correction is conducted as presented in *Forsberg (1984)*. The attraction of the residual masses on points at the surface of topography is calculated following Eq. (2.69). As Eq. (2.69),

$$\begin{aligned}
 \delta g_{RTM-A}(P_1) &= \delta g(P_1) = G \int_{\varphi} \int_{\lambda} \int_{R+H^{REF}}^{R+H} \frac{\rho(r_1 - r)}{l^3} dr d\lambda d\varphi \\
 \delta g(P_2) &= G \int_{\varphi} \int_{\lambda} \int_{R+H^{REF}}^{R+H} \frac{\rho(r_2 - r)}{l^3} dr d\lambda d\varphi \\
 \delta g_{RTM-A}(P_2) &= \delta g(P_2) + 4\pi G\rho(H_{P_2} - H_{P_2}^{REF})
 \end{aligned} \tag{2.69}$$

Tab. 2.2 – RTM variants with different definitions

RTM-Variants	Runs	Topography Inputs	Gravity effect of DT	Gravity effect of RT	HC	SFP	Approximation errors	reference
RTM-A	1	DT, RT	1) Capped NI; 2) CP resided on DT	1) Capped NI;	present condensation method	present no treatment	1) spectral filter errors 2) errors related HC	<i>Forsberg (1984)</i>
RTM-B	1	RTM height	1) Capped NI; 2) CP on residual terrain	1) Capped NI;	present condensation method	present no treatment	1) spectral filter errors 2) errors related HC 3) mass simplification	<i>Hirt et al (2014)</i>
RTM-C	2	DT, RT	1) capped NI; 2) CP on DT	1) Capped NI; 2) CP on RT	not present	present no treatment	1) spectral filter errors 2) CP inconsistency	<i>Hirt et al (2019a)</i>
RTM-D	2	DT, RT	1) capped NI; 2) CP on DT	1) Capped NI; 2) CP on RT	present analytical continuation via Taylor series	present no treatment	1) spectral filter errors 2) CP inconsistency 3) analytical continuation correlated errors	<i>Bucha et al (2016)</i>
RTM-E	4	DT, RT	1) limited BS and TC; 2) CP on the DT	1) limited BS and TC; 2) CP on the HT	present two limited BS and two TC	present no treatment	1) spectral filter problem 2) CP inconsistency error	<i>Kadlec (2011)</i>
RTM-F	2	DT and RT	1) global NI 2) CP on the DT	1) SGM; 2) CP on the DT	not present	not present	Avoid former mentioned errors	<i>Hirt et al (2019a)</i>

CP – computation points; DT – Detailed topography; RT – Reference topography; HC – Harmonic correction; SFP – Spectral filter problem; BS – Bouguer shell; TC – terrain correction.

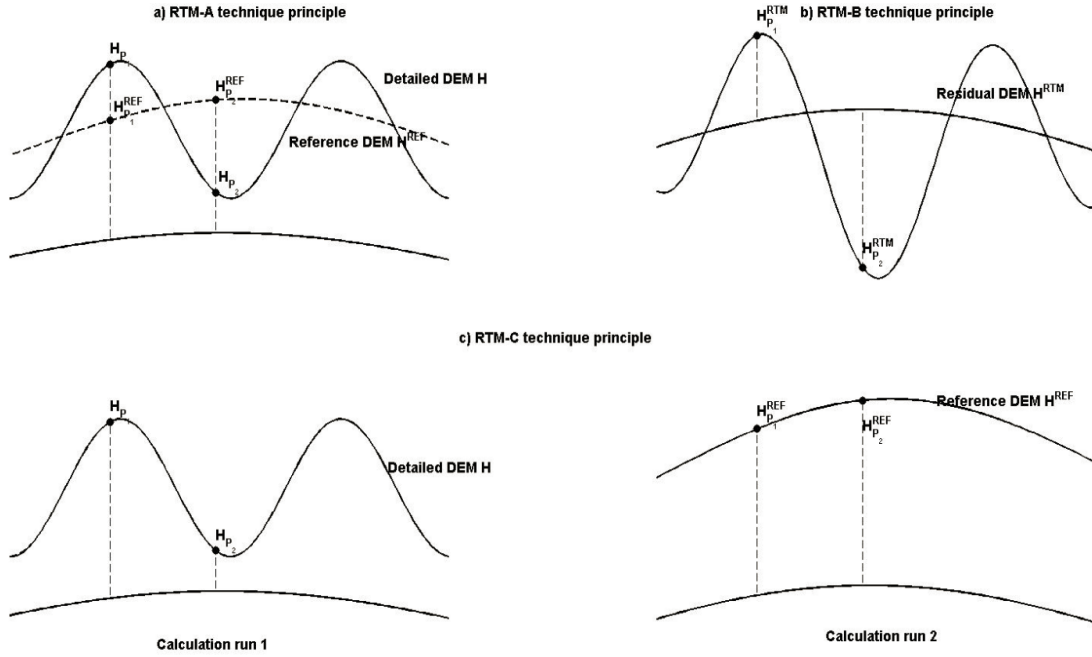


Fig. 2.10 – RTM forward modeling methods

where $P_1 (\varphi_1, \lambda_1, r_1)$ and $P_2 (\varphi_2, \lambda_2, r_2)$ are the calculation points with $H_{P_1} > H_{P_1}^{REF}$ and $H_{P_2} < H_{P_2}^{REF}$, while δg indicates the gravity disturbance, the mass-density value ρ , and l represents the distance between calculation point and integration elements.

Two topographic grids are required in the RTM-A variant. The mass-distributions of integration have vertical radius r varying from $R + H^{REF}$ to $R + H$. The condensation harmonic correction is applied as additive correction to the directly calculated RTM gravity values over points P_2 with $H_{P_2} < H_{P_2}^{REF}$. Besides, the spectral filter problem is present but not treated in the RTM-A variant.

In the RTM-B variant, for simplification of input datasets, residual masses with a thickness of $H^{RTM} = H - H^{REF}$ are assumed to be directly attached to the surface of a reference sphere or spheroid (Fig. 2.10 (b)). Besides, the calculation point is shifted downward from the surface of detailed topography to the surface of residual heights, e.g., $R + H_{P_1}^{RTM}$ for point P_1 and $R + H_{P_2}^{RTM}$ for point P_2 . The numerical evaluation is conducted following Eq.(2.70),

$$\begin{aligned} \delta g_{RTM-B}(P_1) &= \delta g(P_1) = G \int_{\varphi} \int_{\lambda} \int_R^{R+H_{RTM}} \frac{\rho(r_1 - r)}{l^3} dr d\lambda d\varphi \\ \delta g(P_2) &= G \int_{\varphi} \int_{\lambda} \int_R^{R+H_{RTM}} \frac{\rho(r_2 - r)}{l^3} dr d\lambda d\varphi \\ \delta g_{RTM-B}(P_2) &= \delta g(P_2) + 4\pi G \rho H_{P_2}^{RTM} \end{aligned} \quad (2.70)$$

and harmonic correction is added in the same way to the RTM-A variant. The spectral filter problem is presented but not treated in the RTM-B derived gravitational field. The geometry of residual masses in the RTM-B technique is defined by only one DEM grid H_{RTM} . The geometrical locations of integration masses and calcula-

tion points are changed. The downward movement of residual masses also causes the reduction in the masses of integration. Besides the errors correlated to spectral filter and non-harmonic problems, the errors due to mass-simplification also come into play when using the RTM-B technique.

In order to avoid the approximation effect of harmonic correction in techniques of RTM-A and RTM-B, RTM-C is developed. Two numerical integration procedures are implemented, one places the computation points on the Earth's surface (Fig. 2.10 (c) left panel) and the other on the reference surface (Fig. 2.10 (c) right panel). In the first integration, the attraction caused by masses of detailed topography on point (P_1) are calculated (Eq.(2.71)),

$$\delta g_{top}(P_1) = G \int_{\varphi} \int_{\lambda} \int_R^{R+H} \frac{\rho(r_1 - r)}{l^3} dr d\lambda d\varphi \quad (2.71)$$

The calculation point P_1 resides on the surface of the detailed topography. In the second integration, the long-wavelength gravity field implied by a reference topography is calculated following Eq.(2.72),

$$\delta g_{ref}(P'_1) = G \int_{\varphi} \int_{\lambda} \int_R^{R+H^{REF}} \frac{\rho(r'_1 - r)}{l^3} dr d\lambda d\varphi \quad (2.72)$$

The evaluation point P'_1 resides on the surface of the reference topography. RTM-C gravitational field (Eq.(2.73)) is the composite contribution of Eq. (2.71) and Eq. (2.72),

$$\delta g_{RTM-C}(P_1) = \delta g_{top}(P_1) - \delta g_{ref}(P'_1) \quad (2.73)$$

In these two steps of numerical integration, calculation points are located outside the masses of integration. Therefore, the directly achieved gravitational potentials are harmonic, and the harmonic correction is entirely avoided in the RTM-C variant. However, the RTM-C variant introduces a geo-location inconsistency because the two RTM gravity constituents are not computed at the same 3D location (cf. *Hirt et al* (2019a)).

In the works of *Omang et al* (2012), *Bucha et al* (2016) and *Harrison and Dickinson* (1989), RTM gravitational field was defined as the attraction of the topography minus the analytically continued external attraction of the reference topography, named RTM-D here. Similar to the RTM-C variant, the residual gravitational field is obtained based on two numerical integrations, but the geo-location inconsistency is overcome through the analytical continuation of the band-limited gravity signals from the reference surface to the topographic surface. In the basic idea to the analytical continuation, the gravitational field produced by

the reference topography can be expanded into a Taylor series, resulting in the variant RTM-D (*Bucha et al (2016)*):

$$\begin{aligned}
V_{top}(P_2) &= G \int_{\varphi} \int_{\lambda} \int_R^{R+H} \frac{\rho}{l} dr d\lambda d\varphi \\
V_{ref}(P'_2) &= G \int_{\varphi} \int_{\lambda} \int_R^{R+H^{REF}} \frac{\rho}{l} dr d\lambda d\varphi \\
V_{ref}(P_2) &= \sum_{k=0}^{\infty} \frac{1}{k!} \frac{\partial^k V(P'_2)}{\partial r^k} \Delta h^k \\
V_{RTM-D}(P_2) &= V_{top}(P_2) - V_{ref}(P_2)
\end{aligned} \tag{2.74}$$

with k indicating the order of Taylor series expansion, Δh being the radial difference between P and P' . From the numerical point of view, the RTM-D technique requires the radial derivatives of the potential to be known up to some finite order of k . Considering the smoothing character of reference topography, it would be sufficient to consider them only up to the first- or second-term (*Bucha et al (2016)*).

In the RTM-E variant, the RTM gravitation effects are split into four parts (*Kadlec (2011)*), the effect of a Bouguer layer Δg_B of thickness $H(P)$ (from detailed DEM) and corresponding terrain effect referring to the Earth's surface (Δg_{TE}), and Bouguer effect Δg_B^{REF} of thickness $H^{REF}(P)$ (from smoothed DEM) and the corresponding terrain effect referring to reference surface (Δg_{TE}^{REF}). Unlike the infinite Bouguer plate approximation in RTM-A and RTM-B, the limited Bouguer effect truncated at a threshold distance (commensurate with terrain effect calculation) from the computational point is adopted in the RTM-E. Besides, the Bouguer layer is modeled either by a Bouguer plate (in planar approximation) or by a Bouguer shell (in spherical approximation). In addition to the harmonic correction for the gravity anomaly, the concept for the harmonic correction of the gravitational potential and its second-order radial derivative was also developed by *Kadlec (2011)*:

$$\begin{aligned}
\Delta g_{RTM-E} &= -G\rho \int_S \int_{H^{REF}}^H \frac{z' - z}{l^3} dz dS \\
&= G\rho \int_S \left(\int_0^{H^{REF}} \frac{z' - z}{l^3} dz - \int_0^H \frac{z' - z}{l^3} dz \right) dS \\
&= G\rho \int_S \left(\int_0^{H^{REF}(P)} \frac{z' - z}{l^3} dz + \int_{H^{REF}(P)}^H \frac{z' - z}{l^3} dz - \int_0^{H(P)} \frac{z' - z}{l^3} dz - \int_{H(P)}^H \frac{z' - z}{l^3} dz \right) dS \\
&= \Delta g_B + \Delta g_{TE} - \Delta g_B^{ref} - \Delta g_{TE}^{ref}
\end{aligned}$$

The RTM-E variant totally avoids the non-harmonic problem, but is subject to the radial position inconsistency in the same way as in RTM-C technique.

In all of the above variants, the residual gravity field is evaluated based on numerical integration in the spatial domain (Fig. 2.7). The accuracy of the above RTM variants is affected by one or more errors related to 1) harmonic correction, 2) spectral filter problem, 3) mass-simplification or 4) calculation points inconsistency.

In contrast to the RTM technique in the spatial domain, the long-wavelength gravitational field in the SGM technique is obtained via an exterior spherical harmonic analysis. The base functions are harmonic functions anywhere outside the geocenter. The problem of non-harmonicity is not occurring in the SGM technique. Therefore, RTM in the spectral domain does not require a special treatment of the non-harmonicity problem. However, as introduced in Section 2.2.2, because of the requirement for SHA of integer powers of height function in the SGM technique, enormous computation costs occur in the case of high-resolution height-density models. This greatly limits the application of the SGM method when converts a high-resolution DEM, such as DEM at 3" resolution, to its implied gravity field model.

Different from the former methods based on forward modeling in the spatial domain or in the spectral domain, *Hirt et al* (2019a) developed a new method to compute the RTM gravitational field via a combination of gravity forward modeling in the spatial domain and in the spectral domain.

- The NI method provides the full-scale gravitational field δg_{NI} through numerical integration around the global topographic masses. The calculation points reside on the Earth's surface which is represented by a detailed DEM. The obtained full-scale gravitational potential is harmonic at every point outside the Earth.
- The band-limited gravitational field δg_{SGM} is generated by the SGM technique over that of a reference topography. To overcome the high-frequency spectral filter problem, the reference gravitational field is expanded to an ultra-high degree. Besides, the harmonicity of the gravitational potential is implicitly ensured in exterior spherical harmonics. Therefore, the function of the band-limited gravitational field is harmonic outside the Earth.
- RTM gravity field is the composition of the full-scale and band-limited gravitational field signals,

$$\delta g_{RTM-F} = \delta g_{NI} - \delta g_{SGM} \quad (2.75)$$

The non-harmonic problem encountered in the traditional RTM technique is not present.

Compared to the RTM techniques A-E, the solution of RTM-F is not affected by high-frequency spectral filter problem, harmonic correction problem, and the other two approximations (mass simplification and computation point inconsistency). Therefore, it is considered to be superior to the traditional RTM variants A-E. As an independent RTM technique, RTM-baseline can be used as an external check for performance of other RTM techniques, see in Chapter 4 and Chapter 5. As indicated in *Hirt et al* (2019a), for global-scale forward modeling application of 1" or 3" DEMs, "the computational requirements for a full-scale global NI will be challenging, though with the increased availability of super-computing resources becoming feasible".

2.4 Combination of GGM and RTM

In practice, the design of GGMs faces certain difficulties, associated with the lack of gravity measurements over underdeveloped regions and the unavailability of part of the gravimetric information for free use. Therefore, the now publicly available GGMs, like EGM2008, are not capable of delivering the short-scale components of Earth's gravity field. The effect of the unmodeled high-frequency signals is known as the omission error. The omission error in EGM2008 could reach several cm of height anomalies in global standard deviation (STD) (*Jekeli et al (2009)*). More specifically, the high-frequency gravity signals strongly depend on the ruggedness of topography, which has been estimated in *Rexer and Hirt (2015)* through comparison with the GGMplus gravity model *Hirt et al (2013)*. The omission errors which are not modeled by contemporary GGMs can reach the locally extreme root-mean-square (RMS) signals up to 38 mGal in Himalayas *Rexer and Hirt (2015)*. In order to extend the spectral content of spherical harmonic GGMs, especially in rugged areas, amounts of many experiments have been done on the techniques for refining the GGMs in the continental regions (*Hirt et al (2013)*, *Martinec (1993)*, *Koneshov et al (2017)*, *Kvas et al (2019)*, *Pavlis et al (2007)*, *Zingerle (2019)*). These approaches are based on the high-resolution elevation model of the Earth's surface topography which allows the detailed modelling of the Earth's gravitational field without using additional gravimetry data.

In this thesis, the high-frequency gravity field signals were calculated by the RTM technique, then were combined with the EGM2008 to obtain the refined model. The procedures as following (*Hirt et al (2010a)*, *Hirt (2010)*):

- long-wavelength part of gravity disturbance δg_{GGM} is computed from EGM2008 SHCs up to degree of 2,190 and order of 2,159.
- the high-frequency spectral power of gravity disturbance δg_{RTM} beyond degree 2,159 is delivered by RTM technique.
- optional high-frequency filtering error correction δg_{HF} based on spectral technique (Section 2.3).

Assuming the spectral consistency between band-limited topography and implied gravity field, a simple spectral combination yields,

$$\delta \tilde{g} = \delta g_{GGM} + \delta g_{RTM} \quad (2.76)$$

Considering the ultra-high frequency gravity signals implied in the reference surface, the estimations are

$$\delta \tilde{g} = \delta g_{GGM} + \delta g_{RTM} + \delta g_{HF} \quad (2.77)$$

RTM performance in the refinement of the global gravity field has been verified, e.g. in *Hirt et al (2013)* and *Koneshov et al (2017)* through comparison with ground measurements. In other words, the level of agreement of the modeled gravity field with ground gravity observations provides a measure for the efficiency of RTM

approach. With same GGM model, the performance of RTM variances can be assessed from how strongly the misfit – between the refined and the actual gravity field – can be reduced.

Chapter 3

Databases

Limited by the resolution and quality of the available satellite, aerial and terrestrial gravity observations, it is difficult to directly describe the high-frequency content of the Earth's gravity field on the global scale. Instead, with knowledge about the key features of fluctuations of the Earth's topography and the structure of crustal density-distribution, the high-frequency gravity signals can be obtained in the framework of forward modelling. Therefore, the accurate gravity forward modelling depends on the availability of high-quality topography data and mass density information. Any errors in the datasets of geometric and density information will be propagated into the forward modeled gravity field. The first part of this chapter (Section 3.1) gives an overview of datasets, including DEMs (Section 3.1.1), the density models (Section 3.1.3) and their preprocessing. Three main aspects of input datasets have been considered:

- Contemporary, the most frequently used global DEMs in the forward modelling are radar-based products, i.e., SRTM DEMs. Depending on the radar penetration characteristics, the radar-based DEMs provide the interferometric height of a radar-signal-reflective surface rather than the bareground Earth's surface. Many published works focusing on assessing the accuracy of released SRTM DEMs using independent datasets either from ground elevation observations or from LiDAR-derived DEMs, found that the SRTM elevation was located somewhere between the Earth's bare-ground surface and the canopy top over vegetated areas. In such cases, a tree-bias comes into effect and would be forward modeled when using radar-based DEMs in the procedure of high-frequency gravity field retrieving. In Section 3.1.2, a global tree bias map will be introduced. Regionally, four study areas – Australian Alps, Tasmania, Amazon forest area, and Canadian Rocky mountain area – those are covered with the world's highest forest, were selected. SRTM V4.1 and MERIT DEM respectively represent the Earth's top and solid surface in regional studies.
- However, the Consortium for Spatial Information (CGIAR-CSI) published SRTM V4.1. It has been confirmed to contain relative geolocation shifts from NASA SRTM V2.1 and its derived products (e.g., MERIT DEM) (*Casenave et al (2016)*). The induced spatially correlated elevation differences would reach up to tens of meters. The geolocation shifts over and around the study areas, i.e., Tasmania and Amazon forest areas, were detected and corrected (Section 3.1.2).

- The more detailed the better principle is generally accepted in forward modelling. In reality, the topographic density model of high accuracy and resolution is rarely available. Instead, a constant density assumption of $2,670 \text{ kg/m}^3$ is often used in practical calculations. This means that the high-frequency gravity signals implied by density-anomalies remain neglected when using constant-density assumption in forward modelling. For the purpose of studying the lateral density effect in gravity forward modeling, a digital density model over New Zealand will be introduced in Section 3.1.3.

As soon as errors in mass-density, mass-geometry, or the modelling techniques are present, any forward modeled gravitational field is only an approximation of the true field. The validations provide an indicator of how much the modeled values deviate from the true values. The external data sets and models, e.g., terrestrial gravity measurements (3.2.1), GPS/levelling data (3.2.2) and GGM models (3.2.3), are used here for such validations.

3.1 Forward modelling datasets and preprocessing

3.1.1 DEM Models

A DEM is a discretized representation of the continuous surface of the Earth by a set of discrete points with known horizontal and vertical locations (*Hirt (2014), Li et al (2004)*). The vertical heights are usually georegistered to the reference surface, e.g., geoid or ellipsoid. Such datasets can be measured by various techniques

- **cartography:** cartographic digitization using existing topographic maps and digitizers;
- **land surveys:** by using total station theodolite and GPS for regional and direct measurement of the solid surface of the Earth;
- **remote sensing:** the interpretation of image data acquired from airborne or satellite platforms. The resulting imagery can be obtained from three types of sources: aerial photography (*Paine and Kiser (2012), Suárez et al (2005), Li et al (2004)*), Lidar (*Liu (2008), Suárez et al (2005), Li et al (2004)*) and Radar (*Farr et al (2007), Li et al (2004)*).

In case of photogrammetry, the digital surface models (DSMs, e.g., AW3D and ASTER and SPOT-based DEMs), providing the elevation heights of the Earth's top surface with all landscapes such as trees and buildings on it, are measured and reconstructed through stereo pairs of aerial images. Land surveys based on total station or GNSS, as well as measurements from air-based Lidar (Light Detection And Ranging) are the standard techniques in high-accurate regional digital terrain models (DTMs) construction. The DTMs provide elevation heights of the bare-ground surface without tree or building heights. In case of radar-based DEMs,

they provide the interferometric height of a radar-signal-reflective surface which is located between the ground surface and the top of the canopy. In this work, we use the terms “mixed-DSM/DTM” for the radar-based SRTM DEMs. With the newly released radar-based TanDEM-X 90m (at spatial resolution of 3”) DEM (<https://tandemx-science.dlr.de/>), similar vegetation-related offsets may be expected (e.g., *Rexer and Hirt (2016)*). Frequently used global DEMs and their properties are listed in Tab. 3.1.

SRTM DEMs

One of the biggest and most complete missions in terms of coverage was the SRTM. It was a joint mission conducted by NASA and NGA between the 11th and 20th February 2000. During the mission of SRTM, the Earth surface between 60° N and 56° S was completely recorded by the C-band (with a wavelength of 5.6 cm) radar and partially by X-band (with a wavelength of 3.1 cm) radar. Because of the short wavelength, the used C-band and X-band cannot completely penetrate the canopy. Therefore, by the synthetic aperture radar (SAR) imagery acquired from SRTM, the height models generated do not represent the bare-ground surface of the Earth over vegetated areas.

Several versions of SRTM DEM have been published by different public and private providers:

- The GLCF (Landsat Global Inland Water) provides the unfinished version 1 and finished version 2 data as GeoTIFF in tiles of 1° × 1°. The SRTM products at resolution of 1” (SRTM 1), 3” (SRTM3), and 30” (SRTM30) are available in both the native geographic coordinate system and in UTM coordinate system. Water bodies and coastlines have been incorporated.
- The USGS (United States Geological Survey) provides version 1 and version 2 data as HGT binary format in tiles of 1° × 1°. The datasets are available at resolutions of 1”, 3” and 30”, as water bodies and coastlines are incorporated.
- The CGIAR-CSI (Consultative Group on International Agricultural Research Consortium for Spatial Information) provides several void-filled SRTM DEMs, which were built from the NASA version 2.0 DEM product. The datasets are available in both GeoTIFF and ASCII formats.
- The USCD (University of California San Diego) provides the global topography/bathymetry grid at resolution of 30” (SRTM30_PLUS) and 15” (SRTM15_PLUS).

The most up-to-date SRTM products are listed in Tab. 3.2. The void-filled SRTM V4.1 at a resolution of 3” from the CGIAR-CSI server was used in our work. The SRTM V4.1 heights are referred to the EGM96 geoid in vertical datum and georeferenced horizontally to the WGS84 ellipsoid. The accuracy of SRTM elevations is reported to be 16 m in vertical direction and 20 m in horizontal direction (*Farr et al (2007)*).

MERIT DEM

The publicly available SRTM DEMs, however, still contain non-negligible height errors, e.g., bias, stripe and spark noises, tree height bias and etc. Each component of the height errors may reach a magnitude as large as 10s of meters, and such errors can be significantly problematic for many geoscience applications. Therefore,

Tab. 3.1 – Summary of basic characteristics of global DEMs

Model	Coverage	Surface type	Resolution	Accuracy	Horizontal, Vertical datum	Publisher	References
ETOPO1	globe	continent: DSM; ocean: Sea-floor	1'	less than 10 m	WGS84, MSL	NOAA	<i>Amante and Eakins (2009)</i>
GTOPO30	global continental areas	DSM	30"	~ 30 m	WGS84, MSL	USUG	<i>Center and GTOPO30 (1996)</i>
ACE2	global continental areas	mixed-DSM/DTM	3", 9", 30", 5'	better than 16 m	WGS84, MSL	EAPRS, ESA	<i>Berry et al (2010)</i>
GMTED2010	global continental areas	mix-DSM/DTM	7.5", 15", 30"	less than 25 m	WGS94, EGM96	USUG, NGA	<i>Danielson and Gesch (2011)</i>
AW3D (ALOS)	continental areas 60°S~60°N	DSM	30 m	≥ 2.5 m	WGS84, EGM96	ALOS project, EOIRC, JAXA	<i>Tadono et al (2014)</i>
ASTER GDEM V2	continental areas 83° S ~ 83° N	DSM	30 m	17 m	WGS84, EGM96	USGS, NGA, METI	<i>Fujisada et al (2012)</i>
SPOT 3D (commercial)	2/3 of land surfaces	DSM	20 m	10 m	WGS84, EGM96	Spot Image company	<i>SPOT (2006)</i>
SRTM DEMs	continental areas 56°S~60°N	mixed-DSM/DTM	≥ 30 m	16 m	WGS84, EGM96	NASA, CGIAR-CS	<i>Farr et al (2007)</i>
Tandem-X 90m	90°S~90°N	mixed-DSM/DTM	30 m	12 m	WGS84, EGM96	DLR	<i>Wessel et al (2018)</i>
SRTM30plus	78°S~80°N	continent: mixed-DSM/DTM; ocean: Bathymetry	30"		WGS84, EGM96	UCSD	<i>Becker et al (2009)</i>
SRTM15+ V2	90°S~90°N	continent: mixed-DSM/DTM; ocean: Bathymetry	15"		WGS84, EGM96	UCSD	<i>Tozer et al (2019)</i>
Earth2014	90°S~90°N	layer-based model	1' and 5'		WGS84, EGM96	Curtin University, TU Munich	<i>Hirt and Rexer (2015)</i>

it is hardly possible to detect signals smaller than the error levels of the applied DEMs (*Schumann and Bates (2018)*, *Patel et al (2016)*), such as its applications in water resources studies (*Schumann et al (2008)*) and high-frequency gravity field modelling (*Yang et al (2019)*).

The 3" global MERIT (Multi-Error-Removed Improved-Terrain) DEM dataset by *Yamazaki et al (2017)* was developed and publicly released in 2017. The MERIT DEM was constructed by combining SRTM V2.1 over continental areas within $\pm 60^\circ$ in latitude, and AW3D (ALOS World 3D) DEM data north of 60° latitude. In the construction of MERIT DEM, DEM datasets collected and maintained by Viewfinder Panoramas were involved for the SRTM voids filling. Additionally, stripe noise, absolute-biases, and tree canopy bias were also modeled and removed (*Yamazaki et al (2017)*). For the present work, the MERIT DEM is further refined by removing outliers based on the maximum slope approach (*Hirt (2018)*). The MERIT DEM represents, in good approximation, the bare ground surface.

Geolocation Shifts between SRTM V4.1 and MERIT DEM

Due to changes of the dataset basis from SRTM V2.0 in SRTM V4.1 construction to SRTM V2.1 in MERIT DEM construction, there exist geolocation shifts between MERIT DEM and SRTM V4.1. There are apparent relative geolocation shifts over our study areas: over Tasmania continental area with latitude less 43° S in Fig. 3.1 (a) and over Amazon area with latitude above 0° N and longitude within 60.01° W and 60.0005° W in Fig. 3.2 (a). Fig. 3.1 (b) shows the elevation differences between MERIT DEM and SRTM V4.1 DEM after one pixel northward shifting over Tasmania error exist areas. Fig. 3.2 (b) shows the elevation differences between MERIT DEM and SRTM V4.1 DEM after one pixel northward shifting with latitude above 0° N over the Amazon Area, and one pixel eastward shifting with longitude between 60.01° W and 60.0005° W). Please refer to *Casenave et al (2016)* for more consideration of geolocation shifting.

Ocean topography

Tab. 3.2 – Publicly available SRTM DEMs

Dataset	Resources	Spatial Resolution ["]	Reference
SRTM1	http://rmd.neoknet.com/srtm1	1	<i>Farr et al (2007)</i>
SRTM3	https://dds.cr.usgs.gov/srtm/version2_1	3	<i>Farr et al (2007)</i>
SRTMG1	https://e4ftl01.cr.usgs.gov/MEASURES/SRTMGL1.003/	1	<i>Farr et al (2007)</i>
SRTMG3	https://e4ftl01.cr.usgs.gov/MEASURES/SRTMGL3.003/	3	<i>Farr et al (2007)</i>
SRTM V4.1	http://data.cgiar-csi.org/srtm/tiles	1	<i>Jarvis et al (2008)</i>
SRTM V4.1_250m	http://srtm.csi.cgiar.org/	7.5	<i>Jarvis et al (2008)</i>

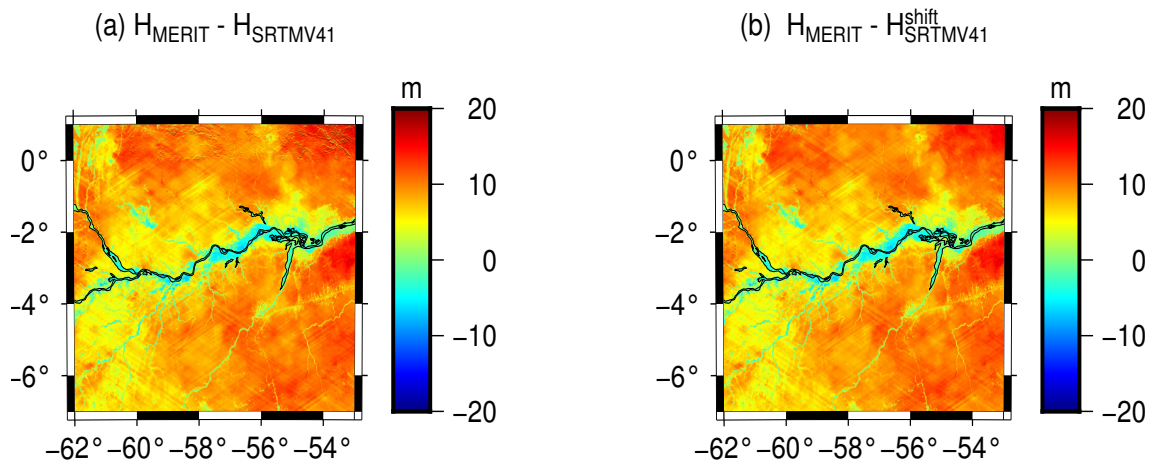


Fig. 3.1 – SRTMV4.1 geolocation shifts over Amazon area: (a) Height differences between MERIT elevation H_{MERIT} and SRTM V4.1 elevation $H_{SRTMV41}$; (b) Height differences between MERIT elevation and shifted SRTM V4.1 elevation $H_{SRTMV41}^{shift}$.

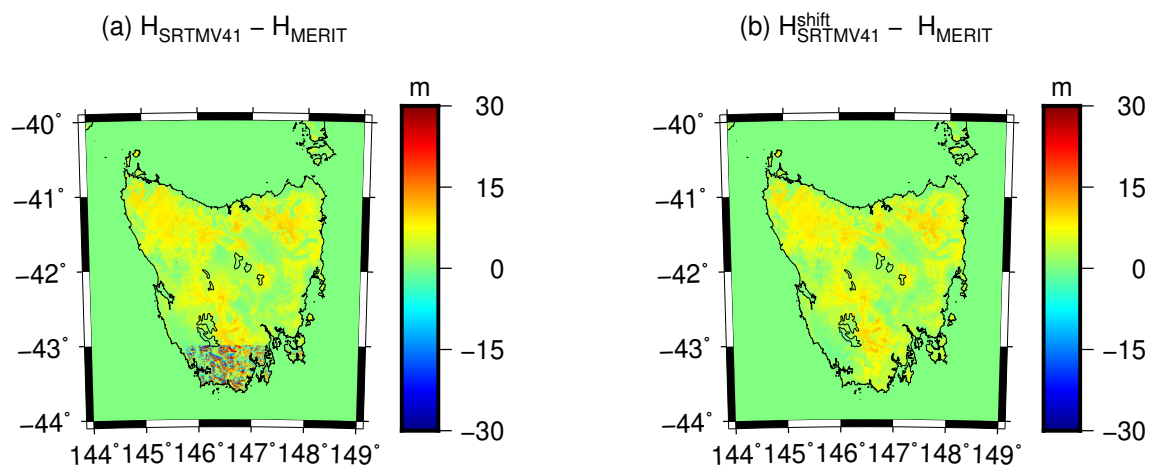


Fig. 3.2 – SRTMV4.1 geolocation shifts over Tasmania area south of -43° latitude: (a) Height differences between MERIT elevation H_{MERIT} and SRTM V4.1 elevation $H_{SRTMV41}$; (b) Height differences between MERIT elevation and shifted SRTM V4.1 elevation $H_{SRTMV41}^{shift}$.

Topographic mapping with orbiting radar and photogrammetry has been the focus of the current exploration of planets such as the Earth, and is providing high-resolution topographic maps over continental areas. With the availability of the digital sounding data and radar altimetry measurements, the digital bathymetry model (DBM), such as the global seafloor topography by *Smith and Sandwell (1997)*, could be generated through a combination-process of gravity anomalies measured by satellite altimetry and ocean-depths based on ship-depth sounding. Over the past decade, several combined models have been built through merging DEM data over continental areas and a set of bathymetric datasets over ocean areas. One of the highest-resolution combined DEM/DBM model is the 30 arc-second resolution SRTM30 PLUS model (*Becker et al (2009)*) which was constructed through a combination of 1) SRTM30 over continental area, 2) ice topography from ICESat topography, 3) more than 290 million soundings, and 4) seafloor topography estimates from altimetry over ocean areas. Additionally, SRTM15+ (*Tozer et al (2019)*) at a resolution of 15" was published as the most up-to-date DEM/DBM.

The publicly available DBM and DEM/DBM models, however, are generally known to a lower resolution than the publicly available Earth's continental topography. This is ascertained by the resolution gap of available DEMs and DBMs. In order to overcome the resolution gap between DBM and high-resolution DEM (e.g., 3" SRTM DEMs over continental areas), DEM/DBMs will be firstly obtained by merging SRTM30plus with those adopted high-resolution DEMs, e.g., SRTM1, SRTM3 and SRTMV4.1, SRTM250, then compressed the water masses into rock-equivalent masses as described in Eq. (2.68).

Spherical harmonic reference topography

The RTM approach requires a smooth reference surface to be subtracted from the finer elevation model. As is well known, the reference surface could be represented either by a spherical harmonic topography directly derived from correlated finer DEMs through SHA, or by a down-sampled high-resolution topography model (*Forsberg (1984)*). The use of spherical harmonic topography has been confirmed to be better in spectral filtering when RTM technique is to be deployed in the augmentation of GGMs at short scales (*Hirt et al (2010a)*). In this study, the spherical harmonic reference topography is adopted as a high-pass filter in the procedure of the RTM technique. In order to study the RTM's performance in high-frequency gravity field determination and its application to refine GGMs beyond their maximum resolution, the spherical harmonic reference topography would have the same maximum degree as the applied GGMs. In the following studies, the SH coefficients of Earth2014 (*Hirt and Rexer (2015)*) to the degree and order of 2,160 are used to represent the long-wavelength topography when using SRTM DEMs' in the RTM technique. The 3" MERIT topographic surface is also expanded into a set of SH coefficients to degree 2,160, for details refer to *Hirt et al (2019a)*. The reference elevations H_{ref} at geocentric coordinates (φ, λ) are synthesized using:

$$H_{ref} = \sum_{n=0}^{N_{max}} \sum_{m=0}^n (\overline{HC}_{nm} \cos m\lambda + \overline{HS}_{nm} \sin m\lambda) \overline{P}_{nm}(\sin \varphi) \quad (3.1)$$

where $N_{nmax} = 2,160$ is the maximum expansion degree, \overline{HC}_{nm} and \overline{HS}_{nm} indicate the fully-normalized SHCs of height, and $\overline{P}_{nm}(\sin \varphi)$ indicates the fully-normalized associated Legend functions of degree n and order m .

3.1.2 Global Tree Canopy models

In practical applications of gravity forward modelling, a “bare-earth” or “bare-ground” DEM that provides the height of the physical terrain surface below the tree canopy is required. Up to the present, the most significant sources of Earth topography data are radar-based SRTM DEMs which are expected to contain the tree-offsets over vegetated areas. Depending on the property of forests such as vegetation structures, heights, and the distribution density, the tree-offsets in the mixed-DSM/DTM data set may vary from 0 to tens of meters (O’Loughlin *et al* (2016), Yamazaki *et al* (2017)). With knowledge of tree heights and radar penetration depth, it is possible to estimate the tree bias contained in the SRTM DEMs (O’Loughlin *et al* (2016), Yamazaki *et al* (2017)).

The penetration depth of radar depends on the interaction between the electromagnetic and structural properties of the scattering medium (Braun and Fotopoulos (2007)). Over the vegetated area, the location of reflecting height center is a rather complicated function of both sensor and vegetation structure characteristics (Baugh *et al* (2013)). The comparison between SRTM DEMs with ICESat GLA elevation products, regional bare-ground DEMs or the national elevation database has demonstrated that the tree-bias errors are influenced by canopy branches, tree types and ground-reflective properties (Bhang *et al* (2007), Braun and Fotopoulos (2007)). Sub-pixel percent tree cover was also found to be linearly correlated to the radar penetration depth (Carabajal and Harding (2006), Miliareis and Delikaraoglou (2009)). Besides, 50 m MODIS Landsat Vegetation Continuous Fields (DiMiceli *et al* (2017), Sexton *et al* (2013)) and the Global 1 km Forest Canopy Height map (Simard *et al* (2011)) were used to study the relationship between tree heights and observed tree biases in SRTM DEMs. Based on these studies, various methods for vegetation bias identification were built and evaluated in O’Loughlin *et al* (2016) through comparison with the baseline bias of height differences between SRTM DEM and ICESat ground elevation observations.

In our studies, a global map was used to represent the tree height bias contained in the SRTM DEMs. The map was developed by Yamazaki *et al* (2017) in the context of the MERIT-DEM project to construct a bare-ground model from SRTM data. As introduced in Section 3.1, the base model comprised of DEMs – SRTM V3 and AW3D – was firstly generated. Errors related to voids, stripe noise and absolute biases were then reduced from the base DEM. In terms of estimation of tree-bias, the lowest heights from ICESat laser altimetry are used as reference ground elevations. The differences between DEM and ICESat heights were introduced as a measure for the tree-height bias, and the modelling was refined by taking external information on the tree coverage density and tree canopy height into account. Please refer to Yamazaki *et al* (2017) for full details about the tree bias modelling.

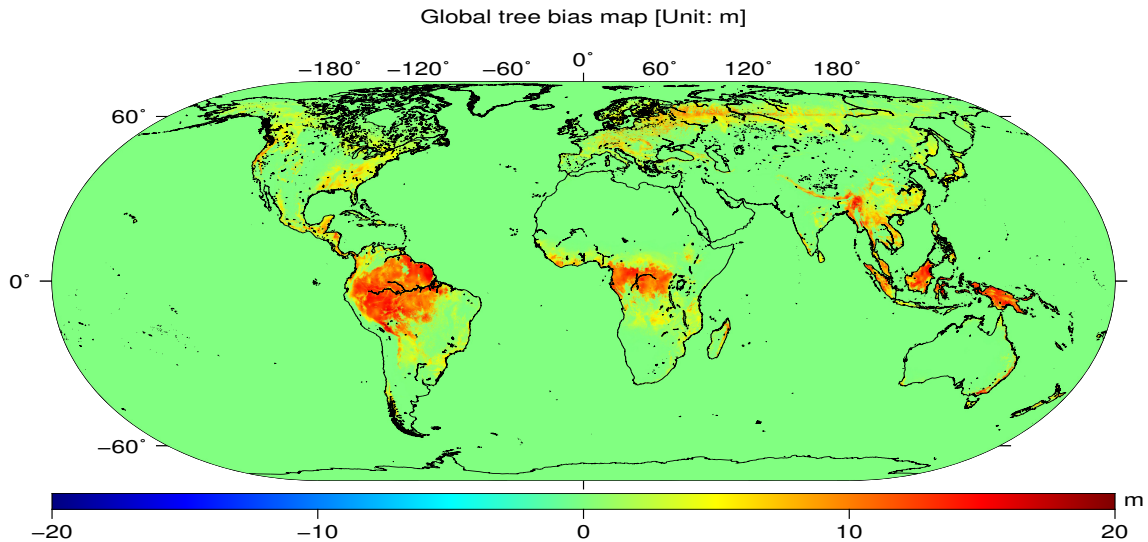


Fig. 3.3 – Global tree bias map in 1 km resolution (*Yamazaki et al (2017)*).

For our study, the tree-canopy bias map at a resolution of 30" (Fig. 3.3) which is equivalent to a spectral resolution of harmonic degree 21,600, was provided by *Yamazaki et al (2017)*. The tree biases vary from ~ 0 m to ~ 23.93 m over vegetated areas, with the largest tree biases present in tropical rainforest areas, and notable biases visible over evergreen forest area over South-east Asia and Australian Alps, and needle-leaved forests in Europe and North-America. The obvious tree bias discontinuity along 60° N (Fig. 3.3) reflects the merging of different input data sources, SRTM V2.1 and AW3D in the MERIT DEM.

3.1.3 Density Models

Another significant parameter in the definition of Earth's mass-elements is mass-density. In reality, the topographic mass-density model of high accuracy and resolution is rarely available. Because the continental crust of the Earth mainly lies above the mean sea level, the density usually assumed is equal to a mean crustal density value $2,670 \text{ kg/m}^3$ over continental areas. The uniform value $2,670 \text{ kg/m}^3$ was first computed by calculating an overall mean of density value of five types of surface rocks collected during the period of 1811 to 1882 (*Hinze (2003)*). This simple calculation is based on a small and poorly distributed sampling of crystalline rock terrains. However, roughly only one portion of terrain is composed of crystalline, while another 75% of the continental surface is underlain by sedimentary rocks. The computed average density of continental crust based on the areal proportion of sedimentary and shield rocks is $\sim 2,600 \text{ kg/m}^3$ (*Hinze (2003)*). Additionally, the densities of sedimentary rocks generally increase with age of the lithification and metamorphism. Therefore, calculations of forward modelling of limited regions are more appropriate to use an average density that is compatible with local geology rather than $2,670 \text{ kg/m}^3$. Naturally, high-frequency gravity signals implied by density anomalies would not be retrieved when using constant density assumption.

Over the last decades, several global Earth's structure models were obtained by means of seismic velocities or mass density, such as Parameter Earth Model (PEM) (*Dziewonski et al (1975)*), Preliminary Reference

Earth Model (PREM) (*Dziewonski and Anderson (1981)*), ak135-f (*Kennett et al (1995)*), and upper mantle models GyPSuM (*Simmons et al (2010)*) provide layer-based radial density structure. The currently published 3-D global Earth's models provide only crust and upper mantle density structure with coarse resolution, e.g., the most up to date models PREM500, CRUST1.0 and LITHO1.0 were defined in $1^\circ \times 1^\circ$ spatial resolution. A spherical harmonic global depth-dependent density model ESCM180 was developed by *Chen and Tenzer (2015)* through a combination of CRUST1.0 and more detailed information on the topography, bathymetry, ice sheet, and geoid. The ESCM180 was expanded up to degree and order of 180, which equals to 1° in spatial resolution. However, the density model of resolution $1^\circ \times 1^\circ$ is still fairly coarse compared to DEMs of resolution up to $3'' \times 3''$.

In practice, a regional/local density model was available for this study. It offers much higher detail resolution than 1° , such as the first New Zealand digital density map at a resolution of $1' \times 1'$ (*Tenzer et al (2011)*). The New Zealand density map was obtained by a combination of datasets from 1) 123 main geological categories of Quarter-million MAP (QMAP), 2) 8,933 density measurements from PETLAB which covers 56 main rock types, and 3) supplementary geological sources (e.g., literature, similarity assumption with other rock types) covering 67 main rock types. By merging maps of geological units with density measurements, the final digital density map (Fig. 3.4) at a resolution of $1' \times 1'$ was obtained. The near subsurface rock density varies from ~ 900 to $\sim 3300 \text{ kg/m}^3$, with an average value of 2440 kg/m^3 which is found to be lower than the uniform rock density 2670 kg/m^3 . It is worth mentioning that the density model was derived by means of density measurements mostly representing the uppermost rock units (e.g., 5 to 10 m thick). As a consequence, geological structures of deep-laying underneath units are not necessarily represented by this model.

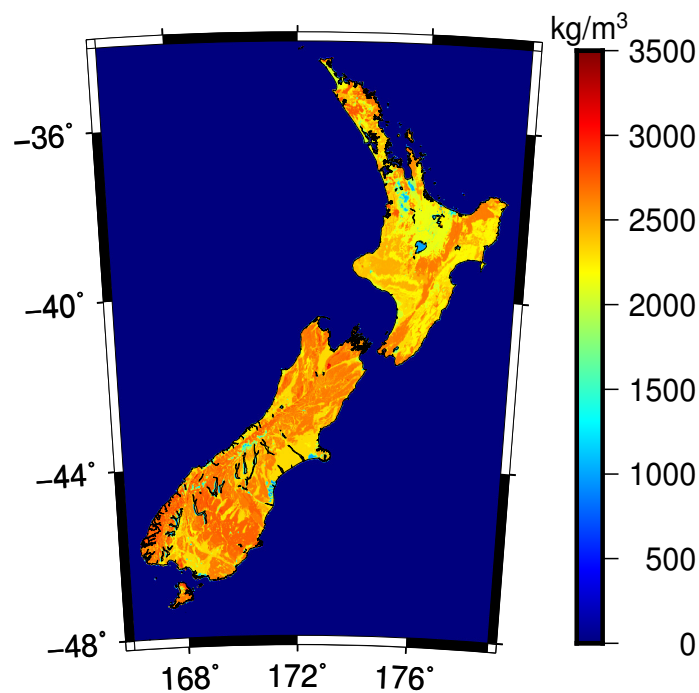


Fig. 3.4 – New Zealand density model (modified after Tenzer et al., 2011a)

3.2 Ground measurements and models for validation

3.2.1 Terrestrial Gravity Measurements

The ground gravity measurements, which theoretically contain the full field signal, provide a reference to validate the performances of RTM technique with various parameters in this thesis. As discussed in Section 2.4, the RTM gravity components can be used to augment a GGM such as EGM2008 at short spatial scales. The differences between the synthesized model and ground measurements provide an indicator for the quality of the modeled gravity field. For validations, we use ground gravity observations over three regions: New Zealand, Australia, and the Canadian Rocky Mountain area.

Over New Zealand, there are in total 40,366 ground gravity measurements available, including 20,230 measurements on the North Island and 20,136 on the South Island. The gravity databases are provided in terms of gravity acceleration values at 3D geodetic coordinates (geodetic latitude, longitude, and ellipsoidal height) by GNS Science (<https://www.gns.cri.nz>). The database is inhomogeneously distributed over the North Island and the South Island with an approximate average spatial distance of one observation per 7.5 km^2 (Amos (2007)). Denser observations are available for the most part of New Zealand that is well accessible, while the observation density is lower over rough alpine topography. The accuracy level of these gravity measurements was estimated to be ~ 0.1 to ~ 0.5 mGal (Amos (2007), Claessens *et al* (2009)). The gravity measurements were originally based on the Potsdam gravity datum. There is a constant difference of ~ 15.21 mGal between the Potsdam gravity datum and the IGSN71 gravity datum on which the EGM2008 is based on.

The Australian National Gravity Database (ANGD) consists of ~ 1.6 million national gravity measurements (<http://www.ga.gov.au/scientific-topics/disciplines/geophysics/gravity>) conducted over the entire **Australian Continent** between 1938 and 2012. These datasets inhomogeneously distribute over entire Australia, with station spacing varying from 11 km in remote areas to 1.5 km in urban areas. The accuracy of gravity measurements and geolocation information were improving in the course of time. The database provides information on Earth's gravity acceleration, as well as 3D geodetic locations. The heights are given in the form of ellipsoidal height, referenced to the WGS84 ellipsoid. The geodetic latitude and longitude are provided in the Australian Geodetic Datum 1994 (AGD1994). The deviations between AGD1994 and WGS84 are found to be below the meter-level and are ignored in the following studies (ICSM (1994), Rexer and Hirt (2016)). In this work, 74,265 ground gravity observations over Tasmania and 23,260 observations over the Alps from the ANGD were used for regional validations.

The Natural Resource Canada (<http://gdr.agg.nrcan.gc.ca/gdrdap/dap/info-eng.php>) held and maintained the Canadian Gravity Anomaly Data Base (CGAD) which consists of a multitude of gravity measurements conducted over the entire **Canadian continent** from as early as 1994. The database provides values of the

Earth's gravitational acceleration and 3D geodetic locations at around 230,000 stations. The gravity accelerations are referenced to the IGSN71 datum, and 3D coordinates are provided in the frame of GRS80. In this work, 962 terrestrial gravity accelerations over the Rocky Mountainous area was used for regional validation.

Gravity acceleration values rather than gravity disturbances or gravity anomalies are provided in these three databases. In our studies, gravity disturbances are firstly computed as the differences between the observed gravity accelerations and normal gravity at the same 3D points. The computation of normal gravity above the ellipsoid, with a positive height h from station to reference ellipsoid, refers to *Torge and Müller (2012)*. Given a normal ellipsoid and its parameters: semi-major axis a , semi-minor axis b , the angular velocity ω , and geometric flattening f , the theoretical gravity γ_0 on the surface of the ellipsoid is a second-order series expansion of equation:

$$\gamma_0 = \gamma_e(1 + f_1 \sin^2 \varphi - \frac{1}{4}f_4 \sin^2(2\varphi)) \quad (3.2)$$

with γ_e and γ_p being the theoretical gravity at the equator and poles, respectively, $m = \frac{\omega^2 a^2 b}{GM}$, $f_1 = \frac{\gamma_p - \gamma_e}{\gamma}$, $f_4 = -\frac{1}{2}f_2 + \frac{5}{2}fm$.

The normal gravity at a station with geodetic latitude φ and ellipsoid height h is calculated by (*Torge and Müller (2012)*):

$$\gamma(h) = \gamma_0(1 - \frac{2}{a}(1 + f + m - 2f \sin^2 \varphi)h) \quad (3.3)$$

The gravity disturbance is

$$\delta g = g_{obs} - \gamma \quad (3.4)$$

with g_{obs} indicating the measured gravity acceleration.

3.2.2 GPS/leveling datasets

Similar to the validation using terrestrial gravity observations, the inter-comparison of the modeled geoid, GPS-derived geodetic heights, and spirit-leveled heights at discrete points gives a reasonable indication of the quality of RTM derived geoid heights. There are 1,272 available GPS/leveling points, distributed irregularly, on the North and South Island and Stewart Island/Rakiura in New Zealand. For all points the geodetic heights from GPS-measurements, as well as leveling heights are available. The Geodetic coordinates of GPS/leveling points are related to the NZGD2000 ellipsoidal system. The spirit-levelled normal heights of all points refer to the 12 local vertical datums (LVDs). Quasi-geoid heights are calculated in two steps:

- the unification of height datums, which will be described in detail in Chapter 5;
- the calculations of quasi-geoid ζ_{obs} as difference of GPS geodetic height h_{ell} and unified normal height h_{normal}

$$\zeta_{obs} = h_{ell} - h_{normal} \quad (3.5)$$

3.2.3 GGM gravity field

The global gravity models (GGMs) addressed in this work related to series expansions in terms of SHCs, modeled the long-wavelength features of the Earth's gravitational field. Assuming the origin of the spheroid of global SHA coinciding with the geocenter, the spatial gravity values are usually described by expanding the gravitational potential in a series with first-degree terms set to 0 (Eq. (3.6)). A comprehensive set of models can be accessed from the International Centre for Global Earth Models (ICGEM), GFZ Potsdam, through <http://icgem.gfz-potsdam.de/ICGEM/>.

The disturbing gravitational potential of GGMs outside the Earth's masses in the spherical harmonic expansion is given by the well-known formula (*Barthelmes (2013), Hofmann-Wellenhof and Moritz (2006)*):

$$T(\varphi, \lambda, r) = \frac{GM}{r} \sum_{n=0}^{N_{max}} \left(\frac{R}{r}\right)^n \sum_{m=0}^n (\Delta\bar{C}_{nm} \cos m\lambda + \Delta\bar{S}_{nm} \sin m\lambda) \bar{P}_{nm}(\sin \varphi) \quad (3.6)$$

where GM is a product of the universal gravitational constant and the mass of the Earth (also known as the geocentric gravitational constant), (r, φ, λ) are the spherical coordinates of the external evaluation point with the radial distance r and φ, λ spherical latitude and longitude. R is the mean radius of the Earth. $\bar{P}_{nm}(\sin \varphi)$ are the fully normalised associated Legendre functions for degree n and order m , $\Delta\bar{C}_{nm}$ and $\Delta\bar{S}_{nm}$ are the fully normalized SHCs.

The widely used Earth's Gravitational Model EGM2008 (*Pavlis et al (2012)*) is chosen to recover long- to medium-wavelength gravity field signals coarse than 5'. The EGM2008 was released by the USA National Geospatial-Intelligence Agency. It combined the following data sets:

- low- and medium-resolution GRACE data in terms of the global ITG-GRACE03s (*Mayer-Gürr et al (2010), Pavlis et al (2012)*);
- a global dataset of 5' × 5' Earth's surface gravity anomalies built from a combination of terrestrial, airborne and altimetry data;
- and filled up with topography information in case of data gaps.

The ellipsoidal spherical harmonics were firstly obtained by spherical analysis of the downward continued gravity anomaly grid, then were transformed into SHCs which could be manipulated by many widely used software packages (e.g., isGraflab *Bucha and Janák (2014)*). The EGM2008 is expanded up to order 2,159 and degree 2,190, which corresponds to a spatial resolution down to ~ 10 km. The accuracy of EGM2008 is reported to be at the level of 0.2 \sim 0.3 m when compared to globally distributed GPS/leveling data (*Bilker-Koivula (2014), Ellmann (2010), Lee et al (2017), Odera (2016), Tóth and Szűcs (2011)*).

In this work, EGM2008 to degree and order 2,159 provides the long- and medium-wavelength gravitational signal through harmonic synthesis of the SHCs in the band of degrees 2 to 2,159 (reference to Eq. (3.7) for

gravity disturbance δg and Eq. (3.8) for geoid heights τ using isGraflab (Bucha and Janák 2013a, Bucha and Janák 2013b)).

$$\delta g(\varphi, \lambda, r) = \frac{GM}{R^2} \sum_{n=2}^{N_{max}} \left(\frac{R}{r}\right)^{n+2} (n+1) \sum_{m=0}^n (\Delta \bar{C}_{nm} \cos m\lambda + \Delta \bar{S}_{nm} \sin m\lambda) \bar{P}_{nm}(\sin \varphi) \quad (3.7)$$

$$\zeta(\varphi, \lambda, r) = \frac{GM}{R\gamma} \sum_{n=2}^{N_{max}} \left(\frac{R}{r}\right)^{n+1} \sum_{m=0}^n (\Delta \bar{C}_{nm} \cos m\lambda + \Delta \bar{S}_{nm} \sin m\lambda) \bar{P}_{nm}(\sin \varphi) \quad (3.8)$$

The evaluation points (φ, λ, r) are measured at the irregular surface of the Earth in all cases.

Chapter 4

TGF Software for Gravity Forward Modelling

This work has been documented in the manuscript "Yang, M., Hirt, C., Pail, R., 2019. TGF: A New MATLAB-based Software for Terrain-related Gravity Field Calculations." The majority of the following text is based on this publication submitted for peer-review.

In physical geodesy, forward modelling is a key mathematical technique to obtain gravity field values such as geoid or gravity effects generated by topography. Considerable efforts over past decades have been devoted to the mathematical computation of forward modelling approach in the spatial domain relying on analytical or numerical formulas of various geometries, i.e., prism, tesseroid and point mass. Over the decades, a variety of executable programs and softwares (listed in Tab. 2.1) were developed depending on various discretization techniques, e.g., the "TC" program (Forsberg (1984)) for point-wise numerical integration with analytical solution (Nagy *et al* (2000), Nagy *et al* (2002)) of the flat-topped prism (Forsberg (1984)), FFT grid-wise terrain correction program "tcfour" in GRAVSOFTE package (Forsberg (1984), Nielsen *et al* (2012)), Fortran algorithm "tcq" using Gaussian quadrature (Hwang *et al* (2003)), Fortran program "POLYHEDRON" for analytical calculation of gravitational field with arbitrary shaped polyhedron (Tsoulis and Petrović (2001), Tsoulis (2012)), and C programming "Tesseroids" which combines Gauss-Legendre Quadrature (GLQ) with tesseroid-based discretization and regularization technique (Uieda *et al* (2016)). In theory, high-resolution DEMs in company of complex geometries, e.g., as represented through 3" DEMs and a set of polyhedra, yield a better and more accurate topography-mass representation, but at the price of numerical efficiency of Newtonian integration (Wild-Pfeiffer (2008)). A rearmost Matlab tool – GTeC (Cella (2015)) – combines three types of geometries, flat-topped square prism, triangle prism and polyhedron in different integration zones. It is able to be used in the point-wise calculation of terrain correction and Bouguer effect, but limited to gravity anomalies.

So far however, to the best of our knowledge there is no freely available gravity forward modelling program software that (1) is capable of calculating ten various gravity field functionals (2) in different spectral bandwidths, including the high-frequency gravity field modelling (also known as RTM) and the full-scale topographic gravity field modelling (3) through a combination of four different types of elementary mass-elements, i.e., polyhedron, prism, tesseroid and point mass, 4) with coding made in Matlab. In order to fill this gap, we have developed

a new Matlab-based terrain gravity field (TGF) software which enables the calculation of terrain-implied gravity field in the spatial domain. The TGF combines four types of discretization methods: polyhedron, prism, tesseroid and point mass through manual definition of four integration zones. In addition, the computations can be carried out in the modes of density model or constant density assumption, and spherical approximation or ellipsoidal approximation.

The goal of this chapter is to introduce the new software TGF: its design (Section 4.1.1), structure and functions (Section 4.1.2), external and internal evaluations in the scope of topographic and RTM gravity field calculation (Section 4.2). Based on the investigations concerning the trade-off between accuracy and numerical efficiency, suitable parameters are recommended allowing accurate yet efficient RTM computations.

4.1 Description of the software

4.1.1 TGF: combination of geometric models

The primary shortcoming of forward modelling is that, in principle, the accurate and detailed mass-density distribution of the inner Earth must be known. In the procedure of mass-volume modelling, the continuous topographic masses are firstly modeled and represented by a number of discrete samples related to measurements of topographic height and density-distribution, which is denoted **sampling** here. It delivers values of height and density at 3D scattered geophysical locations and provides a database for following processes, i.e., regularization and discretization. The **regularization** procedure includes 1) to choose the geometrical representation of the real surface, and 2) to define the integration elements in the basis of selected representation surface. In general practice, the terrain masses are divided into a mesh model which can be arbitrarily synchronized to the grid of the available DEMs (Fig. 4.1 (a)). The processes of sampling and regularization are therefore integrated into the building of DEMs:

- data collection of measurements;
- interpolation of measurements;
- geodetic coordinate system unification.

The focus of this section is the combination of four types of **discretization elements** (Fig. 4.1 (d)), including polyhedron, prism, tesseroid and point mass, in representation for general volume elements. In the TGF software, the mass-distributions around calculation points are divided into different zones: four zones for calculations of RTM gravity field (Fig. 4.1 (c)) and five zones for full-scale gravity field calculations. Since the gravitational attraction of mass attenuates with increasing distance from the evaluation point, the masses in the vicinity of the computation point play the most important role in the procedure of forward modelling. It is generally agreed to assign more and more accurate geometry from outer to inner zones: polyhedron to the closest

zone, prism to the near zone, tesseroid to the third zone, and point mass to the distant zone. In addition, using a separate DEM input for each zone could also take advantage from an increasing accuracy toward the point station. For example, topographic grids with higher and higher resolution are adopted from outer to inner zones, when digital elevation models with different resolutions are available.

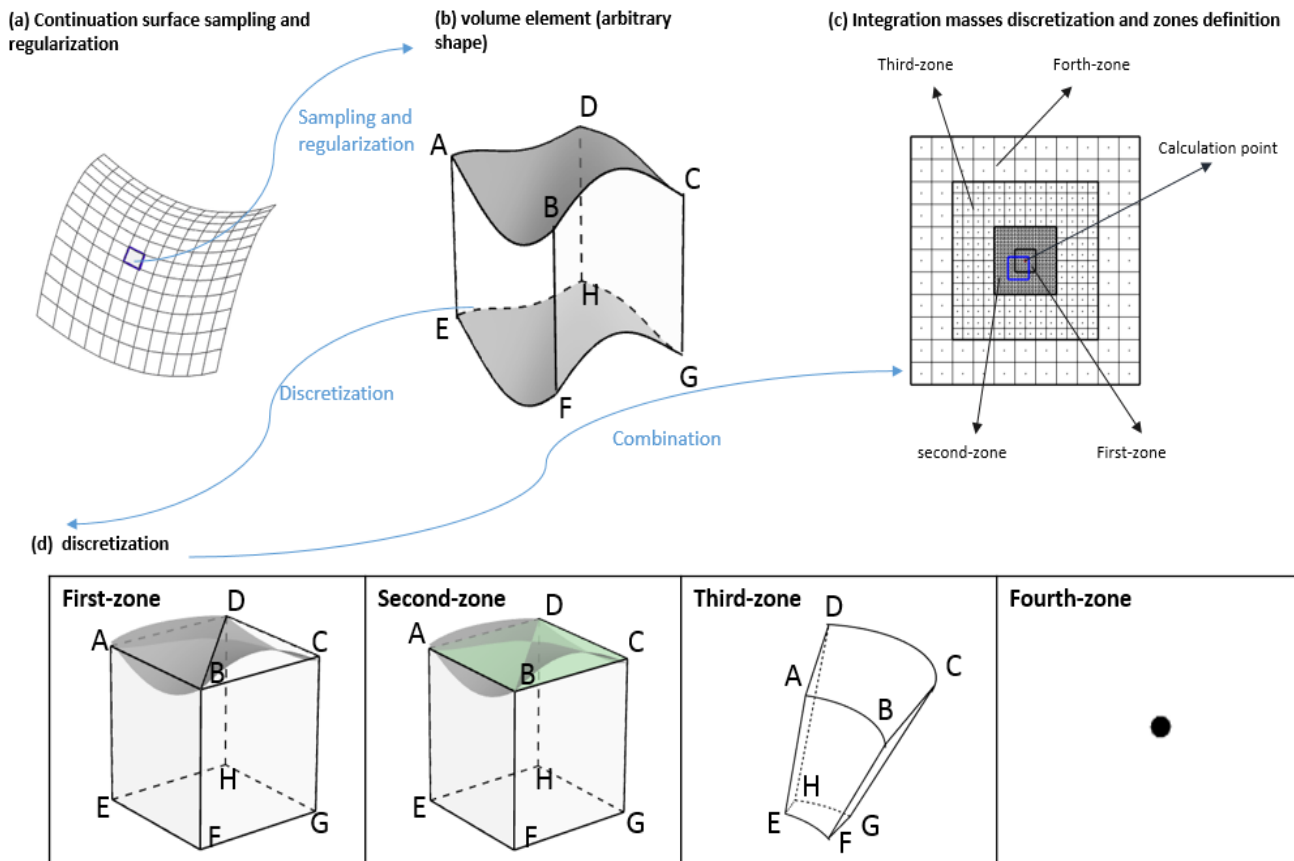


Fig. 4.1 – Discretization and regularization of the mass-distributions

In the closest zone, mass-density distributions cover a “spherical box” closely surrounding the computation point and extending to the distance of r_1 in degree from evaluation point (Fig. 4.1 (c)). The “spherical box” is bounded by lines of constant longitudes (λ_1 and λ_2), and constant latitudes (φ_1 and φ_2). There are $\lambda_2 - \lambda_1 = 2r_1$ and $\varphi_2 - \varphi_1 = 2r_1$. The mass-density distributions located in the vicinity zone are sampled and regularized by the inputted elevation grids ‘DetailedDEM’ and ‘DetailedREF’ (Fig. 4.4), and geological information such as ‘MassDensity’ or constant density value. Then the high-accurate polyhedron is used to model and approximate each general mass-element. The polyhedron, as shown in Fig. 4.1 (d), consists of five quadrilateral faces and two inclined triangular tops, with their corners coinciding with the grid nodes (cell-center) of applied DEMs (Fig. 4.2), and horizontal sides are equal to the applied DEM’s grid resolution. The tops are defined by four adjoining grid nodes of the inputted ‘DetailedDEM’ (Fig. 4.4), their heights at top corners (A, B, C and D in Fig. 4.1 (d)) sharing the elevation values over respective grid nodes of ‘DetailedDEM’, while the lower square face (‘EFGH’ in Fig. 4.1 (d)) is defined by ‘DetailedREF’ (Fig. 4.4) and holds the average height of lower boundary-grid nodes at ‘E’, ‘F’, ‘G’, and ‘H’. It is worth noting that, with the above polyhedral definition, special

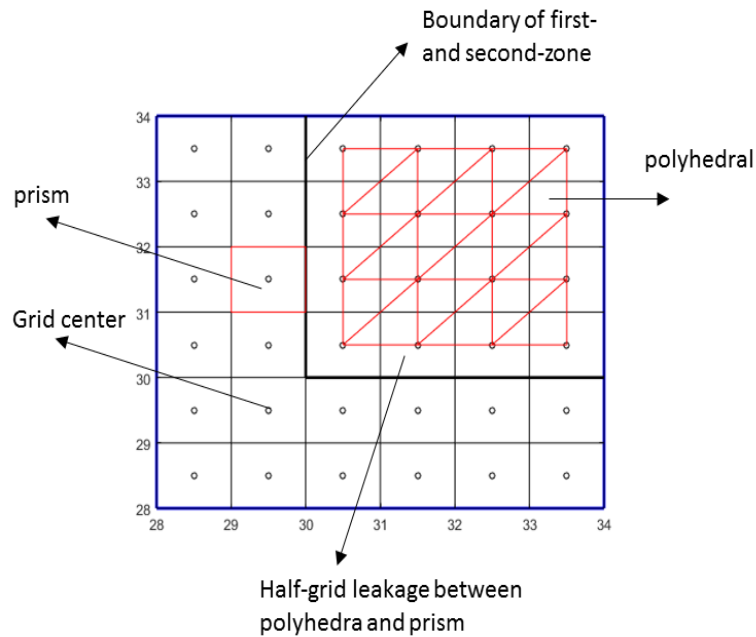


Fig. 4.2 – Leakage problem between polyhedral-zone and prism-zone

cases might exist as shown in Fig. 4.3, where the tops' corners are located on the two different sides of the bottom surface. This means that tops and lower square face might meet in a line. Non-analytical solution exists for Newton's integral of such geometries. In the TGF software, such cases are automatically detected based on the relationships among points and planes. Each of such irregular geometries is divided into two new polyhedrons, one polyhedron is bounded by 'DetailedDEM' defined surface and a surface of constant radial height -10000 m, another bounded by 'DetailedREF' defined reference surface and the constant surface with radial height -10000 m. Refer to the 3 cases of Fig.4.3, the gravity potential of the irregular geometry is the composite contribution of these two polyhedrons.

The Fortran code 'polyhedron.f' by *Tsoulis* (2012) is adopted for the numerical evaluation of Newtonian integration of a polyhedron. It is able to be compiled in the Matlab through the MEX. The MEX is a built-in utility that enables Matlab to call codes in Fortran by compiling the Fortran codes into a Matlab Executable called binary MEX-files. The binary MEX-files are dynamically linked subroutines that are called and executed as regular Matlab functions. The corresponding .mex file is therefore necessary for running Fortran code in the MATLAB-based TGF software. In the TGF software package, the mex-files in '.mexa64' and '.mexw64' file formats were built. This enables the TGF program software to run in Linux (64-bit) and Windows (64-bit). For other systems, corresponding MEX-files are required beforehand. In such cases, a compatible Fortran compiler for MATLAB is necessary, please refer to <https://de.mathworks.com/support/compilers.html> for supported compilers by MathWorks products. If there are multiple versions of compilers, use 'mex -setup FORTRAN' to select and change the default compiler for building Fortran algorithm. MEX-files are then obtained by mex-setup, selecting the default outline compiler and build .mex file.

The second zone extends up to a distance of r_2 from calculation point and shares the same DEM grids ('DetailedDEM' and 'DetailedREF') with the polyhedral zone. Mass elements in the second zone are approximated using flat-topped prism. As shown in Fig. 4.1 (c) and Fig. 4.2, the flat-topped prism (Fig. 4.1 (d)) located at the center of each grid, with lateral and vertical sides corresponding, respectively, to the grid size and to the vertical radius. The analytical solutions of flat-topped prism potential and its derivatives are coded as Nagy *et al* (2000) and Nagy *et al* (2002). The Earth's curvature and effect of plumbines' convergence are fully taken care of by the methodology of transforming between the local topographic systems at the source and the computation point as in Section 2.2.3 (Heck and Seitz (2007)). Because the polyhedron using DEM grid center as corners, while prism center is coinciding with the grid center, there is a square-circle leakage of half DEM resolution between prism zone and polyhedral zone shown in Fig. 4.2 – representing the adjacent zone (blue square area in Fig. 4.1 (c)) of prism and polyhedron. These masses are evaluated based on prism assumption in the TGF software.

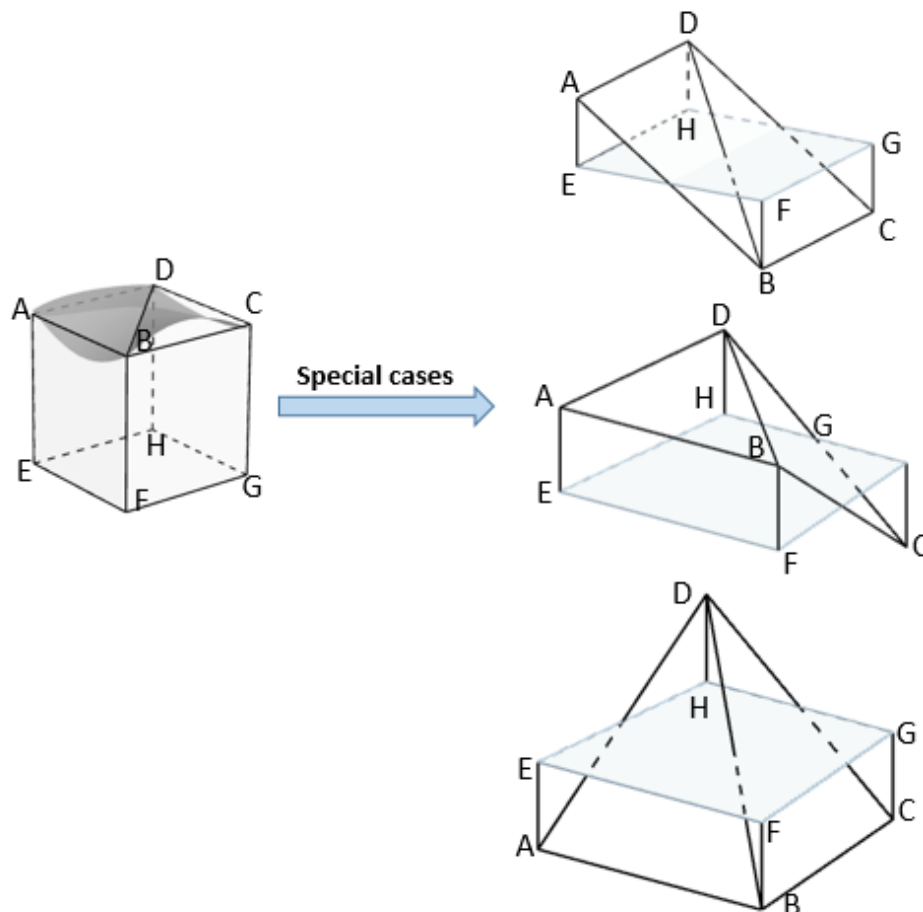


Fig. 4.3 – Special cases for polyhedral

Tesseroids are adopted to mimic the mass elements located in the third zone. As shown in Fig. 4.1 (d), the tesseroid (Fig. 4.1 (d)) is composed of three pairs of surfaces bounded by a pair of longitudes, a pair of latitudes, and a pair of radius boundaries. Since there is no analytical solution for tesseroid integrals, the numerical

evaluation is performed by expanding the integral kernel to a third-order Taylor series. This method is applied in the TGF software (*Grombein et al (2013)*). In this software, no special effort (like subdivision) was made for tesseroïd integration of adjacent masses. Therefore, to avoid numerical problems, the tesseroïd representation is not recommended for masses integration of the very near zones around the computation point (*Heck and Seitz (2007)*, *Grombein et al (2013)*), instead polyhedral is to be preferred.

In the fourth zone and fifth-zone, point-mass of tesseroïd equivalent masses, together with coarse DEM grids are used for efficiency. It is estimated to be more than ten times faster than the numerical evaluation of polyhedrons and prisms (*Yang et al (2018)*).

4.1.2 TGF: structure and function

The TGF program works in two modes: in the interactive mode with GUI interface and in the batch mode without the GUI interface. The GUI interface, shown in Fig. 4.4, enables visual and easy manipulation with all functionalities of the software. The GUI consists of four panels: the input of computation points, definition of the mass-density distributions, specification of functionals and computation zones, and output files.

Panel 'Computation Points': First, computation points must be imported in the 'Computation Points' module using the 'Computation Points' button, and can be displayed by button 'Display'. The data file of computation points is in binary format, and has a standardized structure $[N \varphi \lambda h]$ with N being station number, φ latitudes, λ longitudes and h heights, respectively. The type of coordinates should be consistent with those of the reference model, e.g., geodetic latitude and ellipsoidal height when referring to an ellipsoid, spherical latitude and orthometric height when using the sphere of radius R as a reference model.

Panel 'Forward Masses': The mass-elements for integration are defined in the 'Forward Masses' panel by importing datasets of geometry and density. The mass-elements considered for integration are divided into four zones. The size of the zones can be defined manually depending on the user's requirements by setting the distance from the calculation point of both inner and outer boundaries. The mass-elements located in four zones are modeled by three sets of DEM inputs. A set of detailed DEMs (pushbuttons – 'DetailedDEM', 'DetailedREF' for RTM computation) counted finest details define the mass-elements located in zones of polyhedron and prism. 'TessMasses' with 'TESSDEM' and 'TESSREF' models the mass-elements of tesseroïd applied zone, and a set of coarse DEMs (pushbuttons – 'CoarseDEM', 'CoarseREF' for RTM computation) are required for point mass modelling. The loaded DEM could be visualized for pre-access using the respective 'display' button. 'displayRTM', 'displayTRTM' and 'displayCRTM' buttons visualize the height differences between the Earth's surface and its smooth reference surface, they work only when RTM gravitational field has been selected. In the panel 'Forward Masses', it is possible to choose between modes of constant density assumption and of density model. The checkbox 'idensity' provides a flag for mass-density, 0 for constant density, 1 for density map. In mode of constant density, a uniform density value in g/cm^3 , e.g. $2.67 g/cm^3$ is

applied. Since all four forward modelling methods are based on the homogeneous solution of specific integration, only a 2D horizontal density map is used and required when various density is selected. Elevation data is provided in binary format of structure '[minphi maxphi resphi minlam maxlam reslam elevation]', minimum, maximum and resolution of DEM grid latitude, minimum, maximum and resolution of DEM grid longitude, and DEM height. Similarly, mass density model is of vector format '[minphi maxphi resphi minlam maxlam reslam density]'.

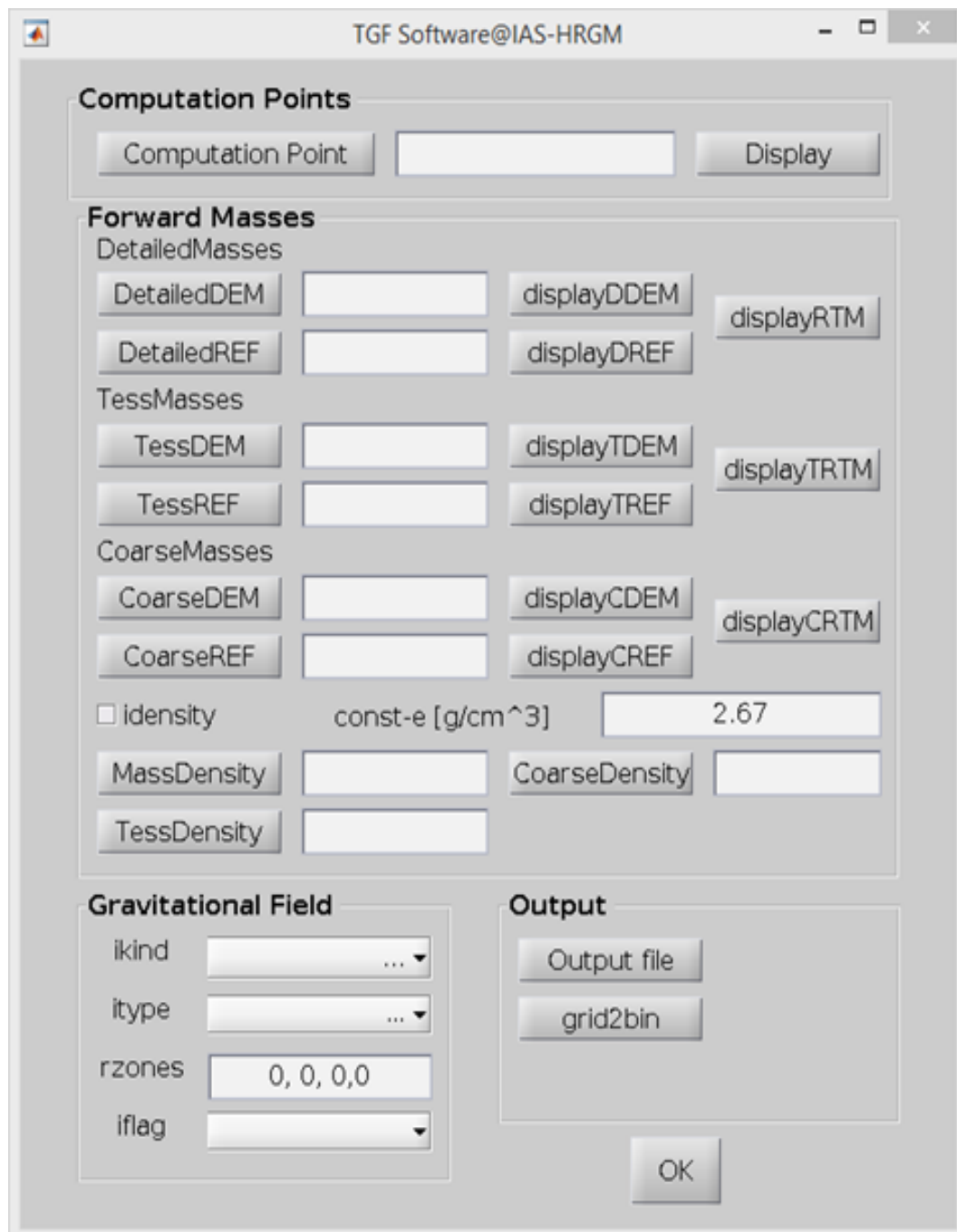


Fig. 4.4 – TGF software GUI interface

Panel 'Gravitational Field': The panel 'Gravitational Field' defines the parameters required for TGF in gravity forward modelling. For example, as listed in the Tab. 4.1, 'ikind' enables calculation of two types of terrain correction, with values of 1 for the topographic gravitational field, and 2 for RTM gravitational field. With 'itype', it is possible to calculate various gravity functionals, i.e., values of 0 for height anomaly/geoid height (ζ), 1 for vertical deflections (ξ, η) and gravity disturbances (δg), 4 for vertical deflections and gravity anomaly (Δg), 2 for gravity tensor elements, 10 for ten elements (geoid, gravity disturbance, vertical deflections and gradient tensor), 103 for geoid height, vertical deflections and gravity disturbance, and 104 for geoid, vertical deflections and gravity anomaly. The mathematical definitions of these gravity functionals are given in Section 2.2 and formulas of Eqs. (2.17 - 2.22). 'rzones' defines the boundaries of four integration zones. The 'iflag' is used to choose the reference model, with '0' when referring to a sphere of radius of $R = 6,378,137$ m, and '1' when referring to an ellipsoid (WGS84 parameters are adopted in the TGF software).

The grid file is able to be converted to binary format using pushbutton 'grid2bin' (Fig. 4.5). Input the minimum, maximum and resolution of latitude and longitude, and locate the grid file. Press the pushbutton 'ok' to get the binary file with format of '.bin'.



Fig. 4.5 – The grid2bin interface

Output files in 'xx.dat' are the output file containing the columns of 3D coordinates, gravitational components at computation points. The report file, which contains the information about the computation, is automatically named with suffix '_report.txt', e.g., 'xx_report.txt'.

In the framework of batch mode, the abovementioned processes and calculations can be run completely without using the GUI through the following command:

```
TC_GUI(vstpar, ComPoints, DetailedDEM, DetailedREF, MassDensity, TessDEM, TessREF, TessDensity, CoarseDEM, CoarseREF, CoarseDensity, GlobalDEM, GlobalREF, outname, ikind, itype, idensity, flag_earth, rzones, e);
```

The input variables are same with in the interactive mode which has been detailed described before.

Tab. 4.1 – Parameter specification for TGF forward modeling

Nr	Parameter	Explanation	Values
1	idensity	Flag for mass-density 0 – constant value is used 1 – density map is used	0 or 1
2	ikind	Flag for type of modelling 1 – topographic masses are used 2 – residual masses are used	1 or 2
3	itype	Specification of field functional 0 – geoid height 1 – VODs and gravity disturbance 4 – VODs and gravity anomaly 2 – all tensor elements 10 – all functional 103 – geoid height, DOVs and gravity disturbance 104 – geoid height, DOVs and gravity anomaly	0, 1, 2, 4, 10, 103, or 104
4	iflag	Flag for Earth approximation 0 – spherical approximation 1 – ellipsoidal approximation	0 or 1
5	rzones	Vector of four elements specifying the computation zones in [degree] $rzones = [r_1 \ r_2 \ r_3 \ r_4]$ r_1 = radius for polyhedra r_2 = radius for prisms r_3 = radius for tesseroids r_4 = radius for point mass	0.001° to global

4.2 Numerical test and validation of the software

4.2.1 Computation time of four forwarding methods

Four types of discretization geometries, i.e., polyhedron, prism, tesseract, and point mass, were compared in terms of computation time. In Fig. 4.6, the computation time for each element is normalized with respect to the computation time when polyhedron is used to calculate ten gravity functionals. Concerning the computation time required to calculate potential, using polyhedron in forward modelling takes most the time compared to the three other geometries. This is caused by 7 faces and 26 segments in a polyhedron model which requires time-consuming 26 log and 26 arctan evaluations (*Tsoulis (2012)*). The computation of prism potential takes almost the same time as polyhedron because of 24 log and 24 arctan terms for each prism. With respect to the required time for prism potential, the calculation of its first- and second-derivatives become more and more efficient with reduction of log and arctan. The computation of prism tensor takes only $\sim 10\%$ of the time in comparison with the potential of prism, and only half of first derivative of prism. The algorithm applied for calculation of tesseract gravity field takes only $\sim 6\%$ to $\sim 19\%$ time of polyhedron. Point mass computation is the most efficient one, more than twenty times more efficient than that of the polyhedron. Because it would introduce large errors in the vicinity of computation point (*Wild-Pfeiffer (2008)*), point-mass is usually applied in the modelling of the far-zone mass-elements. Similar comparisons of numerical precision and efficiency were conducted by *Heck and Seitz (2007)*, *Wild-Pfeiffer (2008)* and *Tenzer et al (2010)* among forward modelling of geometries like line integral, rectangular prism, Gauss cubature, linear vertical mass and point-mass.

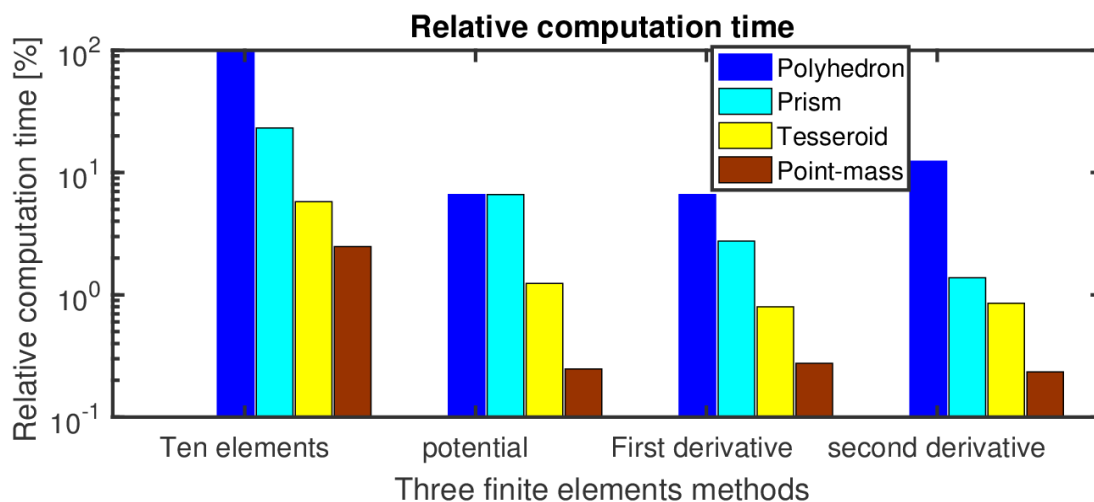


Fig. 4.6 – Relative computation time of various forward modeling methods

4.2.2 External validation in topographic field calculation

In order to demonstrate TGF's performance in topographic gravity field calculation, external validations have been implemented based on the comparisons with independent calculations using the Curtin's in-house Newtonian integrator (CNI), as described in *Kuhn and Hirt (2016)*. The CNI software has already been comprehensively tested in calculations and literature, e.g., *Hirt and Kuhn (2014)*, *Kuhn and Hirt (2016)*, *Hirt et al (2016a)*, *Hirt et al (2019a)* and *Hirt et al (2019b)*, and demonstrated its capability to calculate full-scale topographic gravity at a precision level of 0.1 mGal or better. Here, we use the gravity field calculated by CNI to validate the TGF software. The agreement between gravity field computations from TGF and CNI softwares would provide an insight into the accuracy of the topographic gravity field calculated by TGF software.

For this external validation experiment, the test area is located at the most rugged Himalaya area bounded by $27^{\circ}N \sim 28^{\circ}N$ in latitude and $87^{\circ}E \sim 88^{\circ}E$ in longitude. The topographic masses considered for forward modelling are bounded by the mean sea level of EGM96 and the Earth's surface of 3'' MERIT DEM. A constant mass-density value $\rho = 2,670 \text{ kg/m}^3$ was used in this validation. As gravity functional, gravity disturbances at 15'' resolution over the study area were computed with TGF δg_{TGF} and CNI software δg_{CNI} separately. In the gravitational field calculations, as described in Tab. 4.2, the global masses are subdivided into five zones, approximated and modeled by prisms up to 15° in the vicinity around each calculation point and tesseroids to the more distant masses, up to 180° radius. Tab. 4.2 gives the detailed definition of each zone, including the approximation geometries, resolutions of applied DEM and extension of each zone.

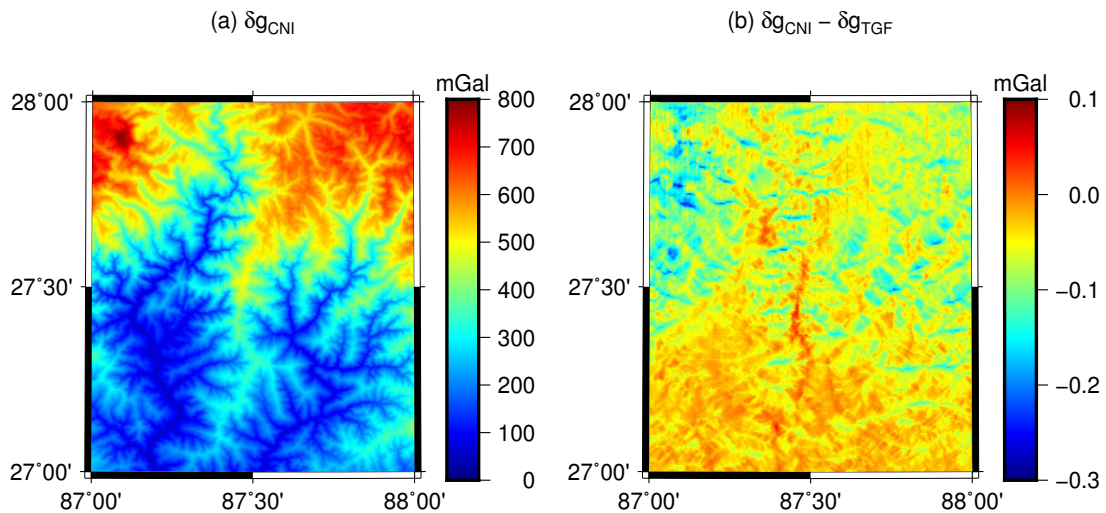


Fig. 4.7 – External validation over Himalaya mountainous area. δg_{CNI} represents topographic gravity disturbances calculated by Curtin software, δg_{TGF} represents topographic gravity disturbances calculated by TGF software.

Fig. 4.7 and Tab. 4.3 show the comparison results of the topographic gravity disturbances calculated by TGF δg_{TGF} with respect to the corresponding values by CNI δg_{CNI} . As is shown in Fig. 4.7, the discrepancies between the two sets of calculations are always smaller than 0.3 mGal, with a mean value of the differences

of ~ -0.06 mGal and RMS of 0.07 mGal. Overall, the results based on this independent validation delivered a satisfactory check on the TGF software. The statistical results suggest promising results of TGF software in the calculation of full-scale topographic gravity field, and demonstrated its calculation accuracy would be at ~ 0.1 mGal level. In addition, the reason for small differences could be partially attributed to different DEMs were adopted in the fourth zone of integration, 1' MERIT DEM for TGF calculations while 3' MERIT DEM for CNI.

Tab. 4.2 – The resolutions and extensions in topographic and RTM gravity field calculation

zones	1	2	3	4	5
CNI					
geometry	prism	prism	prism	prism	tesseroid
extension	20'	2°	6°	15°	global
resolution	3''	15''	1'	3'	15'
TGF					
geometry	polyhedron	prism	prism	prism	tesseroid
extension	0	20''	2°	15°	global
resolution	3''	3''	15''	1'	15'
RTM					
geometry	polyhedron	prism	tesseroid	point-mass	n/a
extension	1.2'	1.8'	9'	1°	n/a
resolution	3''	3''	3''	30''	n/a

Tab. 4.3 – External validation for topographic gravity calculation over Himalaya regions (Unit: mGal)

	min	max	mean	RMS
δg_{CNI}	41.32	785.42	335.71	378.70
δg_{TGF}	41.31	785.52	335.76	378.76
$\delta g_{CNI} - \delta g_{TGF}$	-0.29	0.06	-0.06	0.07

* with δg_{CNI} indicating gravity disturbances calculated through the CNI program; δg_{TGF} gravity disturbances calculated via the TGF program software

4.2.3 External validation of RTM gravity field calculation

To validate the performance using TGF software in RTM gravity calculation, another validation experiment was carried out here through a comparison with a new, highly accurate RTM baseline solution defined in *Hirt et al (2019a)*. The RTM baseline solution was obtained from a combination of 1) full-scale gravity values from a global NI and 2) the long-wavelength signal from the SGM technique. The full-scale gravity signals were calculated using numerical integration in the spatial domain with CNI software. Topographic heights taken from MERIT DEM represent the upper boundary and the EGM96 geoid the lower boundary of the topographic masses. The masses over the entire globe were divided into five zones, with resolution levels and grid extensions displayed in Tab. 4.2. For modelling the long-wavelength gravity signal, a series of SHCs of heights were firstly obtained via the surface SHA of the MERIT DEM to degree and order of 2,159. In order to reduce the effect of aliasing, the 3'' MERIT DEM was downsampled to 15'' resolution and subsequently was expanded to SHCs of degree $N_{max} = 43,200$, from which only the coefficients with $n \leq 2,159$ were adopted. The ultra-high-resolution SGM technique expands the topographic potential implied by the reference topography into integer powers of heights, and the long-wavelength gravity signals are subsequently obtained using accurate SHS of the topographic potential coefficients. In both calculations, a constant mass-density $\rho = 2,670 \text{ kg/m}^3$ was assumed. The differences between NI and SGM provide an independent check on the capability of TGF in short-scale RTM gravity field modelling.

Tab. 4.4 – External validation through baseline over Himalayas and Switzerland areas

	min (mGal)	max (mGal)	mean (mGal)	RMS (mGal)
External validation over Himalayas				
δg_{RTM}	-224.06	109.05	-11.76	39.52
$\delta g_{baseline} - \delta g_{RTM}$	-6.13	11.60	0.16	0.78
$\delta g_{baseline} - \delta g_{RTM} \text{ with } H_{RTM} > 0$	-2.28	2.36	-0.04	0.22
$\delta g_{baseline} - \delta g_{RTM} \text{ with } H_{RTM} \leq 0$	-6.13	11.60	0.36	1.07
External validation over Switzerland				
δg_{RTM}	-217.73	100.91	-11.84	41.53
$\delta g_{baseline} - \delta g_{RTM}$	-9.14	7.19	0.09	0.62
$\delta g_{baseline} - \delta g_{RTM} \text{ with } H_{RTM} > 0$	-4.17	3.95	-0.03	0.38
$\delta g_{baseline} - \delta g_{RTM} \text{ with } H_{RTM} \leq 0$	-9.14	7.19	0.22	0.79

* with δg_{RTM} indicating RTM gravity disturbances calculated through the TGF program software; $\delta g_{baseline}$ novel RTM baseline solution obtained by a combination of NI and SGM. $H_{RTM} = H - H_{REF}$ denotes the residual height.

The key inputs for RTM gravity field calculations were 3'' MERIT DEM, MERIT SHCS to degree 2,160 and a constant mass-density $2,670 \text{ kg/m}^3$. With TGF, the residual masses within 1° angle distance from the calculation point were considered and divided into four zones. Tab. 4.2 gives the definition of each zone, including approximation methods, DEM resolution and zones extension used in TGF. Polyhedron and prism with 3'' DEM were primarily applied in the vicinity zones of up to 0.02° and 0.03° angle distance around each calculation point, while tesseroid with 3'' DEM extending to 0.15° , and point-mass for the outside distances with DEM of 30'' resolution.

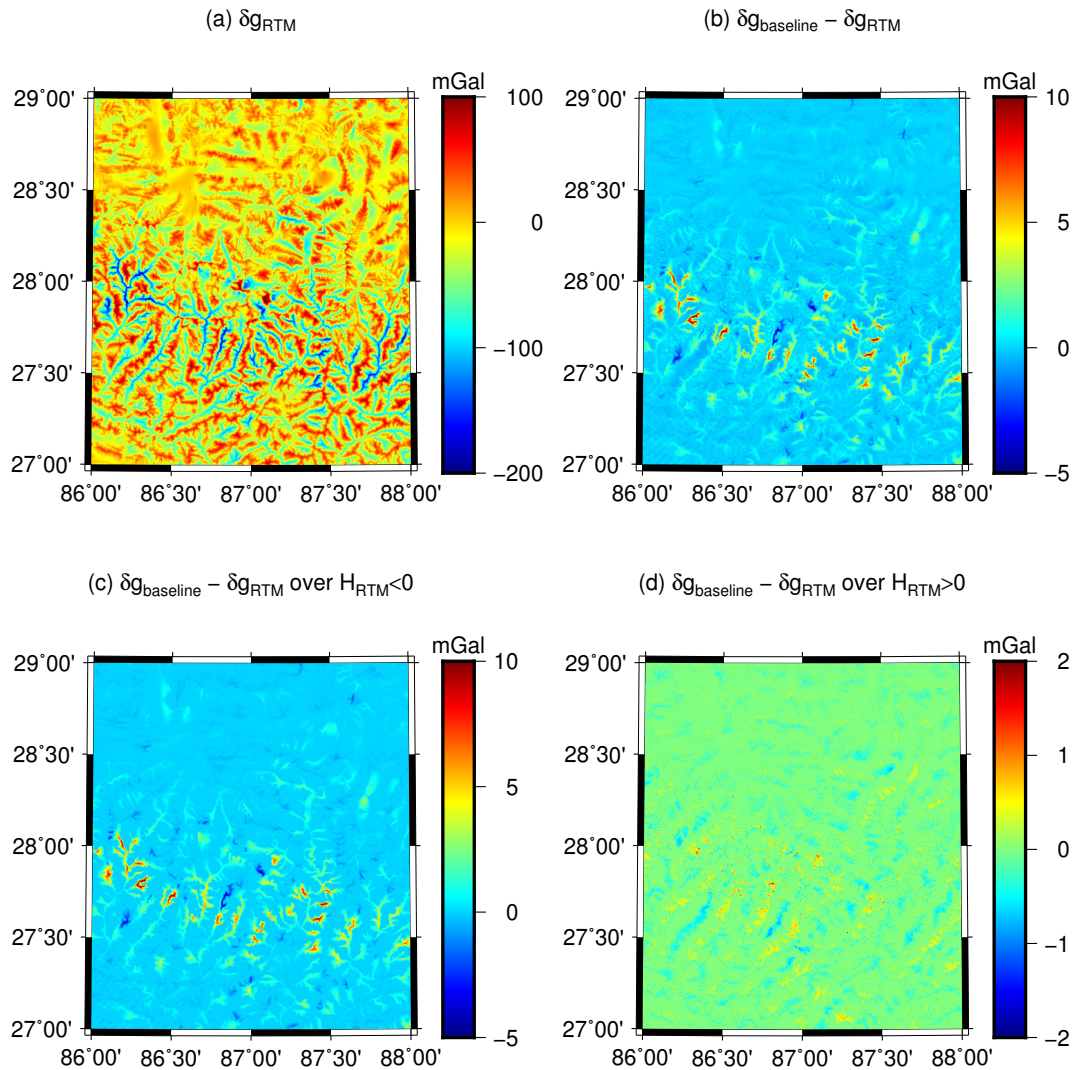


Fig. 4.8 – External validation based on baseline (*Hirt et al (2019a)*) over Himalaya mountainous area. H_{RTM} represents RTM height, it is the height difference between surface topography and reference topography, with $H_{RTM} = H - H_{REF}$

Validation experiments were carried out over two study areas with extremely rugged topography on the Earth's surface:

- 1) Himalaya mountainous area ($27^\circ \sim 29^\circ N$ in latitude and $86^\circ \sim 88^\circ E$ in longitude) with an elevation ranging up to 8,000 m,

- 2) Switzerland around Alpine region ($45^\circ \sim 47^\circ N$ in latitude and $7^\circ \sim 9^\circ E$ in longitude) with short-scale terrain variations of $\pm 2,000$ m.

RTM gravity disturbances at $15''$ grid over the study areas were calculated by the TGF software and subsequently compared with the RTM baseline solutions. The comparison results show the error level that can be attributed to methodologies applied in the TGF software. Therefore, they provide a measure for the computational accuracy of the TGF software.

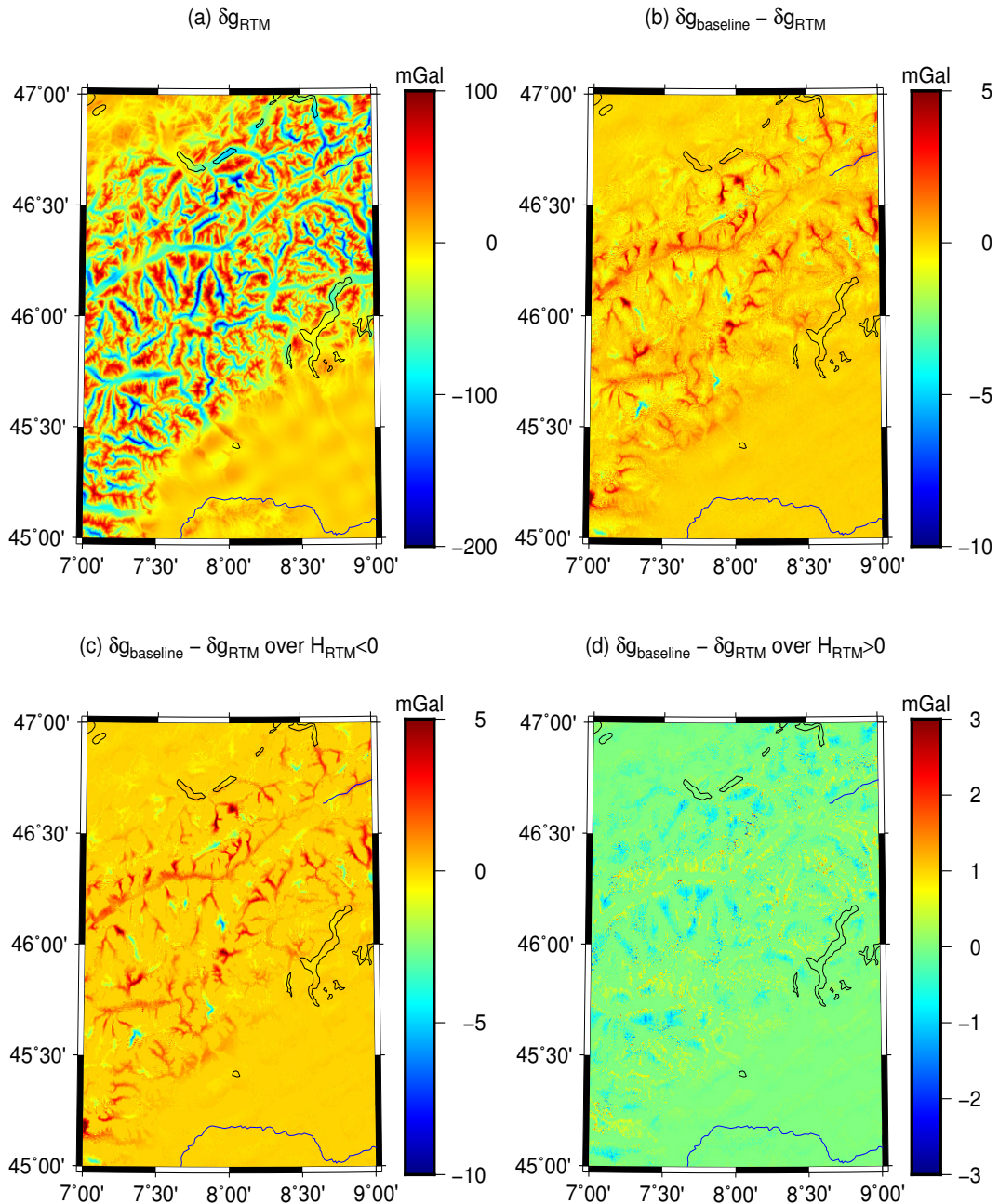


Fig. 4.9 – External validation based on baseline (*Hirt et al (2019a)*) over Switzerland. H_{RTM} represents RTM height, it is the height difference between surface topography and reference topography, with $H_{RTM} = H - H_{REF}$

Validation results are shown in Fig. 4.8 for Himalaya mountain area and in Fig. 4.9 for Switzerland respectively, and the descriptive statistics are displayed in Tab. 4.4. The RMS differences between TGF-based RTM gravity

disturbances and reference values from global numerical integration and SGM are found to be smaller than ~ 0.8 mGal over the two study areas. The maximum differences are within 12 mGal, and most extreme values are associated with negative residual heights H_{RTM} (Fig. 4.8 (b) and (c), Fig. 4.9 (b) and (c)). Over these points where $H_{RTM} < 0$, the RMS increases from ~ 0.78 mGal to ~ 1.07 mGal for Himalaya mountains, ~ 0.62 mGal to ~ 0.79 mGal over Switzerland. Over points with $H_{RTM} < 0$, computation points are below the reference surface. The TGF calculated RTM gravitational components through spatial domain techniques are non-harmonic. To compare with the harmonic baseline values, the $4\pi G\rho H_{RTM}$ harmonic correction was applied for points $H_{RTM} < 0$. Fig. 4.8 (b) and (c), Fig. 4.9 (b) and (c), demonstrate that $4\pi G\rho H_{RTM}$ HC approximation may influence the quality of RTM gravity up to amplitudes of ~ 11.6 mGal (also see *Hirt et al* (2019a)).

For points outside the RTM reference topography where no harmonic correction is required, the differences are as low as ~ 0.22 mGal RMS over Himalaya and ~ 0.38 mGal RMS over Switzerland. Part of these residuals might be attributed to the effect of different modeling of masses between RTM and NI (Tab. 4.2). Some short-wavelength residuals are introduced through the different modeling in the near-zone (e.g. polyhedral vs. flat-topped prisms), while a longer-wavelength signal should be introduced through the use of different resolutions for far-zone masses. The further study to an estimate of using polyhedral vs. flat-topped prisms will be done in the next sections.

Overall, our validation results show the sub-mGal computational precision that can be achieved with TGF for residual gravity field computations.

4.2.4 Efficiency and internal validation

An important aspect of topographic gravitational field calculation is the computational effort related to the evaluation of Newtonian integration. For gravity forward modelling in the spatial domain, the calculation time is linearly correlated with the number of calculation points and the number of mass-elements for integration. This means a great challenge when global integration is implemented down to the DEM resolution globally, for example converting $3''$ MERIT DEM to its implied full-scale gravity field. Over the past decades, many procedures have been proposed for an efficient calculation of gravitational field generated by topography. *Hirt et al* (2019b) calculated the full-scale topographic gravity field generated by $3''$ MERIT DEM via combining spatial and spectral domain gravity forward modelling techniques. The long-wavelength gravity signal was efficiently calculated using the SGM technique, and the high-frequency signal was modeled in the spatial domain through RTM technique with numerical integration being restricted to the neighborhood of the evaluation points.

In TGF, the spatial domain numerical evaluation methods have been developed and programmed for given geometries, i.e., polyhedra, prism, tesseroid and point mass. However, as the above shows, the computation time often appears as a limiting practical issue considering specific geometry for large and complex problems.

Depending on the attenuation and fluctuation nature of the RTM gravitational field, the geometry switches relying on the trade-off between accuracy and efficiency, and coarse DEM is adopted and truncation at a distant zone.

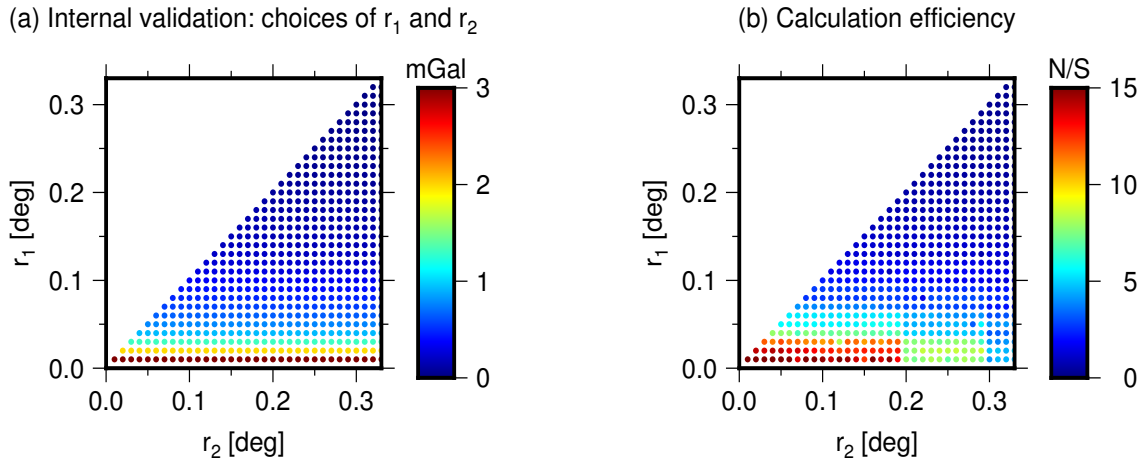


Fig. 4.10 – Forward modeling internal accuracy and efficiency with radius of polyhedron (r_1) and prism (r_2). (r_1) is the radius of using polyhedron, varying from 0.00° to 0.33° with step of 0.01° , (r_2) is the radius of using prism, varying from 0.00° to 0.33° with step 0.01° . Left: Inertial accuracy; Right: evaluation points per second

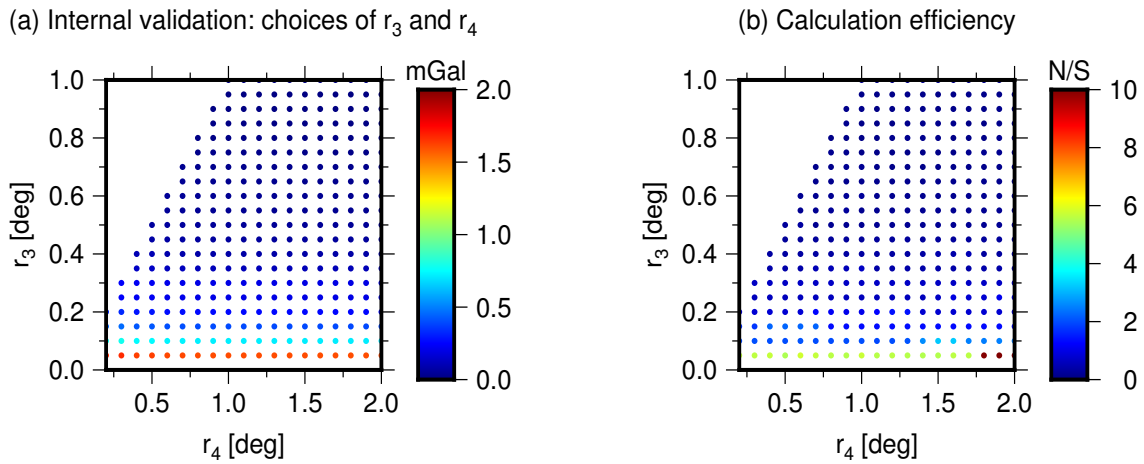


Fig. 4.11 – Forward modeling internal accuracy and efficiency with radius of tesseroid (r_3) and point-mass (r_4). (r_3) is the radius of using tesseroid, varying from 0.05° to 1° with step of 0.05° , (r_4) is the radius of using point-mass, varying from 0.2° to 2° with step 0.01° . Left: Internal accuracy; Right: evaluation points per second

In this section, we investigated the trade-off between the achieved RTM accuracy and computation efficiency through a comparison with the defined internal testbed. In all calculations, RTM masses of a constant density $\rho = 2,670 \text{ kg/m}^3$ were defined by residual masses between the $3''$ MERIT DEM and the MERIT SHCs2160 (directly derived from $3''$ MERIT DEM). With TGF, the mass-distributions around each calculation point were divided into four zones, using polyhedron up to a radius of r_1 in the vicinity of the calculation point, and prism extending to a distance of r_2 , then using tesseroid to distance r_3 , and truncated to r_4 with point mass. There is $r_1 \leq r_2 \leq r_3 \leq r_4$. In the internal validation, RTM gravity disturbances calculated from a set of optimal integration parameters, here with polyhedron with $3''$ DEM within the vicinity of 0.33° distance, tesseroid with

3'' DEM extending to 1° , and point-mass for outside and truncated to 2° , were denoted as internal testbed which provide reference values for the following experiments.

The study area – a $0.1^\circ \times 0.1^\circ$ square – consisted of 576 calculation points (at 15'' grid resolution) was located at the Earth's roughest Himalaya area, where forward modelling errors can be expected to be largest. The RTM gravity disturbances at 576 calculation points were calculated with various combinations of geometry and radius by TGF, then were compared with the internal testbed. In order to investigate the forward modeling accuracy and computation time with radius choices of polyhedron and prism, the following procedure for internal validation was implemented:

- 1) The calculation of internal testbed over 576 evaluation points with radius of zones, $r_1 = 0.33^\circ$, $r_2 = r_1$, $r_3 = 1^\circ$, $r_4 = 2^\circ$;
- 2) The definition of a series of radius variants (r_1, r_2, r_3, r_4) , where $r_1 = 0 : 0.01 : 0.33$, $r_2 = 0 : 0.02 : 0.33$, with fixed $r_3 = 0.15^\circ$ and $r_4 = 2^\circ$.
- 3) Calculation of the RTM gravity field with each set of radius variant.
- 4) Comparison between calculated gravity disturbances and the internal testbed.
- 5) Statistical analysis of residuals.

The comparison results are shown in Fig. 4.10 (a) in terms of RMS of the differences between calculated gravity disturbance and the internal testbed. In the vertical axis, when the radius of polyhedron-zone increases from 0° to 0.09° , the results achieved a boost in accuracy, from several mGal to better than 1 mGal. As seen in Fig. 4.10, in order to achieve 1 mGal accuracy or better, the polyhedron is required to extend further than 0.03° distance from the calculation point. Because gravity signal decays with the distance from the attracting masses increases, using polyhedron rather than prism at distance further than 0.09° would gain little enhancement. In the horizontal axis, with fixed polyhedron radius, the extension of the prism, does not bring significant improvement. Fig. 4.10 (b) shows the calculation efficiency when using various radius datasets in RTM gravity field calculations. It is obvious that accurate computation will always compromise efficiency. Using a polyhedron extending to 0.03° , the software would achieve the calculation efficiency of 8 points per second.

To investigate the choice of spheroid and point mass, further experiments were done, where extensions were implemented with $r_3 = 0.05 : 0.05 : 1$, $r_4 = 0.2 : 0.1 : 2$ and fixed $r_1 = r_2 = 0.03^\circ$. The calculated RTM gravity disturbances, based on each set of radius, were then compared with the internal testbed. The comparison results are shown in Fig. 4.11, internal comparison in terms of RMS of the differences in panel (a) and calculation efficiency with unit points/second in panel (b). When using spheroid up to a distance of 0.10° and point-mass to 0.5° , the RMS of the differences is less 1 mGal and calculation efficiency is 12 points per second.

Computation generally takes more time the radius of integration increases. More safely, radius of integration zones with $r_1 = 0.03^\circ$, $r_2 = 0.03^\circ$, $r_3 = 0.15^\circ$ and $r_4 = 0.8^\circ$ are recommended for 1 mGal accurate RTM gravity

signal retrieving with TGF. For most areas where topography is smoother than that in our test case, the results based on $r_1 = 0.02^\circ$ for polyhedron are accurate enough to recover 1 mGal gravity signals. In that case with radius dataset $r_1 = 0.02^\circ$, $r_2 = 0.03^\circ$, $r_3 = 0.15^\circ$ and $r_4 = 0.8^\circ$, TGF could achieve an efficiency of 10 points per second.

4.2.5 Polyhedron and prism comparison

In order to assess the approximation errors associated with the use of polyhedron and prism, RTM gravity disturbances with polyhedron and prism approximations in the vicinity of calculation points were calculated separately and were subsequently compared with RTM baseline solutions. In addition, we used the ground gravity observations in Canada and New Zealand as further means to benchmark the computation performance.

Tab. 4.5 – Descriptive statistics of gravity differences between baseline, and RTM gravity disturbances based on polyhedron and prism approximation respectively

	min(mGal)	max(mGal)	mean(mGal)	RMS(mGal)
$\delta g_{baseline} - \delta g^{RTM-prism}$	-5.36	11.78	0.25	1.05
$\delta g_{baseline} - \delta g^{RTM-poly}$	-5.73	11.45	0.32	1.07
$\delta g^{RTM-prism} - \delta g^{RTM-poly}$	-2.27	2.49	0.08	0.24

* with $\delta g_{baseline}$ indicating the novel RTM baseline solution obtained by a combination of NI and SGM. $\delta g^{RTM-prism}$ denotes the RTM gravity disturbances calculated by TGF program software based on prisms in the closest zone, while $\delta g^{RTM-poly}$ being obtained based on polyhedrons in the closest zone.

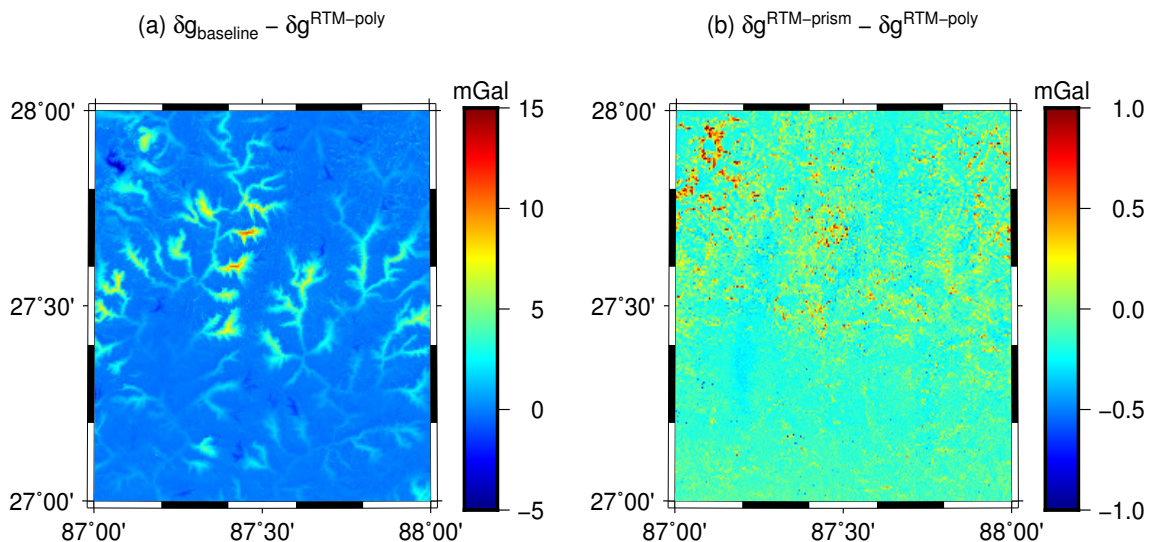


Fig. 4.12 – Comparison of prism and polyhedron. Left: RTM-baseline minus RTM-A results using polyhedron in the adjacent zones; right: differences of RTM-A results using polyhedron and prism

In the validation with RTM baseline solution, the study area was located at in a $1^\circ \times 1^\circ$ square ranging from $87 \sim 88^\circ E$ in longitude and $27 \sim 28^\circ N$ in latitude over Himalayan mountain ranges. The calculation points were

homogeneously distributed in the area at a resolution of $15''$. The residual masses were bounded by $3''$ MERIT DEM and MERIT SHCs 2,160, and with a uniform density value $\rho = 2,670 \text{ kg/m}^3$. RTM gravity disturbances were calculated, where $\delta g^{RTM-poly}$ is based on polyhedron approximation in the vicinity of calculation point while $\delta g^{RTM-prism}$ is based on prism approximation. Tab. 4.5 and Fig. 4.12 show the comparison results. The differences between $\delta g^{RTM-poly}$ and $\delta g^{RTM-prism}$ hold a high-frequency trend and vary from $\sim -2.27 \text{ mGal}$ to $\sim 2.49 \text{ mGal}$, with a mean value of 0.08 mGal and RMS of 0.24 mGal . Prism-based gravity disturbances have a better agreement with the baseline solution, which is seen from the smaller RMS value of 1.05 mGal compared to 1.12 mGal . This is probably due to the fact that flat-topped prism rather than polyhedron was adopted in the global numerical integration which our baseline solution relies on. As such, the power of the test using NI minus SGM as baseline is limited, ground-truth testing should be implemented and could provide a more robust feedback.

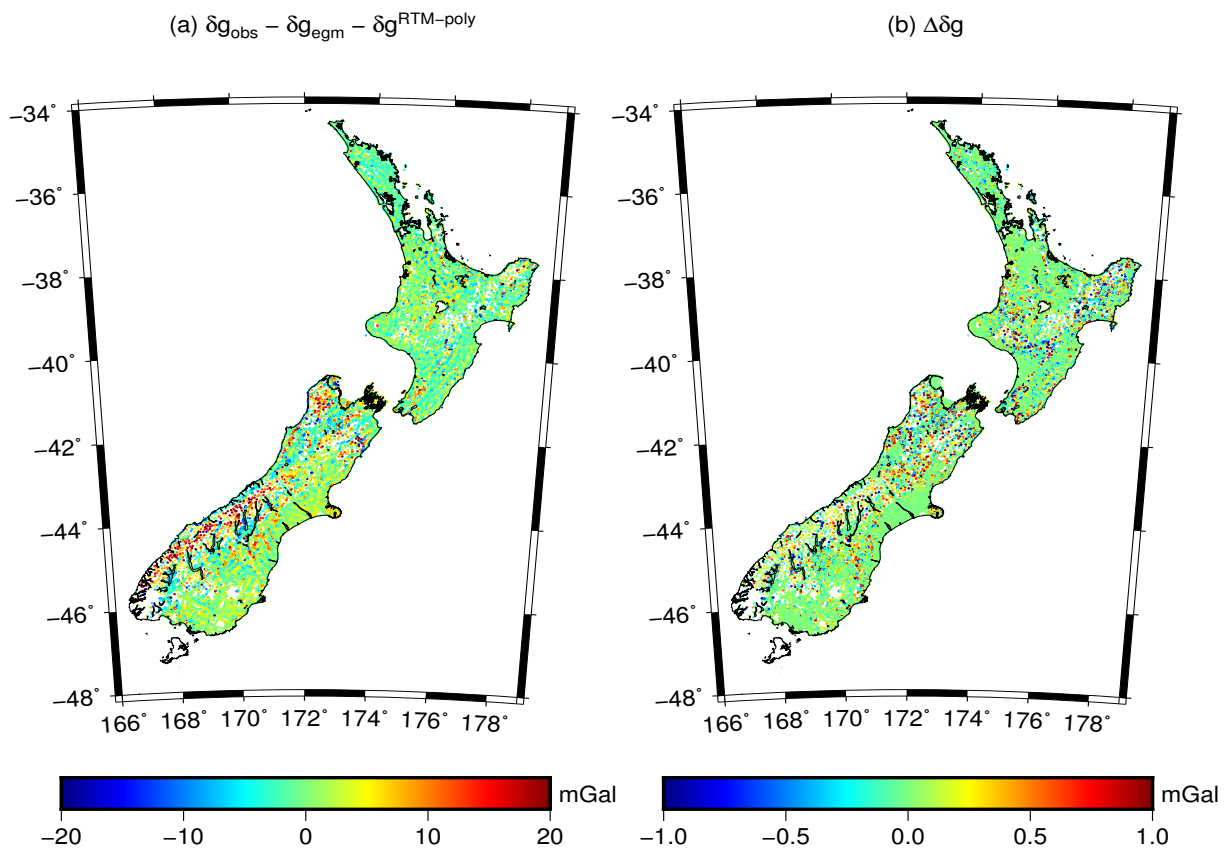


Fig. 4.13 – Comparison of prism and polyhedron over New Zealand. Left: $\delta g_{obs} - \delta g_{egm} - \delta g^{RTM-poly}$; right: $\Delta \delta g = |\delta g_{obs} - \delta g_{egm} - \delta g^{RTM-prism}| - |\delta g_{obs} - \delta g_{egm} - \delta g^{RTM-poly}|$

Further experiments were implemented based on 40,366 terrestrial gravity observations over New Zealand and 29,338 gravity measurements over Canada. The RTM gravity disturbances at station height interpolated from $3''$ MERIT DEM, were modeled and computed based on RTM-A technique. $\delta g^{RTM-prism}$ indicates RTM gravity disturbances calculated based on prism approximation in the vicinity, while polyhedron for $\delta g^{RTM-poly}$ at the same mass elements. Tab. 4.6, Fig. 4.13 and Fig. 4.14 show the comparison results over New Zealand and Canada. In these two areas, using polyhedron instead of prism achieves smoother residual gravity signals

Tab. 4.6 – Descriptive statistics of gravity differences between ground observations, EGM2008 and RTM gravity disturbances based on polyhedron and prism approximation respectively

	min(mGal)	max(mGal)	mean(mGal)	rms(mGal)
Validations over New Zealand				
$\delta g_{obs} - \delta g_{egm} - \delta g^{RTM-prism}$	-94.79	90.10	1.06	4.72
$\delta g_{obs} - \delta g_{egm} - \delta g^{RTM-poly}$	-95.27	83.05	0.89	4.70
$\Delta \delta g$	-4.52	2.13	0.00	0.25
Validations over Canada				
$\delta g_{obs} - \delta g_{egm} - \delta g^{RTM-prism}$	-163.82	58.99	2.79	6.99
$\delta g_{obs} - \delta g_{egm} - \delta g^{RTM-poly}$	-164.15	58.91	2.69	6.95
$\Delta \delta g$	-2.92	22.29	0.03	0.25

* with δg_{obs} indicating the observed gravity disturbances. δg_{egm} denotes the long-wavelength gravity disturbances calculated from EGM2008 to degree 2,190 and order 2,159. $\delta g^{RTM-prism}$ denotes the RTM gravity disturbances calculated by TGF program software based on prism in the closest zone, while $\delta g^{RTM-poly}$ being obtained based on polyhedron in the closest zone. $\Delta \delta g = |\delta g_{obs} - \delta g_{egm} - \delta g^{RTM-prism}| - |\delta g_{obs} - \delta g_{egm} - \delta g^{RTM-poly}|$ are the absolute residuals.

where $\delta g_{obs} - \delta g_{egm} - \delta g^{RTM-poly}$ with smaller RMS of ~ 3.84 mGal. Fig. 4.13 (b) and Fig. 4.14 (b) show the absolute residuals using prism and polyhedron, the red color indicates that polyhedron performs better than prism. This is obvious over rugged areas.

4.2.6 RTM gravity field over Zugspitze area

This work has been documented in the manuscript "Yang, M., Hirt, C., Pail, R., 2019. TGF: A New MATLAB-based Software for Terrain-related Gravity Field Calculations.". Most of materials presented in this subsection has been taken directly from the manuscript.

In order to exemplify the spectrum of the implemented gravity field functionals – from potential values to first- and second-order derivatives – TGF was applied for RTM gravity field calculations over a test area located in the Zugspitze area of the German Alps (with longitude between 10.95° E and 11.25° E, and latitude between 47.35° N and 47.5° N). The 3" MERIT-DEM represents the Earth's surface and MERIT SHCs 2,160 the reference surface, the RTM heights vary between -600 m and 1,200 m (Fig. 4.15). This makes the test area a good example for high-frequency gravity field studies over mountain areas. 972,000 calculation points are arranged on a 1" resolution grid over the study area. The calculated RTM gravity field components with TGF are displayed in Figs. 4.16 and 4.17. All computations use a uniform rock density of $2,670 \text{ kg/m}^3$ and are based on spherical approximation, and the regularization and discretization method follows the parameters listed in

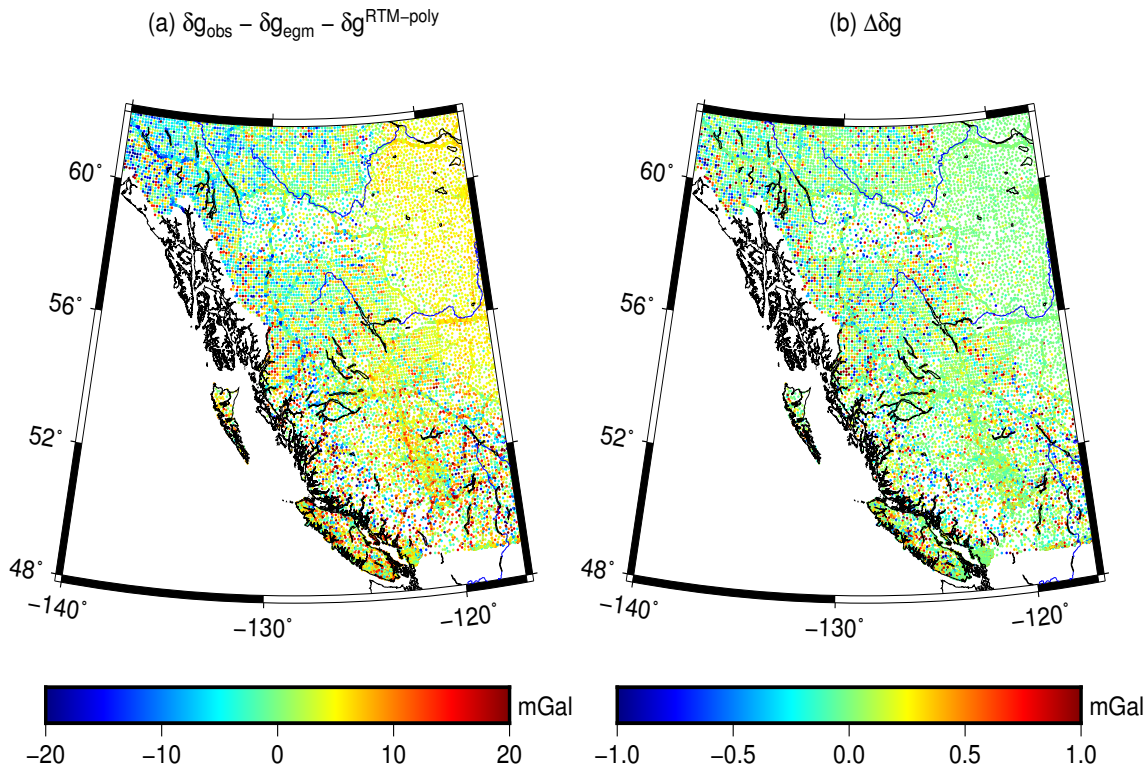


Fig. 4.14 – Comparison of prism and polyhedron over Canada. Left: $\delta g_{\text{obs}} - \delta g_{\text{egm}} - \delta g^{\text{RTM-poly}}$; right: $\Delta \delta g = |\delta g_{\text{obs}} - \delta g_{\text{egm}} - \delta g^{\text{RTM-prism}}| - |\delta g_{\text{obs}} - \delta g_{\text{egm}} - \delta g^{\text{RTM-poly}}|$

Tab. 4.2. Note that, in order to avoid numerical instabilities for the tensor components, the calculation points are located 1 m above the Earth's surface.

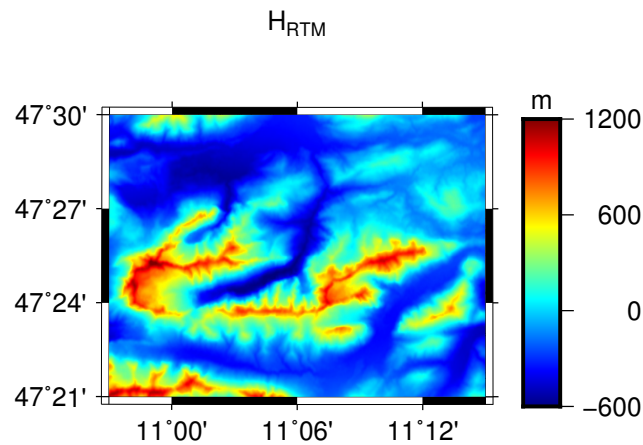


Fig. 4.15 – Residual height over Zugspitze (German Alps) area

Fig. 16 displays the calculated: panel (a) – residual geoid heights (varying in the range of 20 cm, Panel (b) – residual gravity disturbance ranging from ~ -120 mGal to ~ 80 mGal, and north-south (Panel (c)) and east-west (Panel (d)) components of vertical deflections. The large magnitude of these components shows the relevance of high-frequency gravity signals in global or regional gravity field determination.

Fig.17 shows the calculated elements of the Marussi tensor, with the first column illustrating the diagonal components V_{xx} (Panel (a)), V_{yy} (Panel (c)) and V_{zz} (Panel (e)), and the second column the off-diagonal compo-

nents V_{xy} (Panel (b)), V_{xz} (Panel (d)) and V_{yz} (Panel (f)). TGF may prove a beneficial tool for studying the short-scale signal characteristics of the high-order derivatives of the potential.

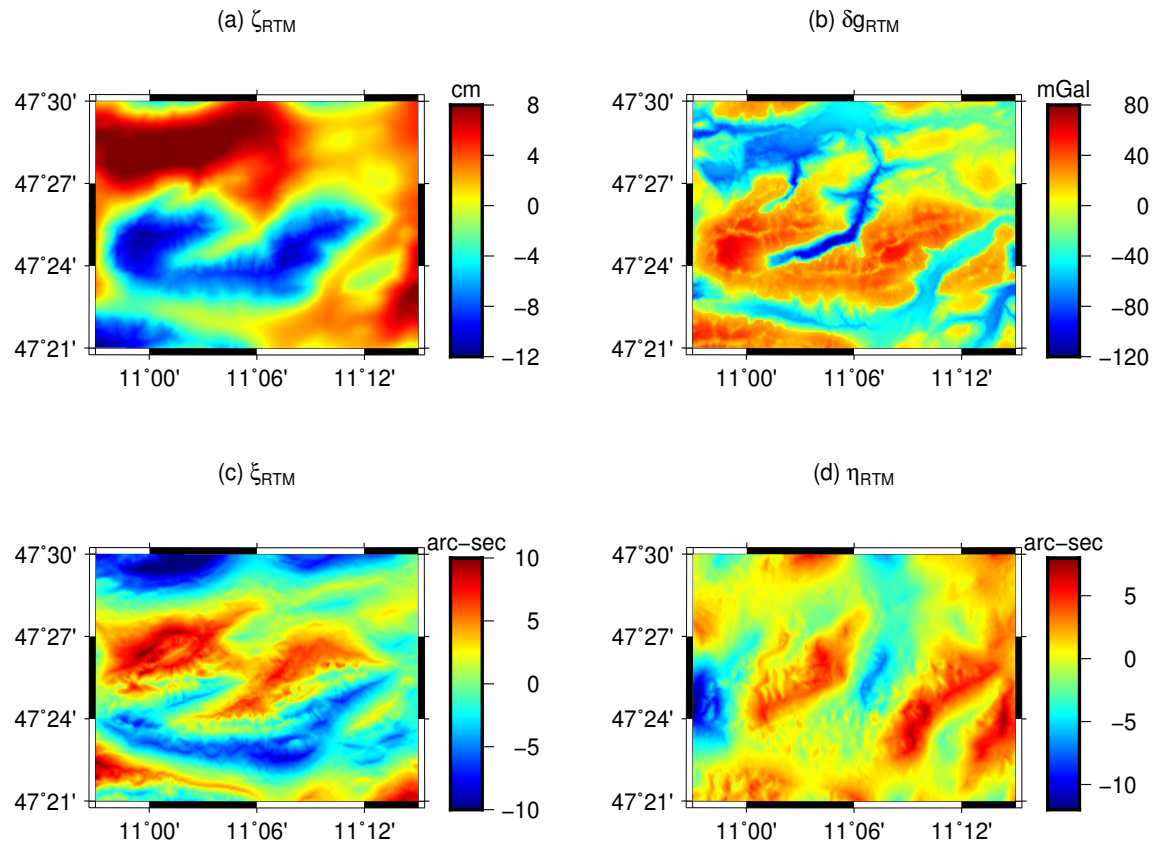


Fig. 4.16 – Residual gravity field calculated by TGF software. With τ_{RTM} indicating residual geoid height signals, σ_{RTM} residual gravity disturbances, ξ_{RTM} and η_{RTM} representing north-south and east-west components of vertical deflection separately.

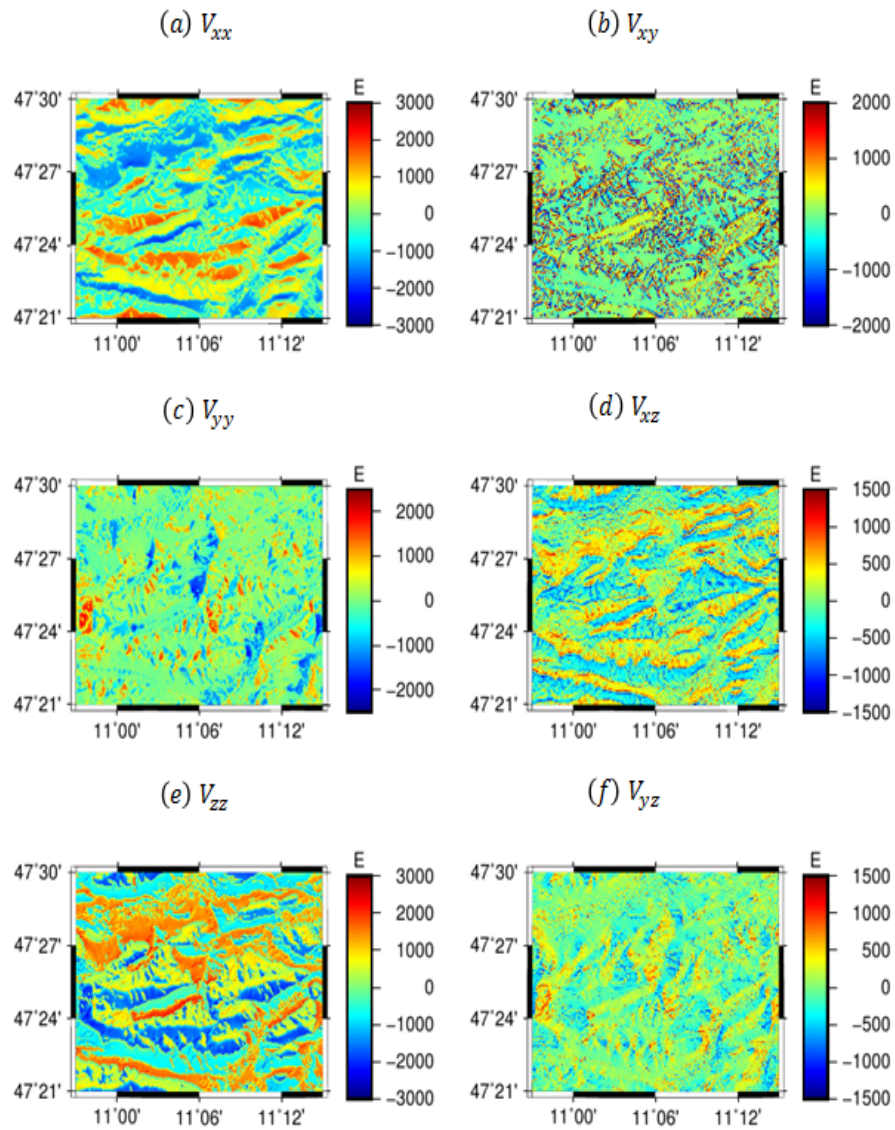


Fig. 4.17 – RTM tensor components of gravity field over Zugspitze (German Alps) area.

Chapter 5

Numerical investigation of RTM techniques

In practice, the RTM technique cannot retrieve the true high-frequency gravity signal, owing to various types of assumptions and simplifications in the evaluation of RTM gravity field. The principle of the RTM technique in the spatial domain as displayed in Fig. 2.7 covers the most often used parameters for each step. The errors and approximations in the parameters can lead to errors in the modeled RTM gravity field. Such errors may emerge from 1) spectral inconsistency in the geometric and gravity domain, 2) various reference geometries, 3) errors in the position of computation points, 4) errors in the databases such as DEMs and density models for mass-element definition, 5) errors related to sampling, and 6) inaccurate harmonic correction when using RTM technique. These sources of error will lead to the primary effect (mGal level) in the derived gravity field (Fig. 5.1). Additionally, the errors related to discretization and regularization will produce the secondary effect (Fig. 5.1).

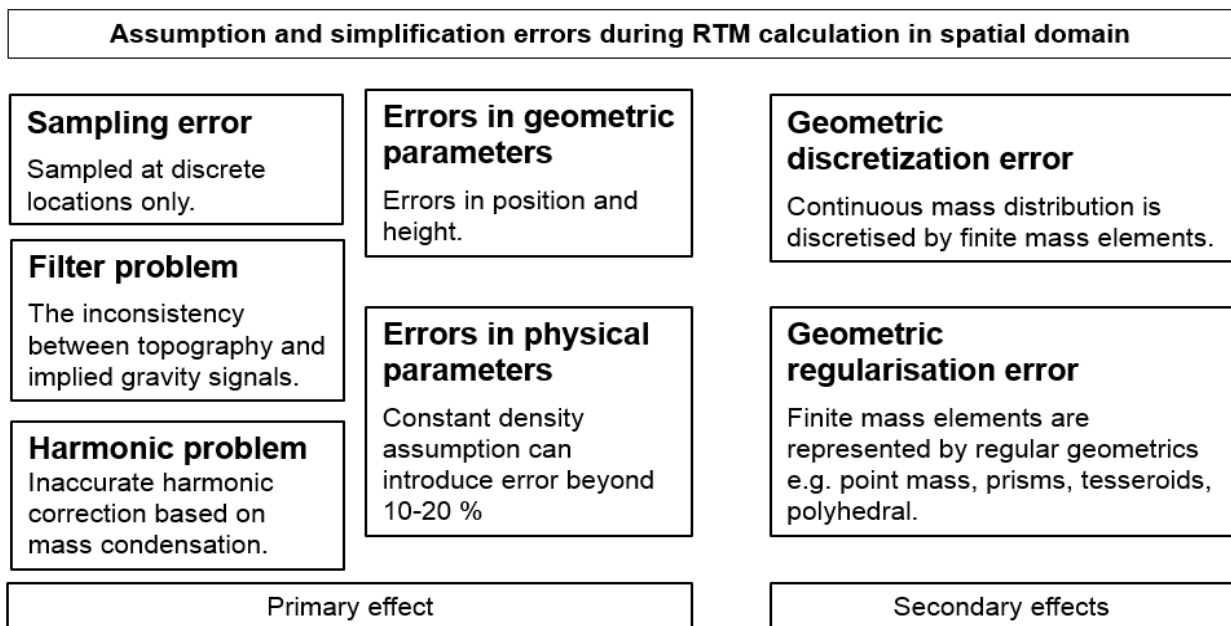


Fig. 5.1 – RTM error sources.

The main purpose of this chapter is to study various sources of error and estimate their amplitudes in the forward modeled gravity field. The sources of error in this study are divided into two categories and introduced in the following:

- (1) **Modelling errors:** the RTM modelling errors related to three types of RTM variants A-C (Section 5.1.1) and the Earth approximation errors involved by the ellipsoidal and spherical approximations (5.1.2);
- (2) **Observation errors:** the performance of a regional mass-density map, regional optimum density vs constant mass-density assumption in the RTM gravity forward modelling (Section 5.2.1), and the effect of tree-canopy bias in gravity forward modelling (Section 5.2.2).

5.1 Modelling errors

5.1.1 RTM modelling error

The subsequently presented results have been published in Hirt et al (2019a) where the PhD student contributed the computations, software preparation, and data analysis.

Three frequently used RTM techniques, RTM-A, RTM-B and RTM-C discussed in Section 2.3, were assessed using the novel RTM baseline solution relying on a combination of global numerical integration and ultra-high order spectral forward modelling, denoted as $\delta g_{baseline} = \delta g_{NI} - \delta g_{SGM} - \delta g_{HF}$. As introduced in Section 2.3, the RTM baseline solution is not subject to various approximation errors, such as high-frequency filter problem, harmonic correction problem, and two other approximations, that of mass simplification and computation point inconsistency. Therefore, the RTM baseline solution is considered to be superior to RTM techniques A-C. In the following, the RTM baseline solution provided a reference to measure and quantify various types of approximation errors, i.e., harmonic correction, mass simplification, and computation point inconsistency. As test areas we used two rough mountainous areas on the Earth: (1) Himalayas area (bounded by longitude within 86° E and 88° E, latitude within 27° N and 29° N, with an elevation range of $\sim 4,000$ m), and (2) Switzerland including the Alpine region (with latitude ranging from 45° N and 47° N, and longitude within 7° E and 9° E).

In the evaluation of Newtonian integration, the Earth was assumed to be a sphere of a constant radius $R = 6,378,137$ m and topographic masses of a constant crustal density value $\rho = 2,670$ kg/m³. Radial surfaces were represented by the MERIT DEM at $3''$ resolution and its directly derived spherical harmonic DEM model to the degree and order of 2,160 (MERIT SHCs2160). The computation points were cell-centered grid at $15''$ resolution (480×480 points for each study area). The calculations were defined as follows:

- The baseline $\delta g_{baseline} = \delta g_{NI} - \delta g_{SGM} - \delta g_{HF}$. The full-scale gravity signal δg_{NI} was calculated via the Curtin's Newtonian integrator (CNI), with regularization and discretization methods defined in Tab.

4.3. The calculation of the band-limited gravity signals δg_{SGM} generated by the reference topography was described in (Hirt et al (2019a), Hirt et al (2019b)). δg_{HF} was the high-frequency correction beyond degree and order of 2,159 contained in the reference topography. Computation points were located on the Earth's surface (MERIT DEM) for all calculations of three items δg_{NI} , δg_{SGM} and δg_{HF} .

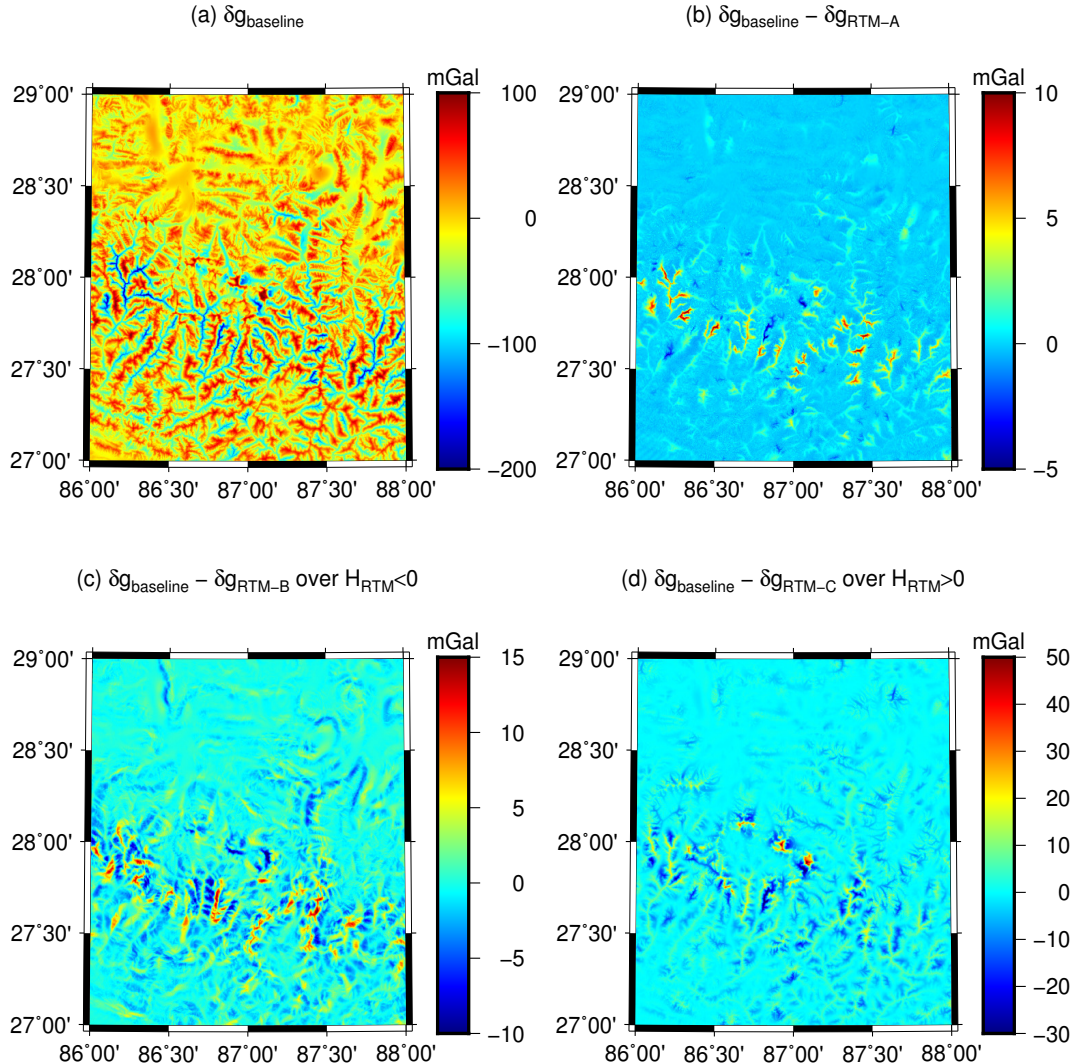


Fig. 5.2 – RTM techniques validation over Himalayas areas. With $\delta g_{baseline}$ indicating the RTM baseline solution, δg_{RTM-A} RTM gravity disturbances via RTM-A technique, δg_{RTM-B} RTM gravity disturbances via RTM-B technique, and δg_{RTM-C} RTM gravity disturbances via RTM-C technique.

- The residual gravity disturbance δg_{RTM-A} calculated via RTM-A technique was defined as Eq.(2.69) and harmonicity corrected by Eq.(2.68) at non-harmonic points. MERIT DEM and MERIT SHCs2160, as inputs, defined the upper and lower boundaries of mass-distributions. The calculation points were located on the surface of MERIT DEM.
- Similar to the RTM-A technique, the evaluation of gravitational field δg_{RTM-B} in the framework of the RTM-B technique was in one-run calculation, and non-harmonic fields were corrected by Eq. (2.68). In the RTM-B technique, the masses with thick of H_{RTM} (residual height after removing MERIT SHCs2160

from MERIT DEM) were fixed on the reference sphere surface. The calculation points resided on the surface of residual DEM defined by H_{RTM} .

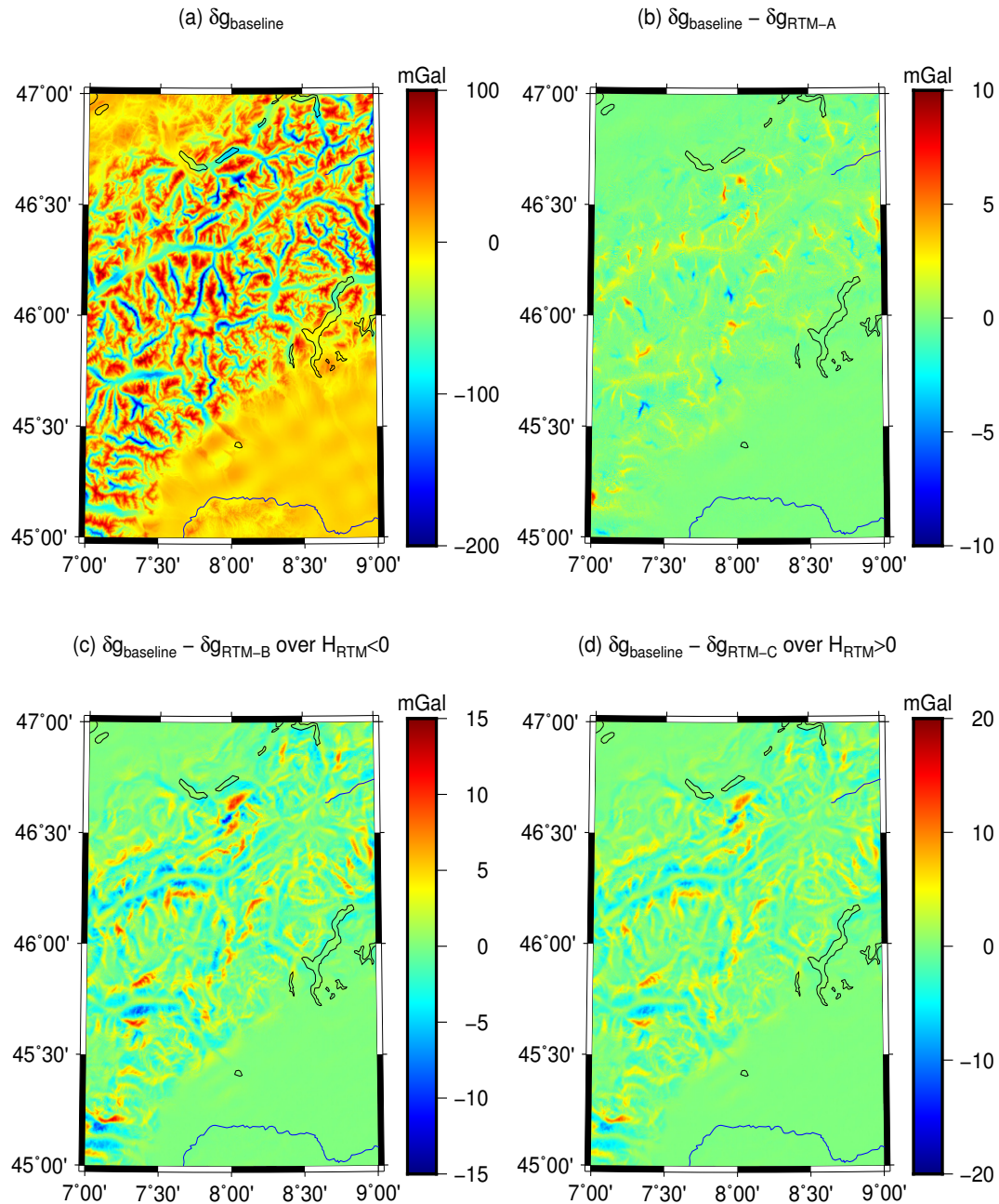


Fig. 5.3 – RTM techniques validation over Swiss Alps. With $\delta g_{baseline}$ indicating the RTM baseline solution, δg_{RTM-A} RTM gravity disturbances via RTM-A technique, δg_{RTM-B} RTM gravity disturbances via RTM-B technique, and δg_{RTM-C} RTM gravity disturbances via RTM-C technique.

- For the *RTM-C technique*, two-run calculations were implemented. In the first run, integration masses were defined between MERIT DEM and sphere surface. The calculation points were located on the surface of MERIT DEM. In the second run, integration masses were defined between MERIT SHCs2160 and surface of the reference sphere. The calculation points resided on the surface of MERIT SHCs2160. The difference of the two sets of calculations was the composed RTM gravity effect δg_{RTM-C} .

The subsequent results were presented in Hirt et al (2019a).

Figs. 5.2 and 5.3 show the validation results – comparisons between RTM baseline solution and the RTM techniques A-C, and for a summary of the descriptive statistics see in Tab. 5.1. Over both study areas, Himalayas (Fig. 5.2) and Swiss Alps (Fig. 5.3), the integration results based on the RTM-A technique achieved the best agreement with the RTM baseline values (Figs. 5.2 (b) and 5.3 (b)). In terms of RTM gravity disturbances, the deviations of δg_{RTM-A} from $\delta g_{baseline}$ held the smallest RMS values ~ 0.78 mGal over Himalayas area and ~ 0.62 mGal over Swiss Alps. The deviations were consistently at the sub-mGal levels over areas with $H_{RTM} > 0$ (Figs. 4.8 (c) and 4.9 (c)), while the larger differences with several mGal level showed up over valleys (Figs. 4.8 (d) and 4.9 (d)). For valley points that encountered non-harmonic problems, Eq. (2.68) was applied to estimate the harmonic correction values. Therefore, the larger deviations could be attributed to the approximation errors (e.g., caused by mass compressing and Bouguer plate approximation) related to the harmonic correction of Eq. (2.68). Additionally, the positive values of deviations suggested the insufficient harmonic correction of Eq. (2.68). Similar to the RTM-A, the RTM-B was completed in a one-run calculation and harmonic corrected with Eq. (2.68). Besides the approximation errors of harmonic correction, the RTM-B technique was subject to the re-location of mass-distributions, where residual masses were shifted and fixed on the surface of the reference sphere. This mass simplification reduced the agreement between δg_{RTM-B} and $g_{baseline}$ to the ~ 1.88 mGal (at the Himalayas) and ~ 1.79 mGal (over Switzerland) level in terms of RMS. The RTM-C technique avoided the harmonic correction through two independently runs calculations,

Tab. 5.1 – Comparison of various RTM techniques over Himalayas and Switzerland (cf. Hirt et al (2019a))

	min (mGal)	max (mGal)	mean (mGal)	rms (mGal)
External validation over Himalayas				
$\delta g_{baseline}$	-215.69	109.58	-11.60	39.13
$\delta g_{baseline} - \delta g_{RTM-A}$	-6.13	11.60	0.16	0.78
$\delta g_{baseline} - \delta g_{RTM-B}$	-12.68	15.30	0.03	1.88
$\delta g_{baseline} - \delta g_{RTM-C}$	-38.63	57.94	-0.03	3.67
External validation over Switzerland				
$\delta g_{baseline}$	-218.97	100.55	-11.75	41.33
$\delta g_{baseline} - \delta g_{RTM-A}$	-9.14	7.19	0.09	0.62
$\delta g_{baseline} - \delta g_{RTM-B}$	-11.40	12.47	0.04	1.79
$\delta g_{baseline} - \delta g_{RTM-C}$	-29.27	26.52	-0.01	3.17

* With $\delta g_{baseline}$ indicating the RTM baseline solution, δg_{RTM-A} RTM gravity disturbances via RTM-A technique, δg_{RTM-B} RTM gravity disturbances via RTM-B technique, and δg_{RTM-C} RTM gravity disturbances via RTM-C technique.

but at the expense of approximation errors caused by the calculation point inconsistency (also see *Hirt et al* (2019a)). Owing to the calculation height consistency in two calculations, the discrepancy between δg_{RTM-C} and $\delta g_{baseline}$ rised up to 3 mGal level over two test areas.

5.1.2 Reference geometry error

Accurate numerical evaluation of Newtonian integration requires the pre-knowledge of mass-density distribution, including the 1) horizontal and vertical locations referred to a reference system, 2) geometric information of the mass-elements, and 3) geological mass-density values. In practical studies, the numerical integration over masses within a limited radius (e.g., ~ 10 km) around calculation points, together with the often used planar approximation – the regional area around a calculation point is approximated by a local plane – is sufficient for accurate calculation of RTM gravity field. Over areas with rough topography, such as the Himalayas, 10 km integration radius would cause great truncation errors in the derived gravity field, even for residual topography retrieved gravity signals. Fig. 5.4 displays the comparison results of RTM gravity disturbances calculated with different integration radius at the Himalayas. The calculation points were arranged in terms of a $15'' \times 15''$ grid on the surface of the Earth over test area bounded by latitudes of 27° N and 28° N, longitudes of 87° E and 88° E. MERIT2017 and MERIT2160 SH topography defined the boundaries of RTM masses. In Fig. 5.4, δg_{RTM}^{300km} indicated RTM gravity disturbances with integration radius extended to 300 km from the calculation point, and δg_{RTM}^{50km} , δg_{RTM}^{100km} , δg_{RTM}^{150km} and δg_{RTM}^{200km} limited the integration radius to the distances of 50 km, 100 km, 150 km, and 200 km respectively. Due to the characters that 1) Newtonian integration decays with the distance from calculation point increasing, and 2) the residual heights fluctuate around zero, the contribution of distance masses cancels out to some extent, though does not vanish completely. Here we used δg_{RTM}^{300km} representing the 'true value' of RTM gravity field generated by residual masses. The deviations from δg_{RTM}^{300km} gave a measure of omission errors contained in δg_{RTM}^{50km} , δg_{RTM}^{100km} , δg_{RTM}^{150km} and δg_{RTM}^{200km} . As shown in Fig. 5.4, truncating the integration radius to distances of 50 km and 100 km would yield omission errors as large as several mGal. Toward to mGal level gravity field calculations, 200 km integration radius was necessary over the areas with rough topography. In these cases, the curvature of the Earth has to be taken into consideration, 1) in planar approximation, by vertical shift of the mass-elements as applied in the TC software (*Forsberg* (1984)) or by additional coordinate transformation as introduced in *Heck and Seitz* (2007), 2) or using the more rigorous spherical or ellipsoidal approximation.

In the ellipsoidal approximation, the Earth is approximated by a spheroid with a latitude-dependent Earth radius r_e . The relevant coordinates are, ellipsoidal height h' and geodetic latitude β and longitude λ . In the TGF software, all forward computations model the topographic masses relative to the surface of GRS80 ellipsoid. It is

$$r_e = \frac{a\sqrt{(1-e^2)^2 \sin^2 \beta + \cos^2 \beta}}{\sqrt{1-e^2 \sin^2 \beta}} \quad (5.1)$$

with a being the semi-major axis, e value of the eccentricity. In spherical approximation, Newtonian integration

Tab. 5.2 – Parameter specification for reference approximations

Approximation method	Reference model	Coordinates	Earth's curvature correction
Ellipsoidal approximation	GRS80	geodetic coordinates: (β, λ, h')	n/a
Spherical approximation	Sphere of constant radius R	geocentric coordinate: (φ, λ, r)	n/a
planar approximation	calculation points origined local Cartesian system	local Cartesian coordinates: (x, y, z)	required several 10 km far

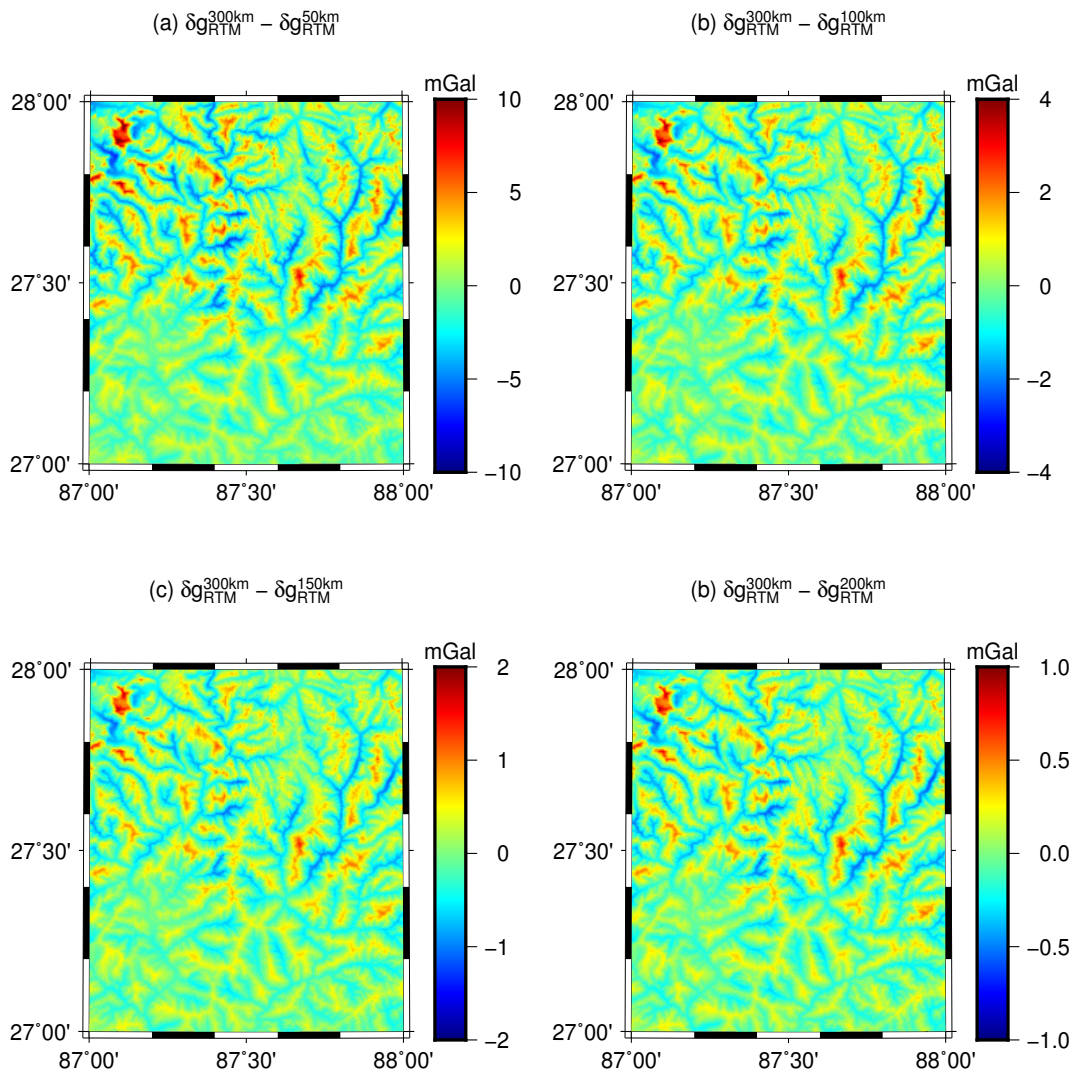


Fig. 5.4 – RTM truncation error over Himalaya areas. δg_{RTM}^{50km} , δg_{RTM}^{100km} , δg_{RTM}^{150km} , δg_{RTM}^{200km} and δg_{RTM}^{300km} indicate the RTM gravity disturbances with integration radius extended to the distances of 50 km, 100 km, 150 km, 200 km and 300 km respectively.

treats the topography relative to a reference sphere, with GRS80 semi-major axis as radius, and the spherical latitudes φ , longitudes λ and vertical distance to the Earth's center r as the coordinate basis. Converting from geodetic coordinates to spherical coordinates follows Eqs. (2.1-2.3).

To test the improvement using the ellipsoidal instead of the spherical approximation in RTM gravity field calculations, four sets of RTM gravity field were calculated separately based on the spherical approximation and ellipsoidal approximation over two study areas of the Himalayas and Swiss Alps. The integration radius was truncated to a distance of 200 km for all calculations. Fig 5.5 displays the comparison results. The differences between calculated RTM gravity disturbances based on the ellipsoidal approximation and on the spherical approximation were within ~ 0.15 mGal with RMS signal strength ~ 0.03 mGal at Himalayas. With increasing latitude, the differences between ellipsoidal approximation and spherical approximation rise to ~ 0.26 mGal in amplitude and to ~ 0.04 mGal in terms of RMS over Switzerland. As a general conclusion, the improvement using ellipsoidal approximation rather than spherical approximation was insignificant at the mGal level in gravity field determination. However, this conclusion was made in the scope of RTM gravity field calculations with integration radius truncated to a limited radius.

5.2 Observation errors

5.2.1 Mass-density errors

This work has been published in Journal of Studia Geophysica et Geodaetica, "Yang, M., Hirt, C., Tenzer, R., Pail, R., 2018. Experiences with the use of mass density maps in residual gravity forward modelling. Stud. Geophys. Geod., 62, Doi: 10.1007/s11200-017-0452-9", available at <https://link.springer.com/article/10.1007/s11200-017-0656-z>.

Up to present, the majority of publicly available gravity field models generated by the topography, such as ERTM2160 (Hirt et al (2014)) and the most recent SRTM2gravity model (Hirt et al (2019b)), were forward modeled using the constant density value (e.g., $2,670 \text{ kg/m}^3$) rather than actual density values. Where actual density values deviate from adopted constant value, errors are present in the RTM mass-model, and hence, in forward modeled RTM gravity field. The gravity values generated by the variation of actual density is named lateral density effect which has been widely considered in the works of literature, e.g., Martinec (1993), Martinec (1994), Kühnreiter (1998), Huang et al (2001), Tziavos and Featherstone (2001), Sjöberg (2004), Eshagh (2009), Tenzer et al (2015a), Root et al (2016). However, these studies were limited to the lateral density effect in topography generated gravity field but not in RTM gravity field modelling. When using a constant density value in the calculation of the RTM gravity field, the high-frequency signals implied by density anomalies would not be retrieved. Depending on the topography, the produced errors might be beyond 10% \sim 20% with quantities ranging from several cm to more than one meter in terms of geoid height errors. Therefore, as a part of

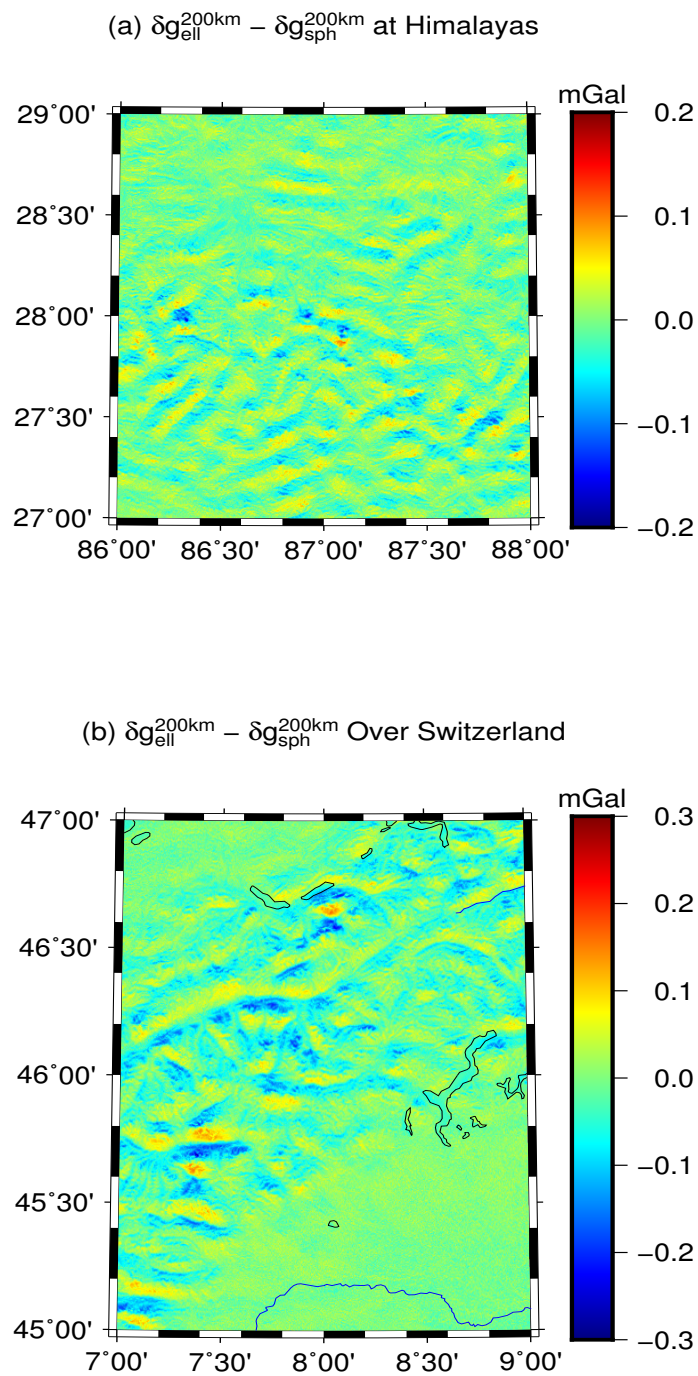


Fig. 5.5 – The comparison between RTM gravity disturbances calculated based on the ellipsoidal approximation $\delta g_{\text{ell}}^{200\text{km}}$ and spherical approximation $\delta g_{\text{sph}}^{200\text{km}}$ over Himalaya areas (panel (a)) and Switzerland areas (panel (b)). The differences range from ~ -0.15 mGal to ~ 0.12 mGal, with a mean value of differences of 0 mGal and a RMS of ~ 0.03 mGal at Himalayas, and vary between ~ -0.26 mGal to ~ 0.17 mGal, with a mean of ~ -0.01 mGal and a RMS of ~ 0.04 mGal over Switzerland areas.

the efforts toward the building of the 'millimeter local/regional geoid', the effect of the density anomalies on the RTM should be carefully taken into consideration.

In this section, the 1' New Zealand digital density map was combined with RTM technique to study its suitability for improved gravity forward modeling. RTM gravity quantities over New Zealand, with different combinations of elevation models and mass-density assumptions (mean crustal density and New Zealand density model) were calculated, and their performance was validated using ground gravity and GPS/leveling measurements. The procedure is as follows:

- I) Observed gravity disturbances δg_{obs} at 40,366 stations were computed with $\delta g_{obs} = g_{obs} - \gamma_{station}$. Thereby, $\gamma_{station}$ are the normal gravity values at station height. The calculation of normal gravity at station height follows Eqs. (3.2) and (3.3), g_{obs} denotes measured values of gravity acceleration.
- II) The long- and medium-wavelength part of gravity disturbances $\delta g_{EGM2008}$ were synthesized from EGM2008 with degree and order truncated to 2,159. The isGraflab (Bucha and Janák (2014)) software was applied in the harmonic synthesis procedure.
- III) The short-scale signals that finer than 5', which were not accounted for by in the $\delta g_{EGM2008}$, were calculated via the RTM technique. Seven sets of the RTM gravity disturbances were evaluated relying on various combinations of datasets: DTMs, and density models and assumptions (Yang et al (2018)). In all calculations of RTM gravity field, the reference surface was represented by the Earth2014 (Hirt and Rexer (2015)) and was truncated to degree and order of 2,159 which is commensurate with the maximum degree of EGM2008 in the calculation of $\delta g_{EGM2008}$.
 - (1) The calculation of $\delta g_{const}^{SRTM250m}$ shared the same input data sets – 250m-resolution SRTM DEM in the lateral-zone and 2,670 kg/m³ constant density value – with the building of ERTM2160 $\delta g_{ERTM2160}$. The comparison between $\delta g_{ERTM2160}$ and $\delta g_{const}^{SRTM250m}$ would further assess the performance of TGF in short-scale gravity field calculations.
 - (2) $\delta g_{const}^{SRTM90m}$ was calculated using 90 m-resolution SRTM DEM in the lateral-zone and 2,670 kg/m³ constant density value.
 - (3) To study the performance of the mass-density maps in RTM gravitational field calculations, we then computed four different sets of RTM gravity disturbances with 30 m DEM in the vicinity areas, as follows:
 - a) considering both, land- and ocean-mass effect, using rock-equivalent DBM/DTM (Section 3.1), we obtain $\delta g_{const}^{SRTM30m}$ with assumed constant density of 2,670 kg/m³;
 - b) when the mass-density map is used instead of the constant density value, $\delta g_{density_map}^{SRTM30m}$ was obtained over New Zealand;
 - c) just considering land-mass effect, setting value of DEM and RET2012 at ocean areas to 0, we obtain $\delta g_{const}^{SRTM30m/LANDonly}$ with constant density assumption of 2,670 kg/m³;

d) and, considering land-mass effect, we obtained, $\delta g_{density_map}^{SRTM30m/LANDonly}$ based on New Zealand mass-density model.

The descriptive statistics of the observed gravity disturbances δg_{obs} and the differences between observed and modeled gravity disturbances, as computed from

$$\begin{aligned}
\Delta \delta g_{const}^{ERTM2160} &= \delta g_{obs} - \delta g_{EGM2008} - \delta g_{ERTM2160}, \\
\Delta \delta g_{const}^{SRTM250m} &= \delta g_{obs} - \delta g_{EGM2008} - \delta g_{const}^{SRTM250m}, \\
\Delta \delta g_{const}^{SRTM90m} &= \delta g_{obs} - \delta g_{EGM2008} - \delta g_{const}^{SRTM90m}, \\
\Delta \delta g_{const}^{SRTM30m} &= \delta g_{obs} - \delta g_{EGM2008} - \delta g_{const}^{SRTM30m}, \\
\Delta \delta g_{density_map}^{SRTM30m} &= \delta g_{obs} - \delta g_{EGM2008} - \delta g_{density_map}^{SRTM30m}, \\
\Delta \delta g_{const}^{SRTM30m/LANDonly} &= \delta g_{obs} - \delta g_{EGM2008} - \delta g_{const}^{SRTM30m/LANDonly}, \\
\Delta \delta g_{density_map}^{SRTM30m/LANDonly} &= \delta g_{obs} - \delta g_{EGM2008} - \delta g_{density_map}^{SRTM30m/LANDonly}
\end{aligned} \tag{5.2}$$

are summarized in Tab. 5.3.

Tab. 5.3 – The statistical information of gravity disturbances δg_{obs} and differences with respect to various models over New Zealand. $\kappa[\%]$ indicates improvement rate

Gravity disturbances	min(mGal)	max(mGal)	mean(mGal)	rms(mGal)	$\kappa[\%]$
δg_{obs}	-158.54	199.32	22.23	49.17	
$\delta g_{obs} - \delta g_{EGM2008}$	-155.32	82.94	-5.91	18.67	62.03
$\Delta \delta g_{ERTM2160}$	-117.75	80.45	0.90	4.97	89.89
$\Delta \delta g_{const}^{SRTM250m}$	-96.42	87.94	1.02	4.79	90.26
$\Delta \delta g_{const}^{SRTM90m}$	-96.30	83.00	0.96	4.71	90.42
$\Delta \delta g_{const}^{SRTM30m}$	-97.52	79.11	0.96	4.69	90.46
$\Delta \delta g_{density_map}^{SRTM30m}$	-96.04	78.52	1.61	5.00	89.83
$\Delta \delta g_{optimum}^{SRTM30m}$	-96.40	74.08	0.75	4.65	90.54
$\Delta \delta g_{const}^{SRTM30m/LANDonly}$	-96.52	79.11	1.02	4.84	90.16
$\Delta \delta g_{density_map}^{SRTM30m/LANDonly}$	-95.95	79.64	1.68	5.17	89.48
$\Delta \delta g_{optimum}^{SRTM30m/LANDonly}$	-96.37	73.73	0.76	4.78	90.27

Tab. 5.3 compared $\delta g_{const}^{SRTM250m}$ the resulting RTM gravity disturbances with TGF and $\delta g_{ERTM2160}$ from the publicly available ERTM2160 model with EGM2008 and ground-truth gravity data. In calculations of $\delta g_{const}^{SRTM250m}$ and $\delta g_{ERTM2160}$, the same topography model (SRTM DEM at 250 m resolution) and a constant density assumption of $2,670 \text{ kg/m}^3$ were adopted. However, the residual mass-elements in the vicinity of each

calculation point were approximated by flat-topped prisms and point mass up to the distant in the calculation of the ERTM2160, while $\delta g_{const}^{SRTM250m}$ was calculated with TFG through a combination of polyhedron, prism, tesseroid and point mass from inner to distant zones. The descriptive statistics of the differences $\Delta\delta g_{ERTM2160}$ and $\Delta\delta g_{constant}^{SRTM250m}$ – between observed gravity, EGM2008 and the RTM variants $\delta g_{const}^{SRTM250m}$, and $\delta g_{ERTM2160}$ – showed that the computations $\delta g_{const}^{SRTM250m}$ with TGF were of somewhat higher quality than ERTM2160. This was seen from the smaller values of RMS of the differences with respect to the ground-truth data, e.g., 4.79 mGal instead of 4.97 mGal for $\Delta\delta g_{constant}^{SRTM250m}$. We attributed this behavior to the more detailed gravity forward modelling in the vicinity-zone when polyhedrons were used in the calculation of $\delta g_{const}^{SRTM250m}$, while prisms in the ERTM2160 computations. This is reasonable considering that polyhedron-discretization method provides a more realistic representation of surface topography especially over rugged terrain. Besides, the resolution of DEMs determines the level of detail of the surface being described, and thus influences the accuracy of the forward modeled gravity field generated by topography. Tab. 5.3 shows the reduction of RMS values of the differences with respect to ground gravity, when the inner-zone DEM resolution was increased to 90 m (4.71 mGal) and to 30 m (4.69 mGal). This demonstrated the effectiveness of higher resolution DEMs, especially 30 m DEM, in the creation of terrain gravity field. Additionally, considering the ocean masses effect implied in SRTM30plus does also make a great improvement of more than 0.3% in both cases of using constant density assumption and New Zealand density map, this is because SRTMplus30 bathymetry also carries short gravitational signals at spatial scales less than 5 arc minutes.

Numerical test, carried out at New Zealand (Tab. 5.3) with ground gravity measurements as references, demonstrated that the use of RTM modeled gravity disturbances significantly improves the accuracy of EGM2008 derived gravity disturbances by a rate of more than $\sim 70\%$. Totally, the estimated gravity disturbances through a combination of EGM2008 and RTM data considerably reduces the RMS values to the level of ~ 4.7 mGal, which equals to an improvement of $\sim 90\%$. As the resolution of the applied DEM increases, improvement rates rise from $\sim 90.26\%$ for 250 m SRTM DEM, to $\sim 90.42\%$ for 90 m SRTM DEM and $\sim 90.46\%$ for 30 m SRTM DEM.

Fig. 5.6 displays the observed gravity disturbances δg_{obs} in Panel (a), and magnitudes of the differences (Panel (d)) between two sets of residual gravity disturbances 1) $\Delta\delta g_{const}^{SRTM30m}$ (Panel (b)) under constant density assumption and 2) $\Delta\delta g_{density_map}^{SRTM30m}$ (Panel (c)) using mass-density map over the whole of the New Zealand. The residual gravity disturbances in both cases (Fig. 5.6(b), (c)) show similar patterns of significantly reduced signal amplitudes in comparison with the observed gravity disturbances in Fig. 5.6 (a). The use of mass-density map (Fig. 5.6 (c)) rather than the uniform rock-density assumption of $2,670 \text{ kg/m}^3$ (Fig. 5.6(b)) in the RTM gravity field modelling, increases the RMS value of residual gravity disturbance from 4.69 mGal for the constant density to 5.00 mGal for the mass-density map (see the descriptive statistics in Tab. 5.3). To further inspect this behavior, the differences between absolute values of two sets of residuals were calculated with Eq.(5.3).

$$z = | \Delta\delta g_{const}^{SRTM30m} | - | \Delta\delta g_{density_map}^{SRTM30m} | \quad (5.3)$$

The quantity z , which is shown in Fig. 5.6 (d), provides insights into the performance of the mass-density map in a comparative form. At individual field point, the quantity z gains a positive value (red color in Fig 5.6 (d)) when the use of the mass-density map yields smaller residuals with respect to those based on usually adopted uniform rock density, and a negative value (blue color in Fig. 5.6 (d)) at a point where constant density performs better than the mass-density map.

Considering the depth-dependent (5-10 m) geological units for the construction of the mass-density map, not all mass-density values provided by the map are representative for more substantial mass distributions underneath. Therefore, further experiments were carried out to investigate the correlation between residual heights and performance of mass-density map. As were shown in Figs. 5.7 and 5.8 – the residual heights (panel a) and quantity z (panel b) over the North (Fig. 5.7) and South Island (Fig. 5.8) – the quantity z is found to be strongly dependent on the roughness of residual terrain. The quantity z tends to be positive over areas with small residual heights, e.g., over volcanic and young sedimentary rocks of the North Island (Northland, Auckland, Coromandel, and Taranaki, and young sedimentary area along the North Island coast), and South Island (West Coast and Canterbury). Over these areas, the near-surface masses play a more dominant role in the forward modelling than deeper masses that are not included by the RTM heights. The RTM gravity signals retrieved with mass-density map yields a better agreement with the ground-truth data in comparison with the constant mass-density assumption, which could be seen from the reddish colors (Figs. 5.7 (b), 5.8 (b)). The mass-density map tends to be more representative for actual topographic density over areas with small residual heights.

However, over areas with large residual heights (few 100 m), e.g., over old and young sedimentary areas in North Island, along Alps Fault and Canterbury basaltic volcanic area in South Island, substantial subsurface mass variations come into play that are not necessarily represented in the mass-density map. They may significantly affect the quality (representativeness) of the mass-density map. Over these regions, RTM technique together with the use of the mass density map produces larger residuals than of using the uniform rock density value of $2,670 \text{ kg/m}^3$. The constant density assumption appears to be more representative than the mass-density map (blue color in Fig. 5.6 (d)). This behavior is most pronounced over the South Island Alps (compare bluish colors in Fig. 5.8(b)). These areas occupy almost half of the study area, so play an important role in the evaluation of the mass-density map.

Fig. 5.9 offers detailed views over parts of the South Island Alps, with residual heights at scattered points in panel (a), the $1'$ mass-density map over this test-area in (b), the residual gravity disturbances with the mass-density map in panel (c) and the quantity z in panel (d). The study area shown in Fig. 5.9 is divided by lakes (along the NE-SW diagonal) into two parts:

- 1) South-east areas with relative flat residual terrain: the mass-density map values over this area are mostly lower than $\sim 2,500 \text{ kg/m}^3$. The RTM technique together with mass-density map produces smaller residuals (blue color in Fig. 5.9 (d)) than using the constant mass-density of $2,670 \text{ kg/m}^3$. The mass-density map tends to be representative here.

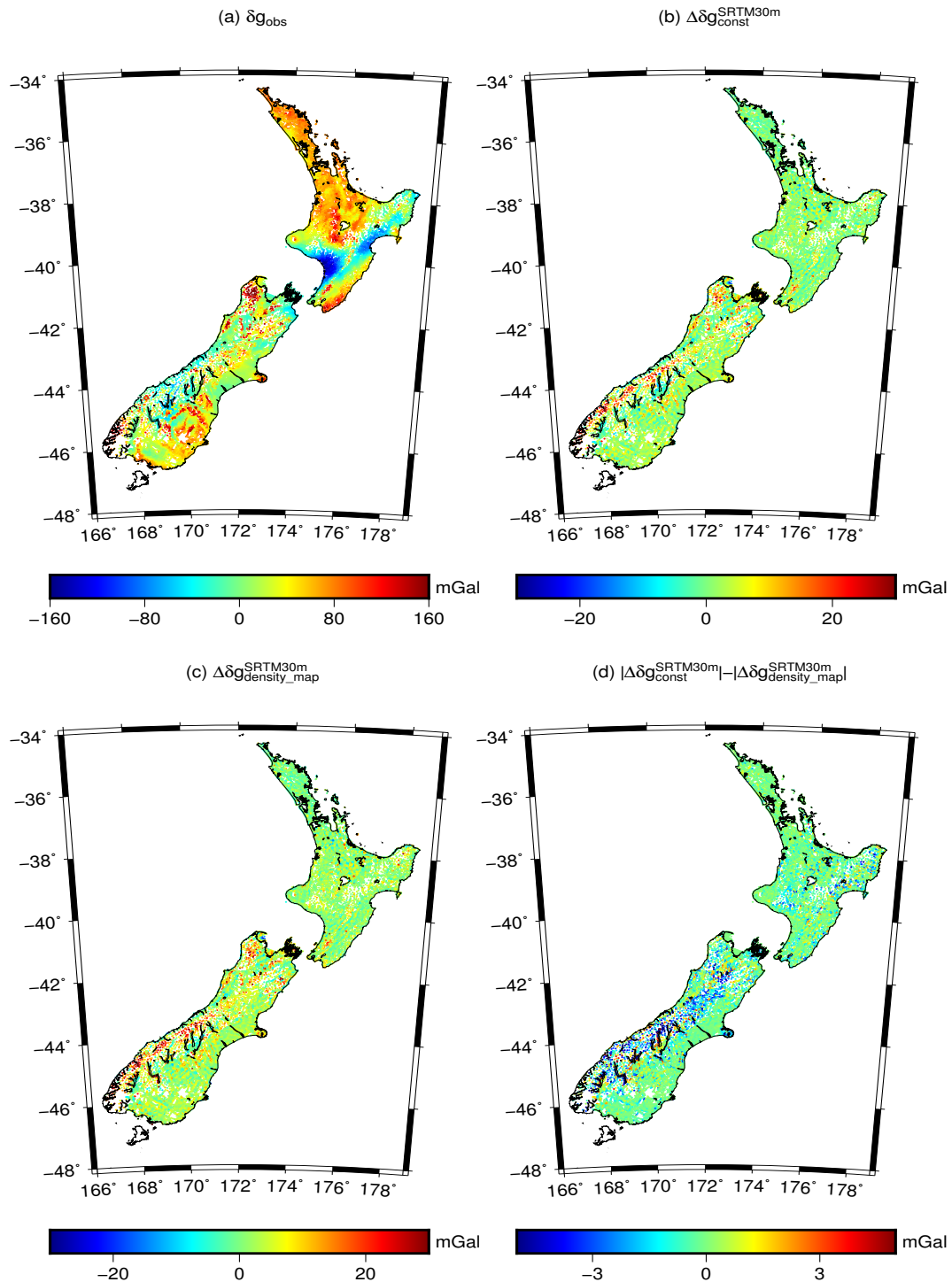


Fig. 5.6 – Gravity disturbances over New Zealand. Panel a: observed gravity disturbances (from the NZ gravity data base), panel b: residuals when subtracting EGM2008 gravity and RTM gravity based on a constant mass-density value, panel c: The same, but the RTM is based on the mass-density map, panel d: comparison between the residuals in panel b and c. In panel d, red indicates better performance of the mass-density map. All units in mGal.

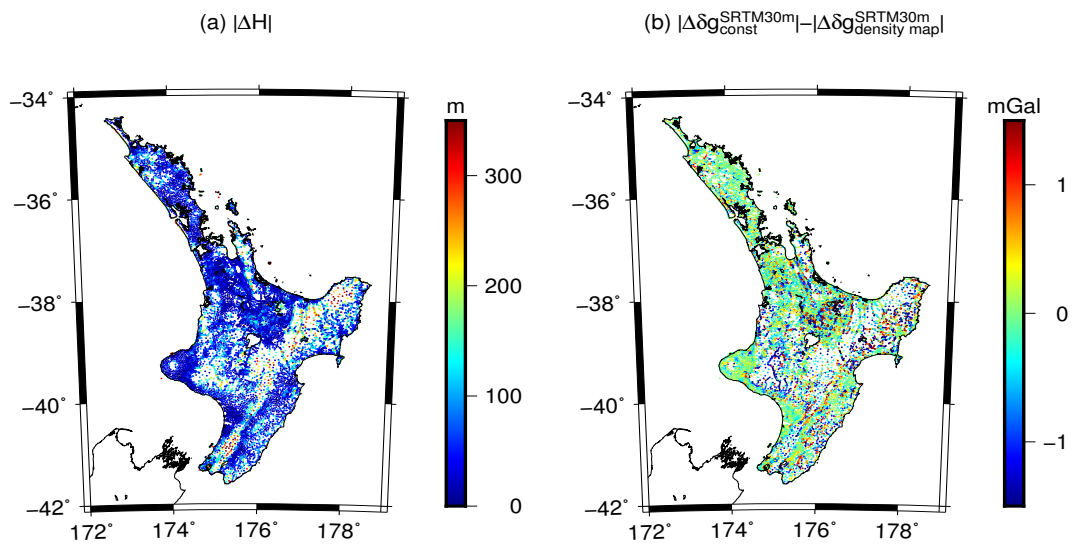


Fig. 5.7 – residual height and residual gravity disturbance comparison over the North Island. Panel a: residual height over North Island, units in meter; panel b: comparison between the residual gravity disturbances based on density map and constant density, units in mGal.

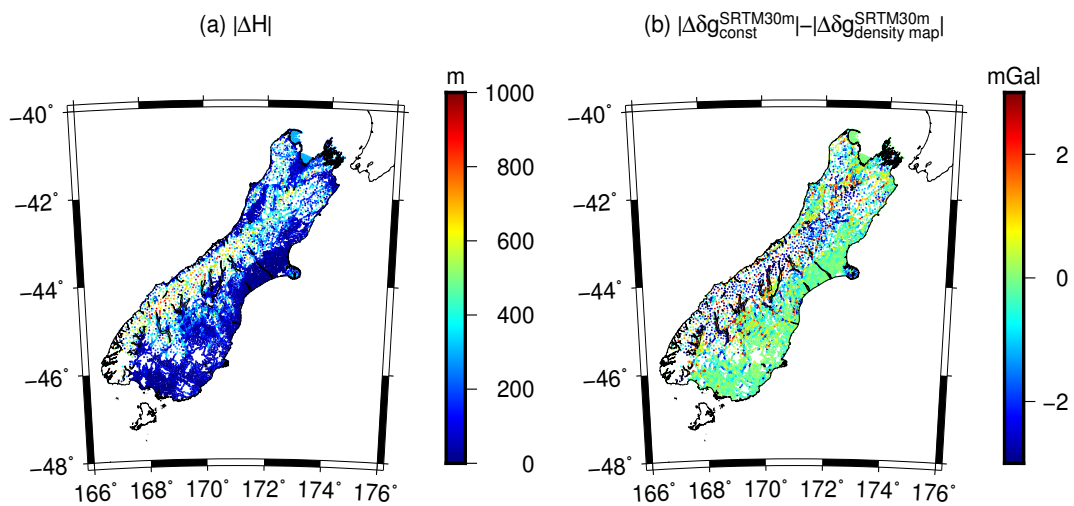


Fig. 5.8 – residual height and residual gravity disturbance comparison over the South Island. Panel a: residual height over South Island, units in meter; panel b: comparison between the residual gravity disturbances based on density map and constant density, units in mGal.

- 2) The north-western part with rugged residual terrain: the mass-density map values are $\sim 2,800 \text{ kg/m}^3$. At most points, the RTM technique together with mass-density map yields larger residuals (red color in Fig. 5.9 (d)) with respect to ground-truth data. This suggests that lower values than provided by the mass-density map are more representative here.

As is shown in Fig. 5.9, most of the ground-truth gravity measurements are carried out along roads. This behavior is reflected in gravity disturbance map as gravity signals along rivers which is usually narrow, steep and marked by sharp valleys over mountain areas. The sediment fillings in these valleys often have a substantially lower mass-density value than the metamorphic rocks. Limited by the coarse resolution of $1'$, these mass-density units along valleys are not able to be discriminated from the mass-density map, instead they are assigned values of $\sim 2,800 \text{ kg/m}^3$. As a result, the RTM modelling with the mass-density map produces larger discrepancies with respect to the ground-truth data than the lower uniform rock value of $2,670 \text{ kg/m}^3$ (seen by the red residuals of ground-stations arranged in river valleys, Fig. 5.9 (d)).

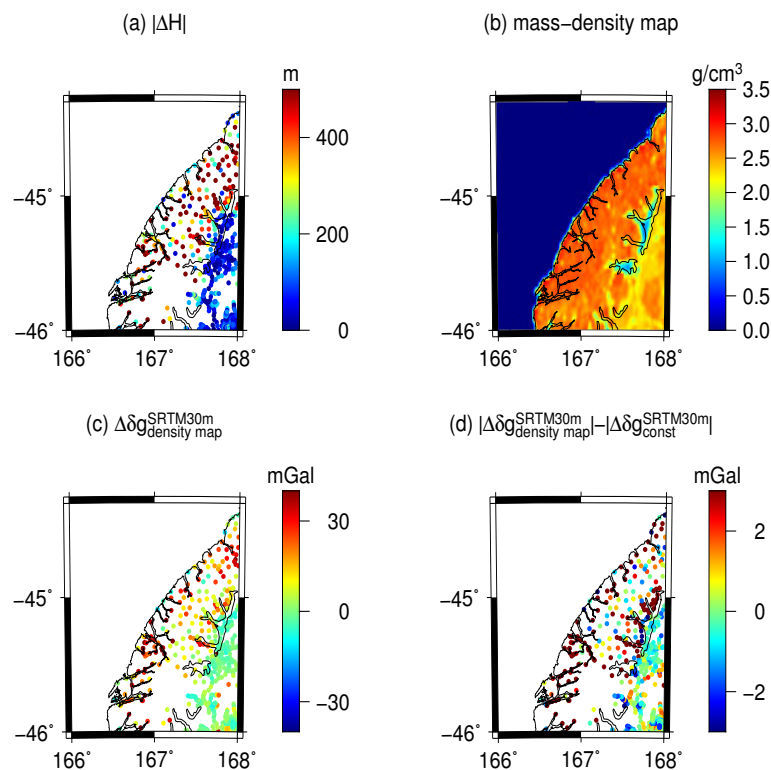


Fig. 5.9 – Heights, mass-densities, and gravity disturbances in South Alps Fault. Panel a: residual height in South Alps Fault, units in meter; panel b: density distribution in South Alps Fault from New Zealand density map, units in g/cm^3 ; panel c: residual gravity disturbance, RTM is based on the mass-density map, units in mGal; panel d: comparison between the residuals based on density map and constant density assumption, units in mGal.

Another set of detailed results is shown in Fig. 5.10 for parts of the South Island. Over the lake region South of Mount Cook, which is a typical area with sedimentary distribution, the mass-density map value is more representative for the actual density of topography, which is seen by the blue residuals (panel d). Opposed to this, the ground-stations with a poorer performance of the density map are mostly located in rough mountainous terrain (panel a and panel d).

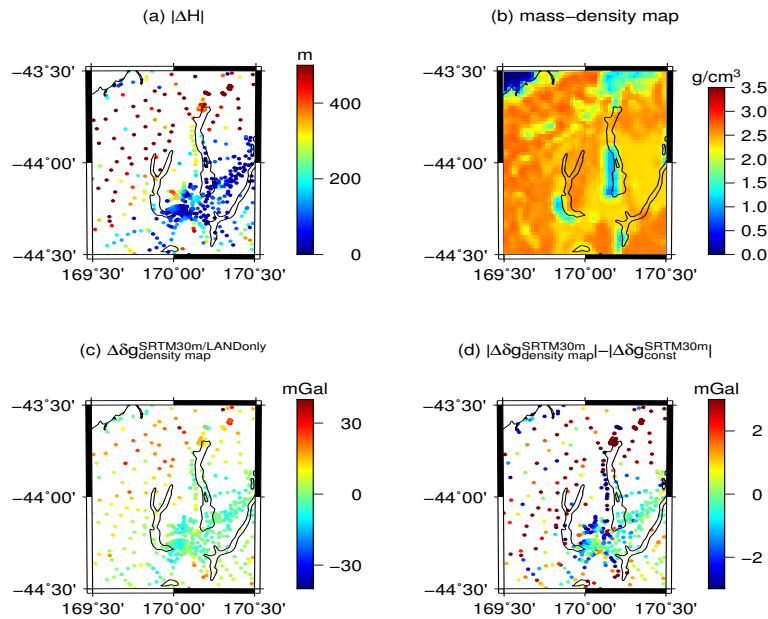


Fig. 5.10 – Heights, mass-densities and gravity disturbances along Mary Range. Panel a: residual height along Mary Range, units in meter; panel b: density distribution along Mary Range from New Zealand density map, units in g/cm^3 ; panel c: residual gravity disturbance, RTM is based on the mass-density map, units in mGal; panel d: comparison between the residuals based on density map and constant density assumption, units in mGal.

Further experiments were carried out to test the performance of the mass-density map in the calculation of RTM geoid heights. Residual geoid heights $\zeta_{ERTM2160}$ interpolated from ERTM2160 and quasi-geoid heights calculated with a GPS/levelling dataset provide reference values for such validations. First, RTM quasi-geoid heights at 3,609 GPS/levelling points were calculated with the mass-density map $\zeta_{density_map}^{SRTM30m}$ and the uniform density value of $2,670 \text{ kg}/\text{m}^3$ $\zeta_{const}^{SRTM30m}$ separately.

Tab. 5.4 provides the descriptive statistics of RTM quasigeoid heights of ERTM2160, TGF results with density map and uniform density, and their comparison. It is seen that the TGF calculated RTM quasi-geoid heights ($\zeta_{const}^{SRTM30m}$) with uniform rock density yields smaller residuals compared to the ERTM2160 quasi-geoid heights ($\zeta_{ERTM2160}$), with a maximum of ~ 2 cm a mean difference of -0.1 cm and RMS of ~ 0.51 cm. Compared to quasi-geoid heights based on constant density, much larger differences are expected when using the density map, with the largest differences of ~ 12 cm, mean of ~ -1.96 cm and RMS of ~ 2.58 cm. This is caused by the fact that the constant density assumption of $2,670 \text{ kg}/\text{m}^3$ was applied in the calculation of $\zeta_{const}^{SRTM30m}$ and $\zeta_{ERTM2160}$, while mass-density map for $\zeta_{density_map}^{SRTM30m}$. The differences between $\zeta_{const}^{SRTM30m}$ and $\zeta_{ERTM2160}$ are varying within ~ 2 cm with a RMS value of ~ 0.51 cm. They show that promising accuracy can be achieved with TGF for residual geoid height computations (Tab. 5.4).

Quasi-geoid heights determined from 1,272 of 3,609 GPS/levelling measurements with GPS heights in order of 1,2,3,4, serve as 'benchmark' for validation of RTM modeled quasi-geoid height with mass-density map. Two sets of RTM quasi-geoid heights $\zeta_{const}^{SRTM30m}$ and $\zeta_{density_map}^{SRTM30m}$ at 1,272 stations were computed and added to the EGM2008 quasi-geoid, the sum was then compared with the 1,272 height anomalies derived from

GPS/levelling. However, GPS/levelling measurements located in the 13 different local vertical datums (LVDs). Therefore, LVD unification is required before validation.

Tab. 5.4 – Descriptive statistics of calculated RTM quasi-geoid heights at 3609 GPS/levelling points

Geoid height	min (cm)	max (cm)	mean (cm)	RMS (cm)
$\zeta_{ERTM2160}$	-12.28	5.51	-0.82	1.95
$\zeta_{const}^{SRTM30m}$	-12.55	5.27	-0.92	2.09
$\zeta_{density_map}^{SRTM30m}$	-6.38	9.71	1.15	2.09
$\zeta_{const}^{SRTM30m} - \zeta_{ERTM2160}$	-2.07	1.48	-0.10	0.51
$\zeta_{density_map}^{SRTM30m} - \zeta_{ERTM2160}$	-1.34	11.32	-1.96	2.58
$\zeta_{const}^{SRTM30m} - \zeta_{density_map}^{SRTM30m}$	-11.09	-0.03	-2.06	2.56

The vertical datum offsets, as is seen in Tab. 5.5, were applied to reduce the effect of different offsets on the statistics. Three sets of LVD offsets were calculated based on various methods. *Claessens et al* (2009) calculated a set of offsets for each local vertical datum based on the iterative method, which is shown in the column 'Iteration 3'. Offsets given in column 'Relative to NZVD2016' were determined as the differences of published reference mark height in the local datum and New Zealand vertical datum (NZVD2016). In the column 'Relative to EGM2008', the LVDs offsets were obtained by calculating the mean of the GGM height anomalies and GPS/levelling height anomalies in each LVD. The differences of LVDs offsets obtained based on different methods vary from several cm to more than 10 cm.

In the following validation, vertical datum unification of GPS/levelling measurements collected at 13 LVDs were firstly carried out with the LVD offsets based on the values given by column 'Relative to NZVD2016'. The height anomalies determined from GPS/levelling measurements provide a reference for validation of RTM geoid heights based on various mass-density assumptions. The comparison results are shown in Tab. 5.6 and Fig. 5.11. After datum unification, the differences between height anomalies derived from GPS/levelling and from EGM2008 vary from -46.04 cm to 58.43 cm, with mean of the differences 2.34 cm and std of 13.51 cm. No improvement is gained after removing RTM quasi-geoid calculated with constant density assumption. This is seen from the larger mean (3.05 cm) and RMS (13.64 cm) values of the differences. However, the combined height anomaly of RTM quasi-geoid with the mass-density map and EGM2008 quasi-geoid achieves a better agreement with GPS/levelling derived height anomalies, seen from smaller mean (1.07 cm) and lower RMS (12.98 cm). When the other sets of LVD offsets are used, in each case the smallest RMS values are obtained when the mass-density map is used, showing the results to be independent of the choice of LVD offsets from Tab. 5.6.

Detailed validation results for all station are shown in Fig. 5.11. The large positive differences were found to occur at GPS/levelling stations, e.g., over geologically younger sedimentary rocks of the North Island, and

points located along the west coast, and rivers of the South Island, where the density map values give a better representation of the actual density. This is consistent with what we learned from the gravity disturbance experiments.

Tab. 5.5 – LVD offsets obtained based on different methods [Units: m]

LVDs	Iteration 3 from Claessens et al. 2011	Relative to NZVD2016	Relative to EGM2008
One three point	-0.063	-0.085	-0.12
Auckland	-0.339	-0.367	-0.354
Moturiki	-0.241	-0.199	-0.288
Gisborne	-0.344	-0.338	-0.371
Taranaki	-0.315	-0.298	-0.315
Napier	-0.203	-0.193	-0.190
Wellington	-0.436	-0.388	-0.435
Nelson	-0.294	-0.329	-0.267
Lyttelton	-0.466	-0.389	-0.300
Dunedin	-0.485	-0.377	-0.215
Dunedin-Bluff	-0.381	-0.318	-0.175
Bluff	-0.360	-0.314	-0.234

Tab. 5.6 – Descriptive statistics of residual height anomaly. where: $\Delta\zeta_{const}^{SRTM30m} = \zeta_{GPS/levelling} - \zeta_{EGM2008} - \zeta_{const}^{SRTM30m}$, $\Delta\zeta_{densitymap}^{SRTM30m} = \zeta_{GPS/levelling} - \zeta_{EGM2008} - \zeta_{densitymap}^{SRTM30m}$

Geoid heights	min(cm)	max(cm)	mean(cm)	std(cm)	rms(cm)
$\zeta_{GPS/levelling}$	387.20	3944.80	1738.64	1007.88	2009.45
$\zeta_{GPS/levelling} - \zeta_{EGM2008}$	-46.04	58.43	2.34	13.51	13.71
$\Delta\zeta_{const}^{SRTM30m}$	-46.74	59.81	3.05	13.64	13.98
$\Delta\zeta_{densitymap}^{SRTM30m}$	-48.11	57.54	1.07	12.98	13.02
$ \Delta\zeta_{const}^{SRTM30m} - \Delta\zeta_{densitymap}^{SRTM30m} $	-3.75	10.62	0.60	2.30	2.37

Another contribution of this work is the determination of local/regional optimum constant density at New Zealand. Because the topographic mass-density normally varies within a range of reasonable bounds (e.g.,

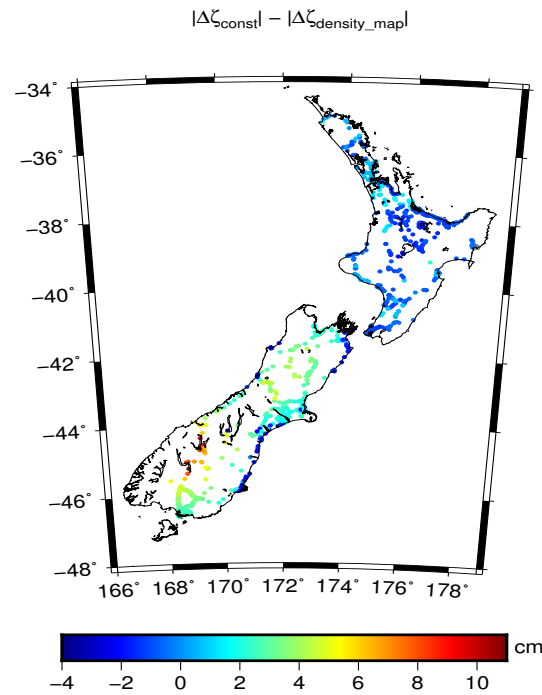


Fig. 5.11 – Comparison between the residual height anomalies based on constant density $\Delta\zeta_{const}^{SRTM30m}$ and density map $\Delta\zeta_{densitymap}^{SRTM30m}$. Units in cm. Higher values indicate better performance of the mass-density map.

2,300 to 3,300 kg/m^3), the density assumption of 2,670 kg/m^3 may not an optimum choice for regional research. For example, when the New Zealand digital density map is used to determine regional mean densities, values of 2,336 kg/m^3 for the North Island, 2,514 kg/m^3 for the South Island, and 2,440 kg/m^3 for the whole New Zealand are obtained. These three mean density values are found to be smaller than the conventionally used 2,670 kg/m^3 . In the regional gravity field modeling, the generally used mass-density approximation of 2,670 kg/m^3 , may introduce errors in the calculated RTM gravity disturbances where the actual mass-density deviates from the adopted value. In this work, the local/regional optimum constant density values are detected for RTM masses over North and South Islands at New Zealand through the analysis of residual gravity signals (after removing RTM augmented EGM2008 gravity field from ground observations). By systematically varying the topographic mass-density within 2,300 ~ 3,300 kg/m^3 , the resulting RMS signal strength of the residual gravity signals can be minimized, and thus used as a means to detect the optimum regional mass-density value that is a better approximation than the conventional value of 2,670 kg/m^3 .

The residual gravity disturbances were calculated with constant density values varying from 2,300 kg/m^3 to 3,300 kg/m^3 using increments of 10 kg/m^3 over North Island, South Island and entire New Zealand. Results are shown in Fig. 5.12 with the computed RMS values of residual gravity disturbance as a function of adopted mass-density values over North Island (panel a), South Island (panel b) and the entire New Zealand (panel c). The blue line indicates that all masses (including ocean and land masses) around the calculation point are included in the numerical integration, while only continental masses are considered for green line. As is shown in Fig. 5.12, all RMS values show the same general behaviors that the RMS values first decline and then increase, and reach their minimum value at what we named optimum mass-density here.

By including high-frequency gravitational signals generated by ocean masses, RTM signals were significantly improved especially over coastal areas. This was demonstrated by smaller RMS values in the three study areas.

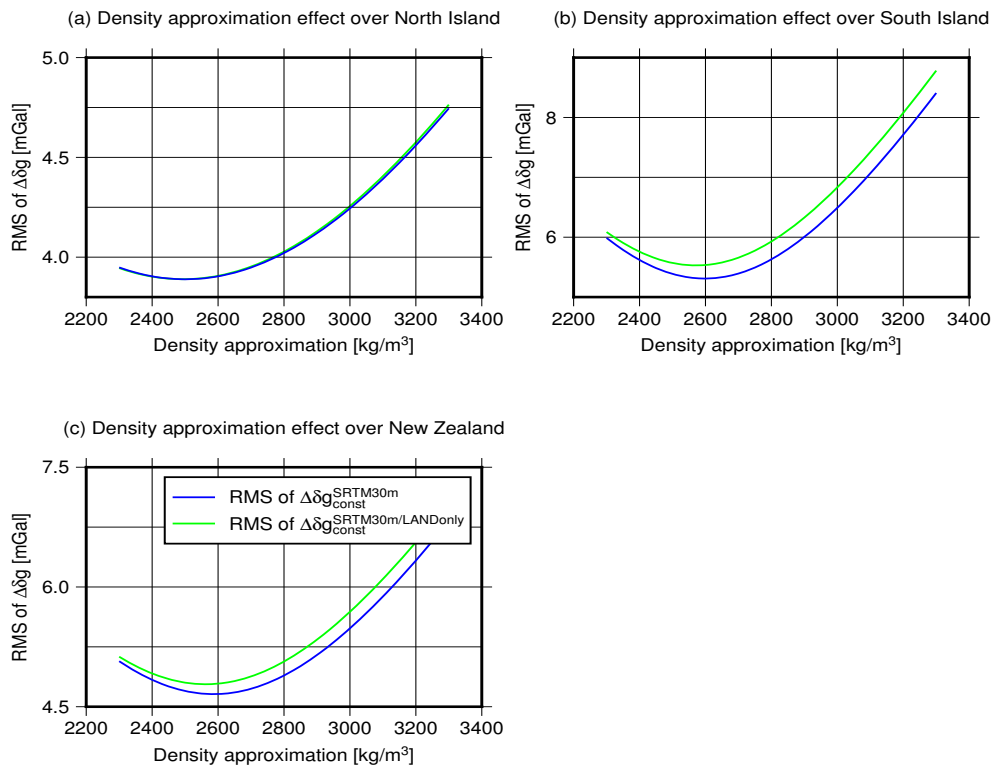


Fig. 5.12 – Results of the density optimization test. Panel a: RMS of residual gravity disturbances, the RTM is based on the density approximation from $2300\text{kg}/\text{m}^3$ to $3300\text{kg}/\text{m}^3$ over North Island; panel b: the same with panel a, but the test area is addressed over South Island; panel c: the same, but the test area is located in the whole New Zealand. The all units are in mGal. Blue line means the masses for RTM include both ocean and land masses within the integral radius, the RMS represented by green line just considered the effect of land masses.

Tab. 5.7 gives the detected optimum densities for North Island with a value of $2,500\text{kg}/\text{m}^3$, for South Island a value of $2,600\text{kg}/\text{m}^3$, and for the whole country a density value of $2,590\text{kg}/\text{m}^3$. In all cases, the detected optimum density values are smaller than generally used $2,670\text{kg}/\text{m}^3$. This could be attributed to large areas of New Zealand overlapped with “Cenozoic, particularly Quaternary, sedimentary and pyroclastic volcanic deposits” (Tenzler *et al* (2011)). Additionally, the geologically younger age of the North Island explains the reason for the lower optimum density of the North Island. Using the optimum density value $2,590\text{kg}/\text{m}^3$ for the evaluation of RTM gravity disturbances over the whole of New Zealand, the combined model of EGM2008 and RTM gravity disturbances explains $\sim 90\%$ of the gravity signals, with an RMS values of the residual signals of 4.65 mGal (Tab. 5.7). It corresponds to an improvement of $\sim 1\%$ in terms of RMS in comparison to results based on the standard density value of $2,670\text{kg}/\text{m}^3$, cf. Tab. 5.7. The absolute differences between residual gravity disturbances computed from density approximation of $2,670\text{kg}/\text{m}^3$ and optimum density values, range from $\sim -9.69\text{mGal}$ to $\sim 4.18\text{mGal}$ with an RMS of the differences of $\sim 0.58\text{mGal}$ for the North Island, and vary from $\sim -6.44\text{mGal}$ to $\sim 4.16\text{mGal}$ for South Island with an RMS value of $\sim 0.90\text{mGal}$ (Tab. 5.8).

The regional mean density values suggested by the New Zealand mass-density map – 2,336 kg/m^3 for North Island, 2,514 kg/m^3 for South Island, and 2,440 kg/m^3 for the whole New Zealand – are lower by 164 kg/m^3 for North Island, 86 kg/m^3 for South Island, and 150 kg/m^3 for the entire New Zealand than the detected optimum densities shown in Fig. 5.12 and Tab. 5.7. To some extent, this is caused by the inhomogeneous distribution of ground gravity observations. For example, mass-density over lakes and glaciers is assigned with different values in two cases, the density of 920 and 1000 kg/m^3 are used for ice and water in the mass-density map, while the optimum density is detected based on a combination of RTM technique together with ground gravity observations. Sparse coverage of ground-truth stations in areas of lower densities (e.g., over lakes and glaciers) attributes the higher values to the optimum densities. Besides, another reason for higher values of the optimum densities would be that the subsurface density effect comes into play over areas with large residual heights. The New Zealand mass-density model was constructed mainly based on the shallow (5-10 m) geological units and measurements. Therefore, not all mass-density map values are representative for the deeper mass inhomogeneities underneath, especially in mountain regions where density could change significantly with depth. In such areas, the optimum density including the effects of deeper density variance would perform better. The greater value of optimum density might suggest the fact that the density value increases with crustal depth. The difference between residual gravity disturbances computed from optimum density and mass-density reaches a maximum value of ~ 31.32 mGal (Tab. 5.8) at Alpine Fault area. This suggests that the effect of deeper sedimentary would reach about 30 mGal (Tab. 5.8). Therefore, in order to obtain a high-quality RTM, a higher-quality 3-D density model is required.

Tab. 5.7 – Optimum density and RMS

	Density [kg/m^3]	RMS[mGal]	Optimum Density [kg/m^3]	RMS[mGal]
With land and ocean effect				
North Island	2670	3.93	2500	3.88
South Island	2670	5.35	2600	5.31
New Zealand	2670	4.69	2590	4.65
With land effect				
North Island	2670	3.93	2490	3.88
South Island	2670	5.60	2560	5.52
New Zealand	2670	4.84	2570	4.78

Tab. 5.8 – Optimum density and RMS

	min[mGal]	max[mGal]	mean[mGal]	RMS[mGal]
North Island				
$ \Delta\delta g_{optimum}^{SRTM30m} - \Delta\delta g_{const}^{SRTM30m} $	-9.69	4.18	-0.03	0.58
$ \Delta\delta g_{optimum}^{SRTM30m} - \Delta\delta g_{density_map}^{SRTM30m} $	-15.38	6.21	-0.14	1.06
$ \Delta\delta g_{const}^{SRTM30m} - \Delta\delta g_{density_map}^{SRTM30m} $	-17.09	6.21	-0.11	0.80
South Island				
$ \Delta\delta g_{optimum}^{SRTM30m} - \Delta\delta g_{const}^{SRTM30m} $	-6.44	4.16	-0.01	0.90
$ \Delta\delta g_{optimum}^{SRTM30m} - \Delta\delta g_{density_map}^{SRTM30m} $	-31.32	24.19	-0.30	2.44
$ \Delta\delta g_{const}^{SRTM30m} - \Delta\delta g_{density_map}^{SRTM30m} $	-28.56	20.96	-0.29	1.99

5.2.2 DEM errors

This work has been published in Geophysical Journal International, “Yang, M., Hirt, C., Rexer, M., Pail, R., Yamazaki, D., 2019. The tree-canopy effect in gravity forward modelling, Geophysical Journal International, 219 (1), October 2019, P 271–289, doi: <https://doi.org/10.1093/gji/ggz264>.”, available at <https://academic.oup.com/gji/article-abstract/219/1/271/5512594>.

High resolution and accurate DEMs are frequently adopted as input data sets to define the topographic geometries in the gravity forward modeling, e.g., for terrain corrections in the context of boundary value problems. For global and continental-wide gravity forward modeling, publicly available DEMs are mostly based on 1) radar interferometry (e.g., SRTM DEMs (Farr et al (2007)) or TanDEM-X DEM (Wessel et al (2018))), or 2) optical image observations (e.g., ALOS AW3D DEM (Tadono et al (2014)) or ASTER DEM (Tachikawa (2001))). Over vegetated areas such as forests and scrublands, the 1) image-based DEMs which measures the top surface of the Earth denoted as DSM and 2) radar-based DEMs which measures the surface between DSM and DTM denoted mixed-DSM/DTM here, do not represent the bare-ground surface, instead contain a tree bias. The presence of vegetation-induced signals in DEMs, denoted here the tree canopy effect, will introduce errors in the forward modeled gravity field. Fig. 5.13 shows the definitions of topographic and residual masses in the frameworks of DTM-based forward modeling and mixed-DSM/DTM-based forward modeling, with calculation points P_1 located at the area without vegetation coverage, and P_2 over vegetated area:

- DTM-based forward modelling: in the framework of DTM-based forward modelling, the integration masses are bounded by the mean sea level (MSL) and the DTM surface for the topographic gravitational field calculations, and the smoothed reference surface and DTM surface for the RTM gravitational field evaluations. The long-wavelength reference surface was derived directly from the detailed DTM through a

surface filtering and spherical harmonic analysis. The evaluation points P_1 and P_2 reside on surface of DTM with evaluation heights of $H_{p_1}^{DTM}$ and $H_{p_2}^{DTM}$.

- mixed-DSM/DTM-based forward modeling: in the framework of mixed-DSM/DTM-based forward modeling, the evaluation points reside on the surface of mixed-DSM/DTM and the integration masses are defined between mixed-DSM/DTM surface and the MSL for full-scale topographic gravity field evaluation, and between mixed-DSM/DTM surface and a reference surface directly derived from this mixed-DSM/DTM model in the RTM gravity field calculations.

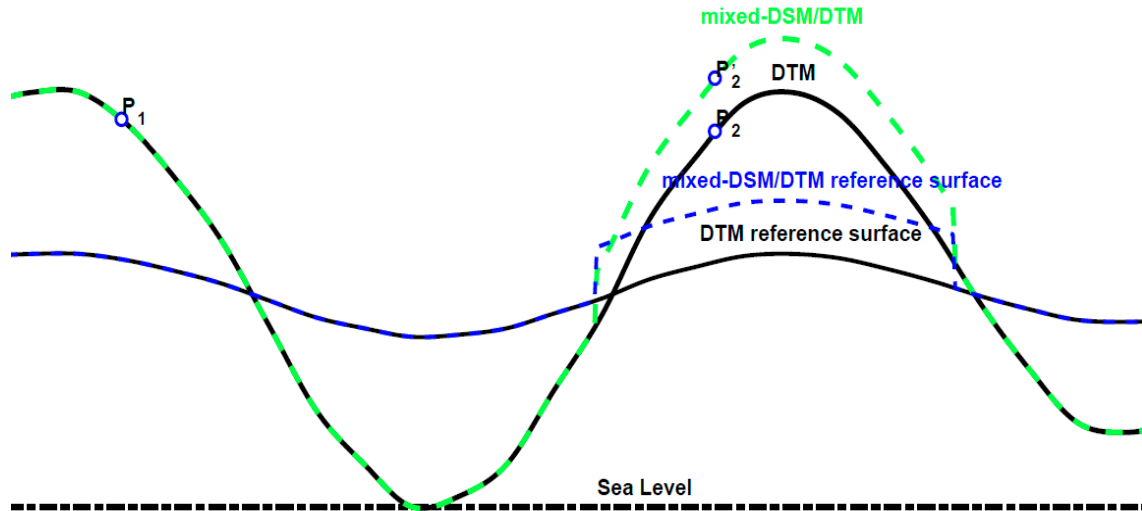


Fig. 5.13 – Tree canopy effect in forward modelling procedure. The green dashed line represents the DSM surface, the black line is the DTM surface, their differences indicate the tree bias; The blue dashed line represents the smooth surface computed directly from DSM, while the fine black line is the DTM smooth reference surface; and the black dashed line stands for the sea level.

For evaluation points located on the Earth's surface where there is no vegetation coverage around this point, like point P_1 , the evaluation heights of P_1 are the same in the frameworks of mixed-DSM/DTM-based and of DTM-based forward modeling with $H_{p_1}^{DTM} = H_{p_1}^{mixed-DSM/DTM}$. The issue for integration masses however depends on the integration radius. If the masses to be integrated are confined to the distance with no vegetation coverage, the boundaries over all integration mass-elements therefore fulfill the equations $H_{fine}^{DTM} = H_{fine}^{mixed-DSM/DTM}$, and $H_{smooth}^{DTM} = H_{smooth}^{mixed-DSM/DTM}$. In such case, the forward modeled gravity quantities over point P_1 are identical in the mixed-DSM/DTM-based forward modeling and the DTM-based forward modeling. When the integration masses extend to the distance with vegetation coverage, the boundary-elevation of integration mass-elements would be different in mixed-DSM/DTM and DTM over vegetated points. Therefore, the forward-modeled gravitational fields would be different in that case.

When the evaluation points are located in a vegetated area, like point P_2 , the tree bias (the difference between the mixed-DSM/DTM and DTM) appears to influence 1) the height of the evaluation point and, more importantly, 2) the topographic mass density distribution in the vicinity of the evaluation point. When an elevation model with tree height biases (such as SRTM) is used instead of a bare-ground model (DTM), the elevation is changed from $H_{p_2}^{DTM}$ to $H_{p_2}^{mixed-DSM/DTM}$ in radial direction with $H_{p_2}^{DTM} = H_{p_2}^{mixed-DSM/DTM} - H_{p_2}^{tree_bias}$,

and additional topographic masses with thick of tree bias are present. For RTM gravitational field modeling, this effect is somewhat mitigated because the long-wavelength part of the tree-height bias is “absorbed” by the reference surface.

The role of the tree canopy in gravity forward modeling calculations is numerically investigated from two aspects:

- (1) Globally, the spectral forward modeling techniques were applied to analyze a 1 km global tree canopy bias model and to quantify its effect on global gravity forward modeling results, full-scale topographic gravitational fields and high-frequency gravitational fields.
- (2) Regionally, the role of the tree canopy effect in high-frequency gravity forward modeling was further studied based on the well-known RTM techniques in the spatial domain. The tree-bias effect was comparison results of SRTM-based forward modeling and results of MERIT-based forward modeling.

Global numerical results

Fig. 5.14 gives the workflow of SGM about the tree-bias effect on full-scale and high-frequency gravitational field modeling. In the global experiments, the MERIT bare-ground topography and a tree-bias map in 30'' grid are the main input data sets. The 3'' MERIT bare-ground topography was firstly down-sampled to 30'' H_{de_MERIT} , before adding the tree bias to rebuild the canopy effected MERIT topography H_{re_MERIT} . The attraction due to a layer with bottom surface equal to $S = \{H_{de_MERIT}\}$ and a tree-effected surface $S = \{H_{re_MERIT}\}$ is evaluated through surface spherical harmonic analysis (SHA) technique. The surface SHCs of topography height H_{de_MERIT} and H_{re_MERIT} over power $k = 1, \dots, 5$ are computed from:

$$\begin{aligned}\bar{H}_{knm}^{re_MERIT} &= \frac{\rho}{4\pi} \int_{\varphi} \int_{\lambda} \left(\frac{H_{re_MERIT}}{R} \right)^k \bar{Y}_{nm}(\varphi_Q, \lambda_Q) \sin \varphi d\varphi d\lambda, \\ \bar{H}_{knm}^{de_MERIT} &= \frac{\rho}{4\pi} \int_{\varphi} \int_{\lambda} \left(\frac{H_{de_MERIT}}{R} \right)^k \bar{Y}_{nm}(\varphi_Q, \lambda_Q) \sin \varphi d\varphi d\lambda\end{aligned}\quad (5.4)$$

In this study, spherical approximation with a sphere radius of $R = 6,378,137$ m, and mass $M = 5.972581E24$ kg are adopted. All SHCs are expanded to degree and order of 21,600. The topography implied full-scale topographic potential $\bar{V}_{nm}^{de_MERIT}$ and $\bar{V}_{nm}^{re_MERIT}$ are then obtained following the equation (2.31). The surface SHCs of the tree bias implied topographic potential is the difference between $\bar{V}_{knm}^{de_MERIT}$ and $\bar{V}_{knm}^{re_MERIT}$:

$$\bar{V}_{nm} = \bar{V}_{nm}^{de_MERIT} - \bar{V}_{nm}^{re_MERIT}\quad (5.5)$$

Fig. 5.15 (a) for \bar{V}_{nm} shows the tree-bias effect on the full-scale topographic gravitational potential implied by \bar{H}_{knm} (with $k = 1, 2, \dots, 5$) in terms of degree variances of surface harmonic coefficients. Due to the comparatively small signal magnitude of the tree-bias, their implied gravitational potential converges fast in higher powers. To calculate the tree-bias implied gravitational field, integer power to the 5th order were more than enough in this work. For the synthesis of \bar{V}_{nm} implied gravity disturbances, the \bar{V}_{nm} coefficients expanded to degree and order of 21,600 were synthesized using the Matlab-based isGraflab (Bucha and Janák (2014)) program

software. Fig. 5.16 (a) shows the tree bias effect in topographic gravitational field $\delta g_{TOP}^{tree\ bias}$ at 1 km resolution global grids. All calculation points reside at the surface of tree-bias. Compared to the terrain masses represented by DTM, more masses are involved in mixed-DSM/DTM based terrain mass-modelling. This behavior is reflected by the positive values of $\delta g_{TOP}^{tree\ bias}$ shown in Fig. 5.16 (a). The tree-bias implied topographic gravity disturbances vary from ~ 0 to ~ 2.68 mGal over continental vegetated areas. The large values are mainly distributed around the broad-leaved forest (e.g. tropical rainforest area) and needle-leaved forest (e.g. continent around $60^\circ N$ in latitude). Depending on the distribution of the forest, the tree-bias effect tends to be a regional long-wavelength signal in the forwarded full-scale gravitational field.

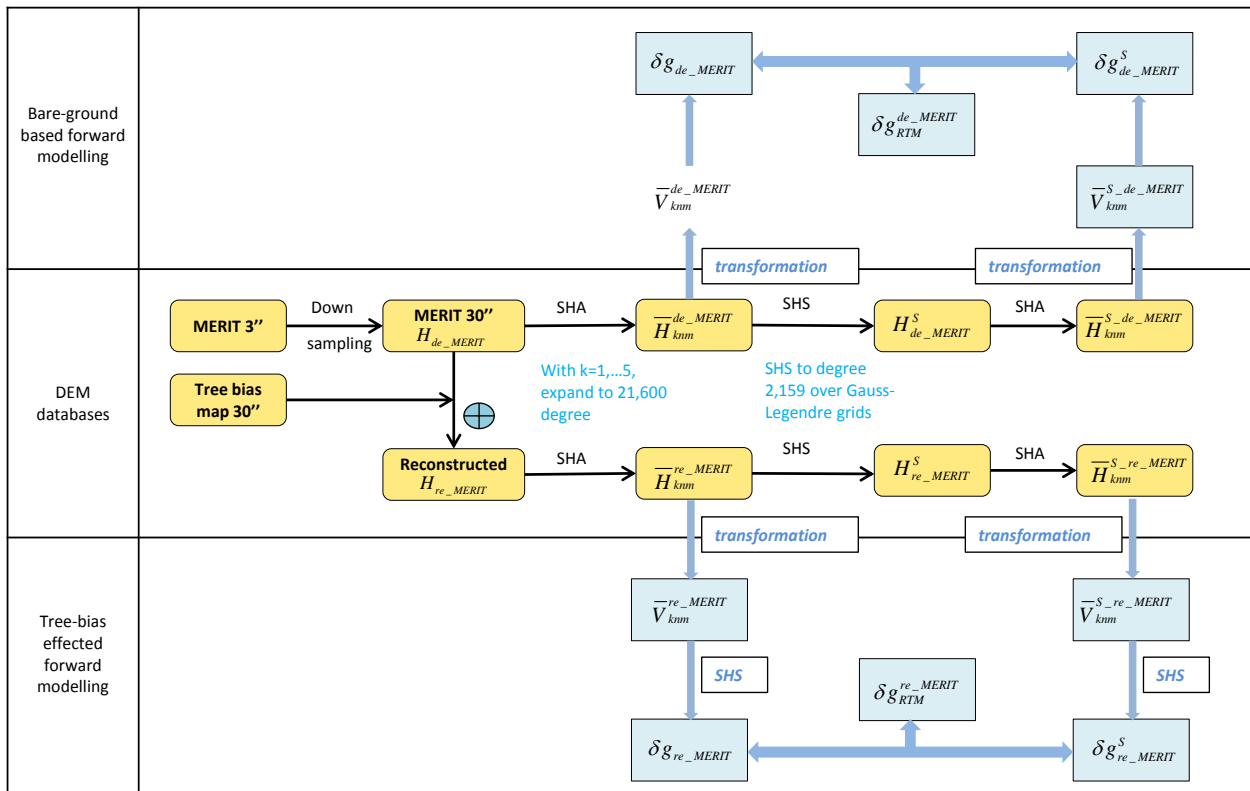


Fig. 5.14 – Flowchart for SFM in global tree bias effect study.

As for the RTM-based experiments, the tree bias affected RTM gravitational signals provide the high-frequency information implied by a high-pass filtered tree canopy bias model. The tree bias effect on the reference topography and its implied gravitational field were firstly computed. To keep consistency with studies in the regional area, the reference surface is defined to hold the same resolution with EGM2008 with SHCs extending to degree and order of 2,159. The long-wavelength tree biases $H_{de_MERIT}^S$ and $H_{re_MERIT}^S$ over Gauss-Legendre grid (Rexer and Hirt 2015) were respectively computed through the spherical harmonic synthesis (SHS) of $\bar{H}_{knm}^{de_MERIT}$ and $\bar{H}_{knm}^{re_MERIT}$ to the maximum degree of 2,159. As mentioned before, smoothed

topographic height functions $(\frac{H_{de_MERIT}^S}{R})^k$ and $(\frac{H_{re_MERIT}^S}{R})^k$ of integer power $k = 1, \dots, 5$ were formed and expanded into SHCs $\bar{H}_{knm}^{S_de_MERIT}$ and $\bar{H}_{knm}^{S_re_MERIT}$. The tree bias effect on the reference potential \bar{V}_{nm}^S is then obtained following the Eq. (2.30). Removing this long-wavelength signal \bar{V}_{nm}^S , which was displayed in Fig. 5.15 (b), from tree bias implied topographic gravitational field \bar{V}_{nm} , the tree bias effect on RTM gravitational signals \bar{V}_{nm}^{RTM} was obtained. The solid harmonic coefficients \bar{V}_{nm}^{RTM} with composite contributions of $k \leq 5$ were expanded to the degree of 21,600. Using isGraflab (*Bucha and Janák (2014)*) program software, the tree-bias implied RTM gravity disturbances were synthesized from \bar{V}_{nm}^{RTM} . The calculation points resided on the surface of residual tree-bias and homogeneously distributed over the entire globe at the resolution of $1'$.

The computed results are shown in Fig. 5.16 (b). Compared to full-scale tree-bias effect in Fig. 5.16 (a), the value of the residual tree height effect in RTM gravity disturbances is considerably reduced, with values varying within 2 mGal. Removing the long-wavelength gravity disturbances implied by $H_{de_MERIT}^S$ and $H_{re_MERIT}^S$, the residual tree bias implied RTM gravity disturbances $\delta g_{RTM}^{tree_bias}$ is of high-frequency nature. The harmonic band consists of degrees 2,160 to 21,600, i.e. it contains signals at scales finer than $5'$ but coarser than $30''$. It is obvious in Fig. 5.16 (b) that amplitudes are largest mostly along the boundaries of forest regions, such as the rainforest areas over Amazon, Indonesia (Fig. 5.17 (a) and (c)) and Africa (Fig. 5.17 (b) and (d)).

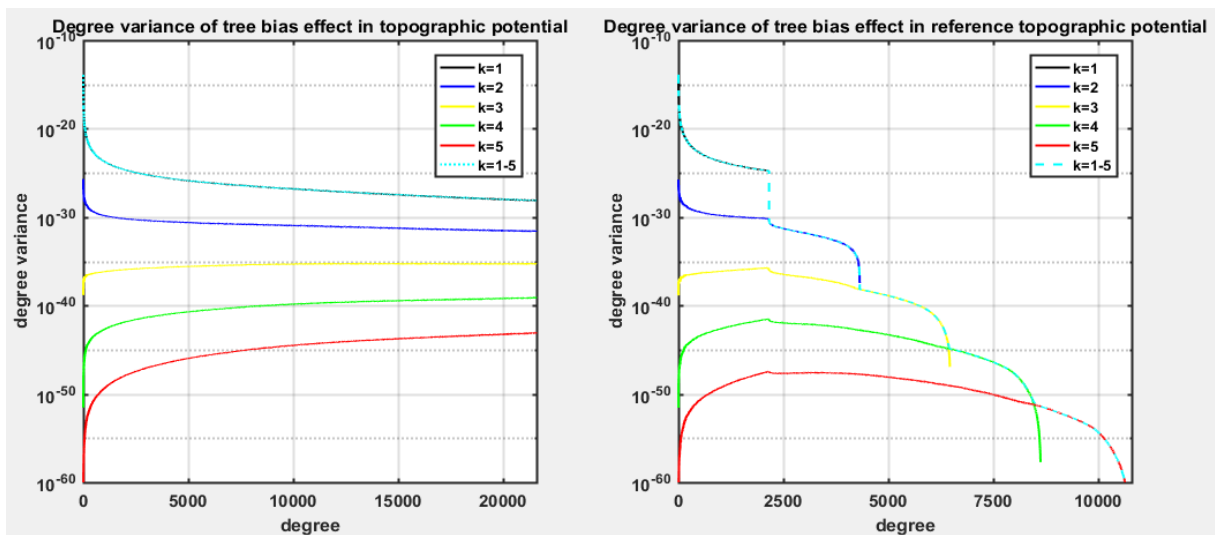


Fig. 5.15 – Degree variances of the tree bias implied topographic potential. Left: degree variances of the 1 km tree bias implied topographic potential. Right: degree variances of the smoothed tree bias implied topographic potential.

Similar to the calculations of the tree-bias implied full-scale and high-frequency gravity disturbances, the global maps of tree bias effect in terms of high-frequency geoid heights $N_{RTM}^{tree_bias}$ and second-radial derivatives

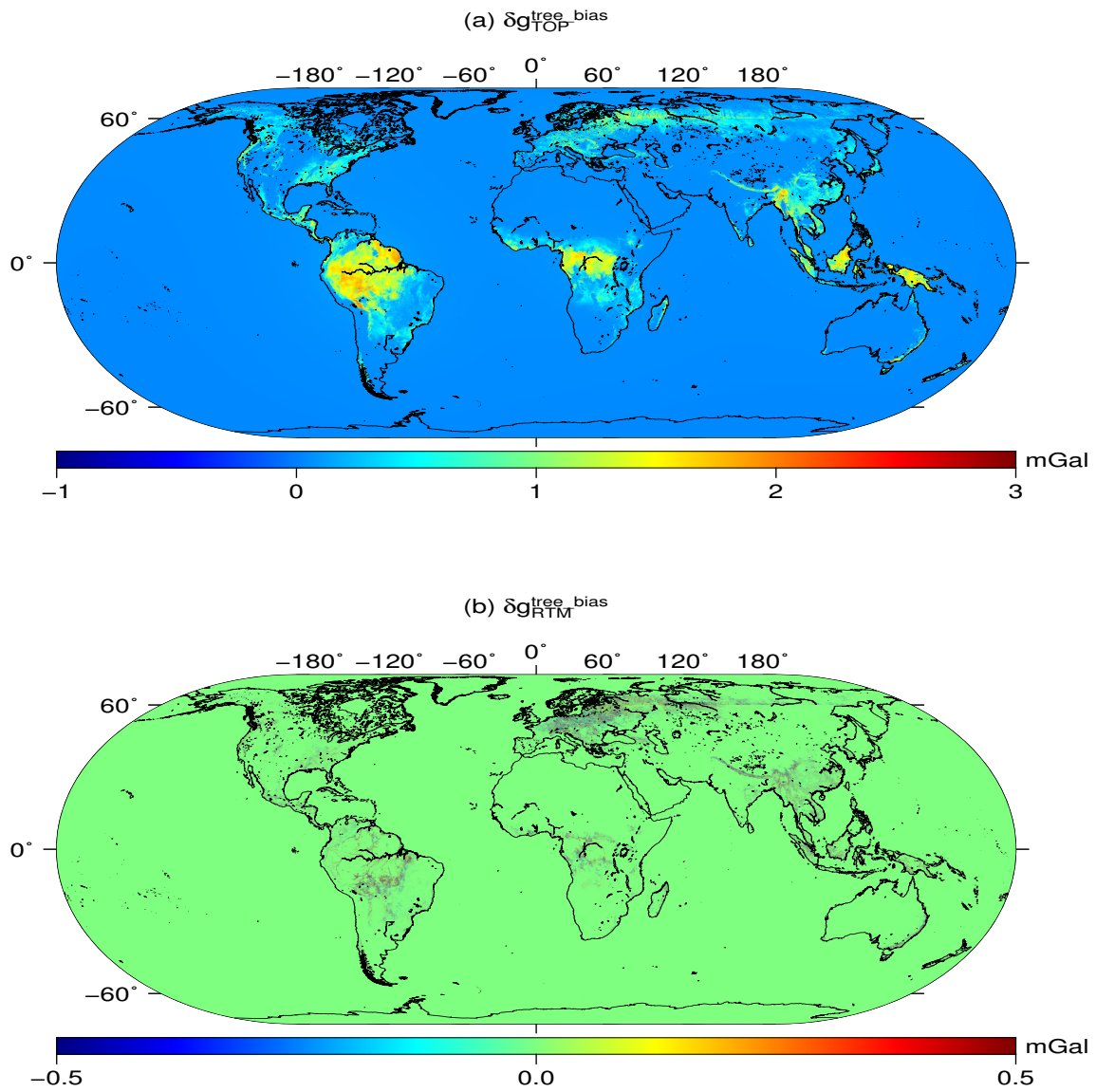


Fig. 5.16 – a) topographic and b) RTM gravity disturbances encountered in global tree canopy model

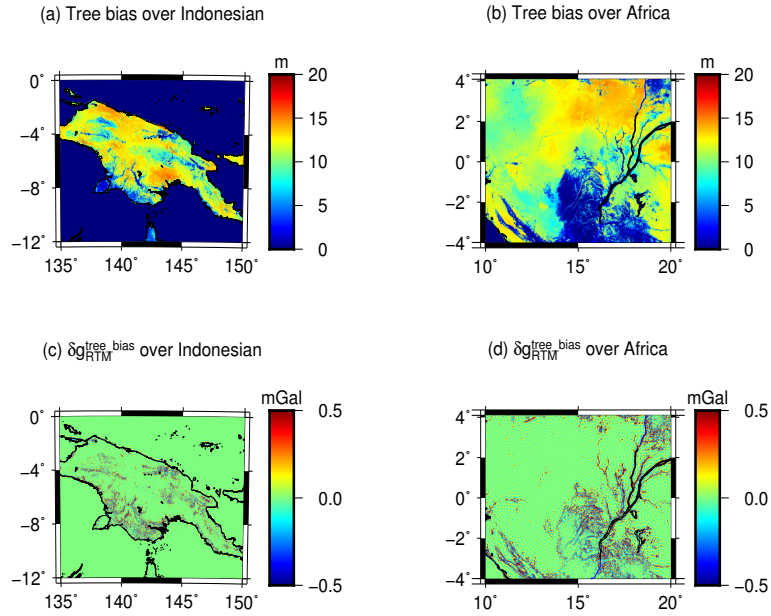


Fig. 5.17 – Tree bias and its effects in high-frequency gravity field modelling. (a) and (b) are tree bias height over Indonesian and Africa rainforest areas; (c) and (d) are tree bias effect in high-frequency gravity field modelling over Indonesian and Africa rainforest areas.

$T_{zz}^{tree_bias}$) were obtained via a spherical harmonic synthesis of the \bar{V}_{nm}^{RTM} coefficients with the isGraflab software (Bucha and Janák 2014) based on following formulas:

$$N_{RTM}^{tree_bias}(r_p, \varphi_P, \lambda_P) = \frac{GM}{r_p^\gamma} \sum_{n=0}^{N_{max}} \sum_{m=0}^n \left(\frac{R}{r_p}\right)^n \bar{V}_{nm}^{RTM} \bar{Y}_{nm}(\varphi_P, \lambda_P) \quad (5.6)$$

$$T_{zz}^{tree_bias}(r_p, \varphi_P, \lambda_P) = \frac{\partial^2 V(r_P, \varphi_P, \lambda_P)}{\partial r_p^2} = \frac{GM}{r_p^3} \sum_{n=0}^{N_{max}} \sum_{m=0}^n (n+1)(n+2) \left(\frac{R}{r_p}\right)^n \bar{V}_{nm}^{RTM} \bar{Y}_{nm}(\varphi_P, \lambda_P) \quad (5.7)$$

Fig. 5.18 shows the calculated results, with panel (a) being the tree-bias effect in RTM geoid height and panel (b) tree-bias effect in the RTM vertical gradient. Similar to the tree-bias effect in RTM gravity disturbances, the tree-bias effect in RTM implied geoid height $N_{RTM}^{tree_bias}$ and radial-tensor $T_{zz}^{tree_bias}$ is of high-frequency nature. The extrema are mostly along the boundaries of the forest distributions. The descriptive statistics of the geoid effects are $-0.31/0.27/0.00/0.01$ cm (min / max/ mean/ RMS), while the tree-bias effects on the vertical gradient are $-17.55/16.29/0.00/0.43$ E (min / max/ mean/ RMS). Compared to its effect in RTM gravity disturbance, tree bias has a negligible effect in geoid height within ~ 0.3 cm, and ~ 0.01 cm in terms of RMS values. However, the considerable effect was introduced in terms of radial-tensor with magnitude up to ~ 18 E. Therefore, special attention regarding tree-bias errors should be paid in high-frequency gravity field retrieving with forward modelling technique, especially for first- and second-derivatives of potential.

Numerical results in regional areas Further studies were carried out to investigate the tree-canopy effect on forward modeled gravity field based on numerical integration in the spatial domain and ultra-high resolution

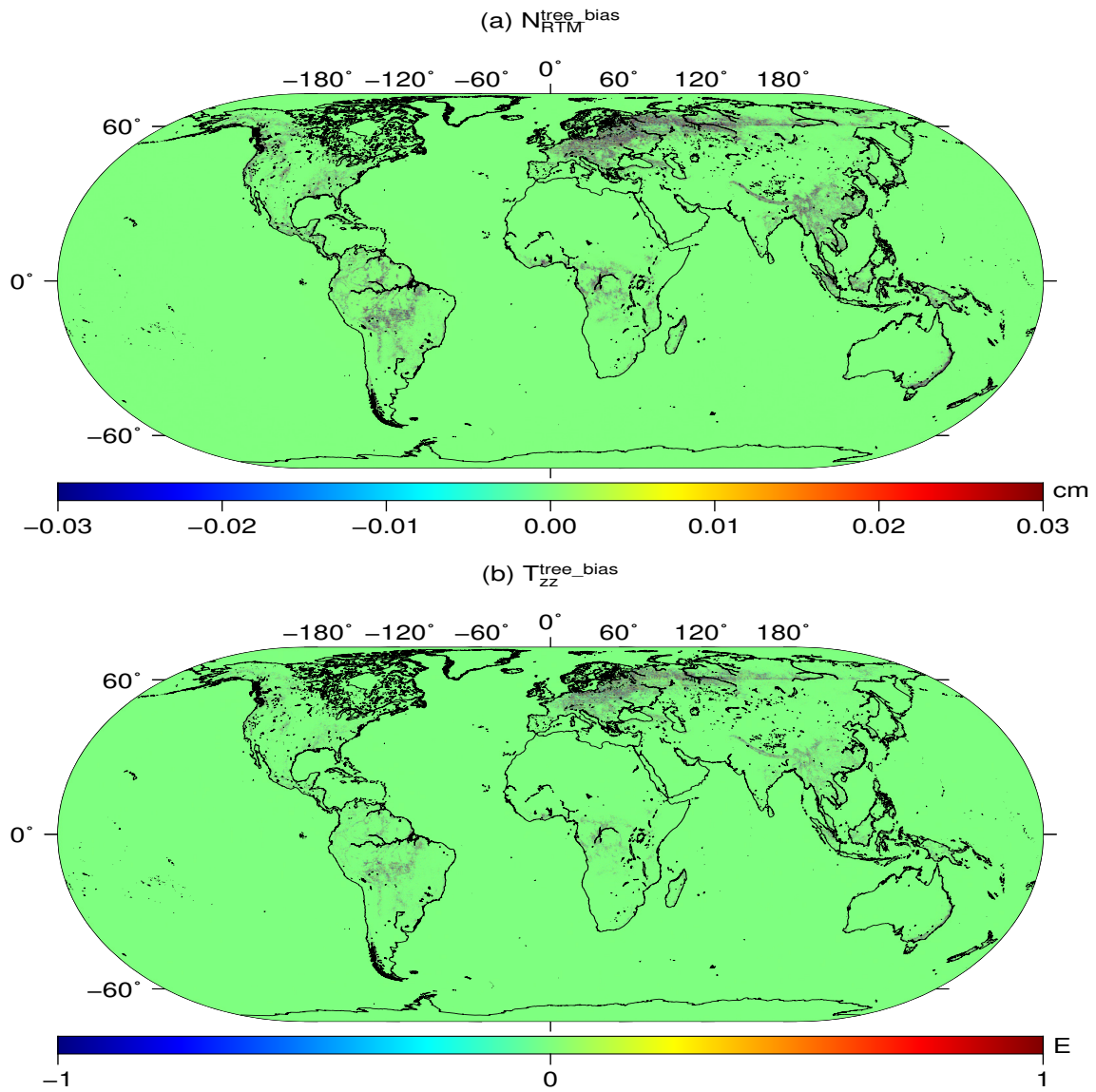


Fig. 5.18 – The (a) RTM geoid height and (b) RTM vertical gradient encountered in global tree-canopy model.

DEMs. Different to methods in the spectral domain which limit the studies to the global spectral analysis of tree-bias implied gravity field at long- and medium-wavelengths, we discuss here the tree-canopy effect in gravity forward modelling calculations with 3'' (~ 90 m) DEM resolution. This enables to investigate very high-frequency gravity signals associated with the tree-bias effect over local areas. Four regional areas, 1) Amazon rainforest area, 2) Tasmania Island over Australia, 3) the Canadian Rocky Mountains and 4) the Australian Alps mountain areas, with a high-rate distribution of forests, were chosen as study areas. Over these four regional study areas, tree canopy effects were studied by using the MERIT bare-ground DEM on the one hand, and the SRTM V4.1 DEM (contaminated with tree-height signals) on the other hand. For our numerical studies, the spatial-domain gravity forward modelling was implemented in two variants:

- 1) For the computation of *topographic gravity related to the tree-bias effect*, the global numerical integration was implemented over all masses between the sea level and the Earth's surface. Masses around the entire globe were divided into four zones, polyhedron and prism with 3'' DEM are primarily applied in the vicinity of 0.15° distance from evaluation point, tesseroid with 6' DEM extending to 10° , and point-mass for the outside distances with DEM of 1° resolution. Using 3'' MERIT DEM and SRTMV4.1 representing the Earth's bareground and top surfaces, respectively, two sets of topographic gravity disturbances were calculated, δg_0^{MERIT} and δg_0^{SRTM} . The differences between SRTM V4.1-based δg_0^{SRTM} and MERIT-based topographic gravity effects δg_0^{MERIT} give insight into the tree bias effect in full-scale forward modeled gravity signals.
- 2) In terms of *RTM gravity field retrieving*, SH reference surfaces that are consistent with the respective data set, MERIT SHCS 2160 for 3'' MERIT DEM and Earth2014 for SRTMV4.1, were adopted to remove the long-wavelength tree height signal from the detailed data sets. As is a common practice in RTM computations (e.g., *Forsberg (1984)*), the numerical integration was spatially limited, here to 2° distance around the computation point. The mass-distributions within 2° angle distance from the calculation point are divided into four zones. In the near zones of up to 0.02° and 0.03° distance around the computation point, polyhedron and prism with 3'' DEM are used for an accurate RTM calculation, while in the far zones, tesseroids are used with 3'' grid resolution to 0.15° and point mass with 30'' grid spacing are adopted to 2° distance. The RTM gravity disturbances based on SRTM datasets $\delta g_{RET2014}^{SRTM}$ and MERIT datasets $\delta g_{MERITSHCS2160}^{MERIT}$ were computed separately. The differences between $\delta g_{RET2014}^{SRTM}$ and $\delta g_{MERITSHCS2160}^{MERIT}$ provide a measure for the tree-canopy effect in high-frequency gravity field modeling.

Over the four study areas, the evaluation points at a resolution of 15'' are homogeneously distributed at the surfaces of the respective DEM data sets. It is worth noting that besides tree canopy bias, the differences between SRTM- and MERIT-based computations may also reflect different voids filling procedures (in MERIT and SRTM V4.1) and approaches used for the reduction of radar error sources (in MERIT). However, the four regional study areas were selected as regions where significant tree height biases can be expected in the SRTM data (*Yamazaki et al (2017)*). Therefore, we assumed that tree canopy effect dominates among error sources over the study areas.

Figs. 5.19, 5.20, 5.21 and 5.22 show the numerical results over four study areas.

The Tasmania area, with latitude ranging from 44° S to 40° S and longitude between 144° E and 149° E, is covered by some of the world's tallest broadleaved trees. The heights of tree bias reach ~ 10 m (Fig. 5.19(b)), with a mean of ~ 4.06 m and an RMS of tree-bias of ~ 5.07 m over continental areas. The differences between SRTM-based and MERIT-based gravitational fields are shown in Fig. 19, panel (d) for full-scale topographic gravity disturbances and panel (f) for RTM gravity disturbances. As was seen in panel (d), the tree canopy offset causes a positive bias, which varies from 0 to ~ 4 mGal depending on the heights of tree bias and holds an RMS value of 0.58 mGal, in the topography-implied gravity disturbances. Compared to the tree canopy effect in topographic gravity disturbances, its effect in RTM gravity disturbance (panel (f)) is greatly reduced to values within ± 2 mGal. The uttermost values generally occur at the boundaries of forest coverage, which is within the expectations. This is consistent with conclusions of the spectral method, that tree bias is dominated by long- and medium-wavelength signal which largely cancels out in the RTM technique, apart from sharp signals occurring at forest boundaries.

Another study area around the Amazon river bounded by meridians of $60^{\circ}/55^{\circ}$ W and latitude parallels of $5^{\circ}/1^{\circ}$ S is host to the world's highest rainforest involving tree bias up to ~ 15 m (Fig. 5.20 (b)) in radar-based heights of SRTM V4.1. This makes it an ideal test area for studies of tree-bias effect. The differences between SRTM-based and MERIT-based gravitational fields are shown in Fig. 20 in terms of gravity disturbances, panel (d) for full-scale topographic signals and panel (f) for RTM gravity signals. The comparison results suggest a similar trend as over Tasmania area. The tree bias produces a locally long- and medium-wavelength effect in topographic gravity disturbances of 0 to ~ 2.4 mGal (Fig. 5.20 (d)), and ~ 2 mGal RTM gravity disturbances (Fig. 5.20 (f)) around boundaries of tree coverage.

The Australian Alps area (Fig. 5.21) ranging from 145.5° E to 150.5° E in longitude and from 38.5° S to 34.5° S in latitude is located in the southeast of the Australian continent. It is home to some of the world's highest broadleaved trees (Fig. 5.21 (b)). The tree bias effect varies within 4 mGal for topographic gravity disturbances (Fig. 5.21 (d)) and within 2 mGal for RTM gravity disturbances (Fig. 5.21 (f)) over edges.

The area located in the Canadian Rocky Mountainous ranges is bounded by longitudes within 118° W and 115° W, and latitudes within 49° N and 51° N (Fig. 5.22). Over the study area, some sparkle noise also comes into play which is obvious in Fig. 5.22 (b). The tree bias effect over this area in topographic gravity disturbances is within 2 mGal and within 1 mGal for RTM gravity disturbances over forest boundaries.

Based on the comparison results over four regional study areas, some general conclusions can be drawn. The tree bias would introduces additional terrain masses which is reflected by the long-wavelength positive differences – from 0 to several mGal – between SRTM-based and MERIT-based topographic gravity disturbances. In the RTM technique, the tree bias dominated by long- and medium-wavelength signal largely cancels out, and the extrema are mostly along the boundaries of the forest distributions.

We also use ground gravity observations to demonstrate the better performance of bare-ground DEM-based forward modelling, and to benchmark the improvement when a bare-ground instead of a tree-height biased

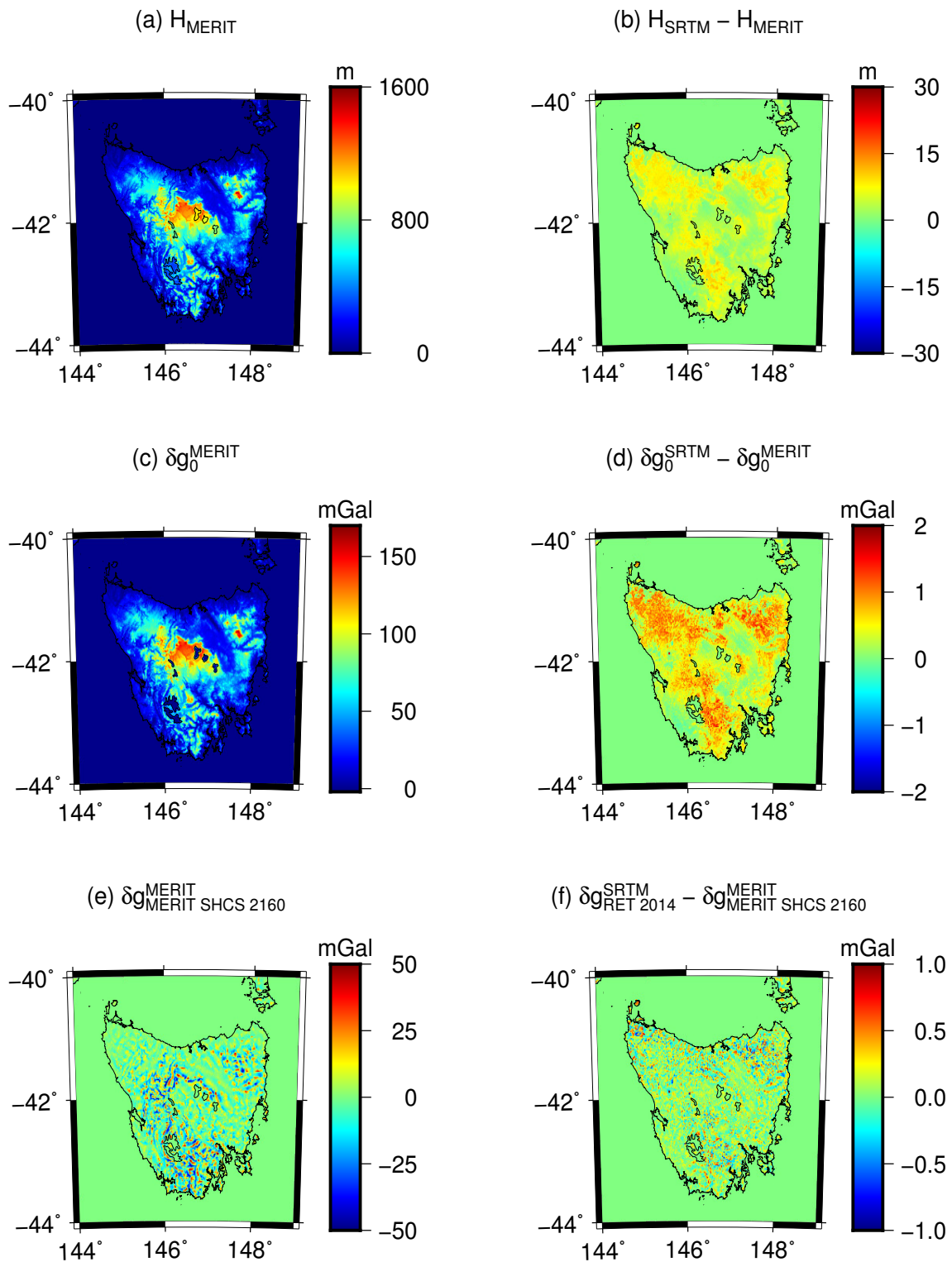


Fig. 5.19 – Tree canopy effect in regionally high-frequency gravitational field modeling over the Tasmania area. (a) MERIT elevations; (b) Height differences between MERIT DEM and shifted SRTM V4.1 DEM; (c) Topographic gravity disturbances implied by the MERIT DEM; (d) Tree canopy effect in topographic gravity disturbances; (e) RTM gravity disturbances based on RTM data using the MERIT DEM and its degree-2160 reference surface as boundaries; (f) Tree canopy effect in RTM gravity disturbances modeling.

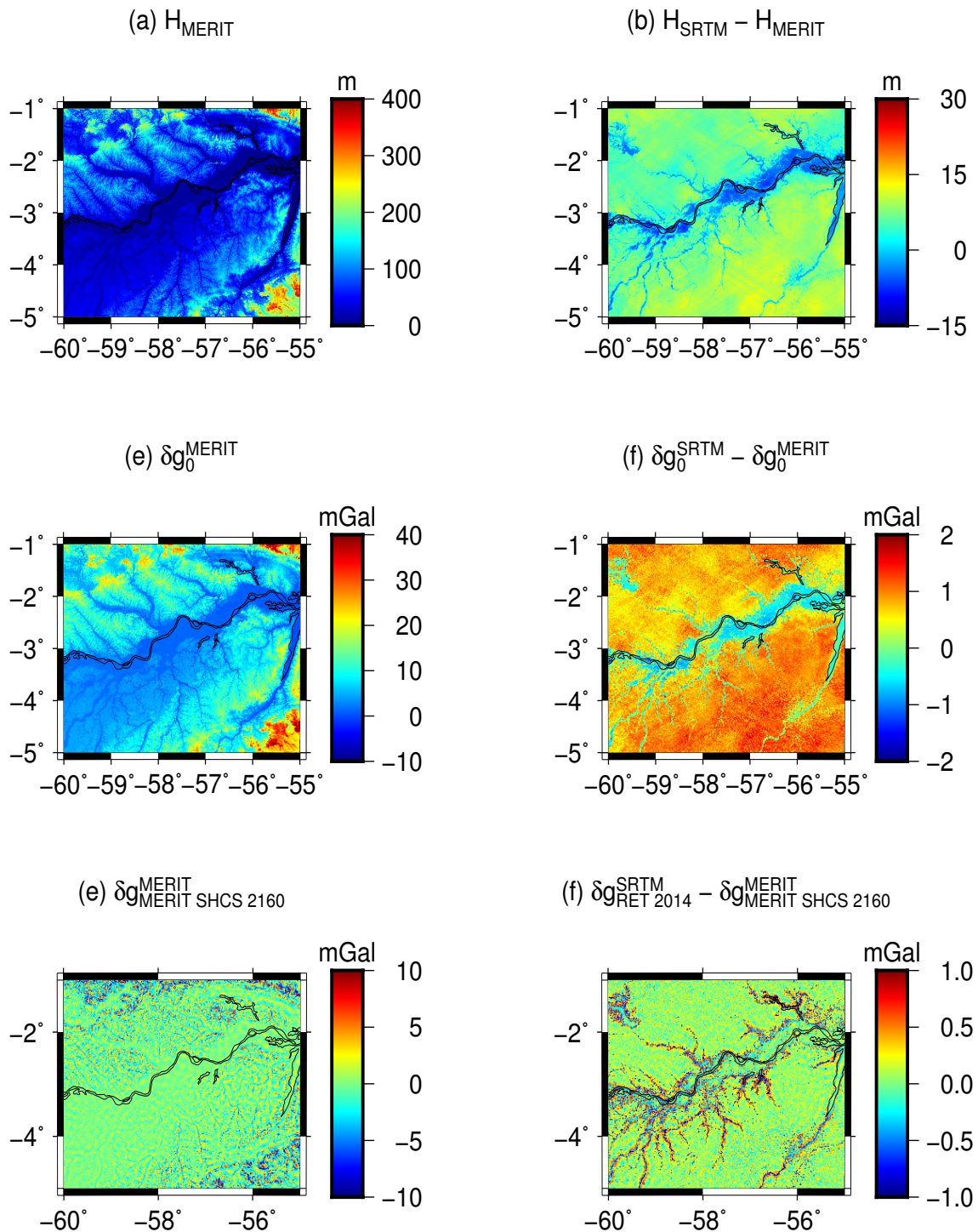


Fig. 5.20 – Tree canopy effect in regionally high-frequency gravitational field modeling over the Amazon area. (a) MERIT elevations; (b) Height differences between MERIT DEM and shifted SRTM V4.1 DEM; (c) Topographic gravity disturbances implied by the MERIT DEM; (d) Tree canopy effect in topographic gravity disturbances; (e) RTM gravity disturbances based on RTM data using the MERIT DEM and its degree-2160 reference surface as boundaries; (f) Tree canopy effect in RTM gravity disturbances modeling.

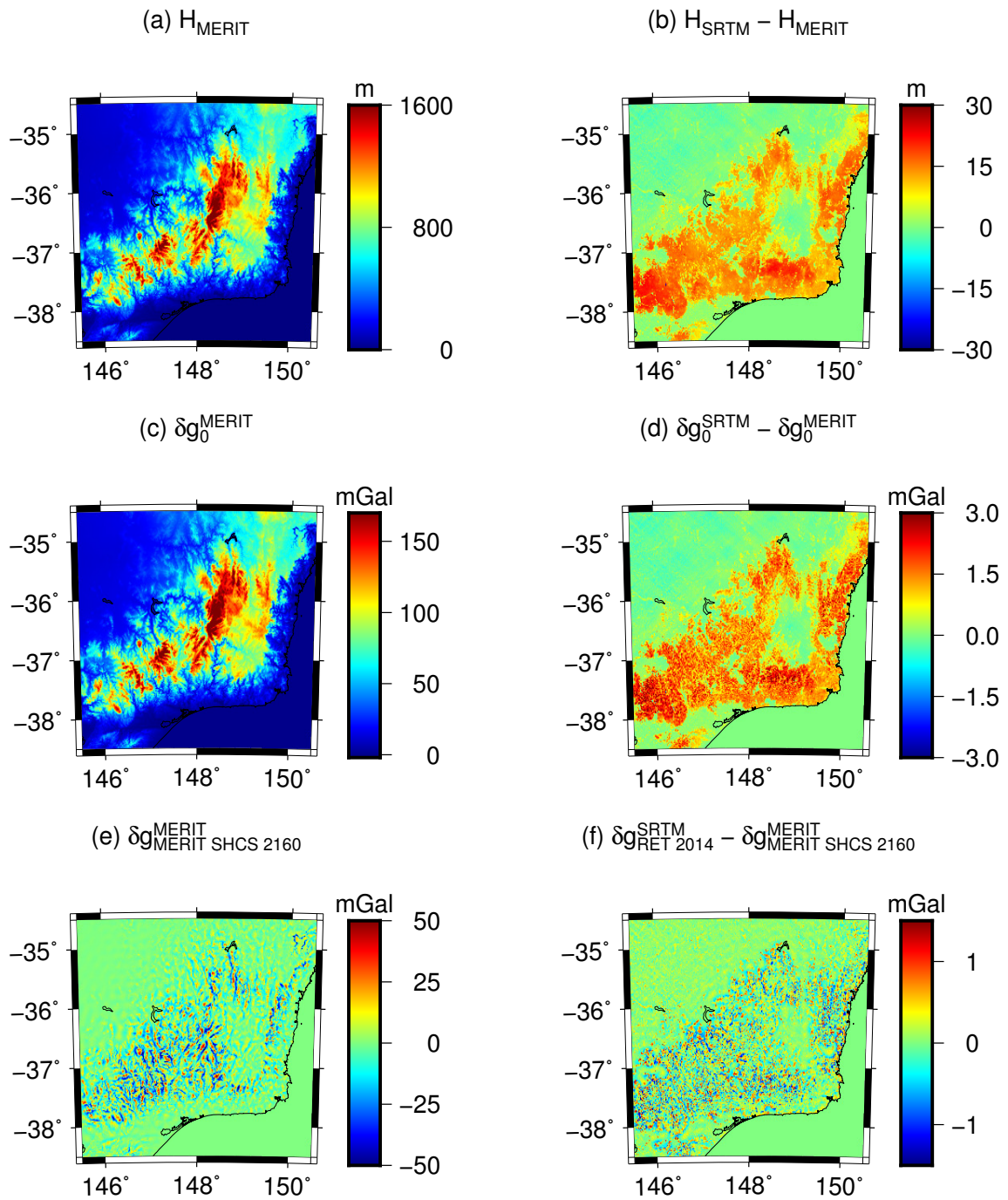


Fig. 5.21 – Tree canopy effect in regionally high-frequency gravitational field modeling over the Australian Alps mountainous area. (a) MERIT elevations; (b) Height differences between MERIT DEM and shifted SRTM V4.1 DEM; (c) Topographic gravity disturbances implied by the MERIT DEM; (d) Tree canopy effect in topographic gravity disturbances; (e) RTM gravity disturbances based on RTM data using the MERIT DEM and its degree-2160 reference surface as boundaries; (f) Tree canopy effect in RTM gravity disturbances modeling.

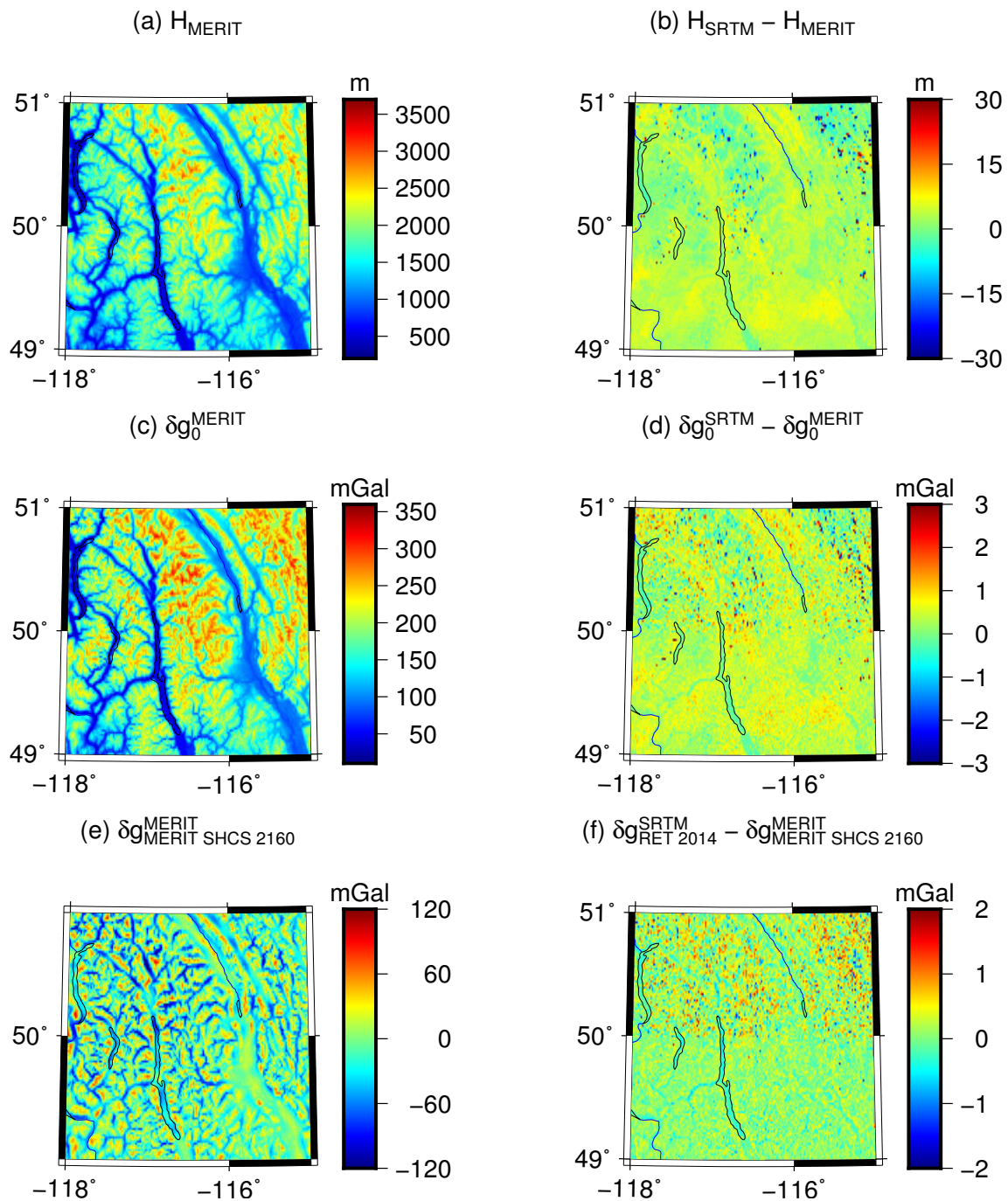


Fig. 5.22 – Tree canopy effect in regionally high-frequency gravitational field modeling over the Canadian Rocky mountainous area. (a) MERIT elevations; (b) Height differences between MERIT DEM and shifted SRTM V4.1 DEM; (c) Topographic gravity disturbances implied by the MERIT DEM; (d) Tree canopy effect in topographic gravity disturbances; (e) RTM gravity disturbances based on RTM data using the MERIT DEM and its degree-2160 reference surface as boundaries; (f) Tree canopy effect in RTM gravity disturbances modeling.

DEM is used. Terrestrial gravity observations were used here for validation by comparison with the synthetic model of EGM2008 and RTM implied gravity disturbances with signals finer than 5'. The residual gravity differences are formulated as:

$$\Delta\delta g = g_{obs} - \gamma - \delta g_{EGM2008} - \delta g_{RTM} \quad (5.8)$$

with g_{obs} indicating the values of measured gravity acceleration at station height and γ being the normal gravity at each station. The difference between g_{obs} and γ yields the 'true-value' of gravity disturbance. $\delta g_{EGM2008}$ is the long-wavelength part of gravity disturbances modeled from EGM2008 and with order and degree truncated to 2,159, while δg_{RTM} is high-frequency signals retrieved using RTM technique. Here, two sets of RTM gravity disturbances, $\delta g_{RET2014}^{SRTM}$ using SRTM V4.1 and Earth2014 and $\delta g_{MERITSHCS2160}^{MERIT}$ using MERIT DEM and MERIT SHCS2160, were calculated. The absolute residual differences between $|\Delta\delta g^{SRTM}|$ and $|\Delta\delta g^{MERIT}|$ provide an insight for the different performance of the two DEM variants. The positive absolute residual differences imply the smaller residual magnitude of $\Delta\delta g = g_{obs} - \gamma - \delta g_{EGM2008} - \delta g_{MERITSHCS2160}^{MERIT}$, and gravitational signals are better modeled with the MERIT-based RTM data.

Validations were carried out at 74,265 ground gravity observations over Tasmania. As is seen in Fig. 5.23, the spatial distribution of the gravity measurements is not uniform and there are significant gaps in large parts of the southwest island. The terrestrial data are sufficiently dense and precise in the well-surveyed regions such as north-east island and along lakes. Over these areas that are highly covered by vegetation, the absolute residual differences show predominately positive values, cf. Fig. 5.23(d) red color, which indicates the better performance of the bare-ground elevation model MERIT. However, over areas such as the western island bounded by the longitudes of $\sim 145.5^\circ$ E to $\sim 147^\circ$ E, land-based gravity measurements are less dense and far from forest boundaries. It is difficult to validate the performance of bare-ground DEM, especially over the southern area where great tree bias effect are involved (Fig. 5.21 (f)).

Tab. 5.9 gives the descriptive statistics of the validation results. The combined gravity disturbances of EGM2008 and RTM high-frequency signal explain $\sim 92\%$ gravitational content of ground observations, and ~ 3 mGal precision implies a wide range of usage of synthetic gravity model in practical applications. The smaller RMS value of ~ 2.59 mGal for the MERIT-based residual gravity disturbances supports the conclusion that bare-ground MERIT performs better than SRTM DEMs in gravity forward modeling. Overall, the tree height bias produces a ~ 0.7 mGal effect in the sense of RMS in RTM gravitational field modelling over Tasmania.

Fig. 5.24 and Tab. 5.10 show the validation results over the Australian Alps areas. The validations based on 23,260 ground gravity observations confirm the better performance of MERIT DEM. This is obvious over the southwest area (reddish color in Fig. 5.24 panel (d)) where dense gravity measurements are available, and from the smaller RMS strength of residual signals, ~ 3.04 mGal for MERIT-based results to ~ 3.12 mGal for SRTM-based results. Over larger parts of the northeast area, sparse gravity measurements make it difficult to validate the performance of bare-ground DEM.

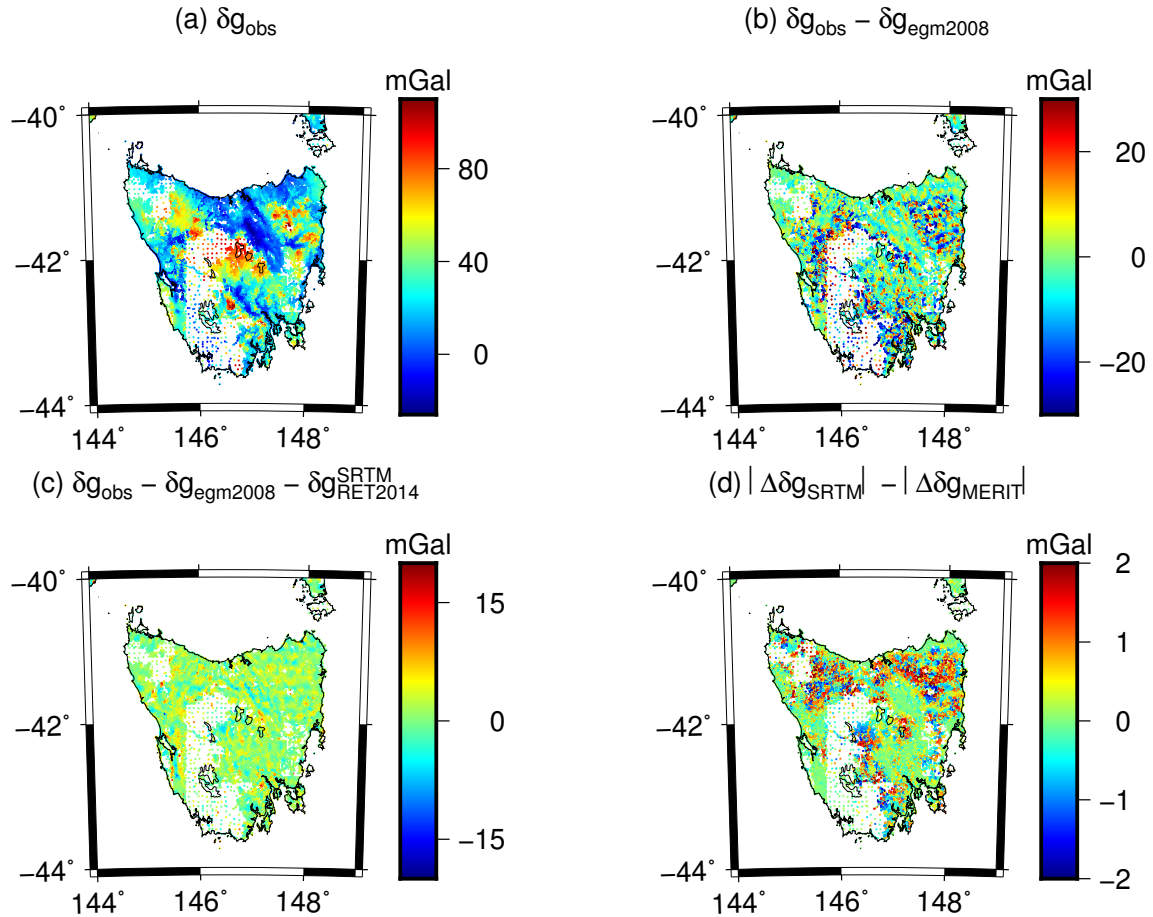


Fig. 5.23 – Validation over Tasmania area with ground gravity observations. (a) Ground gravity disturbances; (b) Removing EGM2008 gravity disturbances from observation; (c) residual gravity disturbances after removal of EGM2008 and RTM gravity disturbances from observation; (d) magnitude differences between SRTM-based residual signals and MERIT-based residual signals, where red indicates MERIT performs better than SRTM V4.1.

Tab. 5.9 – Statistical information of tree height effect on gravity disturbances over Tasmania

	min (mGal)	max (mGal)	mean (mGal)	RMS (mGal)	κ
δg_{obs}	-28.70	136.82	27.86	35.77	
$\delta g_{obs} - \delta g_{EGM2008}$	-37.59	33.23	-2.31	11.56	67.69 %
$\Delta \delta g^{SRTM}$	-15.52	29.28	0.81	2.77	92.26 %
$\Delta \delta g^{MERIT}$	-15.55	28.34	0.28	2.59	92.76 %
$\Delta \delta g^{SRTM} - \Delta \delta g^{MERIT}$	-1.23	7.52	0.53	0.76	
$ \Delta \delta g^{SRTM} - \Delta \delta g^{MERIT} $	-2.80	7.52	0.16	0.71	

* with δg_{obs} indicating observed gravity disturbances; δg_{egm} gravity disturbances calculated from EGM2008 truncated at degree and order of 2, 159; $\Delta \delta g^{SRTM} = \delta g_{obs} - \delta g_{egm} - \delta g_{RET2014}^{SRTM}$ and $\Delta \delta g^{MERIT} = \delta g_{obs} - \delta g_{egm} - \delta g_{MERITSHCS2160}^{MERIT}$ being residual gravity disturbances between observed and synthesized gravity signals, κ is improvement rate.

Fig. 5.25 and Tab. 5.11 show the validation results over the Canadian Rocky Mountain areas. Over Canadian Rocky Mountain area, gravity observations are more sparsely distributed due to difficulties in physically accessing the desired locations, terrain roughness and problems with gravimeter drift. The validations based on 962 ground gravity observations confirm the better performance of MERIT DEM. This is seen from the smaller RMS strength of residual signal, ~ 8.23 mGal for MERIT-based results to ~ 8.28 mGal for SRTM-based results.

Tab. 5.10 – Statistical information of tree height effect on gravity disturbances in the Australian Alps based on 23,260 ground gravity observations

	min (mGal)	max (mGal)	mean (mGal)	RMS (mGal)	κ
δg_{obs}	-40.91	166.97	26.83	42.42	
$\delta g_{obs} - \delta g_{EGM2008}$	-29.21	25.73	-2.22	10.49	75.25 %
$\Delta \delta g^{SRTM}$	-16.70	150.75	0.54	3.12	92.63 %
$\Delta \delta g^{MERIT}$	-16.91	147.62	-0.20	3.04	92.84 %
$\Delta \delta g^{SRTM} - \Delta \delta g^{MERIT}$	-1.88	5.12	0.74	1.25	
$ \Delta \delta g^{SRTM} - \Delta \delta g^{MERIT} $	-4.34	4.98	0.05	1.09	

* with δg_{obs} indicating observed gravity disturbances; δg_{egm} gravity disturbances calculated from EGM2008 truncated at degree and order of 2, 159; $\Delta \delta g^{SRTM} = \delta g_{obs} - \delta g_{egm} - \delta g_{RET2014}^{SRTM}$ and $\Delta \delta g^{MERIT} = \delta g_{obs} - \delta g_{egm} - \delta g_{MERITSHCS2160}^{MERIT}$ being residual gravity disturbances between observed and synthesized gravity signals, κ is improvement rate.

Tab. 5.11 – Statistical information of tree height effect on gravity disturbances in Canadian Rocky Mountain area based on 962 ground gravity observations

	min (mGal)	max (mGal)	mean (mGal)	rms (mGal)	κ
δg_{obs}	-169.65	128.71	33.58	74.35	
$\delta g_{obs} - \delta g_{EGM2008}$	-132.66	105.75	-18.64	47.09	36.67 %
$\Delta \delta g^{SRTM}$	-24.52	44.29	0.69	8.28	88.86%
$\Delta \delta g^{MERIT}$	-25.67	44.10	0.28	8.23	88.93 %
$\Delta \delta g^{SRTM} - \Delta \delta g^{MERIT}$	-6.05	2.16	0.42	0.64	
$ \Delta \delta g^{SRTM} - \Delta \delta g^{MERIT} $	-2.16	6.05	0.03	0.63	

* with δg_{obs} indicating observed gravity disturbances; δg_{egm} gravity disturbances calculated from EGM2008 truncated at degree and order of 2, 159; $\Delta \delta g^{SRTM} = \delta g_{obs} - \delta g_{egm} - \delta g_{RET2014}^{SRTM}$ and $\Delta \delta g^{MERIT} = \delta g_{obs} - \delta g_{egm} - \delta g_{MERITSHCS2160}^{MERIT}$ being residual gravity disturbances between observed and synthesized gravity signals, κ is improvement rate.

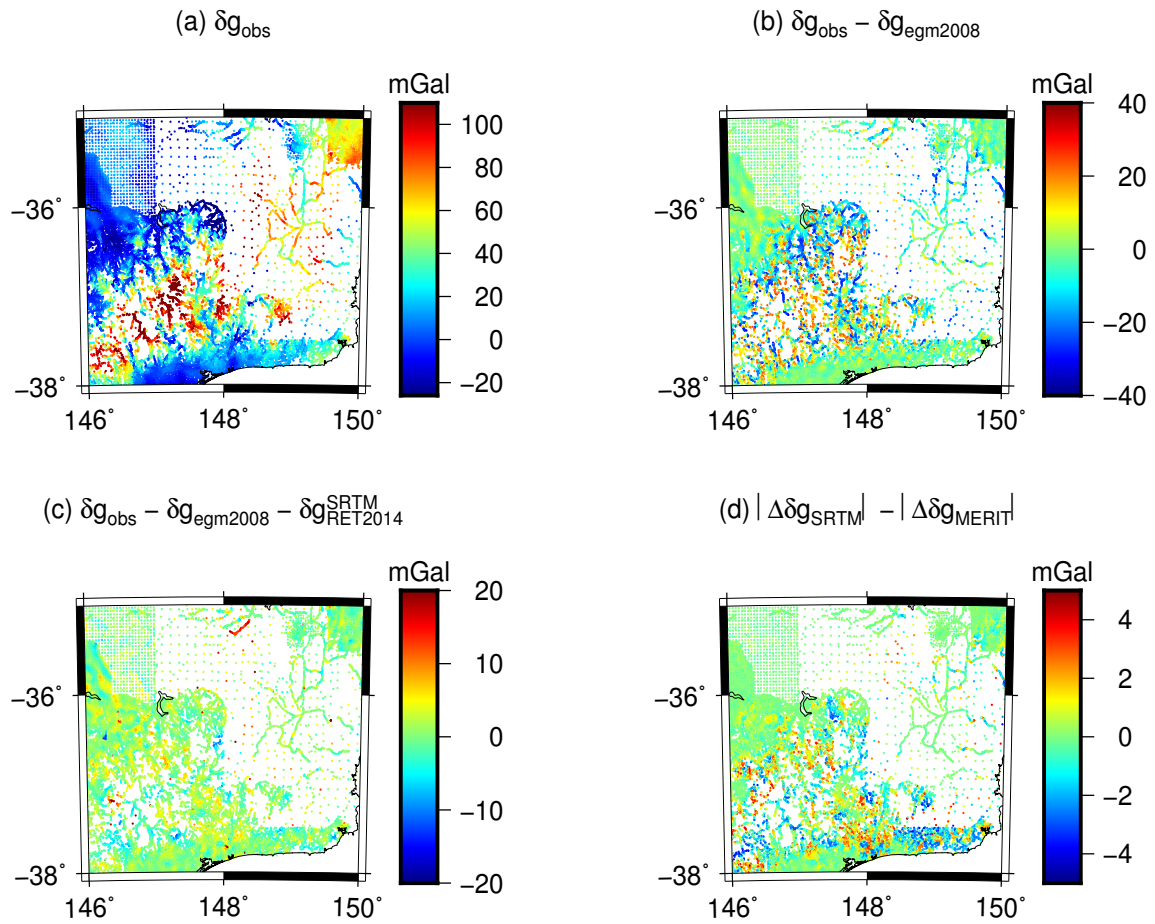


Fig. 5.24 – Validation over Australian Alps area with ground gravity observations. (a) Ground gravity disturbances; (b) Removing EGM2008 gravity disturbances from observation; (c) residual gravity disturbances after EGM2008 and RTM gravity disturbances from observation; (d) magnitude differences between SRTM-based residual signals and MERIT-based residual signals, where red indicates MERIT performs better than SRTM V4.1.

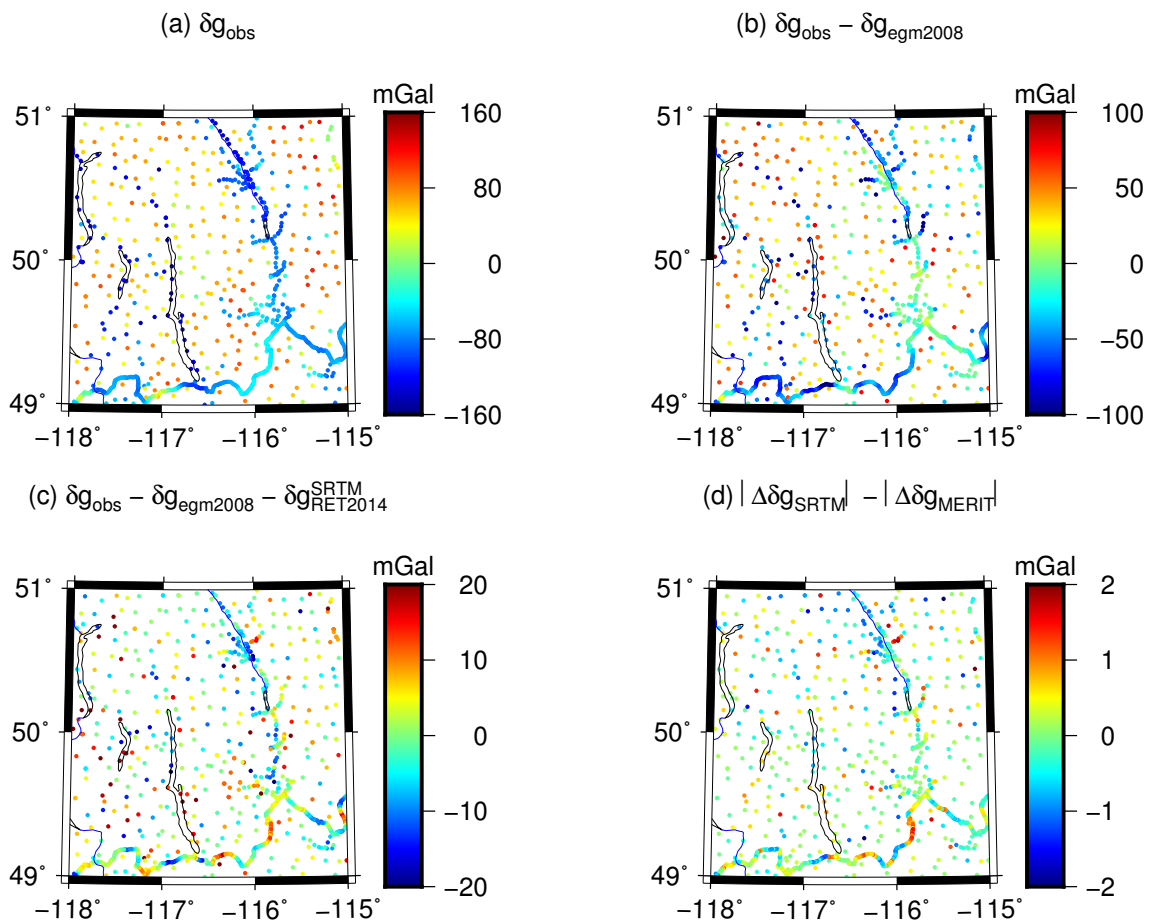


Fig. 5.25 – Validation over Canadian Rocky Mountainous area with ground gravity observations. (a) Ground gravity disturbances; (b) Removing EGM2008 gravity disturbances from observation; (c) residual gravity disturbances after EGM2008 and RTM gravity disturbances from observation; (d) magnitude differences between SRTM-based residual signals and MERIT-based residual signals, where red indicates MERIT performs better than SRTM V4.1.

5.2.3 Summary

In this chapter, we estimated the amplitudes of various errors that might be encountered in the procedure of high-frequency gravity field modelling. The results are estimated in a comparative method and listed the following in Tab. 5.12. Besides, tree canopy effect in full-scale topographic gravity disturbances was estimated to be within ~ 4 mGal over vegetated areas.

Tab. 5.12 – The error sources and its effect in RTM gravity forward modelling (Units: mGal)

Error sources	Study area	Datasets for estimation	Effect in RTM gravity forward modelling
Modelling errors			
RTM-A	1) Himalayas 2) Swiss Alps	1) RTM baseline solution 2) 3" MERIT DEM 3) MERIT SHCS2160 4) $\rho = 2,670 \text{ kg/m}^3$	sub-mGal accuracy (RMS)
RTM-B			~ 2 mGal accuracy (RMS)
RTM-C			$\sim 3 - 4$ mGal accuracy (RMS)
Harmonic correction		Mass condensation formula $4\pi G \rho H_{RTM}$	Residual height dependent, from several mGal to tens of mGal
Mass shift in RTM-B			at several mGal level
computation point inconsistency		RTM-C	at tens mGal level
reference geometry effect		3" MERIT, MERIT SHCS2160, $\rho = 2,670 \text{ kg/m}^3$	latitude dependent, at sub-mGal level
Observation errors			
Mass-density distributions	New Zealand	1" SRTM DEM, Earth2014, $\rho = 2,670 \text{ kg/m}^3$, New Zealand digital density map	Extrema reach tens of mGal depending on the composition effect of RTM height and bias between constant density value and actual density.
Tree-bias effect	global and regional areas	Tree-bias map, SRTM V4.1, Earth2014, 3" MERIT DEM, MERIT SHCS2160, $\rho = 2,670 \text{ kg/m}^3$	~ 2 mGal extrema at forest boundaries

Chapter 6

Summary and outlook

6.1 Summary

This thesis is devoted to the accurate and efficient calculation of the terrain implied gravity field with a focus on the high-frequency gravity field retrieved by using the RTM technique. For this purpose, we have developed the Matlab-based software TGF for gravity forward modelling in the spatial domain. Based on this software, error analysis in the frame of gravity forward modelling with the RTM technique has been performed on various issues, including comparison of various RTM techniques, Earth's approximation by a spheroid or by a sphere, performance of a lateral density model in the RTM gravity field modelling, and the tree bias effect in gravity forward modelling.

The following conclusions are based on the works:

- 1) "Yang, M., Hirt, C., Pail, R., 2019. TGF: A New MATLAB-based Software for Terrain-related Gravity Field Calculations."
- 2) "Yang, M., Hirt, C., Tenzer, R., Pail, R., 2018. Experiences with the use of mass density maps in residual gravity forward modelling. *Stud. Geophys. Geod.*, 62, Doi: 10.1007/s11200-017-0452-9."
- 3) "Yang, M., Hirt, C., Rexer, M., Pail, R., Yamazaki, D., 2019. The tree-canopy effect in gravity forward modelling, *Geophysical Journal International*, 219 (1), October 2019, P 271–289, doi: <https://doi.org/10.1093/gji/ggz264>."

Some of materials presented in this subsection have been taken directly from the respective manuscript.

The TGF software is a Matlab-based software program for gravity forward modelling, which combines four different types of spatial domain techniques: polyhedron, prism, tesseroid and point mass. It is capable of calculating the gravitational potential and its first- and second-derivatives in both full-scale gravity fields generated by the mass-density between the MSL and Earth's surface, and high-frequency gravity fields, also known as RTM gravity fields, of the residual masses bounded by the Earth's surface and the smooth reference surface. In the TGF software, the integration masses are divided into four zones. The user can manually define the radius, and inputs (i.e., the applied height and density datasets) of each zone. In addition, a density model

(e.g., mass-density map) or a constant mass-density assumption can be used, and the computations can be carried out in spherical or ellipsoidal approximation. The TGF software has been validated through independent comparisons: 1) between TGF and CNI calculated full-scaled gravity disturbances, and 2) between the novel RTM-baseline solution and TGF calculated high-frequency gravity disturbances. The residuals, at sub-mGal level in terms of RMS, demonstrated the promising performance of TGF in both applications. Based on the internal validation, parameters were recommended for RTM gravity field calculations, i.e., the polyhedron extending up to a 0.02° distance around the calculation point, the prism with a radius of 0.03° , a tesseroid with a radius to 0.15° , and point mass of 0.8° . With these parameters, the software can achieve a calculation efficiency of 10 points per second. Besides, the comparison between TGF and pre-computed gravity effects from the ERTM2160 gravity model confirmed the better performance of TGF software in RTM gravity field calculations. Furthermore, the TGF software has already been extensively tested and recently applied in the SRTM2gravity project (*Hirt et al (2019b)*) to convert the global $3''$ SRTM topography to implied gravity effects at 28 billion computation points. All of these tests and experiments demonstrate the performance of TGF for processing high-resolution DEMs associated with the roughest topography.

Based on the TGF software, we have studied the various types of approximations and simplifications, and their effects in the procedure of RTM gravity field calculations.

- The starting point was the well-studied RTM modelling techniques that were affected by different types of simplifications and uncertainties, e.g., harmonic correction, spectral filter problem, mass modeling simplification, computation point inconsistency. In this thesis, three types of RTM techniques (RTM-A, RTM-B, RTM-C) were assessed using a novel RTM baseline solution relying on a combination of global numerical integration (NI) and ultra-high spectral gravity modelling (SGM) techniques. In terms of test areas, we used two of the Earth's most roughest areas: the Himalayas and Swiss Alps. All these three techniques were shown to be affected by one or two of the approximation errors. The RTM-A technique, with a single-run integration over residual masses and additive condensation harmonic correction ($4\pi G\rho H_{RTM}$) for non-harmonic points ($H_{RTM} < 0$), has shown the best RMS agreement of ~ 0.78 mGal over the Himalayas and ~ 0.62 mGal over Switzerland. While RTM-A offered excellent sub-mGal agreement (~ 0.22 mGal over Himalaya and ~ 0.38 mGal over Switzerland) with the RTM baseline over harmonic points ($H_{RTM} > 0$), the approximation errors associated with the harmonic correction dominate the error budget over non-harmonic points. In the RTM-B technique, residual masses were fixed directly on the reference sphere or the reference spheroid. Such mass simplifications in the RTM-B technique reduced the agreement level to ~ 1.8 mGal in terms of RMS values. The RTM-C technique avoided the harmonic correction through two runs of calculations, but yielded the errors caused by calculation point inconsistency. These would lead to the largest errors (> 3 mGal) over two study areas.
- The second part of this work consisted of the analysis of Earth approximation errors. Accurate gravity forward modelling in the spatial domain requires integration over the domain of all mass-sources, which

often extend up to the limit of the entire globe for the full-scale gravity field calculations and up to tens of kilometers for RTM gravity field calculations. Considering the curvature of the Earth, the often used local planar approximation is usually not sufficient for accurate computations in such cases. The TGF software, therefore, was adapted for the more rigorous spherical or ellipsoidal approximation levels. In the ellipsoidal approximation, the Earth was approximated by a spheroid with a latitude-dependent Earth radius. The relevant coordinates are the ellipsoidal height h' and geodetic latitude β and longitude λ . All forward computations modeled the topographic masses relative to the surface of the GRS80 ellipsoid. In spherical approximation, Newtonian integration treats the topography relative to a reference sphere, with the GRS80 semi-major axis as radius, and the spherical latitudes, longitudes and heights as coordinate bases. The differences in gravity disturbances generated by residual masses in the framework of ellipsoidal and spherical approximations were within ~ 0.16 mGal, which is insignificant for mGal level gravity field determination.

- Next, the lateral density effect in high-frequency gravity field modelling was investigated. For this problem, we combined the high-resolution New Zealand density map with the RTM technique. Because of the near-subsurface data properties, the performance of the density map was closely related to the terrain roughness. The gravity signals of EGM2008 and the RTM technique based on the density model tended to a better agreement with observed gravity disturbances and height anomalies over areas with small residual heights, and lost its benefits over areas with rough topography where stronger radial density variations might come into play. Density map errors, as well as interpolation of density map during the procedure of modelling residual mass, will also introduce errors in the residual gravity field.
- Another new contribution made by our work was the determination of regionally optimal density values for the topographic masses over New Zealand's North and South Islands. Due to different regional geological proportions of both sedimentary and shield rocks, the density assumption of $2,670 \text{ kg/m}^3$ is not necessarily an optimal choice for regional research. Based on gravity measurements at 40,366 points and a combination of GGM implied long-wavelength signals and RTM generated short-wavelength signals, we determined the regionally optimum densities over the North Island ($2,500 \text{ kg/m}^3$), South Island ($2,600 \text{ kg/m}^3$) and the whole of New Zealand ($2,590 \text{ kg/m}^3$). The mean values from the New Zealand digital density map were $2,336 \text{ kg/m}^3$ for the North Island, $2,514 \text{ kg/m}^3$ for the South Island, and $2,440 \text{ kg/m}^3$ for the whole of the New Zealand, all somewhat smaller than the new estimates we derived based on ground-gravity comparisons. Generally, all regionally-optimal density values were smaller than the commonly used value of $2,670 \text{ kg/m}^3$. This was because, in large areas of New Zealand, the sediment consists of "Cenozoic, particularly Quaternary, sedimentary and pyroclastic volcanic deposits" (Tenzer et al., 2011). Different methods for ice and water mass processing, and of the underlying density effect, can be attributed to the differences between optimum density and mean value of the density map. Using regionally optimum density, instead of $2,670 \text{ kg/m}^3$, delivered some improvements in residual forward modelling, especially over mountainous areas, where the residual gravity signals are larger. Compared to the New Zealand surface density model, this improvement was quite more significant, with extreme

improvement of ~ 30 mGal in terms of residual gravity disturbance gained over the Alps Fault. This suggested that the actual density that should be taken into account in the RTM modelling is highly affected by the deep-lying sedimentary density over areas with large residual height. As a general conclusion, while a higher-resolution mass-density model with lateral and radial information might be useful for improved short-scale gravity forward modelling, the acquisition of data to construct such a truly 3D model might be prohibitively difficult.

- Finally, we studied the tree bias effect in the gravitational field forward modelling using two different numerical evaluation methods: the spectral domain and the spatial domain techniques. In the spectral domain, the global gravitational field signals were obtained based on the spherical harmonic analysis and synthesis of the tree canopy bias which was used as the input in the development of the MERIT DEM model. In the spatial domain, we used MERIT DEM to represent the bare-ground Earth's surface, and SRTM V4.1 to indicate the Earth's surface of tree-bias. The differences between SRTM-based and MERIT-based forward modelled gravitational fields indicated the effect of tree bias in gravitational forward modelling. In addition, we evaluated the performance of SRTM V4.1 and MERIT DEM in the gravity forward modelling using ground gravity observations. In the full-scale gravitational field modelling, evaluation points were lifted and more masses were involved. A positive bias effect of up to ~ 2.68 mGal was encountered in the topographic gravity disturbances over vegetated areas. However, in the RTM procedure, the evaluation points were located on the residual masses, which were bounded by the DEM represented surface and its respective smooth surface. As a result, the long-wavelength portion of the tree height bias was removed in the RTM technique, which reduced the tree-bias effect in the RTM gravitational field determination significantly. Its effect on RTM gravity values was small enough to be ignored over large vegetated areas, but not along forest boundaries where sharp changes occurred. The extreme values over these boundaries were ~ 2 mGal for RTM gravity disturbances along the vegetation boundaries. All of the above numerical studies depended on some approximations and simplifications, as follows. First, for simplification and given to the limited knowledge of geological density, the forward modelling was calculated under spherical approximation and constant density assumption of $2,670 \text{ kg/m}^3$ in both spectral domain and the spatial domain. Second, the $30''$ tree canopy bias map for spectral domain analysis was achieved through the arithmetic mean of the $3''$ raw model. This would smooth the raw signals, especially over forest boundaries, though it was necessary considering the cost of spectral domain solution. Therefore, the evaluated effects can be assumed to be somewhat underestimated. Third, in the spatial domain solution, besides tree canopy bias, different void filling databases and noise processing approaches in the MERIT and SRTM V4.1 construction would also affect the comparison values. This cannot be avoided, even though we selected the regional study areas where tree canopy errors should play the dominant role, e.g., tree bias accounts $\sim 83\%$ height differences over Tasmania. But all of these approximations would not influence the following conclusions and interpretations.

As a general conclusion, 1) all external and internal validations demonstrated the promising performance and potential applications of the TGF software for the calculation of gravitational field generated by topo-

graphic masses; 2) compared to the RTM-B and the RTM-C techniques, the RTM-A technique is recommended in the high-frequency gravity field determination. This was demonstrated via the smallest deviations from the novel RTM baseline solution, within sub-mGal level over roughest areas; 3) the improvement of using ellipsoidal approximation rather than the spherical approximation is small enough to be ignored; 4) high-accuracy inputs, i.e., a higher-resolution mass-density model with lateral and radial information and a better representation of bare-ground Earth's surface, lead to slightly improved short-scale gravity forward modelling. However, the acquisition of data to construct such a truly 3D model might be prohibitively challenging.

6.2 Recommendations for future work

We would like to point out some issues, which have not been solved in this thesis and which should be studied in the future.

1) Refinements of the harmonic correction technique

The often used condensation harmonic correction $4\pi G\rho H_{RTM}$ is based on the assumption of a Bouguer gravitational field. As stated in the thesis, the harmonic correction $4\pi G\rho H_{RTM}$ was demonstrated to be too small, and therefore underestimates the true value of harmonic correction. Depending on the magnitude of residual heights in valleys, this approximation error reaches a few mGal up to tens of mGal. Therefore, the further reduction of these errors should be explored in the future, as already pointed out in Forsberg (2010), Omang et al. (2012) and Bucha et al. (2016). Additionally, harmonic correction for the gravitational components of potential and the Marussi tensors should be studied in the future.

2) Terrain gravity model development over Antarctic

Comprehensive knowledge of the Antarctic gravity field is of great significance in studies of Antarctica's geology, ice sheet dynamics and climate-related subjects. However, the present publicly available gravitational field models generated by topographic masses are limited to the continental areas with latitude from 60° S and 85° N, such as short-scale gravitational field ERTM2160 and the latest published model SRTM2gravity which represents the state-of-the-art in terrain gravity field models, but not for the Antarctic continent. The gravity field model developed by *Hirt et al* (2016b) and topographic gravitational field model of *Rexer et al* (2017) represent the state-of-the-art of topographic gravity modelling over Antarctica, but limited to the resolution of 5' and 2' respectively. Thanks to a constellation of satellites in polar orbit, topography information, either for the surface topography or the bedrock topography from bedmap, have been collected with an unprecedented resolution and accuracy over Antarctica and Arctic continents. Depending on these datasets, it is possible to develop the high-resolution topographic gravity field model over these areas.

3) The contribution of ice and water masses in high-frequency gravity field determination The contemporary products of high-frequency gravity field generated by RTM technique, e.g., ERTM2160 and SRTM2gravity,

rely mainly on continental DEMs which provide heights of the Earth's surface. The contribution of ice and water masses in high-frequency gravity field determination, which has been investigated in *Hirt (2013)* and *Yang et al (2018)*, is not modeled. Additionally, ice-sheet masses over Greenland areas are taken into account in contemporary gravity forward modelling, but are given a value of uniform rock density. In future work, gravity signals associated with ice and water masses at highest possible resolution must be modeled rigorously. The effect of ice-density contrast will be carefully addressed.

4) Regional or global gravity field determination:

The evaluation based on the external and internal experiments has demonstrated the promising performance of TGF in the gravity forward modelling. Its potential employments in planets' gravity field recovery will be further studied in the future. Possible applications for gravity field recovery will be further studied in the future, which include 1) the role of RTM gravity in filtering and downward continuation of airborne- or satellite-altitude measurements; 2) the combination techniques when various datasets (e.g., ground gravity observations, airborne and satellite measurements, and information of topography and density-distribution) applied in regional and global gravity field determination; 3) the contributions of RTM gravity field in the framework of remove-compute-restore in regional gravity field determination; 4) the spectral combination of forward modeled high-frequency gravity field and observed gravity field.

Bibliography

- AllahTavakoli Y, Safari A, Ardalan A, Bahrodi A (2015) Application of the RTM-technique to gravity reduction for tracking near-surface mass-density anomalies: A case study of salt diapirs in Iran. *Studia Geophysica et Geodaetica* 59(3):409–423, DOI 10.1007/s11200-014-0215-9, URL <https://doi.org/10.1007/s11200-014-0215-9>
- Amante C, Eakins BW (2009) ETOPO1 arc-minute global relief model: procedures, data sources and analysis
- Amos M (2007) Quasigeoid modelling in New Zealand to unify multiple local vertical datums. PhD thesis, Curtin University
- Asgharzadeh M, Von Frese R, Kim H, Leftwich T, Kim J (2007) Spherical prism gravity effects by Gauss-Legendre quadrature integration. *Geophysical Journal International* 169(1):1–11
- Balmino G (1994) Gravitational potential harmonics from the shape of an homogeneous body. *Celestial Mechanics and Dynamical Astronomy* 60(3):331–364
- Balmino G, Vales N, Bonvalot S, Briais A (2012) Spherical harmonic modelling to ultra-high degree of Bouguer and isostatic anomalies. *Journal of Geodesy* 86(7):499–520
- Barthelmes F (2013) Definition of functionals of the Geopotential and Their Calculation from Spherical Harmonic Models. GFZ Helmholtz-Zentrum, <http://icgem.gfz-potsdam.de/str-0902-revised.pdf>, DOI 10.2312/GFZ.b103-0902-26, URL urn:nbn:de:kobv:b103-0902-26
- Baugh CA, Bates PD, Schumann G, Trigg MA (2013) SRTM vegetation removal and hydrodynamic modeling accuracy. *Water Resources Research* 49(9):5276–5289
- Becker J, Sandwell D, Smith W, Braud J, Binder B, Depner J, Fabre D, Factor J, Ingalls S, Kim S, et al (2009) Global bathymetry and elevation data at 30 arc seconds resolution: SRTM30_PLUS. *Marine Geodesy* 32(4):355–371
- Berry P, Smith R, Benveniste J (2010) ACE2: the new global digital elevation model. In: *Gravity, Geoid and Earth Observation*, Springer, pp 231–237
- Bhang KJ, Schwartz FW, Braun A (2007) Verification of the vertical error in C-band SRTM DEM using ICESat and Landsat-7, Otter Tail County, MN. *IEEE Transactions on Geoscience and Remote Sensing* 45(1):36–44
- Bilker-Koivula M (2014) Assessment of high-resolution global gravity field models and their application in quasi-geoid modelling in Finland. In: *Gravity, Geoid and Height Systems*, Springer, pp 51–58
- Bonvalot S, Balmino G, Briais A, Kuhn M, Peyrefitte A, Vales N, et al (2012) World Gravity Map, 636 1: 50,000,000 map, Eds. , BGI-CGMW-CNES-IRD, Paris. 637

- Braun A, Fotopoulos G (2007) Assessment of SRTM, ICESat, and survey control monument elevations in Canada. *Photogrammetric Engineering & Remote Sensing* 73(12):1333–1342
- Bucha B, Janák J (2013) A MATLAB-based graphical user interface program for computing functionals of the geopotential up to ultra-high degrees and orders. *Computers & Geosciences* 56:186–196
- Bucha B, Janák J (2014) A MATLAB-based graphical user interface program for computing functionals of the geopotential up to ultra-high degrees and orders: Efficient computation at irregular surfaces. *Computers & Geosciences* 66:219–227
- Bucha B, Janák J, Papčo J, Bezděk A (2016) High-resolution regional gravity field modelling in a mountainous area from terrestrial gravity data. *Geophysical Journal International* 207(2):949–966
- Bucha B, Hirt C, Kuhn M (2019) Cap integration in spectral gravity forward modelling: near-and far-zone gravity effects via Molodensky's truncation coefficients. *Journal of Geodesy* 93(1):65–83
- Carabajal CC, Harding DJ (2006) SRTM C-band and ICESat laser altimetry elevation comparisons as a function of tree cover and relief. *Photogrammetric Engineering & Remote Sensing* 72(3):287–298
- Casenave F, Métivier L, Pajot-Métivier G, Panet I (2016) Fast computation of general forward gravitation problems. *Journal of Geodesy* 90(7):655–675
- Cella F (2015) GTeC—A versatile MATLAB® tool for a detailed computation of the terrain correction and Bouguer gravity anomalies. *Computers & Geosciences* 84:72–85
- Center ED, GTOPO30 E (1996) Global 30 arc-second elevation data set
- Chen W, Tenzer R (2015) Harmonic coefficients of the Earth's spectral crustal model 180–ESCM180. *Earth Science Informatics* 8(1):147–159
- Claessens S, Hirt C (2013) Ellipsoidal topographic potential: new solutions for spectral forward gravity modeling of topography with respect to a reference ellipsoid. *Journal of Geophysical Research: Solid Earth* 118(11):5991–6002
- Claessens S, Hirt C, Featherstone W, Kirby J (2009) Computation of a new gravimetric quasigeoid model for New Zealand. Contract Report for LINZ Curtin University of Technology, Perth p 39
- Clynch JR (2006) Geodetic coordinate conversions i. Geodetic to/from Geocentric Latitude Available online: <http://clynchg3c.com/Technote/geodesy/coordcvt.pdf> (accessed on 9 May 2017)
- Danielson JJ, Gesch DB (2011) Global multi-resolution terrain elevation data 2010 (GMTED2010). , US Geological Survey
- Deng XL, Grombein T, Shen WB, Heck B, Seitz K (2016) Corrections to “A comparison of the tesseroid, prism and point-mass approaches for mass reductions in gravity field modelling”(Heck and Seitz, 2007) and “Optimized formulas for the gravitational field of a tesseroid”(Grombein et al., 2013). *Journal of Geodesy* 90(6):585–587
- Denker H (2013) Regional gravity field modeling: theory and practical results. In: *Sciences of Geodesy-II*, Springer, pp 185–291
- DiMiceli C, Carroll M, Sohlberg R, Huang C, Hansen M, Townshend J (2017) Annual global automated MODIS vegetation continuous fields (MOD44B) at 250 m spatial resolution for data years beginning day 65, 2000-2010

- Dziewonski A, Hales A, Lapwood E (1975) Parametrically simple Earth models consistent with geophysical data. *Physics of the Earth and Planetary Interiors* 10(1):12–48
- Dziewonski AM, Anderson DL (1981) Preliminary reference Earth model. *Physics of the Earth and Planetary Interiors* 25(4):297–356
- Ellmann A (2010) Validation of the new Earth Gravitational Model EGM08 over the Baltic countries. In: *Gravity, Geoid and Earth Observation*, Springer, pp 489–496
- Eshagh M (2009) The effect of lateral density variations of crustal and topographic masses on GOCE gradiometric data—A study in Iran and Fennoscandia. *Acta Geodaetica et Geophysica Hungarica* 44(4):399–418
- Farr TG, Rosen PA, Caro E, Crippen R, Duren R, Hensley S, Kobrick M, Paller M, Rodriguez E, Roth L, et al (2007) The shuttle radar topography mission. *Reviews of Geophysics* 45(2)
- Foroughi I, Vaníček P, Kingdon RW, Goli M, Sheng M, Afrasteh Y, Novák P, Santos MC (2019) Sub-centimetre geoid. *Journal of Geodesy* 93(6):849–868, DOI 10.1007/s00190-018-1208-1, URL <https://doi.org/10.1007/s00190-018-1208-1>
- Forsberg R (1984) A study of terrain reductions, density anomalies and geophysical inversion methods in gravity field modelling. , Ohio State Univ Columbus Dept Of Geodetic Science and Surveying
- Forsberg R (2010) Geoid determination in the mountains using ultra-high resolution spherical harmonic models—the Auvergne case. The apple of the knowledge, In Honor of Professor Emeritus Demetrius N Arabelos pp 101–111
- Forsberg R, Tscherning CC (1981) The use of height data in gravity field approximation by collocation. *Journal of Geophysical Research: Solid Earth* 86(B9):7843–7854
- Förste C, Bruinsma S, Abrikosov O, Flechtner F, Marty JC, Lemoine JM, Dahle C, Neumayer H, Barthelmes F, König R, et al (2014) EIGEN-6C4-The latest combined global gravity field model including GOCE data up to degree and order 1949 of GFZ Potsdam and GRGS Toulouse. In: *EGU General Assembly Conference Abstracts*, vol 16
- Fujisada H, Urai M, Iwasaki A (2012) Technical methodology for ASTER global DEM. *IEEE Transactions on Geoscience and Remote Sensing* 50(10):3725–3736
- Fukushima T (2012) Numerical computation of spherical harmonics of arbitrary degree and order by extending exponent of floating point numbers. *Journal of Geodesy* 86(4):271–285
- Gilardoni M, Reguzzoni M, Sampietro D (2016) GECO: a global gravity model by locally combining GOCE data and EGM2008. *Studia Geophysica et Geodaetica* 60(2):228–247
- Grombein T, Seitz K, Heck B (2013) Optimized formulas for the gravitational field of a tesseroid. *Journal of Geodesy* 87(7):645–660
- Grombein T, Seitz K, Heck B (2013, P647) Optimized formulas for the gravitational field of a tesseroid. *Journal of Geodesy* 87(7):645–660
- Grombein T, Luo X, Seitz K, Heck B (2014) A wavelet-based assessment of topographic-isostatic reductions for GOCE gravity gradients. *Surveys in Geophysics* 35(4):959–982

- Grombein T, Seitz K, Heck B (2016) The Rock–Water–Ice topographic gravity field model RWI_TOPO_2015 and its comparison to a conventional Rock-Equivalent version. *Surveys in Geophysics* 37(5):937–976
- Grüninger W (1990) Zur topographisch-isostatischen Reduktion der Schwere. na
- Harrison J, Dickinson M (1989) Fourier transform methods in local gravity modeling. *Bulletin géodésique* 63(2):149–166
- Heck B, Seitz K (2007) A comparison of the tesseroid, prism and point-mass approaches for mass reductions in gravity field modelling. *Journal of Geodesy* 81(2):121–136
- Heck B, Seitz K (2007, P.126) A comparison of the tesseroid, prism and point-mass approaches for mass reductions in gravity field modelling. *Journal of Geodesy* 81(2):121–136
- Hinze WJ (2003) Bouguer reduction density, why 2.67? *Geophysics* 68(5):1559–1560
- Hirt C (2010) Prediction of vertical deflections from high-degree spherical harmonic synthesis and residual terrain model data. *Journal of Geodesy* 84(3):179–190
- Hirt C (2013) RTM gravity forward-modeling using topography/bathymetry data to improve high-degree global geopotential models in the coastal zone. *Marine Geodesy* 36(2):183–202
- Hirt C (2014) Digital terrain models. *Encyclopedia of Geodesy* pp 1–6
- Hirt C (2016) Gravity forward modelling. In: *Encyclopedia of Geodesy* (ed. E. Grafarend), Springer, Berlin, New York, DOI doi:10.1007/978-3-319-02370-0_106-1
- Hirt C (2018) Artefact detection in global digital elevation models (DEMs): The Maximum Slope Approach and its application for complete screening of the SRTM v4. 1 and MERIT DEMs. *Remote Sensing of Environment* 207:27–41
- Hirt C, Kuhn M (2014) Band-limited topographic mass distribution generates full-spectrum gravity field: Gravity forward modeling in the spectral and spatial domains revisited. *Journal of Geophysical Research: Solid Earth* 119(4):3646–3661
- Hirt C, Rexer M (2015) Earth2014: 1 arc-min shape, topography, bedrock and ice-sheet models—available as gridded data and degree-10,800 spherical harmonics. *International Journal of Applied Earth Observation and Geoinformation* 39:103–112
- Hirt C, Featherstone W, Marti U (2010a) Combining EGM2008 and SRTM/DTM2006. 0 residual terrain model data to improve quasigeoid computations in mountainous areas devoid of gravity data. *Journal of Geodesy* 84(9):557–567
- Hirt C, Marti U, Bürki B, Featherstone W (2010b) Assessment of EGM2008 in Europe using accurate astrogeodetic vertical deflections and omission error estimates from SRTM/DTM2006. 0 residual terrain model data. *Journal of Geophysical Research: Solid Earth* 115(B10)
- Hirt C, Kuhn M, Featherstone W, Göttl F (2012) Topographic/isostatic evaluation of new-generation GOCE gravity field models. *Journal of Geophysical Research: Solid Earth* 117(B5)
- Hirt C, Claessens S, Fecher T, Kuhn M, Pail R, Rexer M (2013) New ultrahigh-resolution picture of Earth's gravity field. *Geophysical Research Letters* 40(16):4279–4283

- Hirt C, Kuhn M, Claessens S, Pail R, Seitz K, Gruber T (2014) Study of the Earth short-scale gravity field using the ERTM2160 gravity model. *Computers & Geosciences* 73:71–80
- Hirt C, Reußner E, Rexer M, Kuhn M (2016a) Topographic gravity modeling for global Bouguer maps to degree 2160: Validation of spectral and spatial domain forward modeling techniques at the 10 microGal level. *Journal of Geophysical Research: Solid Earth* 121(9):6846–6862
- Hirt C, Rexer M, Scheinert M, Pail R, Claessens S, Holmes S (2016b) A new degree-2190 (10 km resolution) gravity field model for antarctica developed from grace, goce and bedmap2 data. *Journal of Geodesy* 90(2):105–127
- Hirt C, Bucha B, Yang M, Kuhn M (2019a) A numerical study of residual terrain modelling (RTM) techniques and the harmonic correction using ultra-high-degree spectral gravity modelling. *Journal of Geodesy* pp 1–18
- Hirt C, Yang M, Kuhn M, Bucha B, Kurzmann A, Pail R (2019b) SRTM2gravity: an ultrahigh resolution global model of gravimetric terrain corrections. *Geophysical Research Letters* 46(9):4618–4627
- Hofmann-Wellenhof B, Moritz H (2006) *Physical geodesy*. Springer Science & Business Media
- Huang C, Yang L, Wylie BK, Homer C (2001) A strategy for estimating tree canopy density using Landsat 7 ETM+ and high resolution images over large areas
- Hwang C, Wang CG, Hsiao YS (2003) Terrain correction computation using Gaussian quadrature. *Computers & Geosciences* 29(10):1259–1268
- ICSM (1994) Geocentric datum of Australia (gda)—technical manual— v2.3 (1). Canberra ACT: Intergovernmental Committee on Surveying Mapping
- Jacoby W, Smilde PL (2009) *Gravity interpretation: fundamentals and application of gravity inversion and geological interpretation*. Springer Science & Business Media
- Jarvis A, Reuter HI, Nelson A, Guevara E, et al (2008) Hole-filled SRTM for the globe Version 4, available from the CGIAR-CSI SRTM 90m Database
- Jekeli C (2015) *Potential theory and the static gravity field of the earth*
- Jekeli C, Yanh H, Kwon JH (2009) Evaluation of EGM08—globally and locally in South Korea. *Newton's Bulletin Issue* (4):38–49
- Kadlec M (2011) *Refining gravity field parameters by residual terrain modeling*. PhD thesis p 150
- Kennett BL, Engdahl E, Buland R (1995) Constraints on seismic velocities in the Earth from traveltimes. *Geophysical Journal International* 122(1):108–124
- Konoshov V, Nepoklonov V, Polovnev O (2017) One technique for refining the global Earth gravity models. *Izvestiya, Physics of the Solid Earth* 53(1):108–115
- Kuhn M, Hirt C (2016) Topographic gravitational potential up to second-order derivatives: an examination of approximation errors caused by rock-equivalent topography (RET). *Journal of Geodesy* 90(9):883–902

- Kuhn M, Seitz K (2005) Comparison of Newton's Integral in the Space and Frequency Domains. In: Sansò F (ed) *A Window on the Future of Geodesy*, Springer Berlin Heidelberg, Berlin, Heidelberg, pp 386–391
- Kühtreiber N (1998) Precise geoid determination using a density variation model. *Physics and Chemistry of the Earth* 23(1):59–63
- Kvas A, Mayer-Gürr T, Krauss S, Brockmann JM, Schubert T, Schuh WD, Pail R, Gruber T, Jäggi A, Meyer U (2019) The satellite-only gravity field model GOCO06s. *GFZ Data Services*
- Laske G, Masters G, Ma Z, Pasyanos M (2013) Update on CRUST1.0—A 1-degree global model of Earth's crust. In: *Geophys. Res. Abstr*, EGU General Assembly Vienna, Austria, vol 15, p 2658
- Lee SB, Auh SC, Seo DY (2017) Evaluation of global and regional geoid models in South Korea by using terrestrial and GNSS data. *KSCE Journal of Civil Engineering* 21(5):1905–1911
- Li Z, Zhu C, Gold C (2004) *Digital terrain modeling: principles and methodology*. CRC press
- Liu X (2008) Airborne LiDAR for DEM generation: some critical issues. *Progress in Physical Geography* 32(1):31–49
- Mader K (1951) Das Newtonsche Raumpotential prismatischer Körper und seine Ableitungen bis zur 3. Ordnung Österr Z f, *Vermessungswesen*, Sonderheft 11
- Martinec Z (1993) Effect of lateral density variations of topographical masses in view of improving geoid model accuracy over Canada. Contract report for Geodetic Survey of Canada
- Martinec Z (1994) Direct topographical effect of Helmert's condensation for a spherical approximation of the geoid. *Manuscr Geodaet* 19:257–268
- Mayer-Gürr T, Eicker A, Kurtenbach E, Ilk KH (2010) ITG-GRACE: global static and temporal gravity field models from GRACE data. In: *System Earth via Geodetic-Geophysical Space Techniques*, Springer, pp 159–168
- Miliareisis G, Delikaraoglou D (2009) Effects of percent tree canopy density and DEM misregistration on SRTM/NED vegetation height estimates. *Remote Sensing* 1(2):36–49
- Mohr PJ, Taylor BN, Newell DB (2012) CODATA recommended values of the fundamental physical constants: 2010. *Journal of Physical and Chemical Reference Data* 41(4):1527
- Nagy D, Papp G, Benedek J (2000) The gravitational potential and its derivatives for the prism. *Journal of Geodesy* 74(7-8):552–560
- Nagy D, Papp G, Benedek J (2002) Corrections to “the gravitational potential and its derivatives for the prism”. *Journal of Geodesy* 76(8):475–475
- Nielsen J, Tscherning CC, Jansson TR, Forsberg R (2012) Development and User Testing of a Python Interface to the GRAVSOFT Gravity Field Programs. In: *Geodesy for Planet Earth*, Springer, pp 443–449
- Odera PA (2016) Assessment of EGM2008 using GPS/levelling and free-air gravity anomalies over Nairobi County and its environs. *South African Journal of Geomatics* 5(1):17–30

- O'Loughlin F, Paiva R, Durand M, Alsdorf D, Bates P (2016) A multi-sensor approach towards a global vegetation corrected SRTM DEM product. *Remote Sensing of Environment* 182:49–59
- Omang OC, Tscherning CC, Forsberg R (2012) Generalizing the harmonic reduction procedure in residual topographic modeling. In: VII Hotine-Marussi Symposium on Mathematical Geodesy, Springer, pp 233–238
- Pail R, Goiginger H, Schuh WD, Höck E, Brockmann JM, Fecher T, Gruber T, Mayer-Gürr T, Kusche J, Jäggi A, et al (2010) Combined satellite gravity field model GOCO01S derived from GOCE and GRACE. *Geophysical Research Letters* 37(20)
- Paine DP, Kiser JD (2012) *Aerial photography and image interpretation*. John Wiley & Sons
- Panning M, Romanowicz B (2006) A three-dimensional radially anisotropic model of shear velocity in the whole mantle. *Geophysical Journal International* 167(1):361–379
- Patel A, Katiyar S, Prasad V (2016) Performances evaluation of different open source DEM using Differential Global Positioning System (DGPS). *The Egyptian Journal of Remote Sensing and Space Science* 19(1):7–16
- Pavlis N, Holmes S, Kenyon S, Factor J (2013) Correction to “The development and evaluation of the Earth Gravitational Model 2008 (EGM2008)”. *Journal of Geophysical Research: Solid Earth* 118(5):2633–2633
- Pavlis NK, Rapp RH (1990) The development of an isostatic gravitational model to degree 360 and its use in global gravity modelling. *Geophysical Journal International* 100(3):369–378, DOI 10.1111/j.1365-246X.1990.tb00691.x, URL <https://doi.org/10.1111/j.1365-246X.1990.tb00691.x>, <http://oup.prod.sis.lan/gji/article-pdf/100/3/369/1911926/100-3-369.pdf>
- Pavlis NK, Factor JK, Holmes SA (2007) Terrain-related gravimetric quantities computed for the next EGM. In: *Proceedings of the 1st International Symposium of the International Gravity Field Service (IGFS)*, Istanbul, pp 318–323
- Pavlis NK, Holmes SA, Kenyon SC, Factor JK (2012) The development and evaluation of the Earth Gravitational Model 2008 (EGM2008). *Journal of Geophysical Research: Solid Earth* 117(B4)
- Petrović S (1996) Determination of the potential of homogeneous polyhedral bodies using line integrals. *Journal of Geodesy* 71(1):44–52, DOI 10.1007/s001900050074, URL <https://doi.org/10.1007/s001900050074>
- Ramillien G, Lombard A, Cazenave A, Ivins E, Llubes M, Remy F, Biancale R (2006) Interannual variations of the mass balance of the Antarctica and Greenland ice sheets from GRACE. *Global and Planetary Change* 53(3):198–208
- Reigber C, Schwintzer P, Neumayer KH, Barthelmes F, König R, Förste C, Balmino G, Biancale R, Lemoine JM, Loyer S, et al (2003) The CHAMP-only Earth gravity field model EIGEN-2. *Advances in Space Research* 31(8):1883–1888
- Rexer M (2016) Ultra-high-degree extension (v1. 0) of SHTOOLS
- Rexer M (2017) Spectral solutions to the topographic potential in the context of high-resolution global gravity field modelling. PhD thesis, Technische Universität München
- Rexer M, Hirt C (2015) Spectral analysis of the Earth's topographic potential via 2D-DFT: a new data-based degree variance model to degree 90,000. *Journal of Geodesy* 89(9):887–909

- Rexer M, Hirt C (2016) Evaluation of intermediate TanDEM-X digital elevation data products over Tasmania using other digital elevation models and accurate heights from the Australian National Gravity Database. *Australian Journal of Earth Sciences* 63(5):599–609
- Rexer M, Hirt C, Claessens S, Tenzer R (2016) Layer-based modelling of the Earth's gravitational potential up to 10-km scale in spherical harmonics in spherical and ellipsoidal approximation. *Surveys in Geophysics* 37(6):1035–1074
- Rexer M, Hirt C, Pail R (2017) High-resolution global forward modelling: a degree-5480 global ellipsoidal topographic potential model. In: *EGU General Assembly Conference Abstracts*, vol 19, p 7725
- Rexer M, Hirt C, Bucha B, Holmes S (2018) Solution to the spectral filter problem of residual terrain modelling (RTM). *Journal of Geodesy* 92(6):675–690
- Root B, Novák P, Dirx D, Kaban M, van der Wal W, Vermeersen L (2016) On a spectral method for forward gravity field modelling. *Journal of Geodynamics* 97:22–30
- Roussel C, Verdun J, Cali J, Masson F (2015) Complete gravity field of an ellipsoidal prism by Gauss–Legendre quadrature. *Geophysical Supplements to the Monthly Notices of the Royal Astronomical Society* 203(3):2220–2236
- Rummel R, Rapp RH, Suenkel H, Tscherning CC (1988) Comparisons of global topographic/isostatic models to the Earth's observed gravity field
- Sansò F, Sideris MG (2013) *Geoid determination: theory and methods*. Springer Science & Business Media
- Schumann G, Matgen P, Cutler M, Black A, Hoffmann L, Pfister L (2008) Comparison of remotely sensed water stages from LiDAR, topographic contours and SRTM. *ISPRS journal of photogrammetry and remote sensing* 63(3):283–296
- Schumann GJP, Bates PD (2018) The need for a high-accuracy, open-access global DEM. *Frontiers in Earth Science* 6:225
- Sexton JO, Song XP, Feng M, Noojipady P, Anand A, Huang C, Kim DH, Collins KM, Channan S, DiMiceli C, et al (2013) Global, 30-m resolution continuous fields of tree cover: Landsat-based rescaling of MODIS vegetation continuous fields with LiDAR-based estimates of error. *International Journal of Digital Earth* 6(5):427–448
- Simard M, Pinto N, Fisher JB, Baccini A (2011) Mapping forest canopy height globally with spaceborne lidar. *Journal of Geophysical Research: Biogeosciences* 116(G4)
- Simmons NA, Forte AM, Boschi L, Grand SP (2010) GyPSuM: a joint tomographic model of mantle density and seismic wave speeds. *Journal of Geophysical Research: Solid Earth* 115(B12)
- Sjöberg LE (2004) The effect on the geoid of lateral topographic density variations. *Journal of Geodesy* 78(1-2):34–39
- Smith D, Robertson D, Milbert D (2001) Gravitational attraction of local crustal masses in spherical coordinates. *Journal of Geodesy* 74(11-12):783–795
- Smith WH, Sandwell DT (1997) Global sea floor topography from satellite altimetry and ship depth soundings. *Science* 277(5334):1956–1962
- SPOT I (2006) SPOT DEM Precision Product description.

- Šprlák M, Gerlach C, Pettersen B (2012) Validation of GOCE global gravity field models using terrestrial gravity data in Norway. *Journal of Geodetic Science* 2(2):134–143
- Suárez JC, Ontiveros C, Smith S, Snape S (2005) Use of airborne LiDAR and aerial photography in the estimation of individual tree heights in forestry. *Computers & Geosciences* 31(2):253–262
- Tachikawa T (2001) ASTER Global Digital Elevation Model Version 2 – Summary of Validation Results. sl: ASTER GDEM Validation Team
- Tadono T, Ishida H, Oda F, Naito S, Minakawa K, Iwamoto H (2014) Precise global DEM generation by ALOS PRISM. *ISPRS Annals of the Photogrammetry, Remote Sensing and Spatial Information Sciences* 2(4):71
- Tamisiea M, Mitrovica J, Milne G, Davis J (2001) Global geoid and sea level changes due to present-day ice mass fluctuations. *Journal of Geophysical Research: Solid Earth* 106(B12):30,849–30,863
- Tapley BD, Chambers DP, Bettadpur S, Ries JC (2003) Large scale ocean circulation from the GRACE GGM01 geoid. *Geophysical Research Letters* 30(22)
- Tenzer R, Hamayun Z, Prutkin I (2010) A comparison of various integration methods for solving Newton's integral in detailed forward modelling. In: *Gravity, Geoid and Earth Observation*, Springer, pp 361–368
- Tenzer R, Sirguey P, Rattenbury M, Nicolson J (2011) A digital rock density map of New Zealand. *Computers & Geosciences* 37(8):1181–1191
- Tenzer R, Gladkikh V, Novák P, Vajda P (2012) Spatial and spectral analysis of refined gravity data for modelling the crust–mantle interface and mantle-lithosphere structure. *Surveys in Geophysics* 33(5):817–839
- Tenzer R, Chen W, Jin S (2015a) Effect of upper mantle density structure on Moho geometry. *Pure and Applied Geophysics* 172(6):1563–1583
- Tenzer R, Chen W, Tsoulis D, Bagherbandi M, Sjöberg LE, Novák P, Jin S (2015b) Analysis of the refined CRUST1.0 crustal model and its gravity field. *Surveys in Geophysics* 36(1):139–165, DOI 10.1007/s10712-014-9299-6, URL <https://doi.org/10.1007/s10712-014-9299-6>
- Torge W, Müller J (2012) *Geodesy*. Walter de Gruyter
- Tóth G, Szűcs E (2011) On the determination of a new combined EGM2008 based quasi-geoid model for Hungary. *Acta Geodaetica et Geophysica Hungarica* 46(4):417–430
- Tozer B, Sandwell D, Smith W, Olson C, Beale J, Wessel P (2019) Global bathymetry and topography at 15 arc seconds: SRTM15+. *Earth and Space Science*
- Tscherning C (1976) Computation of the second-order derivatives of the normal potential based on the representation by a Legendre series. *Manuscr Geod* 1:71–92
- Tsoulis D (2001) Terrain correction computations for a densely sampled DTM in the Bavarian Alps. *Journal of Geodesy* 75(5-6):291–307
- Tsoulis D (2012) Analytical computation of the full gravity tensor of a homogeneous arbitrarily shaped polyhedral source using line integrals. *Geophysics* 77(2):F1–F11

- Tsoulis D, Petrović S (2001) On the singularities of the gravity field of a homogeneous polyhedral body. *Geophysics* 66(2):535–539
- Tsoulis D, Novák P, Kadlec M (2009) Evaluation of precise terrain effects using high-resolution digital elevation models. *Journal of Geophysical Research: Solid Earth* 114(B2)
- Tziavos I, Featherstone W (2001) First results of using digital density data in gravimetric geoid computation in Australia. In: *Gravity, Geoid and Geodynamics 2000*, Springer, pp 335–340
- Tziavos IN, Sideris MG (2013) Topographic reductions in gravity and geoid modeling. In: *Geoid Determination*, Springer, pp 337–400
- Uieda L, Barbosa VC, Braitenberg C (2016) Tesseroids: Forward-modeling gravitational fields in spherical coordinates. *Geophysics* 81(5):F41–F48
- Vergos GS, Grigoriadis VN, Tziavos IN, Kotsakis C (2014) Evaluation of GOCE/GRACE Global Geopotential Models over Greece with Collocated GPS/Levelling Observations and Local Gravity Data. In: Marti U (ed) *Gravity, Geoid and Height Systems*, Springer International Publishing, Cham, pp 85–92
- Vergos GS, Erol B, Natsiopoulos DA, Grigoriadis VN, Işık MS, Tziavos IN (2018) Preliminary results of GOCE-based height system unification between Greece and Turkey over marine and land areas. *Acta Geodaetica et Geophysica* 53(1):61–79, DOI 10.1007/s40328-017-0204-x, URL <https://doi.org/10.1007/s40328-017-0204-x>
- Wang YM (2012) On the omission errors due to limited grid size in geoid computations. In: *VII Hotine-Marussi Symposium on Mathematical Geodesy*, Springer, pp 221–226
- Wessel B, Huber M, Wohlfart C, Marschalk U, Kosmann D, Roth A (2018) Accuracy assessment of the global TanDEM-X Digital Elevation Model with GPS data. *ISPRS Journal of Photogrammetry and Remote Sensing* 139:171–182
- Wieczorek MA (2007) Gravity and topography of the terrestrial planets. *Treatise on Geophysics* 10:165–206
- Wieczorek MA (2015) Gravity and topography of the terrestrial planets. *Treatise on Geophysics* 10(257):153–193
- Wieczorek MA, Meschede M (2018) Tools for working with spherical harmonics. *Geochemistry, Geophysics, Geosystems* 19(8):2574–2592
- Wild-Pfeiffer F (2008) A comparison of different mass elements for use in gravity gradiometry. *Journal of Geodesy* 82(10):637–653
- Willberg M, Gruber T, Vergos GS (2017) Analysis of goce omission error and its contribution to vertical datum offsets in greece and its islands. In: Vergos GS, Pail R, Barzaghi R (eds) *International Symposium on Gravity, Geoid and Height Systems 2016*, Springer International Publishing, Cham, pp 143–148
- Willberg M, Zingerle P, Pail R (2019) Residual least-squares collocation: use of covariance matrices from high-resolution global geopotential models. *Journal of Geodesy* DOI 10.1007/s00190-019-01279-1, URL <https://doi.org/10.1007/s00190-019-01279-1>
- Yamazaki D, Ikeshima D, Tawatari R, Yamaguchi T, O'Loughlin F, Neal JC, Sampson CC, Kanae S, Bates PD (2017) A high-accuracy map of global terrain elevations. *Geophysical Research Letters* 44(11):5844–5853

- Yang M, Hirt C, Tenzer R, Pail R (2018) Experiences with the use of mass-density maps in residual gravity forward modelling. *Studia Geophysica et Geodaetica* 62(4):596–623
- Yang M, Hirt C, Rexer M, Pail R, Yamazaki D (2019) The tree canopy effect in gravity forward modelling. *Geophysical Journal International*
- Zingerle JMPRGW Philipp; Brockmann (2019) The polar extended gravity field model tim-r6e. GFZ Data Services DOI <http://doi.org/10.5880/ICGEM.2019.005>

Appendix A

Publications

Partial results appearing in Chapters 4, 5 have been peer-reviewed prior to publications in international academix journals:

Yang, M., Hirt, C., Tenzer, R., Pail, R., 2018. Experiences with the use of mass density maps in residual gravity forward modelling. *Stud. Geophys. Geod.*, 62, Doi: 10.1007/s11200-017-0452-9.

Yang, M., Hirt, C., Rexer, M., Pail, R., Yamazaki, D., 2019. The tree-canopy effect in gravity forward modelling, *Geophysical Journal International*, 219 (1), October 2019, P 271–289, doi: <https://doi.org/10.1093/gji/ggz264>.

The contents in Chapter 4 is currently under review:

Yang, M., Hirt, C., Pail, R., 2019. TGF: A New MATLAB-based Software for Terrain-related Gravity Field Calculations.

Other related publications and submissions:

Hirt, C., Yang, M., Kuhn, M., Bucha, B., Kurzmann, A., Pail, R., 2019a. SRTM2gravity: an ultrahigh resolution global model of gravimetric terrain corrections. *Geophys. Res. Lett.*, 46, doi: <https://doi.org/10.1029/2019GL082521>.

Hirt, C., Bucha, B., Yang, M., Kuhn, M., 2019b. A numerical study of residual terrain modelling (RTM) techniques and the harmonic correction using ultra-high degree spectral gravity modelling, revised, *J. Geod.*, online first.

Bucha, B., Hirt, C., Yang, M., Kuhn, M., Rexer, M., 2019. Residual terrain modelling (RTM) in terms of the cap-modified spectral technique: RTM from a new perspective, *Journal of Geodesy*.

I warrant that I have obtained, where necessary, permission from the copyright owners to use any third-party copyright material reproduced in the thesis, or to use any of my own published work in which the copyright is held by another party.

Appendix B

Statement of contribution of others

The statement of contribution of signed by co-authors follows:

B.1 Publication I: Experiences with the use of mass density maps in residual gravity forward modelling

Reference: (located in Chapter 5)

Yang, M., Hirt, C., Tenzer, R., Pail, R., 2018. Experiences with the use of mass density maps in residual gravity forward modelling. Stud. Geophys. Geod., 62, Doi: 10.1007/s11200-017-0452-9.

Copyright:

This work originally has been published in Journal of Studia Geophysica et Geodaetica, available at <https://link.springer.com/article/10.1007/s11200-017-0656-z>, and is reused here with permissions of Springer. The copyright has been transferred to Springer Netherlands.

Declaration of own contribution

The following people and institutions contributed to the publication of this work:

Tab. B.1 – Statement of Co authorship

Authors	Name of School
Meng Yang (MY)	Institute for Astronomical and Physical Geodesy, Technical University of Munich
Christian Hirt (CH)	Institute for Astronomical and Physical Geodesy, Technical University of Munich
Robert Tenzer (RT)	Department of Land Surveying and Geo-Informatics, Hong Kong Polytechnic University
Roland Pail (RP)	Institute for Astronomical and Physical Geodesy, Technical University of Munich

CH had the idea to study the performance of mass-density map in RTM gravity forward modelling. RT provided us with digital density map of New Zealand. MY developed the software and computed all numerical results. The analysis and interpretation of the results originate from MY and were improved by discussions with CH and RP. MY wrote the first draft of the manuscript and CH has contributed significantly to the writing process of the manuscript. Overall, own contribution of MY is estimated at 70% to the planning, execution and preparation of the work for the paper.

Confirmation by the Co-Author:

I hereby confirm the correctness of the declaration of own contribution by Meng Yang for the publication:

Yang, M., Hirt, C., Tenzer, R., Pail, R., 2018. Experiences with the use of mass density maps in residual gravity forward modelling. Stud. Geophys. Geod., 62, Doi: 10.1007/s11200-017-0452-9.

Christian Hirt

Signature: 

Date: 6 Sept. 2019

Robert Tenzer

Signature: 

Date: 10 Sept. 2019

Roland Pail

Signature: 

Date: 12.9.2019

B.2 Publication II: The tree canopy effect in gravity forward modelling

Reference: (located in Chapter 5)

Yang, M., Hirt, C., Rexer, M., Pail, R., Yamazaki, D., 2019. The tree-canopy effect in gravity forward modelling, *Geophysical Journal International*, 219 (1), October 2019, P 271–289, doi: <https://doi.org/10.1093/gji/ggz264>.

Copyright:

This work has been accepted and will be published in *Geophysical Journal International*, available at <https://academic.oup.com/gji/article-abstract/219/1/271/5512594>, and is reused here with permissions of Oxford University Press. The copyright belongs to the publisher, Oxford University Press.

Declaration of own contribution

The following people and institutions contributed to the publication of this work:

Tab. B.2 – Statement of Co authorship

Authors	Name of School
Meng Yang (MY)	Institute for Astronomical and Physical Geodesy, Technical University of Munich
Christian Hirt (CH)	Institute for Astronomical and Physical Geodesy, Technical University of Munich
Moritz Rexer (MR)	Institute for Astronomical and Physical Geodesy, Technical University of Munich
Roland Pail (RP)	Institute for Astronomical and Physical Geodesy, Technical University of Munich
Dai Yamazaki (DY)	Institute of Industrial Science, The University of Tokyo, Tokyo, Japan

CH and MY had the idea to study the tree canopy in generally used mix-DSM/DTM and its effect in RTM gravity forward modelling. DY provided a 30" global tree-bias model. MR assisted MY with numerical experiments in global spectral analysis of tree canopy effect. MY and CH contributed to the conception and design of the research project. MY was primarily responsible for the numerical experiments and data analysis with guidance from CH and RP and prepared the first draft of the manuscript. CH assisted MY with interpretation and redrafted sections of the manuscript for publication. Overall, own contribution of MY is estimated at 90% to the planning, execution, and preparation of the work for the paper.

Confirmation by the Co-Author:


I hereby confirm the correctness of the declaration of own contribution by Meng Yang for the publication:

Yang, M., Hirt, C., Rexer, M., Pail, R., Yamazaki, D., 2019. The tree-canopy effect in gravity forward modelling, *Geophysical Journal International*, 219 (1), October 2019, P 271–289, doi: <https://doi.org/10.1093/gji/ggz264>.

Christian Hirt

Signature:  Date: 6. Sept. 2019

Moritz Rexer

Signature:  Date: 9. Sept. 2019

Roland Pail

Signature: *R Pail* Date: *12. P. 2019*

Dai Yamazaki

Signature: *Dai Yamazaki* Date: *8 Sep, 2019*

B.3 Submission III: TGF: A New MATLAB-based Software for Terrain-related Gravity Field Calculations

Reference: (located in Chapter 5)

Yang, M., Hirt, C., Pail, R., 2019. TGF: A New MATLAB-based Software for Terrain-related Gravity Field Calculations.

Copyright:

This work has been prepared and will be submitted to the journal Computers & Geosciences. As long as it is published, the copyright will be transferred to the publisher.

Declaration of own contribution

The following people and institutions contributed to the publication of this work:

Tab. B.3 – Statement of Co authorship

Authors	Name of School
Meng Yang (MY)	Institute for Astronomical and Physical Geodesy, Technical University of Munich
Christian Hirt (CH)	Institute for Astronomical and Physical Geodesy, Technical University of Munich
Roland Pail (RP)	Institute for Astronomical and Physical Geodesy, Technical University of Munich

CH developed the idea to create the forward modelling software and defined the required software capabilities, and the necessary validation experiments. MY was responsible for the software implementation and carried out all numerical tests and validation experiments, created all figures and tables in the paper, and wrote the first draft of the manuscript. It was edited to incorporate some comments and suggestions made by the supervisors CH and RP. Overall, own contribution of MY is estimated at 70% to the planning, execution and preparation of the work for the paper.

Confirmation by the Co-Author:

I hereby confirm the correctness of the declaration of own contribution by Meng Yang for the publication:

Yang, M., Hirt, C., Pail, R., 2019. TGF: A New MATLAB-based Software for Terrain-related Gravity Field Calculations.

Christian Hirt

Signature:  Date: 6. Sept. 2019

Roland Pail

Signature:  Date: 12. 9. 2019